

# FAST STARS IN THE MILKY WAY

DOUGLAS BOUBERT



Churchill College  
University of Cambridge  
July 2018

This dissertation is submitted for the degree of Doctor of Philosophy.



## SUMMARY

---

I present a comprehensive investigation of fast stars in the Milky Way, from brisk disc stars to stars escaping the Galaxy. My thesis is that fast stars are the smoking guns of extreme stellar collisions and explosions, and so can act as an intermediary to studying these theoretically-unconquered astrophysical processes.

In Chapter 1 I give a history of fast stars, address what it means for a star to be fast, and describe the processes that accelerate stars. I concisely summarise the *Gaia* mission, whose recent data releases heavily influenced this thesis.

Supernovae in binary systems can fling away the companion; if a *runaway* companion can be associated with a supernova remnant, then together they reveal the evolution that led to the supernova. However, these associations are difficult to establish. In Ch. 2, I develop a sophisticated Bayesian methodology to search the nearest ten remnants for a companion, by combining data from *Gaia* DR1 with a 3D dust-map and binary population synthesis. With *Gaia* DR2, I will identify companions of tens of supernova remnants and thus open a new window to studying late-stage stellar evolution.

It is unknown why 17% of B stars are spinning near break-up; these stars are termed *Be stars* because of emission lines from their ejected material. Their rapid spin could be due to mass transfer, but in Ch. 3 I show this would create runaway Be stars. I demonstrate using a hierarchical Bayesian model that these exist in sufficient numbers, and thus that all Be stars may arise from mass transfer.

The stars escaping the Milky Way are termed *hypervelocity stars*. In Ch. 4, I overturn the consensus that the hypervelocity stars originated in the Galactic centre by showing that a Large Magellanic Cloud (LMC) origin better explains their distribution on the sky. In Ch. 5 I present three ground-breaking hypervelocity results with *Gaia* DR2: 1) only 41 of the 524 hypervelocity star candidates are truly escaping, 2) at least one of the hypervelocity stars originates in the LMC, and 3) the discovery of three hypervelocity white dwarf runaways from thermonuclear supernovae.





## DECLARATION

---

This dissertation is the result of my own work and includes nothing which is the outcome of work done in collaboration except as declared in the Preface and specified in the text.

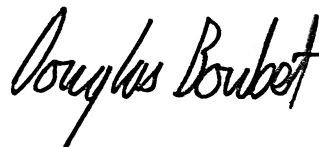
It is not substantially the same as any that I have submitted, or, is being concurrently submitted for a degree or diploma or other qualification at the University of Cambridge or any other University or similar institution except as declared in the Preface and specified in the text. I further state that no substantial part of my dissertation has already been submitted, or, is being concurrently submitted for any such degree, diploma or other qualification at the University of Cambridge or any other University or similar institution except as declared in the Preface and specified in the text.

It does not exceed the prescribed 60,000 word limit.

The bulk of this thesis has previously been published in the following works:

- Chapter 2 draws from Boubert, Fraser, Evans, Green, and Izzard (2017).
- Chapter 3 draws from Boubert and Evans (2018).
- Chapter 4 draws from Boubert and Evans (2016) and Boubert, Erkal, Evans, and Izzard (2017).
- Chapter 5 draws from Boubert, Guillochon, Hawkins, Ginsburg, and Evans (2018), Erkal, Boubert et al. (2018) and Shen, Boubert et al. (2018).

*Cambridge, July 2018*



---

Douglas Boubert



‘Never,’ said Hagrid irritably, ‘try an’ get a straight answer out of [an astronomer]<sup>1</sup>. Ruddy star-gazers.

Not interested in anythin’ closer’n the moon.’

— J.K. Rowling, *Harry Potter and the Philosopher’s Stone*

Dedicated to the loving memory of James Hill.

1931 – 2017

---

<sup>1</sup> Original quotation refers to centaurs.



*He was sorely tempted, too, by the perfect, moving model of  
the galaxy in a large glass ball, which would have meant he  
never had to take another Astronomy lesson.*

— J.K. Rowling (Harry Potter and the Prisoner of Azkaban)

## ACKNOWLEDGMENTS

---

A perfect, moving model of the Galaxy would be a more magical feat than anything in J. K. Rowling's universe, but those thanked here have helped me take astrophysics a few small steps towards it.

I would like to thank my supervisor Wyn Evans for a fulfilling three years. He took me on to study hypervelocity stars when that field looked to be cut-and-dry; it is due to him that I am lucky enough to have the study of fast stars as my vocation. Wyn knew both when to let me go wandering and when to guide me in a productive direction. I don't think he expected me to take him down the binary stellar physics rabbit hole and I am grateful that he trusted me enough to go along with those projects.

*'So you're slowly turning Wyn  
into a stellar physicist? Haha...'  
Martin C. Smith*

I would like to thank every member of the Cambridge Streams research group, especially Vasily Belokurov for his unquenchable enthusiasm, Denis Erkal for relegating me to #2 in the Large Magellanic Cloud fan club, Jason Sanders for already knowing the answers to my questions, and Sergey Koposov for putting me straight in my Bayesian calculations. Elsewhere in the Institute, Morgan Fraser introduced me to the hunt for supernova remnant companions and Rob Izzard lured me into working on binary stellar evolution.

My time at the Institute of Astronomy was made wonderful by my fellow students Dillon Dong, Siddarth Ghandi, Nick Henden, Adam Jermyn, Ryan MacDonald and Jasleen Matharu, with whom I spent many nights unwinding from a challenging problem over boardgames. In particular, Adam's togetherness as an early-career researcher raised the expectations I had of myself.

I will single out Alastair Houston as being my closest friend in Cambridge and a wellspring of fun and advice.

This last year saw me rapidly mature as a scientist and a great deal of that is thanks to my remarkable partner, Alison Todd. Her adventures in neuroscience inspire me and her loving support lifts me up. I love her.

And finally to Dad, Mum, Neil and Tracey for being endlessly proud and supportive. As proud as they are to have me as a son, I am more proud to have them as my parents.



## CONTENTS

---

1	INTRODUCTION	1
1.1	Structure of the Milky Way and Local Group	1
1.2	Is this star fast?	5
1.3	A brief history of fast stars	6
1.3.1	Proper motion and radial velocity	7
1.3.2	OB runaways	9
1.3.3	Pulsars	10
1.3.4	Be stars	11
1.3.5	Hypervelocity stars	13
1.3.6	What to call a fast star?	18
1.4	How to make a fast star	18
1.4.1	Remnant of a supernova	19
1.4.2	Companion of a supernova	19
1.4.3	N-body dynamical interaction	19
1.4.4	Combination	20
1.4.5	Translation	20
1.5	The era of Gaia	21
1.6	From open questions to answers	22
2	SEARCHING FOR FORMER COMPANIONS OF SUPERNOVA REMNANT PROGENITORS	23
2.1	History of Prior Searches	24
2.2	Sources of data	25
2.2.1	Summary of stellar data	25
2.2.2	Summary of individual SNRs	26
2.3	Search with only kinematic constraints	28
2.4	Bayesian search with binaries, light and dust	32
2.4.1	Binary star evolution grid	32
2.4.2	Algorithm	34
2.4.3	Fraction of supernovae with runaways	40
2.4.4	Verification	41
2.4.5	Validation	41
2.5	Results	42
2.5.1	Eliminating the contaminants	43
2.5.2	Individual candidates	45
2.6	Discussion	48
2.7	Summary	50
3	ON THE CONNECTION OF THE RUNAWAY BE STARS TO THE BE STAR PHENOMENON	55
3.1	Data	56

3.1.1	The Berger & Gies sample	57
3.1.2	Be Star Spectra database	57
3.1.3	The LAMOST Sample	58
3.1.4	The Combined Catalogue	59
3.2	The Post-Mass-Transfer Channel for Be Stars	60
3.2.1	Be stars from binary population synthesis	61
3.2.2	Properties of the simulated Be star population accounting for selection effects	64
3.2.3	Compact object natal kick uncertainty	68
3.3	Bayesian Framework	70
3.3.1	Bayesian Mixture Model for the Kinematics	71
3.3.2	The Priors	72
3.3.3	The Likelihood	74
3.3.4	Analytic Fit to Runaway Velocity Distributions	75
3.4	The Fraction of Be Runaways	76
3.4.1	Preliminaries	76
3.4.2	Retrieval of simulated data	77
3.4.3	Principal model	80
3.4.4	A Free Log-normal	83
3.5	Discussion	86
3.5.1	Large uncertainty and wide velocity dispersion priors	88
3.5.2	Uncertainty in binary stellar evolution	89
3.5.3	Observational bias against runaway stars	89
3.5.4	Should we find Be stars at high latitude?	90
3.6	Summary	91
4	HYPERVELOCITY STARS AND THE LARGE MAGELLANIC CLOUD	93
4.1	Hills mechanism in the LMC	94
4.1.1	Method	94
4.1.2	Discussion	99
4.1.3	Summary	104
4.2	Runaway stars from the LMC	105
4.2.1	LMC runaway ejection model	106
4.2.2	Properties of LMC Runaways	113
4.2.3	Summary	127
4.3	Conclusion	128
5	HYPERVELOCITY STARS IN THE ERA OF <i>gaia</i> DR2	131
5.1	Revisiting the hypervelocity stars	131
5.1.1	History of searches for late-type hypervelocity stars	132
5.1.2	Results	135
5.1.3	Summary	140



5.2	A hypervelocity star from the LMC	141
5.3	Three new hypervelocity white dwarfs	142
6	CONCLUSION	149
A	APPENDIX	153
A.1	The Local Supernova Remnants (SNRs)	153
A.2	Binary_c	155
A.3	Implementation of MULTINEST	156
A.4	The Open Fast Stars Catalog	157
A.4.1	Determination of boundedness	158
A.4.2	Automatic querying of Gaia and other catalogues	160
A.4.3	The fast star graveyard	160
	BIBLIOGRAPHY	161

## LIST OF FIGURES

---

- Figure 1.1      Transition from circular to hyperbolic orbits as the velocity of a star is increased from  $220 \text{ km s}^{-1}$  to  $800 \text{ km s}^{-1}$ . This figure was generated using MWPOTENTIAL2014 in GALPY (Bovy, 2015), where the potential is tuned so that the circular velocity is  $220 \text{ km s}^{-1}$  at 8 kpc. Note that the terms elliptical, parabolic and hyperbolic are used here in analogy with the orbital families in a Keplerian potential; due to the non-Keplerian nature of the Galactic potential, the orbits are not conic sections.      4
- Figure 1.2      Various distributions for the 3D natal kick velocity distribution of neutron stars from the literature. The solid lines are the single Maxwellian distributions of Hansen and Phinney (1997) and Hobbs, Lorimer, Lyne, and Kramer (2005), the dash-dotted lines are from Hartman (1997) and Faucher-Giguère and Kaspi (2006), and the dashed lines are the double Maxwellian distributions of Arzoumanian, Chernoff, and Cordes (2002) and Faucher-Giguère and Kaspi (2006). Originally published in Boubert and Evans (2018).      11
- Figure 1.3      Hammer projection in right ascension and declination of all candidate hypervelocity stars stars, color-coded by spectral type. The thick gray line shows the plane of the Milky Way, with the large gray dot indicating the location of the Galactic centre. The locations of M31 and the LMC are shown as annotated. An interactive version of this figure is available at the OFSC.      17
- Figure 2.1      The fraction  $F$  of realisations of each star in each SNR which are consistent with being spatially coincident with the centre of the SNR at one point in the past 150 kyr. The criteria for determining whether a realisation is consistent are described in Sec. 2.3.      30

- Figure 2.2 Probability distribution in velocity-colour space of the runaways produced by our binary evolution grid. The top and right plots show 1D projections of the joint probability distribution. 34
- Figure 2.3 The conditional PDF for the dust extinction along the line of sight to G180.0–1.7 calculated by interpolating samples from the Green et al. (2015) dust-map. 37
- Figure 2.4 A diagram of the geometry described in Sec. 2.4.2. The observer is at  $\odot$  and the centre of the supernova remnant is at  $+$ . The two possible locations of the candidate if it is the runaway are marked by  $\times$  and correspond to the intersection of the sphere of radius  $v_{ej}t_{SNR}$  centred on the SNR and the half-line defined by the coordinates of the candidate. 39
- Figure 2.5 Bayes factors for the hypothesis that each star in each SNR is a runaway star versus the hypothesis that it is a contaminant. The false positive and false negative series are described in Sec. 2.4.5. 43
- Figure 2.6 Digitized Sky Survey image of the vicinity of the Rosette Nebula. The runaway star candidate HD 261393 is marked by a white cross, the white cross hairs indicate the geometric centre of the Monoceros Loop and the white circle approximately shows the inner edge of the Monoceros Loop shell. The Rosette Nebula is in the bottom right and the Mon OB2 association extends  $3^\circ$  to the east and north-east towards the centre of the Monoceros Loop. 45

- Figure 2.7 Corner plots of the posterior samples from the model of TYC 2688-1556-1 in G074.0–08.5 with  $1\sigma$ ,  $2\sigma$  and  $3\sigma$  contours. The 1D histograms include the CDF of that parameter and the error bars indicate the median and  $1\sigma$  errorbars of each mode. **Bottom left:** A corner plot showing the model parameters, excluding the five parameters related to the position and peculiar velocity of the SNR which did not have covariances with the other parameters. **Top right:** A corner plot showing a selection of the derived parameters which are functions of the model parameters. 51
- Figure 2.8 As Fig. 2.7 but for the candidate BD+50 3188 in G089.0+04.7. 52
- Figure 2.9 As Fig. 2.7 but for the candidate HD 37424 in G180.0–01.7. 53
- Figure 2.10 As Fig. 2.7 but for the candidate HD261393 in G205.5+00.5. 54
- Figure 3.1 Median peculiar velocities relative to the Milky Way disc of an identical sample of stars using the kinematics from either Berger and Gies (2001) or the catalogue assembled in this work. Thanks to TGAS the kinematics in our catalogue are more accurate and this produces a significant tightening in the distribution. 58
- Figure 3.2 Cumulative number of pairs of stars with a separation less than a given bound. The dashed line is our criterion for a duplicate star and it cleanly divides duplicate stars from true close stellar pairs. 59
- Figure 3.3 Distribution of Be stars in our combined catalogue across the sky. The size of each point is proportional to the parallax. The Galactic centre is at the centre of this image and the celestial equator is shown as a grey dashed line. A subset of the points are coloured orange to indicate stars which do not have an associated spectral type and luminosity class. Such stars are preferentially found in the Southern hemisphere. 61

- Figure 3.4 Median peculiar velocity distribution of Be stars in our combined catalogue. Overplotted is a kernel density estimate. 62
- Figure 3.5 Distribution of the 632 Be stars which have both spectral types and luminosity classes. The counts have been convolved with a Gaussian kernel of width 0.2322 to smooth out shot noise. There is a clear observational bias towards earlier types, while 38 stars are classified as Be stars but do not have a B spectral type. 63
- Figure 3.6 Predicted probability distribution for the runaway velocity and critical equatorial velocity ratio of runaway B stars. The dashed line indicates our fiducial value  $R_{\text{eq}} = 0.85$ . 65
- Figure 3.7 Both selection effects and the uncertainty in the choice of  $R_{\text{eq}}$  (the minimum fraction of the critical rotation velocity for a star to be classed as a Be star) can lead to dramatically different simulated populations of runaway Be stars. **Left:** The runaway fraction among Be stars as a function of  $R_{\text{eq}}$  with and without accounting for the observational selection effect. The grey lines indicate the resulting runaway fraction associated with each choice of  $R_{\text{eq}}$  shown in the lower panel. **Right:** The choice of  $R_{\text{eq}}$  changes the velocity distribution of the runaway Be stars as a function of spectral type. In each panel, we show the velocity distribution for each spectral type from Bo to B9, in addition to the mean accounting for the selection effect. Note that as  $R_{\text{eq}}$  increases the effect of Poisson noise also increases because we are defining fewer stars to be Be stars. 68

- Figure 3.8 The inclusion of observational biases dramatically changes the predicted population of Be stars, under the assumption of  $R_{\text{eq}} = 0.85$ . **Left:** The two panels show the distribution of ages of the Be stars with and without accounting for the observational bias towards early-type Be stars. The grey dashed lines indicate the median age and the coloured regions each account for 20% of the probability. **Right:** Each pie chart gives the proportions of the Be stars for which the progenitor binary is intact, merged or split. If the binary is intact then the stellar type of the companion is given. MS = Main Sequence, WDs = White Dwarf, NS = Neutron Star, BH = Black Hole. 69
- Figure 3.9 Fits of one and two log-normal distributions to the numerical predicted runaway velocity distribution calculated in Section 3.2. In the legend, the  $\mu$  and  $\sigma$  give the parameters of each log-normal distribution and  $F_1$  and  $F_2$  are the fraction of the probability assigned to each component of the double log-normal fit. 76
- Figure 3.10 Corner plot of the posterior for the retrieval. 79
- Figure 3.11 The receiver operating characteristic curve for the classification of runaway stars based on the mean of the posterior probability of being a runaway star being greater than  $x\%$ . The grey dashed line corresponds to a classifier that randomly guesses and which our classification far out-competes. The annotations are of the form ' $x\% \Rightarrow (\# \text{ of True Positives}, \# \text{ of False Positives})'$ '. 80
- Figure 3.12 Corner plot of the posterior for the principal model. 81

- Figure 3.13 The posterior for a model in which the functional form of the runaway velocity distribution is constrained to be a  $\text{LogNormal}(\mu, \sigma)$  distribution, but the  $\mu$  and  $\sigma$  parameters are free to vary. **Upper:** The posterior distributions for  $\mu$  and  $\sigma$  together with the resulting  $\text{Mode}(v_{\text{run}})$ . The green truths indicate the fixed values obtained by fitting a log-normal distribution to the simulated outcomes of binary evolution. **Lower:** The posterior for the runaway fraction and velocity dispersions with the mode of the runaway velocity distribution shown for reference with the upper panel. The green truths indicate the median values obtained from the model where  $\mu$  and  $\sigma$  were fixed as in Sec. 3.3.4. 85
- Figure 3.14 In grey, we show the 1, 2, and  $3\sigma$  contours of the log-normal distributions implied by the posterior of  $(\mu, \sigma)$  shown in Fig. 3.13. The dark line is the log-normal given by the median of the posterior and the purple dashed line is the single log-normal fit to the simulated runaway velocity distribution shown in green in Fig. 3.9. 87
- Figure 4.1 Predicted distribution in Galactic coordinates of HVSs from the LMC at a heliocentric distance  $50 < d < 120$  kpc, using the HVLMC-A model from Section 4.1.1. Density contours are spaced  $10^{1/2}$  apart with the yellow contour denoting the highest density, the green arrow marks the path of the LMC over the last 350 Myr, the purple dashed line is the celestial equator, and the red crosses are the HVS candidates denoted HVS<sub>1</sub>, HVS<sub>2</sub>, etc. by Brown. 95
- Figure 4.2 Density contours in Galactic coordinates for the stars from the three models with heliocentric distance  $50 \leq d \leq 120$  kpc. 99
- Figure 4.3 Mean heliocentric radial velocity for stars at distance  $50 < d < 120$  kpc. 101
- Figure 4.4 Mean equatorial proper motions  $(\mu_\alpha, \mu_\delta)$  and Galactic proper motions  $(\mu_l, \mu_b)$  for stars at distance  $50 < d < 120$  kpc. 102

- Figure 4.5 Spherical harmonics for the distance bin  $50 < d < 120$  kpc. The power spectrum  $S(\ell)$  has been normalised by the total power for each model to give  $\tilde{S}(\ell)$ , since we are primarily interested in the relative power in each mode between models. 104
- Figure 4.6 Probability density distribution in velocity-colour space at the time of ejection from the progenitor binary of the runaways produced by our binary evolution grid assuming LMC metallicity  $Z = 0.008$  and common-envelope ejection efficiency  $\alpha_{\text{CE}} = 1.0$ . 110
- Figure 4.7 **Left:** All-sky present day distribution of runaways produced by our model of the LMC. The blue circle corresponds to the assumed tidal radius of the LMC of 20 kpc. The red crosses are the observed population of B-type HVs. **Right:** Zoom-in at higher resolution to illustrate the structure of our LMC disc. An animation of the evolution of this plot through each snapshot of our simulation is available at <https://youtu.be/eE-1JXBP1J8>. 111



Figure 4.8 Predictions of the kinematics of our LMC runaway model plotted as logarithmically-spaced contours of the number of stars in each bin. The bins are defined by a  $100 \times 100$  grid over the range of each plot. Also shown are observations of OB-stars near the LMC in the literature: the known B-type hypervelocity stars, stars which may have formed from the gas in the leading arm (Zhang et al., 2017), candidate runaways in the LMC (Lennon, van der Marel, Lerate, O’Mullane, & Sahlmann, 2016) and young stars in the outskirts of the LMC (Moni Bidin et al., 2017). The distances for the stars from Zhang et al. (2017) and Moni Bidin et al. (2017) are calculated from distance moduli, proper motions were only available for the Lennon, van der Marel, Lerate, O’Mullane, and Sahlmann (2016) stars and a subset of the hypervelocity stars, and the Lennon, van der Marel, Lerate, O’Mullane, and Sahlmann (2016) stars only have distances by association with the LMC. The grey dashed line marks the celestial equator and SDSS photometry only covers the region above this line. 116

Figure 4.9 The escape velocity curve of our modelled LMC potential (see Section 4.2.2.1). The contours illustrate the distribution of our LMC escapers, the red line is our estimated escape velocity curve and the blue point is the mass constraint for the LMC  $M(8.7 \text{ kpc}) = (1.7 \pm 0.7) \times 10^{10} M_{\odot}$  (van der Marel & Kallivayalil, 2014) converted to escape velocity with  $v_{\text{esc}} = \sqrt{2GM/r}$ , where  $G$  is the gravitational constant and  $r$  is the spherical radius. 117

- Figure 4.10 Predicted properties of LMC runaways which would be observed by *Gaia* plotted as logarithmically-spaced contours of the number of stars in each bin (see Fig. 4.8 for the colourbar). The kinematics are heliocentric and  $G$  is the unreddened apparent magnitude. The grey dashed line indicates the  $G \approx 20.7$  completeness limit for *Gaia* and the red error bars represent the  $\pm 1\sigma$  predicted end-of-mission radial velocity and proper motion errors as a function of  $G$  (described in detail in Sec. 4.2.2.4). 124
- Figure 4.11 All sky distribution of remnants produced by runaway supernovae in our models (Sec. 4.2.2.5). The white solid line indicates the 20 kpc tidal radius of the LMC and the white dashed line is the orbit of the LMC over the last 1.97 Gyr in the frame where the Sun is fixed at  $(x, y, z) = (-R_{\odot}, 0, 0)$ . 125
- Figure 5.1 The probability of a candidate hypervelocity star being bound to the Galaxy versus the difference between the Galactocentric rest-frame velocity and the escape speed. The error bars incorporate errors and correlations in the distances, radial velocities and proper motions of the stars, as well as the uncertainties in the Solar kinematics and the Milky Way escape velocity (see the Appendix for more detail). Some stars are missing either the radial velocity or proper motions and thus the probability is only an upper limit (these objects are indicated with a triangle). The size of the point reflects whether the star is a giant (large), dwarf (medium) or a white dwarf or subdwarf (small). 134
- Figure 5.2 Probability  $P_{\text{bound}}$  that each high-velocity candidate is bound to the Milky Way before ( $x$ -axis) and after ( $y$ -axis) the inclusion of DR2. The shapes of the markers is as in Fig. 5.1. 135
- Figure 5.3 The heliocentric distance distribution of hypervelocity candidates with  $P_{\text{bound}} < 0.5$  (see Tab. 5.1). 138
- Figure 5.4 Same as Figure 1.3, but for hypervelocity candidates with  $P_{\text{bound}} < 0.5$  (see Tab. 5.1). 139

Figure 5.5 Past (dashed components of each curve) and future (solid components of each curve) realizations of the trajectory of the candidate high-velocity late-type star LAMOST J115209.12+120258.0. The size of the Milky Way’s thin disc, assumed to be 32 kpc in diameter and 0.6 kpc in height, is shown by the dashed grey contours. Arrows pointing in the directions of M31 and the LMC are labelled. Orbits were calculated in the MW-Potential2014 potential using the PYTHON Galactic dynamics framework GALPY (Bovy, 2015). The rotation direction of the Milky Way disc is indicated by the long arrow and the short arrows indicate time steps of 10 Myr along the orbit. 140

Figure 5.6 **Left:** Minimum approach distance to the Milky Way and the LMC for the 26 HVSs in our sample. HVS3 stands out as being far more likely to have originated near the LMC than near the Milky Way. **Right:** Probability of passing within 5 kpc of the Milky Way and the LMC over the past 500 Myr. Again, HVS3 clearly stands out as being significantly more likely to originate from near the centre of the LMC ( $p = 0.40$ ) than the MW ( $p = 10^{-4}$ ). Originally published in Erkal, Boubert, Gualandris, Evans, and Antonini (2018). 142

Figure 5.7 Distribution of relative velocities to the LMC and ejection times for HVS3. The dashed lines show the 15.9, 50, and 84.1 percentiles of each 1d distribution. The contours shown are 0.5, 1, 1.5, and  $2\sigma$ . Originally published in Erkal, Boubert, Gualandris, Evans, and Antonini (2018). 144

Figure 5.8 Sample realizations of the orbital solutions (past trajectories in blue; future trajectories in red). The Milky Way’s thin disc is overlaid in gray contours. A face-on view is shown in the left panel; the right panel shows an edge-on perspective. The Sun’s location is marked with a star, and the Galaxy’s rotation and the directions to the LMC and M31 are denoted with arrows. Originally published in Shen et al. (2018). 147

Figure 5.9 The orbital solution of D6-2 overlaid on H $\alpha$  images from Virginia Tech Spectral Line Survey (VTSS; Dennison, Simonetti, and Topasna 1998). The blue and red trajectories extend  $9 \times 10^4$  yr into D6-2’s past and future, respectively. The green circle encompasses the spherical shell of the remnant G70.0-21.5. Originally published in Shen et al. (2018). 148

## LIST OF TABLES

---

Table 2.1	Properties of the sample of supernova remnants, where the errors on the distance are $1\sigma$ and are described in Appendix A.1. 27
Table 2.2	Interpretation of Bayes factors K (Kass & Raftery, 1995). 35
Table 2.3	Model parameters for the runaway hypothesis. 36
Table 2.4	Table of median posterior values for our new candidates. 44
Table 3.1	List of stars identified as highly-likely runaway stars by the method described in Sec. 3.4.3. $P_{\text{run}}$ is the probability that the star is a runaway, $v_{\text{run}}$ is the posterior runaway velocity and $d$ is the posterior distance inferred from the parallax. All of the names are resolvable by Simbad. The starred entries are high-peculiar space velocity stars mentioned by Berger and Gies (2001). Based on Fig. 3.11, we should expect around 4 of these stars to be false positives. 84

Table 4.1	Summary of stellar types at the present day by number of stars which either remain bound to or escape the Large Magellanic Cloud, and the fraction of the latter which are hypervelocity stars with respect to the Milky Way. <b>Key:</b> LM-MS - <i>Low Mass Main Sequence</i> , MS - <i>Main Sequence</i> , HG - <i>Hertzsprung Gap</i> , GB - <i>Giant Branch</i> , CHeB - <i>Core Helium Burning</i> , EAGB - <i>Early Asymptotic Giant Branch</i> , TPAGB - <i>Thermally Pulsating Asymptotic Giant Branch</i> , HeMS - <i>naked Helium Main Sequence</i> , HeHG - <i>naked Helium Hertzsprung Gap</i> , HeGB - <i>naked Helium Giant Branch</i> , HeWD - <i>Helium White Dwarf</i> , COWD - <i>Carbon-Oxygen White Dwarf</i> , ONeWD - <i>Oxygen-Neon White Dwarf</i> , NS - <i>Neutron Star</i> , BH - <i>Black Hole</i> . 115
Table 5.1	The hypervelocity candidates with $P_{\text{bound}} < 0.5$ subdivided by original discovery survey or paper. The Hypervelocity Star Survey (Brown, Geller, & Kenyon, 2014; Brown, Geller, Kenyon, & Kurtz, 2005; Brown, Geller, Kenyon, Kurtz, & Bromley, 2007b) has remarkably discovered 32 of these 41 stars, while the LAMOST HVS Survey (Huang et al., 2017; Zheng et al., 2014) contributes a further 3. 136
Table 5.2	The 26 hypervelocity stars considered in this work. Almost all of the proper motion measurements are from <i>Gaia</i> DR2 except for HVS <sub>1</sub> , HVS <sub>4</sub> , HVS <sub>13</sub> , and HIP60350. <b>References:</b> (1) Brown et al. (2015) (2) <i>Gaia</i> Collaboration et al. (2018), (3) Geier et al. (2015), (4) Brown, Geller, and Kenyon (2014), (5) Zheng et al. (2014), (6) Huang et al. (2017), (7) Heber, Edelmann, Napiwotzki, Altmann, and Scholz (2008), (8) Irrgang, Przybilla, Heber, Nieva, and Schuh (2010). 143
Table 5.3	Properties of the three hypervelocity white dwarfs identified in Shen et al. (2018). This Table is an amalgamation of Table 1 and Table 3 of Shen et al. (2018). 146

## ACRONYMS

---

APASS	AAVSO Photometric All-Sky Survey
BESS	Be Star Spectra database
BH	Black Hole
CDF	Cumulative Density Function
ESA	European Space Agency
HMXB	High Mass X-ray Binary
HVS	Hypervelocity Star
IMF	Initial Mass Function
KDE	Kernel Density Estimate
LAMOST	Large Sky Area Multi-Object Fibre Spectroscopic Telescope
LMC	Large Magellanic Cloud
MW	Milky Way
MBH	Massive Black Hole
NS	Neutron Star
OFSC	Open Fast Stars Catalog
PAN-STARRS	Panoramic Survey Telescope and Rapid Response System
PDF	Probability Density Function
PPMXL	Positions and Proper Motions “Extra Large” catalog
SDSS	Sloan Digital Sky Survey
SMC	Small Magellanic Cloud
SN	Supernova
SNR	Supernova Remnant
STFC	Science and Technology Facilities Council
TGAS	Tycho- <i>Gaia</i> Astrometric Solution

SCIENTIFIC ACKNOWLEDGEMENTS

---

I am thankful to the UK Science and Technology Facilities Council for funding my Ph.D. and the Institute of Astronomy, Churchill College and the University of Cambridge for hosting me. Much of the work presented in this thesis has been published in astronomical journals and I am grateful to the many editors and anonymous reviewers for their constructive comments. I would like to thank Magdalen College, Oxford, for offering me a fellowship to continue these studies in the following years.

I am indebted to the numerous astronomical telescopes, surveys and catalogues who make their data public. I include here their requested acknowledgements:

APASS	This research has made use of the APASS database, located at the AAVSO web site. Funding for APASS has been provided by the Robert Martin Ayers Sciences Fund.
BESS	This work has made use of the BeSS database, operated at LESIA, Observatoire de Meudon, France, and described in Neiner et al. (2011) and found at: <a href="http://basebe.obspm.fr">http://basebe.obspm.fr</a> .
GAIA	This work has made use of data from the European Space Agency (ESA) mission <i>Gaia</i> ( <a href="https://www.cosmos.esa.int/gaia">https://www.cosmos.esa.int/gaia</a> ), processed by the <i>Gaia</i> Data Processing and Analysis Consortium (DPAC, <a href="https://www.cosmos.esa.int/web/gaia/dpac/consortium">https://www.cosmos.esa.int/web/gaia/dpac/consortium</a> ). Funding for the DPAC has been provided by national institutions, in particular the institutions participating in the <i>Gaia</i> Multilateral Agreement.
GREEN (2014)	Ch. 2 made use of the Green (2014) catalogue of supernova remnants (available at <a href="http://www.mrao.cam.ac.uk/surveys/snrs/">http://www.mrao.cam.ac.uk/surveys/snrs/</a> ).
LAMOST	Chs. 3 and 5.1 made use of results obtained by the Guoshoujing Telescope (the Large Sky Area Multi-Object Fiber Spectroscopic Telescope, LAMOST), a National Major Scientific Project built by the Chinese Academy of Sciences. Funding for LAMOST

was provided by the National Development and Reform Commission. LAMOST is operated and managed by the National Astronomical Observatories, Chinese Academy of Sciences.

SDSS I/II	Funding for the SDSS and SDSS-II has been provided by the Alfred P. Sloan Foundation, the Participating Institutions, the National Science Foundation, the U.S. Department of Energy, the National Aeronautics and Space Administration, the Japanese Monbukagakusho, the Max Planck Society, and the Higher Education Funding Council for England. The SDSS Web Site is <a href="http://www.sdss.org/">http://www.sdss.org/</a> . The SDSS is managed by the Astrophysical Research Consortium for the Participating Institutions (a list of whom can be found at <a href="http://classic.sdss.org/members/index.html">http://classic.sdss.org/members/index.html</a> ).
SDSS III	Funding for SDSS-III has been provided by the Alfred P. Sloan Foundation, the Participating Institutions, the National Science Foundation, and the U.S. Department of Energy Office of Science. The SDSS-III web site is <a href="http://www.sdss3.org/">http://www.sdss3.org/</a> . SDSS-III is managed by the Astrophysical Research Consortium for the Participating Institutions of the SDSS-III Collaboration (a list of whom can be found at <a href="http://www.sdss3.org/collaboration/institutions.php">http://www.sdss3.org/collaboration/institutions.php</a> ).
SIMBAD	This research has made use of the SIMBAD database, operated at CDS, Strasbourg, France (Wenger et al., 2000).
SOAR	Part of Sec. 5.1 was based on observations obtained at the Southern Astrophysical Research (SOAR) telescope, which is a joint project of the Ministério da Ciência, Tecnologia, Inovações e Comunicações (MCTIC) do Brasil, the U.S. National Optical Astronomy Observatory (NOAO), the University of North Carolina at Chapel Hill (UNC), and Michigan State University (MSU).
SNRCAT	Ch. 2 made use of the SNRcat catalogue of supernova remnants (Ferrand & Safi-Harb, 2012) accessible at <a href="http://www.physics.umanitoba.ca/snr/SNRcat/">http://www.physics.umanitoba.ca/snr/SNRcat/</a> .

In analysing this data I have used a great number of open source software packages. I include here their requested acknowledgements:



ASTROPY	This research made use of ASTROPY, a community-developed core PYTHON package for Astronomy (Astropy Collaboration et al., 2013, 2018).
ASTROCATS	The Open Fast Star Catalog created in Sec. 5.1 and described further in Appendix A.4 would have been impossible without the ASTROCATS package for constructing curated catalogs of astronomical data (Guilochon, Parrent, Kelley, & Margutti, 2017).
BINARY_C	The investigations in Chs. 2, 3 and 4.2 relied on the binary stellar evolution code BINARY_C and the related population synthesis module BINARY_GRID2 (Izzard, Dray, Karakas, Lugaro, & Tout, 2006; Izzard, Glebbeek, Stancliffe, & Pols, 2009; Izzard, Tout, Karakas, & Pols, 2004). I am extremely appreciative of Mathieu Renzo, Simon Stevenson, Manos Zapartas and the many other authors cited throughout this thesis who have contributed to the development of BINARY_C.
CORNER.PY	The corner plots in Figs. 2.7, 2.8, 2.9, 2.10, 3.10, 3.12 and 3.13 were generated using CORNER.PY (Foreman-Mackey, 2016).
CUBEHELIX	Figs. 2.2, 2.3, 3.5 and 3.6 made use of the CUBEHELIX colour scheme (Green, 2011).
EMCEE	The Markov Chain Monte-Carlo sampler EMCEE was used in Sec. 5.2 to constrain the origin of HVS3 (Foreman-Mackey, Hogg, Lang, & Goodman, 2012).
MATPLOTLIB	Every figure in this thesis was created using the ubiquitous PYTHON plotting package MATPLOTLIB (Hunter, 2007).
MULTINEST	Ch. 2 used the MULTINEST implementation of nested sampling (Feroz, Hobson, & Bridges, 2009; Feroz, Hobson, Cameron, & Pettitt, 2013; Feroz & Hobson, 2008) which I accessed through the PYMULTINEST PYTHON module (Buchner et al., 2014).
NUMPY	I am indebted to the creators of the PYTHON package NUMPY (van der Walt, Colbert, & Varoquaux, 2011). The first line of every script I wrote during my Ph.D. was 'import numpy'.

PANDAS	The PYTHON package PANDAS (McKinney, 2010) was a vital tool for reading the many horrendous file formats used by astronomers .
SCIPY	Many of the analyses in this Ph.D. relied on the numerical implementations in SCIPY (Jones, Oliphant, Peterson, et al., 2001, see <a href="https://www.scipy.org">https://www.scipy.org</a> ) of operations as simple as optimisation, integration and root-finding.
STAN	Obtaining posterior samples from the 5067 parameter model in Ch. 3 was only possible because of the Bayesian inference platform STAN (Carpenter et al., 2017).

## INTRODUCTION

---

The astronomical literature is littered with references to fast stars: flying stars and high proper motion stars; critically-rotating and cannon-ball stars; walkaway, runaway and hypervelocity stars. Astronomers pigeonhole stars with one of these terms if their motion is in any way remarkable, either in projection ('the star is moving across the sky'), translation ('the star is moving through the Galaxy') or rotation ('the star is spinning'). This thesis principally addresses questions related to fast stars in the translational sense, but rotationally fast stars arise tangentially.

Whether a star's motion is remarkable is a qualitative judgement, but it can be simplified to checking whether the star is moving unusually fast for a star at its location and of its age, mass and type. Where the star is in the Milky Way (or indeed Local Group) is an important consideration because it both indicates the most sensible frame in which to consider the velocity of the star and provides the context for the star's properties.

The wide range of terms used in reference to fast stars reflects their extensive history, from Piazzzi's flying star of 1803 to the first discovery of a main-sequence hypervelocity star in 2005. While these fast stars are exciting in their own right, I would argue that the study of fast stars is not merely stamp collecting. By studying fast stars we can infer the phenomena that accelerated them, and because these phenomena are rare and extremely energetic they often lie at the heart of poorly understood regions of astrophysics: from stellar interactions with the massive black hole at the centre of the Galaxy to tight binaries and their resulting supernova explosions.

I was fortunate to be studying for a Ph.D. when the first data from the European Space Agency's *Gaia* space telescope was released. *Gaia* will measure the motion and distance of over a billion stars and is thus revolutionary for the study of fast stars<sup>1</sup>.

### 1.1 STRUCTURE OF THE MILKY WAY AND LOCAL GROUP

Fast stars can presently only be studied within the Local Group of galaxies. The Local Group is principally composed of the Milky Way

---

<sup>1</sup> *Gaia* giveth low-hanging research results; *Gaia* taketh time I should have spent writing this thesis.

and Andromeda (M31) and their respective satellite galaxies. The Milky Way and M31 are both typical spiral galaxies with a mass budget dominated by a spherical dark matter halo and hosting a flattened disc of stars, gas and dust. Both galaxies host massive black holes at their centres and both have unusually massive satellite galaxies (10% probability in comparison to cosmological simulations and SDSS, Busha et al., 2011; Tollerud, Boylan-Kolchin, Barton, Bullock, & Trinh, 2011); M31 is orbited by M33 while the Milky Way is orbited by the Large and Small Magellanic Clouds (LMC and SMC respectively). I will in turn discuss the structure of the Milky Way, the history and properties of the Magellanic Clouds, and what it means for a star to be escaping from the Milky Way.

The Milky Way is composed of dark matter, stars, gas and dust, in order of mass. The dark matter exists in a  $0.8 \times 10^{12} M_{\odot}^2$  halo that is thought to be centrally-concentrated and spherically-symmetric, however it is possible that the halo is triaxial or even has a triaxiality that changes with radius. The dark matter halo of the Milky Way contains many smaller clumps of dark matter ('sub-halos') which are only visible if they also contain stars, in which case they are referred to as dwarf galaxies. At present, the dark matter distribution of the Milky Way can only be studied through the dynamics of stars gravitationally interacting with it.

The Milky Way's stellar component can be divided phenomenologically into three structures, although subdivisions are also commonly discussed,

- *Disc*: The disc is often split into both a thin and thick component based on the chemistry of the stars (stars in the thick disc are metal-poor but alpha-enhanced). The total stellar mass is around  $6.8 \times 10^{10} M_{\odot}$  with a radial scale-length 3000 pc and vertical scale-length 280 pc<sup>2</sup>.
- *Bulge*: The central regions of the Galaxy, including the bar, are referred to as the bulge. The bulge has a stellar mass of  $5 \times 10^9 M_{\odot}^2$  and is often assumed to be spherical.
- *Halo*: The stellar halo is a spherical component of negligible mass with no net rotation but a large velocity dispersion that declines with radius (125 km s<sup>-1</sup> at 20 kpc, 100 km s<sup>-1</sup> at 50 kpc; Battaglia et al., 2005).

There is one further contribution to the Galactic potential from the massive black hole Sgr A\* at the centre of the Milky Way. Sgr A\* has

<sup>2</sup> These masses and scale-lengths come from the widely-used MWPotential2014 potential incorporated in the PYTHON Galactic dynamics framework GALPY (Bovy, 2015).

a mass of  $4.31 \pm 0.36 \times 10^6 M_{\odot}$  (Gillessen et al., 2009) which was determined from orbital fits of the black hole's satellite stars. Apposite to the topic of fast stars, the fastest stars in the Milky Way are those in orbit about Sgr A\*; these stars are known as the S-stars and have orbital velocities up to  $10^4 \text{ km s}^{-1}$  (Meyer et al., 2012, and references therein).

The multiple stellar components arise from the two ways that stars come to be in our Galaxy, either i) born from molecular clouds in the disc or centre or ii) carried in by a dwarf galaxy.

Stars born in the disc inherit the motion of their parent molecular cloud and thus young stars are found orbiting in the plane of the Galaxy on circular orbits at about  $238 \pm 9 \text{ km s}^{-1}$  with only  $20 \text{ km s}^{-1}$  dispersion (e.g. Aumer & Binney, 2009). As these stars age their orbits are excited (a process known as 'disc heating') so that while the mean rotation of the population is preserved, the velocity dispersion in the radial, azimuthal and vertical directions grows monotonically with age up to a total velocity dispersion of about  $50 \text{ km s}^{-1}$  at 10 Gyr (Aumer & Binney, 2009).

Stars carried in by a dwarf galaxy falling onto the Milky Way exhibit no such regular motion. Stars are progressively stripped from the dwarf galaxy as its orbit decays through dynamical friction, forming streams and shells of stellar tidal debris. These features slowly disperse with time, blurring into the stellar halo. The distinguishing feature between the halo and the disc is that dwarf galaxies can accrete onto the Milky Way from any direction, and thus the mean rotation of stars in the halo is zero with a remarkably large dispersion. Another characteristic of the halo is that the stars must be old. While an infalling dwarf galaxy may continue forming stars until its gas is stripped by the Milky Way, the population of young stars in the halo cannot be replenished past that point.

As a consequence there are two routes to produce a fast-moving, G dwarf star: being born in the disc and having its velocity excited gradually over time or being carried in by a fast-moving dwarf galaxy. In stark contrast, there is no route to producing a fast-moving, B dwarf star; these young stars will be born in the disc, live their short main-sequence life and cease nuclear burning before disc heating can significantly excite their orbits. The fast star production mechanisms discussed in Sec. 1.4 are therefore required to explain why 25% of O stars have speeds greater than  $30 \text{ km s}^{-1}$  relative to the mean rotation (termed *runaway* stars, Blaauw, 1956).

If we knew the exact shape and mass of each of these components then, under the assumption that the Milky Way is static and under no external influence, the position and velocity of a star would uniquely

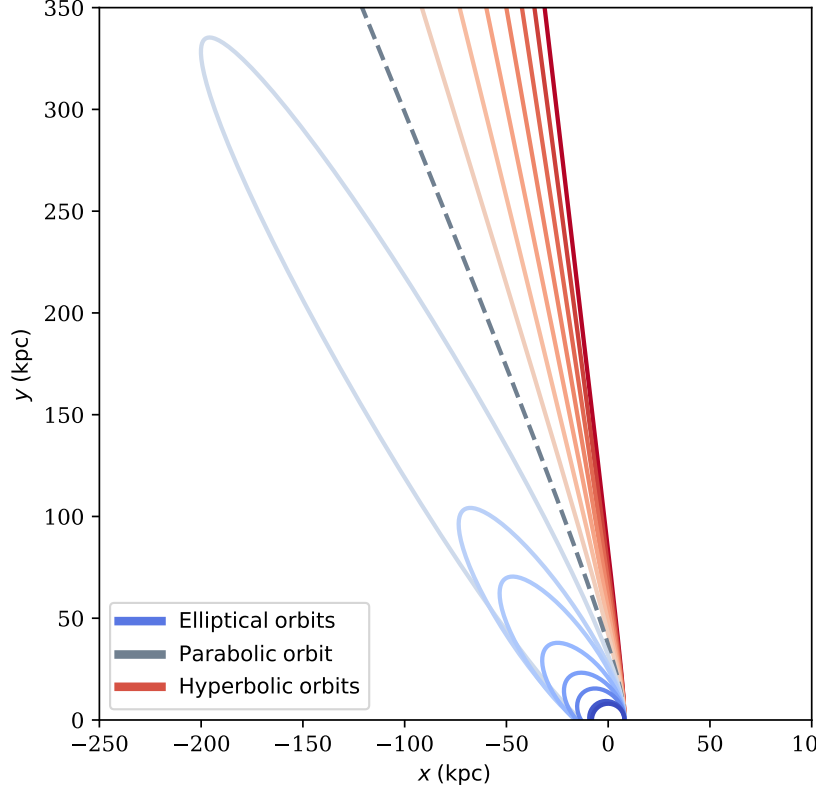


Figure 1.1: Transition from circular to hyperbolic orbits as the velocity of a star is increased from  $220 \text{ km s}^{-1}$  to  $800 \text{ km s}^{-1}$ . This figure was generated using MWPotential2014 in GALPY (Bovy, 2015), where the potential is tuned so that the circular velocity is  $220 \text{ km s}^{-1}$  at 8 kpc. Note that the terms elliptical, parabolic and hyperbolic are used here in analogy with the orbital families in a Keplerian potential; due to the non-Keplerian nature of the Galactic potential, the orbits are not conic sections.

determine the future orbit within the Milky Way; we know, for instance, that the Sun orbits the Milky Way in an approximately circular orbit at a velocity of  $v_c = 238 \text{ km s}^{-1}$  (Schönrich, 2012, although a value of  $220 \text{ km s}^{-1}$  is also frequently used, Bovy et al., 2012). If the Sun's speed were to be increased then that future orbit would become progressively more elliptical with longer and more distant excursions from the Galaxy. Past a certain speed, known as the escape speed, the Sun would not return and instead escape to infinity. This concept is further illustrated in Figure 1.1. In Newtonian terms, the escape speed is the speed at which the kinetic energy equals the potential energy with respect to the Milky Way. Note that the gravitational potential deepens as you approach nearer to the Galaxy, and thus the escape speed must be faster at smaller Galactocentric radii and slower further out; it is easier to escape the Milky Way if you start further away. A star which is travelling faster than the escape speed is called an *unbound* or *hypervelocity* star.

This picture is overly simplistic because the Milky Way is neither isolated nor static. The LMC (total mass  $1.2 \times 10^{11} M_{\odot}$ , Guo, White, Li, and Boylan-Kolchin, 2009) and SMC (total mass  $6.4 \times 10^{10} M_{\odot}$ , ibid.) distort the Milky Way's gravitational potential in a time-evolving way which can affect whether a star will escape the Galaxy. The LMC and SMC are in close proximity to the Milky Way (the LMC is at  $50.1 \pm 2.5$  kpc, Freedman et al., 2000; the SMC is at  $62.8 \pm 2.4$  kpc, Cioni, van der Marel, Loup, and Habing, 2000) and thus are closer to us than the hypervelocity star discovered by Brown, Geller, Kenyon, and Kurtz (2005). Determining whether a star is unbound in this joint time-evolving potential is non-trivial.

Complicating matters further, the Magellanic Clouds are on their first infall to the Milky Way (Besla et al., 2007) and thus are expected to be mostly intact, with both galaxies still actively forming stars. This opens up the possibility of stars being kicked from either of these galaxies and which then may or may not escape the Milky Way. The existence of such stars would make it difficult to decipher the origins of unbound stars in the Milky Way's halo. I explore the implications further in Ch. 4.

## 1.2 IS THIS STAR FAST?

The first step in determining whether a star is fast is to select the most sensible frame in which to gauge the speed. We are free to choose a frame such that a star is moving at  $0.1c$ , but then every star in the Milky Way would be moving at  $0.1 \pm 0.003c$  and we would have no basis on which to call a particular star fast. The term fast can only ever be sensibly discussed relative to a physically-motivated frame and the choice of frame is therefore made based on the Galactic context of the star.

The native frame of astronomical measurements is the frame co-moving with the Sun, the *heliocentric* frame. Most stars near the Sun are disc stars and so it is easiest to interpret the velocities of nearby stars in the frame defined by the mean motion of disc stars at the Sun's location, known as the *Local Standard of Rest* or *LSR*. The velocities of stars in the LSR can be obtained by correcting measured velocities in the heliocentric frame for the peculiar velocity of the Sun relative to the LSR. In a right-handed frame where  $U$  points towards the Galactic centre,  $V$  points in the direction of rotation of the disc and  $W$  points to the Galactic North Pole, the Sun's peculiar velocity (with statistical and systematic uncertainties) is  $(U_{\odot}, V_{\odot}, W_{\odot}) = (11.1 \pm 0.75 \pm 1, 12.24 \pm 0.47 \pm 2, 7.25 \pm 0.37 \pm 0.5) \text{ km s}^{-1}$  (Schönrich, 2012; Schönrich, Binney, & Dehnen, 2010).

*More accurately the native frame is the frame co-moving with whichever telescope or satellite took the measurement, however the conversion from this frame to the heliocentric one is well understood.*

The LSR frame is only convenient for the kinematical analysis of objects close to the Sun, for the simple reason that it is a frame rotating with the Sun and thus one must only go a few kiloparsecs away before the mean rotation of the disc is no longer aligned with the LSR  $V$  axis. An alternative frame is the one with the mean motion of the disc at the location of the star under consideration. A Cartesian frame is not necessarily the most intuitive for discussing the velocities of objects in an axisymmetric galaxy like the Milky Way, and so a cylindrical coordinate system is used where the velocities are  $(v_R, v_\phi, v_z)$ , such that a star on a perfectly circular orbit will have constant  $v_\phi$  and  $v_R = v_z = 0$ . A star travelling radially outward from the centre of the Galaxy would have  $v_\phi = 0$ . The *peculiar velocity* of the star relative to the mean rotation can be calculated and then used to determine whether the star is fast. For a star to be fast it must at least have a peculiar velocity larger than the velocity dispersion of disc stars of comparative age; for instance, the Blaauw (1961) definition of an OB runaway star is a peculiar velocity greater than  $40 \text{ km s}^{-1}$ , which is twice the velocity dispersion of OB stars in the disc. A complication that undermines this definition for older stars is contamination from the stellar halo. The halo has net zero rotation and a large velocity dispersion, and so if a star is older than 1 Gyr and metal-poor then it could be more likely that the star is a member of the stellar halo than a fast member of the disc.

Outside the disc, the *Galactic Standard of Rest* or *GSR* is normally used where the mean rotation of the disc is subtracted from the LSR velocity of the star, which I take to be  $V_c = 238 \pm 9 \text{ km s}^{-1}$  at the Sun's distance  $R_\odot = 8.27 \pm 0.29 \text{ kpc}$  from the Galactic centre (Schönrich, 2012; Schönrich et al., 2010).

### 1.3 A BRIEF HISTORY OF FAST STARS

I present here a brief history of fast stars from 1717 through to the beginning of my doctoral studies in 2015. This history reflects our advancing ability to measure the two components of stellar motion, proper motion and radial velocity, and so I begin with a timeline of their discovery and measurement. I then discuss several interrelated classes of fast star before clarifying the conventions used in naming them. Throughout the text I have highlighted the major open questions which I address in the main body of the thesis.



### 1.3.1 Proper motion and radial velocity

Proper motion was first measured by Halley (1717), who observed that Sirius, Arcturus and Aldebaran had moved  $0.5^\circ$  since the measurements of Greek antiquity, thus proving that stars do move across the sky beyond the apparent motion caused by the Earth's rotation and orbit. The first star to be remarked upon for its high proper motion was the binary system 61 Cygni ( $5.2 \text{ arcsec yr}^{-1}$ )<sup>3</sup> whose proper motion was first measured by Piazzzi (1803) and thus came to be known as 'Piazzzi's flying star'. 61 Cygni retains the title of the highest proper motion star visible to the naked eye. Only three stars have held the title of the highest proper motion star since 61 Cygni, those being Groombridge 1830 (first measured by Argelander, 1842;  $7.1 \text{ arcsec yr}^{-1}$ )<sup>3</sup>, Kapteyn's Star (Kapteyn, 1898;  $8.7 \text{ arcsec yr}^{-1}$ )<sup>3</sup> and Barnard's Star (Barnard, 1916;  $10.4 \text{ arcsec yr}^{-1}$ )<sup>3</sup>. These high proper motion stars would travel an angular distance perceptible to the human eye (approximately 1 arcminute, Yanoff & Duker, 2009) in under a decade, however a star being fast in projection onto the sky does not imply that it has a fast space velocity. The reason for this is made plain in this excerpt from Halley (1717),

Again these Stars being the moſt conſpicuous in Heaven, are in all probability the neareſt to the Earth, and if they have any particular Motion of their own, it is moſt likely to be perceived in them, which in ſo long a time as 1800 Years may ſhew it ſelf by the alteration of their places, though it be utterly imperceptible in the ſpace of a ſingle Century of Years.

Halley (1717)

Distilling this quotation: the motion of nearby stars is greater in projection than the motion of more distant stars, because the proper motion of a star is the space velocity perpendicular to the line of sight divided by the distance. It is thus slightly misleading to describe a high proper motion star as fast, for the star needs only to have a velocity which is slightly different from the Sun's and be sufficiently close. Determining the tangential space velocity of a star thus requires us to obtain the two difficult measurements of proper motion and distance. The distance to a star can be determined through the light of the star (either photometrically or spectroscopically) through comparison to stellar models or stars of known distance, or geometrically through the parallax. Parallax is the apparent angular motion of a star on the

#### **Proper motion:**

*Angular motion perpendicular to the line-of-sight to a star and measurable from the star's change in position across multiple epochs.*

#### **Radial velocity:**

*Motion parallel to the line-of-sight to a star and measurable from the Doppler shift of the star's spectrum.*

<sup>3</sup> These proper motion values come from the *Hipparcos* mission (described later on) as listed at <https://www.cosmos.esa.int/web/hipparcos/high-proper-motion> on 25/06/2018.

sky due to the motion of the Earth around the Sun and is related to the distance through the formula,

$$\text{distance (pc)} = \frac{1}{\text{parallax (arcsec)}}. \quad (1.1)$$

Both parallax and proper motion are measured by angular deviations of the star with time, however proper motion is a linear translation whilst parallax is a closed loop over the space of a year. In modern astrometric catalogues the position of the star at a fixed epoch  $(\alpha, \delta)$ , the parallax  $\varpi$ , and the proper motion  $(\mu_{\alpha*}, \mu_{\delta})$  are determined simultaneously in a five-parameter fit to the position of the star at a number of epochs. Thus, by measuring the position of a star several times over the space of several years, it is possible to determine the proper motion and parallax, and thence whether a star is fast.

Whilst astrometry had a number of early successes, it was rapidly overtaken in the study of Galactic dynamics by the development of spectroscopic radial velocities (see below). Until near the end of the twentieth century astrometry was entirely ground-based, and thus was time-consuming to perform, and was limited by both atmospheric distortions and calibration uncertainties arising from the inability to observe the entire sky with one instrument (van Leeuwen, 2007). It was clear that these three issues could only be solved with a space-based mission and on 8<sup>th</sup> August 1989 the European Space Agency launched *Hipparcos*, with the goal of measuring positions, parallaxes and proper motions at the milliarcsecond level for 120,000 stars (Perryman, 2012). The first *Hipparcos* catalogue was published in ESA (1997), with the less precise data for one million fainter stars published in the *Tycho* catalogue. A notable re-reduction of the *Hipparcos* data by Høg et al. (2000) resulted in the *Tycho-2* catalogue of 2.5 million stars, which was complete to 11<sup>th</sup> magnitude. The typical accuracy of the *Hipparcos* catalogue was 1 mas at 9<sup>th</sup> magnitude and, because a parallax of 1 mas corresponds to a distance of 1 kpc, this meant that the *Hipparcos* catalogue could only be used to investigate the dynamics of the nearest portions of the Galaxy.

The discovery of proper motion by Halley (1717) opened up the determination of the components of space motion which are perpendicular to the line of sight, however that left the component parallel to the line of sight unknown. This component is known as *radial velocity*. It has long been known that an astrometric radial velocity could in principle be calculated from the rate of change of the parallax and proper motion ('already at the beginning of the 20th century', Dravins, Lindegren, & Madsen, 1999), however the effect is expected to be extremely small (e.g. a change in the proper motion of Barnard's

***Astrometric radial velocity:***

*The changing distance causes the parallax and proper motion to change, because both are functions of the reciprocal of the distance.*

star of 1.975 mas over 22 months, Lindegren et al., 2018). Astrometric radial velocities have only recently become measurable for the nearest stars.

Fortuitously, Doppler (1842) postulated that we should observe the light from a moving object to be shifted in frequency proportional to the velocity along the line of sight. Thus, if the spectrum of a star is obtained and the absorption lines are shifted relative to our expectation, we can directly infer the radial velocity of the star. This is the *spectroscopic radial velocity*. Spectroscopic radial velocities are much easier to obtain than astrometric radial velocities, and indeed proper motions, because they can be obtained for stars out to the edge of the Milky Way in a single observation. It was spectroscopic radial velocities rather than proper motions that led to the discovery of the classes of fast stars I will describe in the following sections.

### 1.3.2 OB runaways

As discussed in Sec. 1.1, we should only expect to find OB stars orbiting in the plane of the disc and moving with a small peculiar motion, because OB stars should not live long enough for their orbits to be heated by dynamical interactions. It was thus startling when Blaauw and Morgan (1954) noted that the stars AE Aurigae and  $\mu$  Columbae appeared to be escaping from the Orion association at more than  $100 \text{ km s}^{-1}$ ; on this basis they conjectured that a new physical process involving high mass stars must exist. Hints at this process were given by Blaauw (1956), who showed that i) 25% of O to B0 stars have anomalously high space velocities  $> 30 \text{ km s}^{-1}$  while only 1% of B1-B5 stars are this fast and ii) more than 80% of the fast-moving stars were single compared to only one third of the slow-moving stars being single. Greenstein (1957) proposed that these stars should be called *runaway stars* and raised the point that these runaway OB stars will be found at high Galactic latitudes (i.e. out of the plane). Runaway stars are now commonly attributed to two processes; Blaauw (1961) suggested that a star could be ejected from a binary system by the supernova of its more massive companion, whilst Poveda, Ruiz, and Allen (1967) argued that 3- or 4-body encounters during the collapse of a young star cluster could cause the ejection of one or more of the stars. These two mechanisms are discussed in more detail in Sec. 1.4.

It is not known definitively which mechanism dominates, but the binary ejection scenario is thought to be more likely to due to the ubiquity of binary systems among massive stars (e.g. Branch and Wheeler, 2017). One approach to answering this question is to estab-

lish an association between an individual runaway star and its birth location, which will be marked by either a supernova remnant or star cluster. At present, the only Galactic core-collapse supernova remnant with a secure companion is S147 (Dinçel et al., 2015).

**Open question:** Do the nearby core-collapse supernova remnants contain runaway companions?

Another approach is to study the rotation or chemistry of particularly fast-moving runaway stars; rapid runaway stars from the binary supernova mechanism will have come from extremely tight binaries and thus may have been spun-up by pre-supernova mass transfer or contaminated by supernova ejecta. The binary supernova scenario proposed by Blaauw (1961) links OB runaway stars with two other classes of fast stars: *pulsars* and *Be stars*.

### 1.3.3 Pulsars

When massive stars reach the end of their nuclear-burning lifetime, they undergo a core-collapse supernova. The outer envelope is ejected in the ensuing explosion whilst the core collapses to form a dense remnant neutron star or black hole (e.g. Smartt, 2009). All single stars between 8 and 40  $M_{\odot}$  are expected to go supernova, with most stars more massive than 40  $M_{\odot}$  probably collapsing directly to black holes (Heger, Fryer, Woosley, Langer, & Hartmann, 2003). The neutron stars that are formed inherit an extraordinarily strong magnetic field and a very rapid rate of rotation, leading to the production of a lighthouse beam which we observe through ‘pulses’ of radio emission and from the period of which we can directly infer the period of rotation (e.g. Lyne & Graham-Smith, 1998). That pulsars typically rotate with periods of less than one second makes them fast stars in the rotational sense. However, measurements of the proper motions of pulsars (first achieved by Manchester, Taylor, & Van, 1974) demonstrate that pulsars are also fast stars in the translational sense, with Helfand, Taylor, and Manchester (1977) commenting that in some cases the inferred tangential speed exceeds the Galactic escape speed. These large velocities must be caused by a process during the supernova (an ‘asymmetry in the core collapse or the subsequent ... explosion’, Pfahl, Rappaport, Podsiadlowski, & Spruit, 2001, and references therein), however the precise mechanism for these kicks remains unclear. Many astronomers have attempted to infer the distribution of pulsar kick velocities by fitting analytic functions to observations, and we show a sample of the most popular distributions in Fig. 1.2. Clearly, the true natal kick distribution is not known at present – even fits within the

same work give radically different distributions (i.e. Faucher-Giguère and Kaspi, 2006)! The single Maxwellian distribution of Hansen and Phinney (1997) is assumed throughout this thesis.

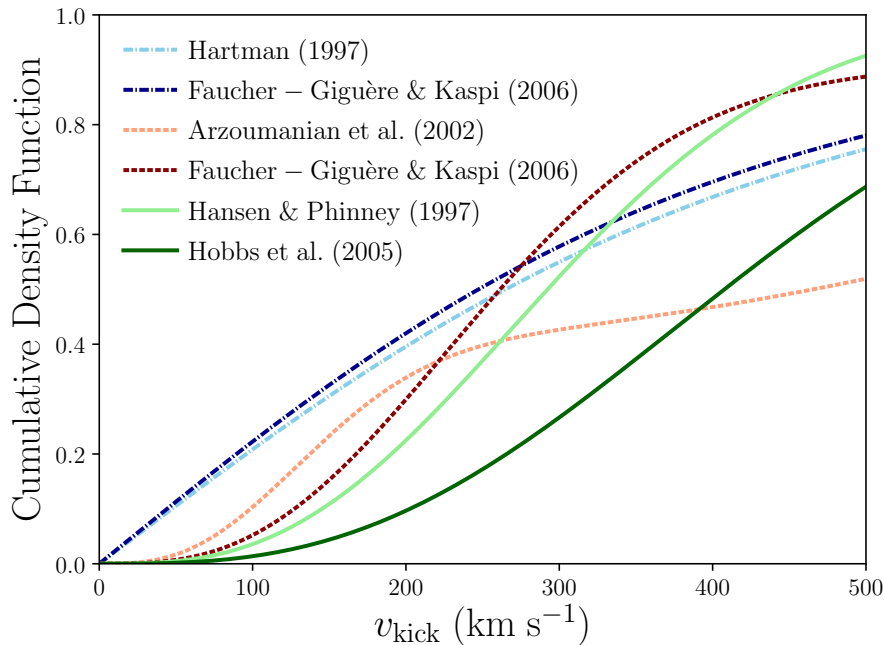


Figure 1.2: Various distributions for the 3D natal kick velocity distribution of neutron stars from the literature. The solid lines are the single Maxwellian distributions of Hansen and Phinney (1997) and Hobbs, Lorimer, Lyne, and Kramer (2005), the dash-dotted lines are from Hartman (1997) and Faucher-Giguère and Kaspi (2006), and the dashed lines are the double Maxwellian distributions of Arzoumanian, Chernoff, and Cordes (2002) and Faucher-Giguère and Kaspi (2006). Originally published in Boubert and Evans (2018).

The connection between OB runaway stars and pulsars is that massive stars are often found in binaries (e.g. Kouwenhoven, Brown, Zwart, & Kaper, 2007, find a  $3\sigma$  lower limit on the binary fraction of the Scorpius OB2 association of 70%) and if the pulsar progenitor loses at least 50% of its mass in the supernova then that binary will likely be unbound (Blaauw, 1961). Depending on the orbital velocity of the companion prior to the supernova, the companion may then be travelling rapidly enough to be classed as a runaway star.

#### 1.3.4 *Be stars*

It is possible for mass transfer in a close, pre-supernova binary to spin the companion up to critical rotation, where material on the equator is no longer gravitationally bound to the star. One particularly powerful observable of critically-rotating B stars are emission lines; material is launched from the equator into a Keplerian decretion disc which reprocesses the light of the star. B stars with emission lines in their

spectra are known as *Be stars*, and it is possible that all Be stars can be explained by mass transfer in pre-supernova binaries.

The Be star designation is historically restricted to stars of luminosity class V-III, as proposed by Jaschek, Slettebak, and Jaschek (1981), and around 17% of B type stars in the Milky Way are classified as Be stars (Zorec & Briot, 1997). The rapid rotation of Be stars is thought to be crucial to the phenomenon, because it minimises the velocity that material in the atmosphere must reach in order to form a Keplerian decretion disc. It has been proposed that all Be stars could be explained through single star physics: a star spins up due to evolutionary processes and then pulsations or magnetic fields launch material into a disc (see e.g., Rivinius, Carciofi, & Martayan, 2013, and references therein). It is also possible that binary star interactions play a role. Harmanec (1987) suggested that the disc is formed of material lost by a Roche-lobe filling companion, however, there is little evidence for such a mass-losing companion for most Be stars. Pols, Cote, Waters, and Heise (1991) proposed an alternative mechanism, now known as the post-mass-transfer model, whereby mass is transferred to a star by a Roche-lobe filling companion and the angular momentum carried by this material spins the star up to or close to critical velocity. This model requires that a star spinning at or near critical velocity can spontaneously form a decretion disc through an unknown mechanism, which could be the pulsations or magnetic fields proposed for single Be star channels.

Evidence for the mass transfer hypothesis comes from the large number of Be stars in binaries. These should be Be+NS (neutron star) binaries if the primary explodes as a supernova. If the primary is sufficiently stripped then it may avoid a supernova explosion and be present as a white dwarf or subdwarf star. There are five known Be+sdO binaries (Gies et al., 1998; Peters, Gies, Grundstrom, & McSwain, 2008; Peters, Pewett, Gies, Touhami, & Grundstrom, 2013; Peters, Wang, Gies, & Grundstrom, 2016; Wang, Gies, & Peters, 2017) and 28 confirmed Be+NS X-ray binaries (Reig, 2011).

If Be stars predominantly originate in massive, mass-transferring binaries, then a significant fraction should be runaway stars. Rinehart (2000) constructed a sample of 5756 B and 129 Be stars from the *Hipparcos* dataset (ESA, 1997) and looked for differences between the peculiar velocity distribution of B and Be stars, concluding that the distributions are identical to within  $1\sigma$  and thus that the post-mass-transfer model is not supported by the data. Berger and Gies (2001) searched for high-velocity Be stars by cross-matching an existing catalogue of Be stars with the *Hipparcos* catalogue (ESA, 1997), finding that 23 of the 344 Be stars in their sample had high peculiar



space velocities. We expect that most systems remain bound after the supernova and so these numbers could be consistent with the post-mass-transfer model.

**Open question:** Do the numbers of runaway Be stars support a mass-transfer origin for all Be stars?

If the post-mass-transfer hypothesis is correct, then it is possible that a single system could result in both a pulsar and a Be star, both objects being fast stars in both a rotational and translational sense.

### 1.3.5 Hypervelocity stars

While the notion of pulsars escaping from the Galaxy was accepted well before the new millennium, the idea of main sequence stars escaping was not. Star-star interactions should not produce a main sequence star travelling faster than the escape speed from the surface of the most massive star (e.g. Tauris, 2015, found that even in the most extremely favourable conditions, the peculiar velocity of late-B runaway stars from binary supernova events should not exceed  $540 \text{ km s}^{-1}$ ). The rotation of the Milky Way's disc could contribute up to an additional  $238 \text{ km s}^{-1}$ , if the B star were to be kicked in the direction of rotation. Due to both obscuration in the Galactic mid-plane and the narrow parameter space where it could occur, it was thought to be unlikely that we would observe an unbound OB runaway star. Brown (2015) estimated the production rate of such stars at  $8 \times 10^{-7} \text{ yr}^{-1}$ .

This made the serendipitous discovery by Brown et al. (2005) of a B-type star travelling with a radial velocity of  $853 \pm 12 \text{ km s}^{-1}$  (corresponding to a GSR velocity of  $709 \text{ km s}^{-1}$ ) at 71 kpc from the Sun rather surprising. Brown et al. (2005) turned to the earlier work of Hills (1988), who had theorised that the tidal disruption of a stellar binary during a close encounter with the massive black hole (MBH) at the Galactic centre could accelerate one member of the binary, in what is now known as the *Hills mechanism*. In addition to conceiving the only known process that could explain the velocity of this star, Hills (1988) coined the term *hypervelocity star* for the then hypothetical stars. The discovery of Brown et al. (2005) was thus christened Hypervelocity Star 1 (HVS1). The second (HVS2, more commonly known as US 708, Hirsch, Heber, O'Toole, & Bresolin, 2005) and third (HVS3, also known as HE 0437-5439, Edelmann, Napiwotzki, Heber, Christlieb, & Reimers, 2005) hypervelocity stars were discovered shortly thereafter.

Hirsch et al. (2005) initially conjectured that US 708, a helium subdwarf O star at 19 kpc and with a GSR velocity of at least  $751 \text{ km s}^{-1}$ ,

**Hypervelocity star:**  
While Hills (1988) used this term specifically to refer to stars ejected by the MBH, a more general usage has emerged where the term 'hypervelocity' is interchangeable with 'unbound'. We adopt the latter definition and thus a hypervelocity star is any star which is unbound from the Milky Way. For more detail see Sec. 1.3.6.

was formed in the merger of two helium white dwarfs during an interaction with the MBH at the Galactic centre. However, Justham, Wolf, Podsiadlowski, and Han (2009) proposed that this star was more consistent with having been the low-mass helium donor to a massive white dwarf and thence having being ejected by the resulting thermonuclear Type Ia supernova. A subsequent spectroscopic and kinematic analysis by Geier et al. (2015) confirmed this as the likely origin channel by demonstrating that the revised distance of  $8.5 \pm 1.0$  kpc and GSR velocity of  $1157 \pm 53$  km s<sup>-1</sup> was inconsistent with US 708 coming from the Galactic centre.

HVS3 is an  $8 M_{\odot}$  B star at a distance of 61 kpc. Edelmann et al. (2005) noted that HVS3 is only  $16.3^{\circ}$  from the centre of the LMC and that (neglecting the potential of the LMC and without measured proper motions) the star was consistent with being ejected from the LMC's centre 35 Myr ago at 600 km s<sup>-1</sup>. An origin in the LMC solves the problem that HVS3 would not live long enough to survive the journey from the Galactic centre to its current location (Edelmann et al., 2005). Perets (2009) suggests that the discrepancy between the flight time from the Galactic Centre and the stellar lifetime may be resolved by assuming that the star was ejected as a hypervelocity binary that later merged due to internal processes; however, the ejection of hypervelocity binaries following the disruption of a stellar triple is extremely unlikely (Fragione & Giacomo, 2018). Gualandris and Portegies Zwart (2007) found that the ejection of this star from the LMC at such a rapid velocity would require the Hills (1988) mechanism to be operating, and that the required black hole would need to be at least  $10^3 M_{\odot}$ . Brown et al. (2010) used proper motions measured with the Hubble Space Telescope to argue that the star likely originated in the Milky Way. However, with additional HST data, Brown et al. (2015) found that HVS3 could have come from either the Milky Way or the LMC.

**Open question:** Is HVS3 the first hypervelocity star known to originate in the Large Magellanic Cloud?

The reason to be confident in the hypervelocity classification of HVS1 is that i) the radial velocity is sufficient to make the star unbound even without knowledge of the proper motion and ii) a B-type main sequence star could only reach the outer halo if it had such an extreme velocity. Brown, Geller, Kenyon, and Kurtz (2006a) exploited these properties to make a successful targeted search for hypervelocity stars by photometrically selecting young main sequence stars far out in the halo, discovering HVS 4, 5 and 6 in the process. Buoyed by this success, the Hypervelocity Star Survey (Brown, Geller, & Kenyon, 2009, 2012, 2014; Brown, Geller, Kenyon, & Kurtz, 2006b;



Brown, Geller, Kenyon, Kurtz, & Bromley, 2007a, 2007b) obtained more than 1500 spectra over 9 years of faint, blue targets based on SDSS photometry and discovered a further 17 secure hypervelocity stars (HVS7-HVS10 and HVS12-HVS24; HVS11 was later found to not be a hypervelocity star) and dozens of candidates.

At first the existence of these stars tied in well with the Hills hypothesis, as described by Brown (2015): the Hills mechanism was the only production mechanism known that could produce stars traveling this fast in the Milky Way; the theoretical estimate of the ejection rate of  $10^{-4} \text{ yr}^{-1}$  (Yu & Tremaine, 2003) matched the observed numbers; the S-stars at the Galactic centre could be explained as the left-behind companion of the Hills mechanism; and the flight time of the hypervelocity stars back to the Galactic centre was broadly consistent with their age. The only hole in this story is that the Hills hypothesis predicts that the hypervelocity stars should be found isotropically across the sky. Far from finding an isotropic distribution, Brown, Geller, Kenyon, and Bromley (2009) found that eight of the 14 discoveries from the Hypervelocity Star Survey at that time were located within the constellations of Leo and Sextans, despite the surveys covering one fifth of the sky. This anisotropy is not simply a selection effect: Brown et al. (2007b) is 100% complete for stars with  $17 < g'_0 < 19.5$  over the  $7300 \text{ deg}^2$  covered by the Sloan Digital Sky Survey Data Release 6 and Brown et al. (2009) is 59% complete for stars with  $19.5 < g'_0 < 20.5$  over the same region. Brown et al. (2009) verified the significance of the anisotropy by showing that the hypervelocity stars are clustered in both Galactic latitude and longitude at  $3\sigma$  significance, in angular separations at  $5\sigma$  significance, and in two-point angular correlation at  $3.5\sigma$  significance. Brown (2015) states that there is currently "no good explanation for the anisotropic distribution of unbound late B-type stars", however the three most notable attempts were:

**DISC OF STARS:** A single MBH can eject hypervelocity stars anisotropically if the population from which the binaries originate is not spherical. For instance, if the binaries are scattered towards the MBH from a stellar disc the stars would be preferentially ejected within the plane of that disc (Lu, Zhang, & Yu, 2010; Zhang, Lu, & Yu, 2010, 2013).

**BINARY BLACK HOLE:** If there was a binary MBH at the centre of the Galaxy (or a temporary intermediate or solar mass black hole-MBH binary) then this could interact with and eject single stars (Yu & Tremaine, 2003); the signature of the binary black hole Hills mechanism is that the highest-velocity ejections would be in the plane of the binary.

**NON-SPHERICAL POTENTIAL:** As noted by Brown (2015), "a non-spherical Galactic potential can modify the observed distribution of [hypervelocity stars]". Triaxial dark matter haloes are predicted from cosmological simulations, and if the Milky Way is significantly triaxial then the distribution of hypervelocity stars on the sky should reflect that.

**Open question:** Why are the late B-type hypervelocity stars in the halo found in one part of the sky?

The motivation to understand the late B-type hypervelocity stars is two-fold: 1) they can be used as probes of the extreme phenomena that ejected them and 2) they are tracers of the Galactic potential from the centre to the outskirts. If the hypervelocity stars originate in the Galactic centre then their orbits should be almost perfectly radial. Gnedin, Gould, Miralda-Escudé, and Zentner (2005) noted that any deviation from that trajectory would encode the triaxiality of the Milky Way halo, although proper motions precise to  $10 \mu\text{as yr}^{-1}$  would be required. Another example is the use of the hypervelocity stars by Rossi, Marchetti, Cacciato, Kuiack, and Sari (2017) to jointly constrain the dark matter halo of the Milky Way and the properties of binary stars at the Galactic centre. Recently, Hattori, Valluri, and Castro (2018) argued that one could use the hypervelocity stars to infer the Solar location and motion independent of other methods, because any error in those quantities would cause us to infer the hypervelocity stars had non-zero angular momentum. These applications of the hypervelocity stars are reliant on them coming from the Galactic centre, although if they originated elsewhere then analogous inferences could be drawn.

The number of candidate hypervelocity stars has ballooned in the years since the discovery of HVS1 and today there are more than 500 candidates in the literature (see Fig. 1.3). Most of the candidates are late-type, high proper motion stars. In a majority of cases, the radial velocity is itself unremarkable and the 'hypervelocity' classification is driven entirely by a large proper motion measurement. As noted in Ziegerer et al. (2015), there is reason to be cautious with tangential velocity hypervelocity stars. The authors assessed the twenty GK candidates in Palladino et al. (2014) and were unable to confirm them, with the ground-based proper motions fingered as the likely culprit. Another possible mode of failure is that the proper motions are accurate but the distance is overestimated, with the result that the total space velocity is overestimated.

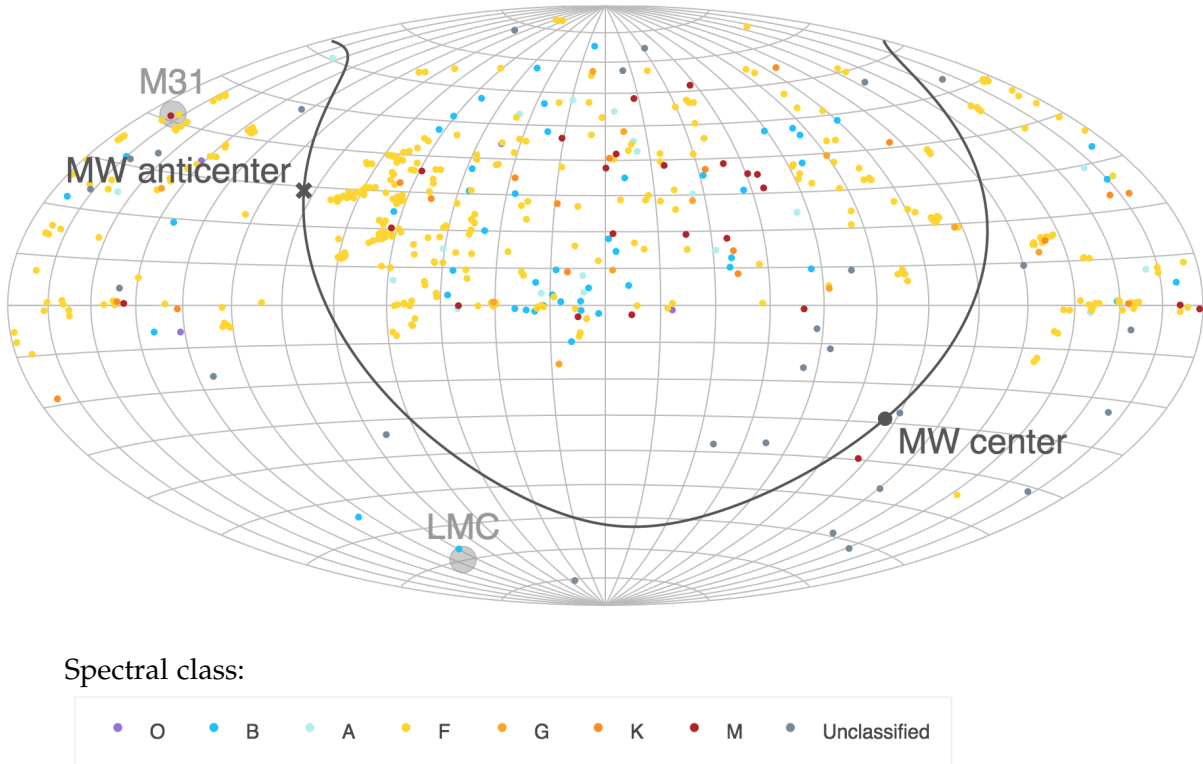


Figure 1.3: Hammer projection in right ascension and declination of all candidate hypervelocity stars, color-coded by spectral type. The thick gray line shows the plane of the Milky Way, with the large gray dot indicating the location of the Galactic centre. The locations of M31 and the LMC are shown as annotated. An interactive version of this figure is available at the OFSC<sup>4</sup>.

**Open question:** How many of the hundreds of hypervelocity star candidates are truly escaping?

An interesting sub-population of the hypervelocity stars are those associated with thermonuclear supernovae. Aside from US 708, the only example is the low-mass, high proper motion white dwarf GD 492 discovered by Vennes et al. (2017) and found to have an atmosphere rich with intermediate-elements. The conclusion reached by Vennes et al. (2017) was that GD 492 is the partially burnt remnant of a subluminal supernova Ia. This means that thermonuclear supernovae can produce both fast-moving remnants and companions, as evidenced respectively by GD 492 and US 708. The number and stellar types of such objects will be indicative of which channel of Type Ia supernovae is dominant.

**Open question:** How rare are hypervelocity objects associated with thermonuclear supernovae?

1.3.6 *What to call a fast star?*

The field of fast-moving stars is beset by a muddle of nomenclature, which stems from the difference between classifying stars by how fast they are moving or by their origin. Among hypervelocity stars this is a crucial distinction. A star may be ejected by the Hills mechanism, but remain bound to the galaxy. Conversely, a star may be unbound, but not produced by the Hills mechanism. Runaway stars are usually defined as OB stars with peculiar velocities in excess of  $40 \text{ km s}^{-1}$  (Blaauw, 1961), with either dynamical ejection from a young cluster or a supernova ejecting the progenitor's companion as their origin. However, the slower cousins of the binary supernova runaways are also termed runaways by several authors, with increasing use of the term walkaways for those runaways ejected slower than  $10 \text{ km s}^{-1}$  (de Mink et al., 2012; de Mink, Sana, Langer, Izzard, & Schneider, 2014; Lennon, van der Marel, Lerate, O'Mullane, & Sahlmann, 2016). A convention sometimes used in the literature is to refer to unbound Hills stars as hypervelocity and unbound runaway stars as hyperrunaway (eg. Brown, 2015; Perets & Šubr, 2012). However, this is open to the objection that it is difficult to determine the origin of the known unbound stars in the Galaxy. For example, they may not originate in the Milky Way and they may not even originate with the Hills mechanism. To clarify the terminology of this thesis, I exclusively use the term *runaway* to refer to stars of all velocities whose binary companion has gone supernova and the term *hypervelocity* to refer to stars of any origin which are unbound from the Milky Way. All stars emitted from a binary tidally disrupted by a black hole are *Hills stars*.

## 1.4 HOW TO MAKE A FAST STAR

**Thermonuclear supernova:**  
The runaway ignition of a white dwarf when it exceeds the Chandrasekher mass threshold.

**Core-collapse supernova:**  
The explosion caused by the collapse of a massive star's core when nuclear burning reaches nickel.

There are many circumstances in which a star can be accelerated to unusually fast speeds, but these can be distilled to three classes,

1. *Remnant of a supernova*
2. *Companion of a supernova*
3. *N-body dynamical interaction*

where the supernova can be either thermonuclear or core-collapse and the dynamical interaction can be  $\{3, 4, 5, \dots\}$ -body. It is not necessary that one of the above mechanisms supplies all of the speed of a fast star, because two or more of these mechanisms could chain (a *combination*) or the fast star could originate in a stellar population that itself is moving (a *translation*). These mechanisms were each touched

on in Sec. 1.3, but to aid clarity of argument they are briefly summarised here.

#### 1.4.1 *Remnant of a supernova*

It is possible for both core-collapse and thermonuclear supernovae to leave behind a remnant. In the case of core-collapse supernovae there is overwhelming evidence that neutron stars or black holes are formed during the supernova (for instance, the existence of pulsars associated with supernova remnants), whilst it has been suggested that partial detonation of a white dwarf (and the survival of a bound remnant) could explain the existence of sub-luminous thermonuclear supernovae (GD 492 was proposed by Vennes et al., 2017 to be one such remnant). Supernova are highly energetic events and thus any asymmetry prior to, during or after the explosion can impart a large kick to a remnant of the exploding star.

#### 1.4.2 *Companion of a supernova*

Both classes of supernova could occur with a close, binary companion. Thermonuclear supernovae are thought to require a binary companion, because an external source of material is needed to push the white dwarf over the Chandrasekhar limit. Core-collapse supernovae can only occur in stars whose initial mass was greater than  $8 M_{\odot}$  (Heger et al., 2003), and such massive stars are expected to mostly be found in binary systems. If the exploding star loses at least half its mass in the supernova, then Blaauw (1961) demonstrated that the binary will be unbound and the companion will escape at roughly the pre-supernova orbital velocity.

#### 1.4.3 *N-body dynamical interaction*

N-body encounters can cause individual components to be ejected at high speed by raising the binding energy of the total configuration. The most common example is the three-body interaction, where a single star and a binary star experience a close encounter and enter into a temporary and chaotic three-body orbit. In these encounters it is possible for any permutation of two of the stars to be bound into a binary, or for all three stars to be left as single stars. Depending on the final configuration it is possible for the stars to gain substantial velocity in this interaction; this principally occurs if the binding energy of the final binary is much greater than the initial binary, either by a more massive star being swapped into the binary or by a tight-

ening of the binary orbit. These interactions occur almost exclusively in dense stellar clusters due to the vanishingly small cross-section for stellar encounters in the field. Poveda et al. (1967) suggested that this process was the origin of the OB runaway stars.

One notable example of an N-body dynamical interaction discussed in the previous section is the Hills mechanism (Hills, 1988), where binary stars are tidally disrupted by Sgr A\* and one or both of the stars are ejected at thousands of kilometres per second.

At the other end of the N-body scale, Perets (2009) argued that the tidal disruption of a dwarf galaxy by the Milky Way could lead to some of the stripped stars travelling at extremely large velocities.

#### 1.4.4 *Combination*

The clearest example of two mechanisms combining occurs when the primary in a system of two massive stars goes supernova and unbinds the binary, and the runaway secondary then itself explodes in a supernova and expels its remnant pulsar; the pulsar's velocity would then be a combination of the runaway velocity and the natal kick. This particular chain should occur quite frequently given that, for example, Kobulnicky and Fryer (2007) found that early-type stars in the Cygnus OB2 association are likely to have a binary fraction greater than 70%, with 40% of those companions being of similar mass to the primary. Pflamm-Altenburg and Kroupa (2010) considered another possibility where a binary star is ejected by dynamical interactions in a star cluster and one of the stars explodes in a supernova, which they called the 'two-step-ejection process'. One can speculate that both these combinations could chain, however the parameter space where this could happen will be highly restricted.

#### 1.4.5 *Translation*

All stellar populations in the Local Group are moving with some velocity in the Galactic rest-frame and stars born in those populations inherit that velocity; for instance, stars born in the disc begin with the  $238 \text{ km s}^{-1}$  rotation speed. Tauris (2015) concluded that the fastest kick a late-B star could receive from the binary supernova scenario is  $540 \text{ km s}^{-1}$ , and thus it is only possible for this star to produce hypervelocity stars with the addition of the disc's rotation. A more extreme example is the proposal by Wang and Loeb (2017) that stars could form in the gaseous outflow from an active galactic nucleus and that these stars would be born travelling fast enough to escape the host galaxy. There are two young, nearby stellar populations with

a large velocity relative to the Milky Way that could be producing fast-moving stars and remain to be investigated: the LMC and SMC. The LMC in particular is moving at  $321 \pm 24 \text{ km s}^{-1}$  (Kallivayalil, van der Marel, Besla, Anderson, & Alcock, 2013) and so could be a source of great numbers of hypervelocity stars.

## 1.5 THE ERA OF GAIA

The successor to *Hipparcos* is the European Space Agency's *Gaia* space telescope, which was launched on 19 December 2013 and will obtain astrometry and photometry of the estimated  $10^9$  stars brighter than  $V \approx 20$  mag. The specific aspects of this mission relevant to fast stars:

1. Time-resolved three-band photometry ( $G, G_{BP}, G_{RP}$ ) for all sources brighter than  $V \approx 20$  mag across the entire sky.
2. Parallaxes and proper motions with errors less than  $10 \text{ } \mu\text{as}$  for stars brighter than  $G \approx 13$  mag, less than  $30 \text{ } \mu\text{as}$  for stars brighter than  $G \approx 15$  mag, and less than  $600 \text{ } \mu\text{as}$  for stars brighter than  $G \approx 20$  mag.
3. Radial velocities for stars brighter than  $G \approx 16$  mag.

The first data release (DR1) on 14 September 2016 and second data release (DR2) on 25 April 2018 occurred during my Ph.D.. These were preliminary releases in advance of the third release (DR3) in late 2020 and the final complete release (DR4) at the end of 2022<sup>5</sup>. DR1 contained the positions ( $\alpha, \delta$ ) and G-band magnitudes of 1,142,679,769 sources and 5-parameter astrometry ( $\alpha, \delta, \varpi, \mu_{\alpha*}, \mu_{\delta}$ ) for the subset of 2,057,050 sources in common between the *Tycho-2* catalogue and *Gaia* DR1 (Gaia Collaboration et al., 2016). The astrometric parameters for this subset were derived using the *Tycho-Gaia* Astrometric Solution (TGAS, Michalik, Lindegren, and Hobbs, 2015) and thus this catalogue subset is often simply referred to as TGAS. The arrival of DR1 at the beginning of the second year greatly influenced the direction of my Ph.D. and Chapters 2 and 3 rely heavily on data from TGAS. DR2 entirely supersedes DR1 and contains 5-parameter astrometry for 1,331,909,727 sources, including almost all the candidate hypervelocity stars. In Chapter 5 I argue that DR2 will be revolutionary for the study of fast stars and present a smörgåsbord of hypervelocity star results based on *Gaia* DR2 astrometry and photometry.

<sup>5</sup> These are tentative dates taken from <https://www.cosmos.esa.int/web/gaia/release> on 2 July 2018.



## 1.6 FROM OPEN QUESTIONS TO ANSWERS

In Sec. 1.3 I outlined a number of open questions in the field of fast stars. I list them again here alongside the chapter in which I address the question and a one-line summary of the chapter:

- **Chapter 2** Do the nearby core-collapse supernova remnants contain runaway companions?  
*I search ten nearby core-collapse supernova remnants for runaway companions using Gaia DR1 and identify four candidates.*
- **Chapter 3** Do the numbers of runaway Be stars support a mass-transfer origin for all Be stars?  
*I conduct a detailed Bayesian analysis of the kinematics of the 632 known Be stars and infer the fraction which are runaway stars.*
- **Chapter 4** Why are the late B-type hypervelocity stars in the halo found in one part of the sky?  
*I investigate my hypothesis that most of these stars are from the LMC and predict hundreds more will be found in the Southern hemisphere.*
- **Chapter 5.1** How many of the hundreds of hypervelocity star candidates are truly escaping?  
*I revisit all 524 candidate hypervelocity stars with Gaia DR2 astrometry and identify that there are only 41 likely escaping stars.*
- **Chapter 5.2** Is HVS3 the first hypervelocity star known to originate in the Large Magellanic Cloud?  
*I summarise my contributions to the proof that this star is from the LMC and discuss the implications of a black hole in that galaxy.*
- **Chapter 5.3** How rare are hypervelocity objects associated with thermonuclear supernovae?  
*I detail my contributions to the search for and discovery of three remarkable hypervelocity white dwarfs in Gaia DR2.*



## SEARCHING FOR FORMER COMPANIONS OF SUPERNOVA REMNANT PROGENITORS

*Based on work originally published in Boubert, Fraser, et al. (2017).<sup>1</sup>*

Supernovae (SNe) mark the deaths of stars. They can be divided into two broad categories: core-collapse SNe from the gravitationally powered explosion of massive stars (e.g. Smartt, 2009), and Type Ia SNe from the thermonuclear destruction of white dwarfs (e.g. Hillebrandt & Niemeyer, 2000). In both cases, there has been considerable interest in recent years in understanding their progenitor systems for reasons as diverse as testing stellar evolutionary models, improving their use as cosmological probes, and understanding their role in driving Galactic evolution.

A vital route to studying the progenitor systems of core-collapse SNe is to identify a runaway companion with the supernova remnant (SNR); the presence of a companion can be used to constrain the initial masses and separation of the two stars, as well as the evolutionary history leading to the explosion. Runaway stars are interesting in their own right for their dynamical properties, with the fastest being unbound from the Milky Way (see Sec. 1.3).

In this Chapter I develop a systematic framework for hunting SN-ejected binary companions within *Gaia* Data Release 1 (DR1; Gaia Collaboration et al., 2016). *Gaia* DR1 can only be used to search for companions for the ten SNRs nearer than 2 kpc, but with *Gaia* DR2 this framework will reveal companions for many of the Galactic SNRs. To place in context the significance of this advancement, I first summarise the prior searches for these companions in Sec. 2.1. The data sources for both the runaways and the SNRs are discussed in Sec. 2.2. I then outline two methods for hunting companions – the first using purely kinematic methods in Sec. 2.3, the second exploiting colour,

<sup>1</sup> Morgan Fraser conceived a project similar to the kinematic method presented in Sec. 2.3. I developed the more sophisticated method presented in Sec. 2.4 in collaboration with Morgan Fraser, Robert G. Izzard and N. Wyn Evans. I was responsible for all implementation and a majority of the analysis in this project. Robert G. Izzard consulted on the use of his binary population synthesis framework `BINARY_C` and suggested many edits to the text. Dave Green consulted on the existing literature surrounding supernova remnants. Morgan Fraser acknowledged Gerry Gilmore for early discussions on this work and was supported by a Royal Society - Science Foundation Ireland University Research Fellowship. Robert G. Izzard thanked the STFC for funding his Rutherford fellowship under grant ST/L003910/1 and Churchill College, Cambridge for his fellowship. This work was partly supported by the European Union FP7 programme through ERC grant number 320360.

magnitude and reddening together with the peculiar velocity of the progenitor binary with a Bayesian framework in Sec. 2.4. For four SNRs (the Cygnus Loop, HB 21, S147 and the Monoceros Loop) I identify likely runaway companions which are discussed in detail in Sec. 2.5.

## 2.1 HISTORY OF PRIOR SEARCHES

There is an extensive history of searches for former binary companions that have survived the SN explosion. At least 70% of massive stars are seen to be in binary systems (e.g. Sana et al., 2012), and, in a handful of cases, a surviving binary companion has been detected in deep imaging of extragalactic core-collapse SNe (Folatelli et al., 2014; Maund & Smartt, 2009). Type Ia SNe require a binary companion to explode (Hillebrandt & Niemeyer, 2000), and may leave behind a detectable non-degenerate companion (e.g. Han, 2008; Noda, Suda, & Shigeyama, 2016; Pan, Ricker, & Taam, 2014, and references therein). For both Type Ia and core-collapse SNe, the stellar parameters of a surviving binary companion can constrain the evolutionary status of the SN progenitor at the point of explosion (Bersten et al., 2012; Maund & Smartt, 2009). A SN progenitor companion may also be polluted with metals from the explosion (Israeli, Rebol, Basri, Casares, and Martín, 1999 and more recently Liu et al., 2015).

Several searches have already been made for runaway stars in Galactic Type Ia SNRs, most notably in Tycho’s SN where a possible candidate (designated Tycho G) has been claimed to be the former binary companion (Bedin et al., 2014; González Hernández et al., 2009; Ruiz-Lapuente et al., 2004). This association has since been disputed (Kerzendorf et al., 2009; Kerzendorf et al., 2013; Xue & Schaefer, 2015). Searches within other Galactic remnants such as that of SN 1006 (González Hernández et al., 2012) and Kepler’s SN (Kerzendorf, Childress, Scharwächter, Do, & Schmidt, 2014) have failed to yield a companion, while a non-degenerate companion has been almost completely ruled out for SNR 0509–67.5 in the Large Magellanic Cloud (Schaefer & Pagnotta, 2012).

Searches for companions to core-collapse SNe have mostly focussed on runaway OB stars near SNRs (Blaauw, 1961; Guseinov, Ankay, & Tagieva, 2005). HD 37424, a main sequence B star, has been proposed to be associated with the SNR S147 (Dinçel et al., 2015). The pulsar PSR J0826+2637 has been suggested to share a common origin with the runaway supergiant Go star HIP 13962 (Tetzlaff, Dinçel, Neuhäuser, & Kovtyukh, 2014), although there is no identified SNR. In the Large Magellanic Cloud, the fastest rotating O-star (VFTS102)

has been suggested to be a spun-up SN companion associated with the young pulsar PSR J0537–6910 (Dufton et al., 2011).

Recently Kochanek (2017b) used Pan-STARRS1 photometry (Chambers et al., 2016), the Green et al. (2015) dust-map and the NOMAD (Zacharias et al., 2005) and HSOY (Altmann, Roeser, Demleitner, Bastian, & Schilbach, 2017) proper motion catalogues to search for runaway former companions of the progenitors of the three most recent, local core-collapse SNe: the Crab, Cas A and SN 1987A. Based on a null detection of any reasonable candidates Kochanek (2017b) put limits on the initial mass ratio  $q = M_2/M_1 \lesssim 0.1$  for the nominal progenitor binary of these SNRs. Kochanek (2017b) note that this limit implies a 90% confidence upper limit on the  $q \gtrsim 0.1$  binary fraction at death of  $f_b < 44\%$  in tension with observations of massive stars.

Another more direct method for studying the progenitors of supernovae is to detect them in pre-explosion imaging. This is limited however to the handful of cases where SNe have exploded in a nearby galaxy with deep, high-resolution images. Furthermore, it is most suited for studying core-collapse SN progenitors (Smartt, 2009) which are luminous supergiants (although see Li, Bloom, et al., 2011 and McCully et al., 2014 for applications to Type Ia SNe). Alternative techniques to infer core-collapse SN progenitor properties using nucleosynthetic yields from late-time spectroscopy of SNe (e.g. Jerkstrand et al., 2014), or hydrodynamic estimates of ejecta mass (Bersten et al., 2014) are always model dependent. For Type Ia SNe, the spectroscopic and photometric signatures of interaction between SN ejecta and a companion may be used to constrain the progenitor system, but are relatively weak effects (Maeda, Kutsuna, & Shigeyama, 2014).

## 2.2 SOURCES OF DATA

The list of candidate stellar companions for each SNR is taken from a cross-match of TGAS and APASS (Sec. 2.2.1). There is no analogously uniform catalogue for SNRs and so we conduct a literature review for each SNR to establish plausible estimates for the central position, distance and diameter, which we discuss in Sec. 2.2.2 and in Appendix A.1.

### 2.2.1 Summary of stellar data

The primary astrometric component of *Gaia* DR1 was the realisation of the *Tycho-Gaia* astrometric solution (TGAS), theoretically developed by Michalik et al. (2015), which provides positions, parallaxes and proper motions for the stars in common between the DR1 and

*Tycho-2* catalogues. At 1 kpc the errors in the parallax from TGAS typically exceed 30%, which limits us to searching only those SNRs within 2 kpc. To better constrain the distance of the candidates we nearest-neighbour cross-match with the AAVSO Photometric All-Sky Survey (APASS) DR9 to obtain the B–V colour. *Gaia* Data Release 2 (DR2) contains the additional blue  $G_{BP}$  and red  $G_{RP}$  magnitudes and thus when this work is re-done in future with the improved astrometric and photometric data of DR2 we will be able to substitute for B–V with the  $G_{BP}-G_{RP}$  colour.

The typical expansion velocities of supernova remnant shells are more than  $1000 \text{ km s}^{-1}$  for the first few  $10^4$  years of their evolution (Reynolds, 2008). Thus, because recent estimates for the maximum velocity of runaways are  $540 \text{ km s}^{-1}$  for late B-types and  $1050 \text{ km s}^{-1}$  for G/K-dwarfs (Tauris, 2015), it is reasonable to assume that the former companion to the supernova progenitor still resides in the SNR. For each of these stars, we have positions  $(\alpha, \delta)$ , parallax  $\varpi$  and proper motions  $(\mu_{\alpha*}, \mu_{\delta})$  with a full covariance matrix Cov, as well as the mean magnitude  $G$  and, for a subset of stars, the APASS B–V colour.

### 2.2.2 Summary of individual SNRs

We select SNRs that are closer than 2 kpc, having stars in our TGAS-APASS cross-match within the central 25% of the SNR by radius, and lying within the footprint of Pan-STARRS so we can use the 3D dust-map of Green et al. (2015). Our choice to search the inner 25% by radius is more conservative than the one sixth by radius searched by previous studies (e.g. Dinçel et al., 2015; Guseinov et al., 2005). Less than 1% of runaways are ejected with velocities in excess of  $200 \text{ km s}^{-1}$  (e.g. Eldridge, Langer, & Tout, 2011) thus considering every star in the SNR would increase the number of potential candidates by an order of magnitude while negligibly increasing the completeness of our search. The SNRs in our sample are typically older than 10 kyr and so will have swept up more mass from the ISM than was ejected, which makes it difficult to type them from observations of their ejecta. We can say that these SNRs are likely the remnants of core-collapse SNe because around 80% of Galactic SNe are expected to be core-collapse SNe (e.g. Li, Chornock, et al., 2011; Mannucci et al., 2005). Moreover, several are identified with regions of recent star formation (i.e. G205.5+00.5 with Mon OB2) or molecular clouds in OB associations (i.e. G089.0+04.7 with molecular clouds in Cyg OB7). The properties of this sample of ten SNRs are given in Tab. 2.1, where

Table 2.1: Properties of the sample of supernova remnants, where the errors on the distance are  $1\sigma$  and are described in Appendix A.1.

SNR	Known as	Position	Diameter (arcmin)	Distance (kpc)	$N_{\text{TGAS}}$	$N_{\text{TGAS+APASS}}$
G065.3+05.7	—	19:33:00+31:10	$310 \times 240$	$0.77 \pm 0.2$	294	7
G069.0+02.7	CTB 80	19:53:20+32:55	80	$1.5 \pm 0.5$	14	11
G074.0−08.5	Cygnus Loop	20:51:00+30:40	$230 \times 160$	$0.54^{+0.10}_{-0.08}$	115	76
G089.0+04.7	HB 21	20:45:00+50:35	$120 \times 90$	$1.7 \pm 0.5$	25	3
G093.7−00.2	CTB 104A, DA 551	21:29:20+50:50	80	$1.5 \pm 0.2$	10	10
G114.3+00.3	—	23:37:00+61:55	$90 \times 55$	$0.7 \pm 0.35$	19	17
G119.5+10.2	CTA 1	00:06:40+72:45	90	$1.4 \pm 0.3$	8	7
G160.9+02.6	HB 9	05:01:00+46:40	$140 \times 120$	$0.8 \pm 0.4$	19	18
G180.0−01.7	S147	05:39:00+27:50	180	$1.30^{+0.22}_{-0.16}$	36	31
G205.5+00.5	Monoceros Loop	06:39:00+06:30	220	$1.2 \pm 0.4$	53	47

$N_{\text{TGAS}}$  is the number of candidates found in TGAS and  $N_{\text{TGAS+APASS}}$  is the number remaining after the cross-match with APASS.

Establishing a potential association between a star and a SNR requires us to demonstrate a spatial coincidence around the time of the SN explosion. The relevant properties of each SNR are then the location of the centre  $(\alpha, \delta)_{\text{SNR}}$ , distance  $d_{\text{SNR}}$ , age  $t_{\text{SNR}}$ , angular diameter  $\theta_{\text{SNR}}$  and either the proper motion  $(\mu_{\alpha*}, \mu_{\delta})_{\text{SNR}}$  or peculiar velocity  $(v_R, v_z, v_{\phi})_{\text{SNR}}$ .

We take the Ferrand and Safi-Harb (2012, known as *SNRcat*) and Green (2014) catalogues as the primary sources of SNR properties. We use the positions and angular diameters from the detailed version of the Green catalogue that is available online<sup>2</sup>. The distance to a SNR is usually uncertain and so we describe the origin of each distance in Appendix A.1.

We do not use estimates of the ages of SNRs because distance estimates to SNRs are degenerate with the age, so these two measurements are not independent. We thus conservatively assume that the SN must be older than 1 kyr and younger than 150 kyr. A younger SN at 1 kpc would very likely be in the historical record (Green & Stephenson, 2003; Stephenson & Green, 2002) and the shell of an older SNR would no longer be detectable.

Determining the location of the centre of a SNR is usually not straightforward. The standard method is to calculate the centroid of the projected structure of the SNR shell on the sky, but this position can be obfuscated by various effects such as the interaction between

<sup>2</sup> Green D. A., 2014, ‘A Catalogue of Galactic Supernova Remnants (2014 May version)’, Cavendish Laboratory, Cambridge, United Kingdom (available at <http://www.mrao.cam.ac.uk/surveys/snrs/>).

the ejecta and the local ISM, overlap between SNRs, and background objects misclassified as belonging to the SNR. G074.0–08.5 (Cygnus Loop) is notable for its peculiarity with a substantial blow-out region to the south of the primary spherical shell (e.g. Fang, Yu, & Zhang, 2017); a naive calculation of the centroid for this SNR would result in a centre which is around 10 arcmin away from the centroid of the shell. We have verified that our results for G074.0–08.5 are robust to this level of systematic error. Some of our SNR central positions have associated statistical errors, but because these estimates do not in general account for systematics we instead use a more conservative constraint. We adopt a prior for the true position of the SNR centre which is a two-dimensional Gaussian with a FWHM given by

$$\theta' = \max(5', 0.05\theta_{\text{SNR}}). \quad (2.1)$$

These values were chosen to attempt to balance the statistical and systematic errors which are present.

We assume that the progenitor system was a typical binary in the Milky Way thin disc and so is moving with the rotational velocity of the disc together with an additional peculiar motion. We sample a peculiar velocity from the velocity dispersions of the thin disc and propagate it into a heliocentric proper motion. We take the Sun to be at  $R_{\odot} = 8.5$  kpc and the Milky Way’s disc rotation speed to be  $v_{\text{disc}} = 240 \text{ km s}^{-1}$  with a solar peculiar velocity of  $(U_{\odot}, V_{\odot}, W_{\odot}) = (11.1, 12.24, 7.25) \text{ km s}^{-1}$  (Schönrich et al., 2010). We neglect uncertainties in these values because they are subdominant.

### 2.3 SEARCH WITH ONLY KINEMATIC CONSTRAINTS

If we had complete kinematic information for every star in a SNR, then the companion should be identifiable as the star which was coincident with the centre at the time of the SN. The kinematic information in TGAS is far from complete (no radial velocities and substantial proper motion uncertainties), but we investigate the efficacy of a simple kinematic method here to provide a benchmark for the more sophisticated Bayesian method in Sec. 2.4. We apply this kinematic method to all stars in TGAS that are within 25% of the radius of the SNR (i.e. not just those with APASS photometry), giving us somewhere in the range of 10–300 stars per SNR.

Given the geometric centre  $(\alpha_{\text{SNR}}, \delta_{\text{SNR}})$  and proper motion  $(\mu_{\alpha^*, \text{SNR}}, \mu_{\delta, \text{SNR}})$  of the remnant and their errors, we can estimate the past location at time  $-t$  of each star by the equations of motion,

$$\alpha_*(t) = \alpha_* - t\mu_{\alpha_*} \quad (2.2)$$

$$\delta(t) = \delta - t\mu_{\delta}, \quad (2.3)$$

and we can write similar expressions for the remnant centre. Note we use  $*$  to denote quantities we have transformed to a flat space, for instance  $\alpha_* = \alpha \cos \delta$ . The angular separation  $\Delta\theta$  is then approximated by,

$$\Delta\theta(t) = \sqrt{[\alpha_*(t) - \alpha_{*, \text{SNR}}(t)]^2 + [\delta(t) - \delta_{\text{SNR}}(t)]^2}. \quad (2.4)$$

The typical angular separations involved are less than a few degrees at all times, hence this approximation is valid to first order. This expression has a clearly defined global minimum given by,

$$T_{\min} = \frac{(\alpha_* - \alpha_{*, \text{SNR}})(\mu_{\alpha_*} - \mu_{\alpha_*, \text{SNR}}) + (\delta - \delta_{\text{SNR}})(\mu_{\delta} - \mu_{\delta, \text{SNR}})}{(\mu_{\alpha_*} - \mu_{\alpha_*, \text{SNR}})^2 + (\mu_{\delta} - \mu_{\delta, \text{SNR}})^2}, \quad (2.5)$$

which can be substituted back into Equation 2.4 to obtain the minimum separation  $\Delta\theta_{\min}$ .

We construct the covariance matrix  $\text{Cov} = D^{1/2}\text{Corr}D^{1/2}$  using the correlation matrix  $\text{Corr}$  and the diagonal matrix of errors  $D = \text{Diag}(\sigma_{\alpha}^2, \sigma_{\delta}^2, \sigma_{\varpi}^2 + (0.3 \text{ mas})^2, \sigma_{\mu_{\alpha}}^2, \sigma_{\mu_{\delta}}^2)$ . We have added on the 0.3 mas systematic error in parallax recommended by Gaia Collaboration et al. (2016). We draw samples from the multivariate Gaussian distribution defined by the mean position  $(\alpha, \delta, \varpi, \mu_{\alpha}, \mu_{\delta})$  and the covariance matrix  $\text{Cov}$  and from the distributions of the SNR centre, distance and peculiar velocity. These latter distributions are described in Sec. 2.2.2. We calculate  $T_{\min}$  and  $\theta_{\min}$  for each of the samples to give distributions for the predicted minimum separation and time at which it occurs.

Once we have these distributions we rank stars by the plausibility of them being the former companion. We do this in a qualitative way by finding the fraction  $F$  of realizations of each star which satisfy: i)  $1 < (T_{\min}/\text{kyr}) < 150$ , ii) the line-of-sight distance between the star and the SNR is less than 153 pc and iii) the minimum angular separation  $\theta_{\min}$  corresponds to a physical separation of less than 1 pc. The latter two of these constraints use the distance to the location of the progenitor binary when the supernova exploded, which can be calculated using the sampled parameters and the time of the minimum separation. The 153 pc limit of the second constraint is simply the distance travelled by a star at  $1000 \text{ km s}^{-1}$  over 150 kyr and is

*The 0.3 mas correction was later clarified to only be relevant if the parallaxes of multiple stars are being averaged. The inclusion of this value here is erroneous, but we have checked that our conclusions do not change if it is removed.*



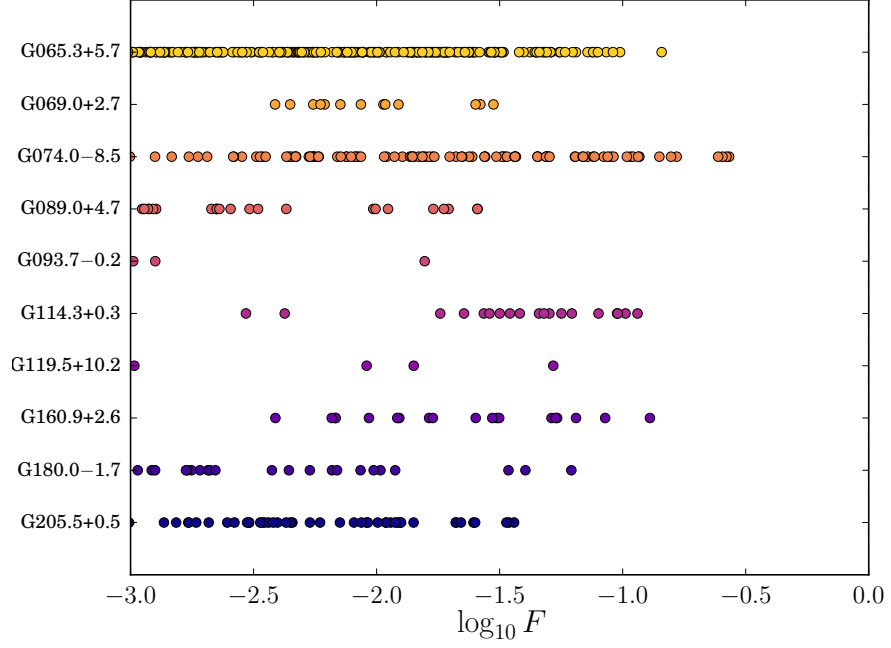


Figure 2.1: The fraction  $F$  of realisations of each star in each SNR which are consistent with being spatially coincident with the centre of the SNR at one point in the past 150 kyr. The criteria for determining whether a realisation is consistent are described in Sec. 2.3.

the maximum likely distance travelled by a runaway associated with a SNR. The 1 pc limit of the third constraint is the maximum likely separation of two stars in a binary and is smaller than the 153 pc limit in the radial direction because we have a measurement of the proper motion of each candidate. The value of  $F$  is shown for every star in each SNR in Fig. 2.1.

We rank the candidates in each SNR by this quasi-statistical measure and consider the star with the highest  $F$  to be the most likely candidate. For some of these stars we have the APASS  $B-V$  photometry and, were this method effective, most of the best candidates would be blue. Of the ten best candidates two have no associated  $B-V$  in the cross-match and five have  $B-V > 1.3$  hence are unlikely to be OB stars. One of the two best candidates without a measured  $B-V$  was HD 37424 in G180.0-01.7 (S147), which is one of the only five stars in G180.0-01.7 which did not have APASS magnitudes; HD 37424 has been previously suggested to be the runaway companion of G180.0-01.7 (Dinçel et al., 2015) and taking  $B-V = 0.073 \pm 0.025$  from that paper we see that our kinematic method would have proposed this star as the companion if it had APASS photometry. The remaining three stars with magnitudes are TYC 2688-1556-1 in G074.0-08.5 (Cygnus Loop) with  $B-V = 0.43$ , BD+50 3188 in G089.0+04.7 (HB 21) with  $B-V = 0.39$  and TYC 4280-562-1 in G114.3+00.3 with  $B-V = 0.39$ . Of these stars only BD+50 3188 is specifically mentioned in the literature with Chojnowski et al. (2015) concluding that it is a



B star. That one of the stars is B type suggests that the other two stars with similar colour are also B type by association, although it is possible that these two stars are less reddened by interstellar dust. Go89.0+04.7 is at a distance of  $1.7 \pm 0.5$  kpc while the other SNRs are much closer at  $0.54^{+0.10}_{-0.08}$  kpc and  $0.70 \pm 0.35$  kpc. The consequence of the B–V measurement being less reddened by dust is that the star is intrinsically redder and so the two untyped candidates may be A type or later.

This conclusion has some obvious problems. First, we are relying on an expectation that most runaways from core-collapse supernova should be OB stars, but we have not established what fraction of runaways from core-collapse SNe we would expect to be later-type than OB. The distribution of mass ratios in massive binary systems is observed to be flat (e.g. Duchêne & Kraus, 2013; Kobulnicky et al., 2014; Sana et al., 2012) which suggests that we would expect most runaways from core-collapse SNe to be bright, blue, OB-type stars: around 80% of companions to massive stars will have masses in excess of  $3 M_{\odot}$  with a median of  $7 M_{\odot}$ . This expectation is in conflict with the result above where five out of the ten best candidates are likely to be low-mass stars. One explanation for this seemingly large fraction of contaminants is that the method efficiently rules out those stars which are travelling in entirely the wrong direction to have originated in the centre of the SNR, but leaves in background stars which are coincident on the sky with the centre of the SNR and whose proper motion is not constrained. Ideally the method should down-weight those stars which are consistent with being background objects.

A second problem is that, because we cannot easily correct the B–V for extinction, the estimated spectral type of our candidates depended on one of them having already been typed. This estimated type is very uncertain and two of the stars could be A type or later. A superior method would determine the type of the star by making use of all the magnitudes in conjunction with a 3D dust-map and the parallax. Third, while we have generated a list of candidates, the ranking in the list is not on a firm statistical basis. There are four stars in Go74.0–08.5 which have  $0.25 < F < 0.28$ , only one of which is our best candidate. It is difficult to defend a candidate when a different statistical measure could prefer a different star.

These problems underscore the need for a Bayesian framework that incorporates kinematics with photometry and dust-maps, and which appropriately weights the possibility that the companion is late-type.

## 2.4 BAYESIAN SEARCH WITH BINARIES, LIGHT AND DUST

### 2.4.1 *Binary star evolution grid*

The three most important parameters which determine the evolution of a binary star are the initial primary mass  $M_1$ , initial secondary mass  $M_2$  and initial orbital period  $P_{\text{orb}}$ . Empirical probability distributions have been determined for these parameters and combining these with a model for binary evolution allows us to calculate a probability distribution for the properties of runaway stars. The properties of runaway stars which we are interested in are the ejection velocity  $v_{\text{ej}}$ , the intrinsic colour  $(B-V)_0$  and the intrinsic *Gaia*  $G$  magnitude  $G_0$  at the time of the supernova.

There are two standard formalisms used when evolving a large number of binary stars to evaluate the probability distribution for an outcome. The first is Monte Carlo-based and involves sampling initial properties from the distributions and evolving each sampled binary. In this approach the initial properties of the evolved binaries are clustered in the high-probability regions of the initial parameter space and low-probability regions might not be sampled at all. The other method is grid-based and selects binaries to evolve on a regularly-spaced grid across the parameter space. This grid divides the parameter space into discrete elements (voxels) and the probability of a binary having initial properties which lie in that voxel can be found by integrating the probability distributions over the voxel. This probability is assigned to the outcome of the evolution of the binary that was picked in that voxel. The probability distribution of the runaway properties can be determined by either method. In the Monte Carlo approach the resulting runaways from the binary evolution are samples from the probability distribution of runaway properties, while in the grid approach the distribution can be obtained by summing the probabilities which were attached to the runaway from each evolved binary.

Our choice of a grid over a Monte Carlo approach was motivated by our need to probe unusual areas of the parameter space. A Monte Carlo approach would require a large number of samples to fully explore these areas, while a grid approach gives us the location and associated probability of each voxel that produces a runaway star as well as the properties of the corresponding runaway star. These probabilities and other properties are thus functions of the initial grid.

We model the properties of stars ejected from binary systems in which one component goes supernova using the `BINARY_C` population-

synthesis framework<sup>3</sup>, described in more detail in Appendix A.2. We pre-compute the binary grid of 8,000,000 binaries with primary mass  $M_1$ , mass ratio  $q = M_2/M_1$  and orbital period  $P_{\text{orb}}$  having the ranges,

$$\begin{aligned} 8.0 &\leq M_1 / M_{\odot} \leq 80.0, \\ 0.1 &M_{\odot} / M_1 \leq q \leq 1, \\ -1.0 &\leq \log_{10}(P_{\text{orb}}/\text{days}) \leq 10.0. \end{aligned} \quad (2.6)$$

We assume the primary mass follows the Kroupa (2001) IMF,

$$N(M_1) \propto \begin{cases} M_1^{-0.3}, & \text{if } 0.01 < M_1 / M_{\odot} < 0.08, \\ M_1^{-1.3}, & \text{if } 0.08 < M_1 / M_{\odot} < 0.5, \\ M_1^{-2.3}, & \text{if } 0.5 < M_1 / M_{\odot} < 80.0, \\ 0, & \text{otherwise.} \end{cases} \quad (2.7)$$

We assume a flat mass-ratio distribution for each system over the range  $0.1 M_{\odot} / M_1 < q < 1$ . We use a hybrid period distribution (Izzard et al., 2018) which gives the period distribution as a function of primary mass and bridges the log-normal distribution for low-mass stars (Duquennoy & Mayor, 1991) and a power law (Sana et al., 2012) distribution for OB-type stars. The grid was set at solar metallicity to model recent runaway stars from nearby SNRs in the disc.

It is useful to distinguish between the runaway parameter space  $(B-V)_0$ – $G_0$ – $v_{\text{ej}}$ , which is best for highlighting the different runaway production channels, and the progenitor space  $M_1$ – $q$ – $P_{\text{orb}}$ , which is best for investigating the connection of those channels to other binary phenomena. For instance, our plot of runaway space in Fig. 2.2 has several gaps towards the top right, which, when viewed instead in the progenitor space, turn out to be regions where the binary has merged prior to the primary going supernova. We note that most of the probability is concentrated on the left edge of the plot in slow runaways of all colours. These correspond to the scenario of binary ejection where the two stars do not interact and the ejection velocity is purely the orbital velocity of the companion at the time of the supernova. The rest of the structure corresponds to cases when at some point in the evolution the primary overflows onto the secondary and forms a common envelope (Ivanova et al., 2013; Izzard, Hall, Tauris, & Tout, 2012). The drag force of the gas on the two stellar cores causes an in-spiral, while the lost orbital energy heats and ejects the common envelope. These runaways are faster due to the larger orbital velocity from the closer orbit, but there is a small additional kick from the impact of SN

<sup>3</sup> We use version 2.0pre22, SVN 4585.

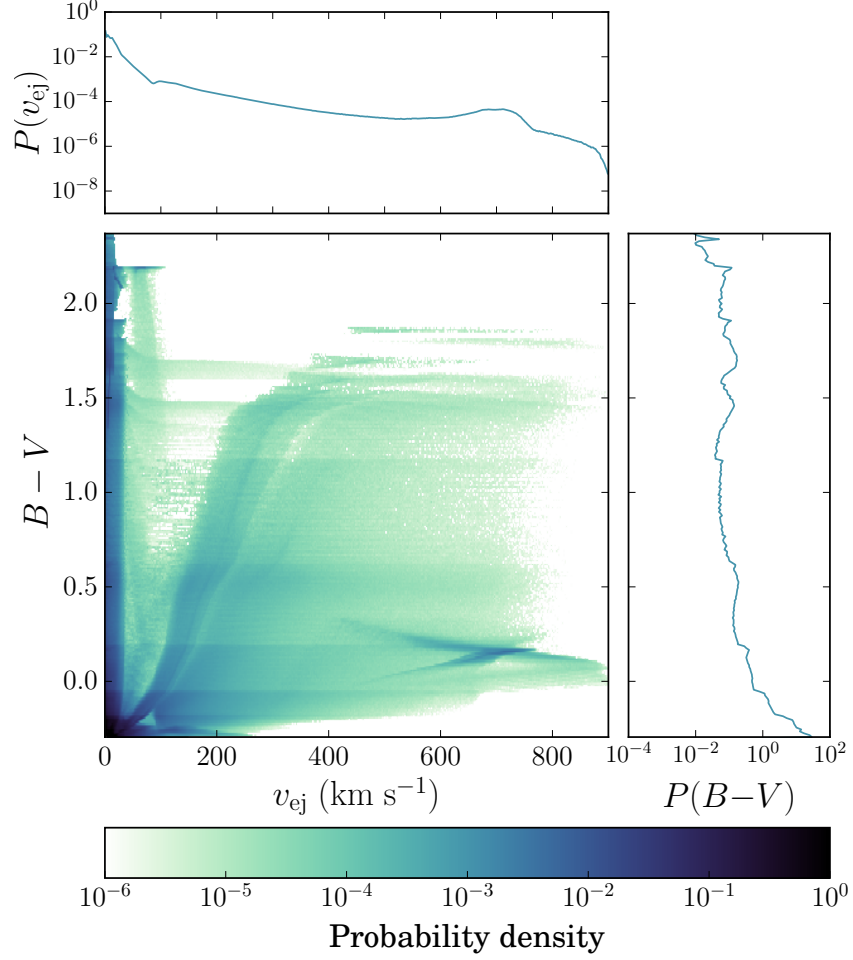


Figure 2.2: Probability distribution in velocity-colour space of the runaways produced by our binary evolution grid. The top and right plots show 1D projections of the joint probability distribution.

ejecta on their surface. There is further discussion of the features in Fig. 2.2 in Sec. 4.2.1.2, where this approach to modelling binary stars is used to simulate runaway stars in the Large Magellanic Cloud.

#### 2.4.2 Algorithm

We want to assess the hypothesis that a given star with observables  $\mathbf{x}$  is a runaway from a SNR. Our null hypothesis  $H_0$  is that a particular star is not the runaway companion and we wish to test this against the hypothesis  $H_1$  that it is. In Bayesian inference each hypothesis  $H$  has a set of model parameters  $\theta$  which can take values in the region  $\Omega$ .  $H$  is defined by a prior  $\mathcal{P}(\theta|H)$  and a likelihood  $\mathcal{L}(\mathbf{x}|\theta, H)$ . The Bayesian evidence for the hypothesis is then  $\mathcal{Z}$ , which is given by the integral

$$\mathcal{Z} = \int_{\Omega} \mathcal{P}(\theta|H) \mathcal{L}(\mathbf{x}|\theta, H) d\theta. \quad (2.8)$$

Table 2.2: Interpretation of Bayes factors  $K$  (Kass & Raftery, 1995).

$2 \ln K$	$K$	Evidence against $H_0$
0 to 2	1 to 3	Not worth more than a bare mention
2 to 6	3 to 20	Positive
6 to 10	20 to 150	Strong
> 10	> 150	Very strong

The evidence is equivalent to  $\Pr(\mathbf{x}|\mathbf{H})$ , i.e. the probability of the data under the hypothesis.

To compare the background ( $H_0$ ) and runaway ( $H_1$ ) hypotheses we calculate the Bayes factor  $K = \mathcal{Z}_1/\mathcal{Z}_0$ , where  $\mathcal{Z}_0$  and  $\mathcal{Z}_1$  are the evidences for  $H_0$  and  $H_1$  respectively. The interpretation of Bayes factors is subjective but a Bayes factor greater than one indicates that  $H_1$  is more strongly supported by the data than  $H_0$  and vice versa. A review on the use of Bayes factors is given by Kass and Raftery (1995) who provide a table of approximate descriptions for the weight of evidence in favour of  $H_1$  indicated by a Bayes factor  $K$ . To aid the interpretation of our results we replicate this table in Tab. 2.2.

To obtain the evidence for  $H_0$  we define a probability distribution using the stars in the TGAS/APASS cross-match that lie in an annulus of width  $10^\circ$  outside the circle from which we draw our candidates. We can describe the distribution of locations of stars in the space  $(\omega, \mu_{\alpha*}, \mu_\delta, G, B-V)$  in a non-parametric way by placing Gaussians at the location of each star and summing up their contributions over the entire space. This method is called kernel density estimation (KDE). Note that we normalise the value in each dimension by the standard deviation in that dimension for the entire sample. This normalisation is necessary because the different dimensions have different units. The prior for each candidate is a Gaussian in each dimension centred on the measured value with a standard deviation given by the measurement error. The likelihood for a point sampled from the prior is the KDE evaluated at that point.

The evidence for  $H_1$  is more complicated to calculate because the model parameters  $\theta$  are properties of the SNR and progenitor binary and thus need to be transformed into predicted observables  $\tilde{\mathbf{x}}$  of the runaway. The likelihood is

$$\mathcal{L}(\mathbf{x}|\theta) = \mathcal{N}(\mathbf{x}|\tilde{\mathbf{x}}(\theta), \text{Cov}(\mathbf{x})), \quad (2.9)$$

where  $\tilde{\mathbf{x}}$  is a function of  $\theta$  and  $\mathcal{N}(\mathbf{a}|\mathbf{b}, \mathbf{C})$  denotes the PDF of a multivariate Gaussian distribution evaluated at  $\mathbf{a}$  with mean  $\mathbf{b}$  and covariance matrix  $\mathbf{C}$ . For this preliminary work we neglect the off-diagonal terms of the covariance matrix.

Table 2.3: Model parameters for the runaway hypothesis.

Parameter	Description
$\alpha_{\text{SNR}}$	RA of the true centre of the SNR
$\delta_{\text{SNR}}$	DEC of the true centre of the SNR
$d_{\text{SNR}}$	Distance to the true centre of the SNR
$t_{\text{SNR}}$	Age of the SNR
$M_1$	Primary mass of the progenitor binary
$q = M_2/M_1$	Mass ratio of the progenitor binary
$P_{\text{orb}}$	Orbital period of the progenitor binary
$E(B-V)$	Reddening along the LoS to the candidate
$v_{\text{R,pec}}$	Peculiar velocity in Galactic R
$v_{\text{z,pec}}$	Peculiar velocity in Galactic z
$v_{\phi,\text{pec}}$	Peculiar velocity in Galactic $\phi$

The prior combines the primary mass  $M_1$ , mass ratio  $q$  and period  $P_{\text{orb}}$  of the progenitor binary with the location  $(\alpha_{\text{SNR}}, \delta_{\text{SNR}})$ , age  $t_{\text{SNR}}$ , distance  $d_{\text{SNR}}$  and peculiar velocity  $v_{\text{pec}}$  of the SNR and the reddening  $E(B-V)$  along the line of sight. These model parameters are given in Tab. 2.3 for reference. The prior is

$$\mathcal{P}(\boldsymbol{\theta}) = \mathcal{N}(\alpha_{\text{SNR}})\mathcal{N}(\delta_{\text{SNR}})\mathcal{N}(d_{\text{SNR}})\mathcal{U}(t_{\text{SNR}})P(M_1, q, P_{\text{orb}}) \\ P(E(B-V)|d_{\text{run}})\mathcal{N}(v_{\text{R,pec}})\mathcal{N}(v_{\text{z,pec}})\mathcal{N}(v_{\phi,\text{pec}}), \quad (2.10)$$

where  $\mathcal{N}(a)$  denotes a univariate Gaussian distribution in  $a$ ,  $\mathcal{U}(a)$  denotes a uniform distribution in  $a$  and the other components are non-analytic. The additional variable  $d_{\text{run}}$  is the predicted distance between the observer and runaway and is a function of the other model parameters. The ranges, means and standard deviations for the first four and last three distributions are given in Sec. 2.2.2 and were used for the simple method in Sec. 2.3.

The function  $P(M_1, q, P_{\text{orb}})$  is the probability that, if there is a runaway star, it originates in a progenitor binary with those properties. This probability can be obtained directly from the PDFs of the binary properties (Sec. 2.4.1) after renormalising to remove the binaries which do not produce runaway stars.

The other non-analytic function  $P(E(B-V)|d_{\text{run}})$  expresses the probability of the reddening along the line of sight to the observed star if it is at a distance  $d_{\text{run}}$ . Green et al. (2015) used Pan-STARRS1 and 2MASS photometry to produce a 3D dust-map covering three quarters of the sky and extending out to several kiloparsecs. Green et al. (2015) provide samples from their posterior for  $E(B-V)$  in each distance modulus bin for each HEALPix ( $n_{\text{side}} = 512$ , corresponding to

a resolution of approximately 7 arcmin) on the sky. We use a Gaussian KDE to obtain a smooth probability distribution for  $E(B-V)$  in each distance modulus bin. We then interpolate between those distributions to obtain a smooth estimate of  $P(E(B-V)|\mu)$  which we illustrate for one sight-line towards the centre of S147 in Fig. 2.3. Note that  $\log_{10} d_{\text{run}} = 1 + \mu/5$ , where  $d_{\text{run}}$  is a function of our other model parameters. Green et al. (2015) used the same definition of  $E(B-V)$  as Schlegel, Finkbeiner, and Davis (1998) so we have converted their  $E(B-V)$  to the Landolt filter system using coefficients from Schlafly and Finkbeiner (2011).

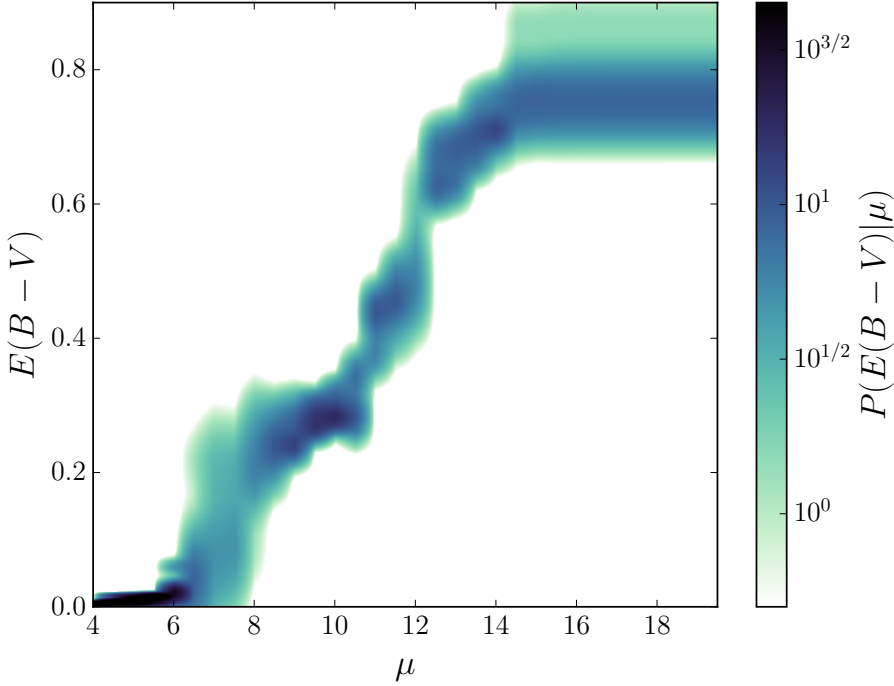


Figure 2.3: The conditional PDF for the dust extinction along the line of sight to G180.0–1.7 calculated by interpolating samples from the Green et al. (2015) dust-map.

The rest of this section is devoted to describing the transform  $\tilde{\mathbf{x}}(\boldsymbol{\theta})$  between the model parameters and the predicted observables. The outcome of the binary evolution is a function solely of the progenitor binary model parameters; the pre-calculated grid of binary stars thus provides the ejection velocity  $v_{\text{ej}}$ , intrinsic colour  $(B-V)_0$  and intrinsic magnitude  $G_0$ , which are essential to mapping the model parameters to predicted observables. In addition, we obtain other parameters of interest such as the present day mass of the runaway star  $M_{\text{run}}$  and the age  $T_{\text{run}}$ .

The kinematics of the SNR centre are fully determined by the position, distance and peculiar velocity, under the assumption that the velocity is composed of a peculiar velocity on top of the rotation of the Galactic disc at the location of the SNR centre. The location of

the runaway on the sky is known because the errors on the observed position of a star with *Gaia* are small enough to be negligible. The remaining kinematics that need to be predicted are the distance  $d_{\text{run}}$  and proper motion. The velocity vector of the runaway  $\mathbf{v}_{\text{run}}$  is the sum of the velocity of the SNR and the ejection velocity vector  $\mathbf{v}_{\text{ej}}$ . The location of the explosion, now the centre of the SNR, continues along the orbit of the progenitor binary within the Galaxy. We advance the centre of the SNR and the runaway along their orbits for the current age of the SNR  $t_{\text{SNR}}$ , noting that this time is so short that any acceleration is negligible and thus the orbits are essentially straight lines. The separation of the centre of the SNR and the runaway at this point is then simply the difference of their velocity vectors multiplied by  $t_{\text{SNR}}$ , i.e.  $\mathbf{v}_{\text{ej}}t_{\text{SNR}}$ . We then fix the kinematics of the model by denoting the present-day centre of the SNR to be at  $(\alpha_{\text{SNR}}, \delta_{\text{SNR}})$  and the present-day distance to the centre of the SNR to be  $d_{\text{SNR}}$ .

To obtain predictions for the proper motions and parallax we consider the intersection of the half-line defined by the observed position of the candidate on the sky and a sphere centred at the distance and position of the SNR. This sphere has a radius given by  $v_{\text{ej}}t_{\text{SNR}}$ , which is the distance travelled by the runaway since the supernova. A diagram of this geometry is shown in Fig. 2.4. If the distance travelled by the runaway is not large enough then the sphere fails to intersect the line and thus the likelihood of this set of parameters is zero. In almost every case there are two intersections which correspond to the runaway moving either away from or towards us. If the SNR is close and old and the runaway is travelling rapidly, there is a pathological case in which there is only one solution because the solution which corresponds to a runaway moving towards us is already behind us. The geometry of the intersection point gives us the distance to the star which we can use to predict the parallax. The predicted proper motion of the runaway depends on the velocity of the progenitor binary. We sample in the velocity dispersion of the Milky Way thin disc and add on the rotation of the disc and ejection velocity of the runaway. This velocity is converted to proper-motions and line-of-sight radial velocities using the transforms of Johnson and Soderblom (1987).

We then obtain a prediction for  $B-V$  by simply using  $B-V = (B-V)_0 + E(B-V)$ . The *Gaia* G band is broader than the V band and so is more sensitive to the slope of the spectrum (Sanders et al., in preparation). One consequence of this is that the relative reddening in the G band  $A(G)/A(V)$  is a function of the intrinsic colour of the star. Assuming that  $A(V) = R_V E(B-V)$ , where the constant  $R_V = 3.1$  is related to the average size of the dust grains and has been empirically determined in the Milky Way (Schultz & Wiemer, 1975), we re-



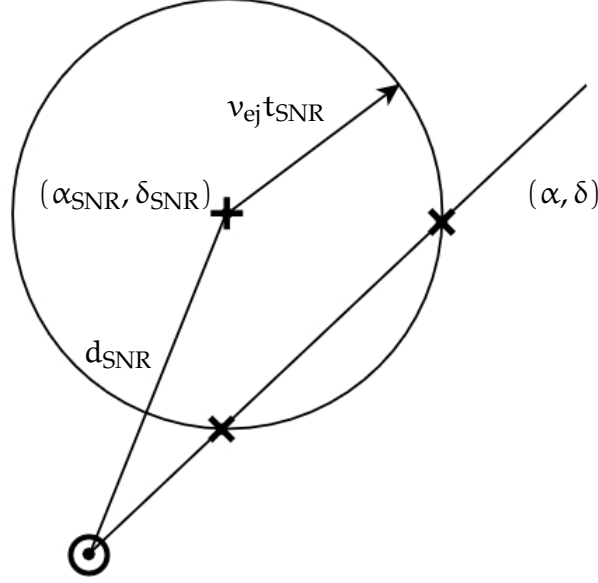


Figure 2.4: A diagram of the geometry described in Sec. 2.4.2. The observer is at  $\odot$  and the centre of the supernova remnant is at  $+$ . The two possible locations of the candidate if it is the runaway are marked by  $\times$  and correspond to the intersection of the sphere of radius  $v_{ej}t_{SNR}$  centred on the SNR and the half-line defined by the coordinates of the candidate.

cast this dependency as  $A(G)/E(B-V)$  as a function of  $(B-V)_0$ . This relation has been calculated empirically by Sanders et al. (in preparation) and thus we have an expression for the apparent magnitude  $G = G_0 + A(G) + \mu$ .

We elected to use nested sampling (Skilling, 2006) to explore the parameter space because it is optimised with estimating the evidence as the primary goal, while more standard Markov Chain Monte Carlo (MCMC) methods are targeted at obtaining samples from the posterior. We use the MULTINEST implementation of nested sampling (Feroz et al., 2009; Feroz et al., 2013; Feroz & Hobson, 2008) which we access through the PYMULTINEST PYTHON module (Buchner et al., 2014). MULTINEST requires that we express our prior as a transform from a unit hypercube to the space covered by our prior. For independent parameters, this is a trivial application of inverting the cumulative distribution function. However, we have two prior probability distributions  $P(E(B-V)|\mu)$  and  $P(M_1, q, P_{orb})$  for which there are no suitable transforms. Note that  $\mu$  is the distance modulus to the runaway which is a complicated function of the position, distance and age of the SNR and the ejection velocity of the runaway. For these parameters, we use the standard method of moving the probability distribution into the likelihood, which is implemented in MULTINEST by assuming a uniform distribution in the prior and including a factor in the likelihood to remove this extra normalisation. Some technical

details of the implementation of this problem in MULTINEST are discussed in Appendix A.3.

Using nested sampling, we explore the parameter space and obtain a value for the log of the evidence for each candidate. We then obtain the Bayes factor by dividing the evidence for  $H_1$  by the evidence for  $H_0$ . A Bayes factor less than one indicates that the null hypothesis is more strongly favoured, i.e. this star is likely a background star. A Bayes factor greater than one suggests that the runaway model is preferred.

#### 2.4.3 Fraction of supernovae with runaways

Only a fraction of supernovae will result in a runaway companion. Some massive stars are born single and companions are not always gravitationally unbound from the compact remnant after the supernova. Companions of massive stars tend to also be massive and so some will themselves explode as a core-collapse supernova, either in a bound system with the compact remnant of the primary or after being ejected as a runaway star (e.g. Zapartas, de Mink, Izzard, et al., 2017). A further contaminant is that binary evolution can cause stars to merge before the primary supernova occurs, through dynamical mass transfer leading to a spiral-in during common envelope evolution. Our model assumes that there was a runaway companion to the SNR and thus the calculated evidence needs to be multiplied by the fraction of SNRs with a runaway.

Evolving a population of binary stars as described above we find that the average number of core-collapse supernovae per binary system with a primary more massive than  $8 M_\odot$  is 1.22. All single stars in the mass range  $8 < M / M_\odot < 40$  are expected to go supernova, with most stars more massive than  $40 M_\odot$  probably collapsing directly to black holes (Heger et al., 2003). Note that in the version of BINARY\_C used for this work a core-collapse supernova is signalled whenever the core of a star collapses to a neutron star or black hole, including the case where the primary collapses directly to a black hole. Such collapses are sufficiently rare that we do not correct for this effect. An assumption on the binary fraction is required to combine statistics for single and binary populations. Arenou (2010) provides an analytic empirical fit to the observed binary fraction of various stellar masses,

$$F_{\text{bin}}(M_1) = 0.8388 \tanh(0.079 + 0.688M_1). \quad (2.11)$$

Based on this binary fraction and grids of single and binary stars evolved with `BINARY_C`, we estimate that 32.5% of core-collapse supernovae have a runaway companion. This fraction is best described as ‘about a third’ given the approximate nature of the prescriptions used to model the binary evolution and the uncertainties in the empirical distributions of binary properties.

#### 2.4.4 *Verification*

We verify our calculation of the evidence above by sampling runaways from the model and using their  $(\varpi, \mu_{\alpha,*}, \mu_{\delta}, G, B-V)$  to generate a kernel density estimate of their PDF. The evidence for a candidate to be a runaway can then be computed identically to the background evidence. In contrast to the method described in Sec. 2.4.2, where the prior and likelihood are functions of the model parameters which are described in Tab. 2.3, this method casts the prior and likelihood as a function of the model observables. In the limit where we draw infinite samples from our model this method will give the same result as the method in Sec. 2.4.2. Drawing samples from the model and constructing a KDE is advantageous for its simplicity. The likelihood function is an evaluation of a KDE and thus is guaranteed to be smooth and non-zero everywhere, meaning that the considerations discussed in Appendix A.3 are not relevant. The first disadvantage of calculating the evidence by this method is that it only gives accurate values of the evidence for regions of the parameter space which are well sampled. The second disadvantage is that by not being explicit about the model parameters we cannot directly constrain them, and so this method does not output the maximum-likelihood distance to the SNR or the mass of the progenitor primary. The implicit method is used in this work solely as a cross-check of our results.

#### 2.4.5 *Validation*

We validate our method by considering approximations to the false positive and the false negative rate. For each SNR we assume there is a nominal SNR at Galactic coordinates  $(l, b) = (l_{\text{SNR}} - 1^\circ, b_{\text{SNR}})$  with the same distance and diameter estimates as the true SNR. We acquire candidates from our TGAS and APASS cross-match and inject an equal number of model runaway stars sampled from our binary grid, calculating equatorial coordinates, parallaxes and proper motions which would correspond to a runaway from that location ejected in a random direction. These artificial measurements are convolved with a typical covariance matrix of errors, here using the mean

covariance matrix in our list of candidates for this nominal SNR. For the dust correction, we randomly select one of the twenty samples provided by the Green et al. (2015) dust-map in each distance modulus bin along each line of sight, corresponding to the sight-line and distance modulus that we have sampled for the runaway. The injected runaways and real candidates are shuffled together so that the algorithm described in Sec. 2.4.2 is applied in the same manner to both the real stars and fake runaways. There is not a real SNR at this location and thus all the real stars selected from the cross-match should be preferred to be background stars, while by construction the fake injected runaways should demand the runaway hypothesis. An injected runaway which returns a Bayes factor  $K < 1$  is a false negative and a real star with  $K > 1$  is a false positive.

At the bottom of Fig. 2.5, we show the calculated Bayes factor  $K$  for all the real stars and injected stars. There are 217 stars in each series. Only three of the real stars are returned as false positives giving a false positive rate of 1.3%. All three of these false positives are from the fake version of G65.3+05.7 which we find is because of the large photometric errors of APASS in this field. These errors are around  $\pm 0.142$  in  $B-V$  which compare to  $\pm 0.055$  for G180.0-01.7. This suggests that the millimag precision of the  $G_{BP}$  and  $G_{RP}$  bands in *Gaia* DR2 will further reduce the false positive rate.

There are 22 false negatives and this corresponds to a false negative rate of about 10%. Given that we only expect a third of SNRs to have an associated runaway companion (see Sec. 2.4.3) and that we only consider ten SNRs, we should have at most one false negative in our observed sample.

We note that there are more stars closer to the  $2 \ln K = 0$  boundary in our science runs (above the line in Fig. 2.5) than were found in the false positive test. This is because runaways are more likely to be OB stars and that OB stars are typically found in star-forming regions. If a SN has occurred then a star-forming region is nearby and so there are OB stars in or close to the SNR which act as contaminants.

## 2.5 RESULTS

We report the seven stars for which the Bayes factor is greater than one by at least the error on the evidence estimated by MULTINEST. In Fig. 2.5, we show the calculated Bayes factor  $K$  for the candidates in each SNR over the range  $(-20, 20)$ . In Sec. 2.5.1 we discuss the three contaminant stars which we are able to rule out and in Sec. 2.5.2 we analyze each of the four real candidates individually. Three of our candidates are new while HD 37424 in S147 has previously been

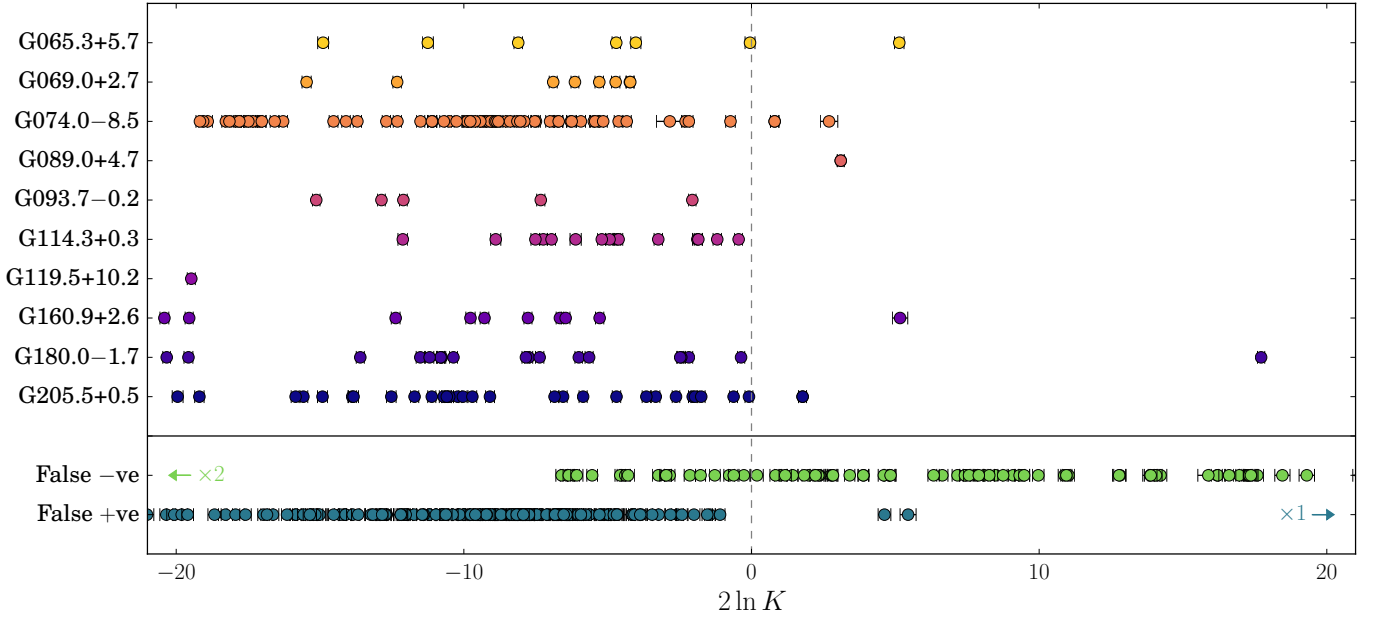


Figure 2.5: Bayes factors for the hypothesis that each star in each SNR is a runaway star versus the hypothesis that it is a contaminant. The false positive and false negative series are described in Sec. 2.4.5.

suggested by Dinçel et al. (2015). We give the properties of these three new candidates in Tab. 2.4.

The only SNR in common with the search for OB runaways by Guseinov et al. (2005) is G089.0+04.7 and they proposed a different candidate, GSC 03582–00029. This star appears to be significantly brighter in the infrared ( $J = 10.2, H = 9.7, K = 9.6$ ) than in the optical ( $B = 11.9$ ) while an OB star should have  $B-K = -1$  (Castelli & Kurucz, 2004), so the classification of this star as OB seems unlikely.

### 2.5.1 Eliminating the contaminants

There are seven stars which have Bayes factors greater than one. The presence of two of these stars for G074.0–08.5 makes it clear that there is at least some level of contamination. We found empirically that there are two ways to produce false positives in our model. First, if the star is a high proper-motion star in the foreground then the evidence for it in the background model can be spuriously low. This can occur because the background is constructed by taking a kernel density estimate of stars around the SNR and it may not contain enough foreground stars to reproduce this population. A low evidence in favour of the background model boosts the Bayes factor so that the runaway model is preferred, even if the star would be a very low-likelihood runaway. Second, if the errors on the photometry from APASS are greater than around 0.1 mag in each of B and V then it is possible for the algorithm to ascribe a high probability to a star being

Table 2.4: Table of median posterior values for our new candidates.

SNR	Go74.0−08.5	Go89.0+04.7	G205.5+00.5
Candidate	TYC 2688-1556-1	BD+50 3188	HD 261393
Sp. Type	—	OB-	B5V
$2 \ln K$	$0.81 \pm 0.15$	$3.10 \pm 0.12$	$1.78 \pm 0.14$
$\Delta\theta$ (arcmin)	11.45	2.43	8.54
$d_{\text{SNR}}$ (kpc)	$0.57 \pm 0.07$	$1.69 \pm 0.26$	$1.32 \pm 0.24$
$t_{\text{SNR}}$ (kyr)	$100.28 \pm 30.02$	$107.17 \pm 27.77$	$115.64 \pm 23.28$
$\log_{10} M_1$ ( $M_{\odot}$ )	$1.11 \pm 0.17$	$1.23 \pm 0.18$	$1.07 \pm 0.12$
$q$	$0.16 \pm 0.05$	$0.52 \pm 0.18$	$0.44 \pm 0.11$
$\log_{10} P_{\text{orb}}$ (days)	$3.72 \pm 0.65$	$2.41 \pm 1.36$	$2.86 \pm 1.34$
$E(B-V)$	$0.06 \pm 0.01$	$0.55 \pm 0.08$	$0.16 \pm 0.04$
$v_{\text{pec}}$ ( $\text{km s}^{-1}$ )	$29.20 \pm 10.34$	$13.70 \pm 10.66$	$16.14 \pm 20.41$
$(B-V)_0$	$0.20 \pm 0.06$	$-0.25 \pm 0.02$	$-0.19 \pm 0.03$
$G_0$	$2.39 \pm 0.27$	$-2.52 \pm 0.47$	$-0.92 \pm 0.49$
$v_{\text{ej}}$ ( $\text{km s}^{-1}$ )	$161.60 \pm 193.32$	$32.25 \pm 17.73$	$38.82 \pm 26.09$
$v_r$ ( $\text{km s}^{-1}$ )	$45.74 \pm 246.32$	$-16.99 \pm 41.04$	$23.82 \pm 51.94$
$M_{\text{run}}$ ( $M_{\odot}$ )	$1.73 \pm 0.13$	$10.85 \pm 2.93$	$5.78 \pm 1.15$

far-away and blue when the candidate is actually a nearby red star. This increases the likelihood in favour of the runaway hypothesis.

If a contaminant is caused by the first of these possibilities, then this is clear from an unusually jagged posterior of the runaway model. Foreground high proper-motion stars tend to not be OB stars and so to explain the star under the runaway hypothesis MULTINEST is forced to sample in regions of the progenitor binary parameter space that produce fast, red runaways. These are rare and lie in the region to the top right of Fig. 2.2 that is not well sampled in the binary grid because there are very few of them. This under-sampling results in a jagged posterior dominated by spikes of high probability, with reported modes that are poorly converged with large errors on  $\ln Z$ . The stars with the highest Bayes factor in both Go74.0−08.5 and G160.9+02.6 are contaminants of this first kind, which can clearly be seen in Fig. 2.5 as both these stars have much broader error bars than the typical candidate.

The second type of contaminant is only a problem in this work because we have chosen to take the photometry from APASS for all the SNRs, while for some fields *Tycho-2* has much smaller errors. This is mainly caused by a known problem in measurements taken for APASS DR8 in Northern fields where the blue magnitudes have larger errors than expected<sup>4</sup>. If the best measurement of  $B-V$  has a large error then the problem discussed above is a feature, because the

<sup>4</sup> <https://www.aavso.org/apass>

Bayesian evidence is the likelihood integrated against the probability of every possible combination of model parameters. The star with the highest Bayes factor in Go65.3+05.7, BD+30 3621, is one such contaminant and was the only star in Go65.3+05.7 with a Bayes factor greater than one. APASS reports a measurement  $(B-V) = 1.10 \pm 0.88$  for this star, but MULTINEST picked out a most likely value of  $(B-V)_0 = -0.22 \pm 0.02$ . The *Tycho-2* catalogue reports  $B-V = 1.37 \pm 0.02$  confirming BD+30 3621 as a late-type star. The large measurement error reported in APASS allowed the model to explore parameter space where this star is much bluer than in reality. The application of our method to later *Gaia* data releases, which will provide  $G_{BP}$  and  $G_{RP}$  with millimag precision across the entire sky, will not suffer this second type of contaminant.

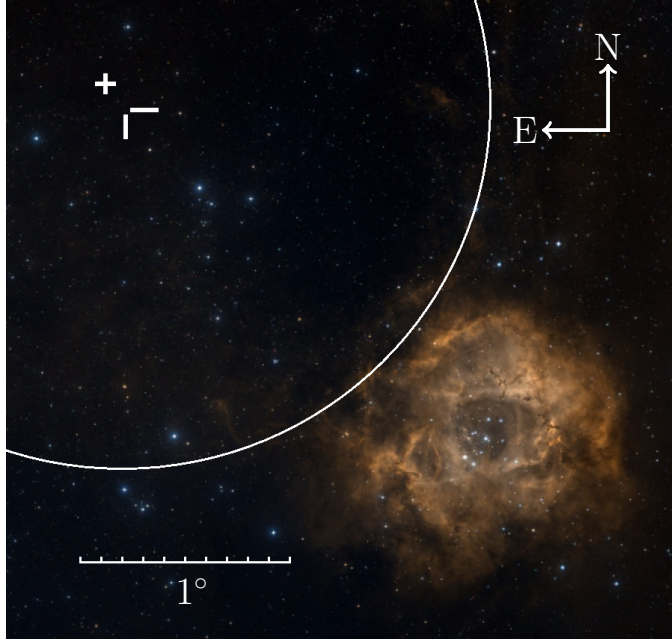


Figure 2.6: Digitized Sky Survey image of the vicinity of the Rosette Nebula. The runaway star candidate HD 261393 is marked by a white cross, the white cross hairs indicate the geometric centre of the Monoceros Loop and the white circle approximately shows the inner edge of the Monoceros Loop shell. The Rosette Nebula is in the bottom right and the Mon OB2 association extends  $3^\circ$  to the east and north-east towards the centre of the Monoceros Loop.

### 2.5.2 Individual candidates

**TYC 2688-1556-1** The star TYC 2688-1556-1 in Go74.0-08.5 (Cygnus Loop) has no known references in the literature. It is a relatively high proper-motion star with  $(\mu_{\alpha*}, \mu_{\delta}) = (3.92 \pm 0.83, -21.03 \pm 1.25)$  mas yr $^{-1}$  reported in TGAS. The colour and magnitude of this star in the TGAS/APASS cross-match suggest this star is likely A type, which



agrees with the posterior for the current mass of the runaway of  $1.73 \pm 0.13 M_{\odot}$ . The posterior for the ejection velocity includes a second mode which corresponds to the clump of stars at  $v_{ej} = 700 \text{ km s}^{-1}$  in Fig. 2.2. Runaways in this region of  $(B-V)_0-v_{ej}$  space have undergone significant mass exchange with the primary and will have had a common envelope phase. This mass exchange shrinks the orbit of the binary which increases the orbital velocity and is the origin of the high velocity of these stars. If this mode is the true origin of TYC 2688-1556-1, then the star is predicted to have lost several solar masses of material, having started off at around  $6 M_{\odot}$  and ended with around  $2 M_{\odot}$ . In this case the star may be chemically peculiar. A more prominent observable of this channel is that it would predict a heliocentric radial velocity around  $+600 \text{ km s}^{-1}$  or  $-600 \text{ km s}^{-1}$ , where the uncertainty is due to the degeneracy in whether the star is moving towards or away from us. Looking at Fig. 2.7, this degeneracy appears as a ‘v’-shaped contour in the  $v_r-v_{ej}$  plot. If the star is from this mode, then it is likely unbound from the Milky Way. The covariance in the most probable mode between  $M_1$  and  $q$  is simply the relationship  $M_2 = qM_1 = \text{const}$ . This covariance is interpreted as there being minimal mass transfer in the binary system so that the mass of the runaway now is approximately the mass it was born with. The secondary mode is clearly visible as lying off this relationship.

*Brown (private correspondence) later obtained a spectrum of TYC 2688-1556-1 and found that it was an F5 with a radial velocity of  $-49 \pm 2 \text{ km s}^{-1}$ , thus ruling out the second mode.*

**BD+50 3188** The B-type star BD+50 3188 in Go89.0+04.7 exhibits emission lines in its spectra and so is classed as a Be star (most recently studied by Chojnowski et al., 2015). The emission lines in Be stars are thought to originate from a low-latitude disc or ring-like envelope (Kogure & Leung, 2014), which in the case of BD+50 3188 is measured to be rotating at  $138 \text{ km s}^{-1}$  (Chojnowski et al., 2015). As discussed in Sec. 1.3.4 and again in Ch. 3, Be stars may gain their rapid spin through mass transfer from a companion. In a fraction of cases that companion should explode in a supernova and kick away the Be star as a runaway. BD+50 3188 is the only Be star within a  $2^\circ$  radius of Go89.0+04.7 and is only 2.4 arcmin from the centre. That it is a Be star with no known binary companion which is spatially co-located with the SNR lends circumstantial evidence to it being the runaway companion of Go89.0+04.7.

**HD 37424** This star is our most likely candidate with a Bayes factor  $K$  of  $2 \ln K = 17.72 \pm 0.13$ . A connection between this star and the SNR G180.0-01.7 was previously drawn by Dinçel et al. (2015), who used the kinematics of the star and the associated central compact object PSR J0538+2817 to show both were in the same location  $30 \pm 4 \text{ kyr}$  ago. Dinçel et al. (2015) estimated that this star has spectral type  $B0.5V \pm 0.5$  and a mass around  $13 M_{\odot}$ , while our method found  $M_{\text{run}} =$



$10.38 \pm 1.04 M_{\odot}$ . Dinçel et al. (2015) used this mass and the lack of nearby O-type stars to argue that the progenitor primary must have a mass that is at most  $20\text{--}25 M_{\odot}$ , with the possibility that the system may have been a twin binary. The most likely mode in our posterior (Fig. 2.9) corresponds to a scenario where the initial masses in the binary were  $M_1 = 20 \pm 5 M_{\odot}$  and  $M_2 = 7 \pm 2 M_{\odot}$ . Our favoured initial primary mass is consistent with the lack of O-type stars while we find that the secondary has actually increased in mass because of mass transfer from the primary to the companion. The possibility of a twin progenitor binary is strongly excluded under our model.

Similarly to Sec. 2.3, we took  $B-V = 0.073 \pm 0.025$  from Dinçel et al. (2015) because HD 37424 is one of the five stars in G180.0–01.7 without APASS photometry. We were motivated to investigate this star despite it not having APASS photometry because it had been previously suggested to be the runaway companion.

**HD 261393** The star HD 261393 in G205.5+00.5 is given a spectral type of B5V by Voroshilov et al. (1985) who also assigned it membership of NGC 2244, an open cluster at the centre of the Rosette Nebula. However, HD 261393 is  $2.5^{\circ}$  from the centre of the Rosette Nebula (Fig. 2.6), so it is more likely to be a member of the adjoining Monoceros OB2 association which extends to the east and north-east by several degrees. Odegard (1986) established that the Monoceros Loop is within the Mon OB2 association and is interacting with, and lies behind, the Rosette Nebula. This conclusion was supported by later work (see Xiao and Zhu, 2012, for a review). Martins, Mahy, Hillier, and Rauw (2012) modelled the stellar properties of ten O type stars in NGC 2244 and the surrounding Monoceros OB2 association and found that the age of the stars is in the range 1–5 Myr. In order for HD 261393 to be a runaway with an age less than 5 Myr, our model would require the primary of the progenitor binary to be at least  $40 M_{\odot}$ . In the posterior shown in Fig. 2.10 a primary of this mass would lie between the 2 and  $3\sigma$  contours. This extra constraint would decrease the Bayesian evidence for a runaway origin and may be enough to result in the background being more favourable. A similar line of reasoning for the mass of the primary was put forward by Gebel and Shore (1972) who argued that the minimum possible mass of the progenitor must exceed the  $25 M_{\odot}$  mass of the most massive O star in the SNR. The models used by Martins et al. (2012) to estimate the age of Mon OB2 did not include the possibility of rejuvenation by mass transfer or merger in binaries which can result in an underestimated age of OB associations (e.g. Schneider et al., 2014, used binary evolution simulations to predict that the  $9 \pm 3$  and  $8 \pm 3$  most massive stars in the Arches and Quintuplet star clusters are likely merger products).

Including the possibility of binary evolution would increase the estimated age of the Mon OB2 association and thus decrease the tension with our model. Gebel and Shore (1972) further speculated that the B type star HD 258982 might be the associated runaway star because it is the only B type star observed at that time in the SNR which displays the CaK absorption line at the  $16 \text{ km s}^{-1}$  of the expanding SNR shell. HD 258982 is around  $1.5^\circ$  away from the geometric centre of the Monoceros Loop and the proper motion of this star had not been measured at the time of Gebel and Shore (1972). In TGAS, this star has a measured proper motion of around  $3 \text{ mas yr}^{-1}$  meaning that the star can have travelled at most  $0.1^\circ$  in the 150 kyr age of the SNR and is effectively ruled out as a possible candidate.

## 2.6 DISCUSSION

We have used two methods to search for and quantify the significance of runaway former companions of the progenitors of nearby SNRs. The first method used kinematics from the *Tycho-Gaia* astrometric solution (TGAS) to find the star most likely to have been spatially coincident with the SNR centre in the past 150 kyr and further filtered those candidates based on their B–V colour to select likely OB stars. The second method is Bayesian in nature and has the advantage that it constrains the properties of both the progenitor binary and the present day runaway.

Both methods returned four candidates and reassuringly three of those were in common. These are TYC 2688-1556-1 in G074.0–08.5, BD+50 3188 in G089.0+04.7 and HD 37424 in G180.0–01.7. The remaining candidate from the kinematic method is TYC 4280-562-1 in G114.3+00.3 which has  $2 \ln K = -4.69 \pm 0.14$  in the Bayesian method and thus is the seventh most likely runaway in this SNR. The remaining candidate from the Bayesian method is HD 261393 in G205.5+00.5, which was ranked fourth in this SNR by the kinematic method.

Three of the candidates proposed by our Bayesian method are new, while HD 37424 was previously suggested by Dinçel et al. (2015). It is reassuring that this star was picked out by both methods and was already in the literature. It has a Bayes factor K of  $2 \ln K = 17.72 \pm 0.13$ , which makes it a very strong candidate. The posterior suggests that this star may have gained several solar masses from the primary prior to the supernova. The best of our novel candidates is BD+50 3188; this is a Be star which can be explained by the star being spun up by mass transfer from the primary prior to the supernova. It is also the only Be star within several degrees of this SNR and is only 2.4 arcmin from the geometric centre. If TYC 2688-1556-1 is the runaway companion of

G074.0–08.5 then it is likely to be an A type. There is a second mode in the posterior for TYC 2688-1556-1 which would correspond to this star having mass transferred onto its primary, however this mode has been ruled out by subsequent spectroscopy motivated by this work. The final candidate from the Bayesian method is HD 261393. It is possible that the progenitor of the Monoceros Loop is part of the recent burst of star formation that has occurred in the Mon OB2 association over the last 1–5 Myr. If this is true, then this extra constraint may mean HD 261393 is more likely to be a background star.

The method that Dincel et al. (2015) used to propose HD 37424 as a candidate was based on a coincident spatial location with the pulsar in the past and thus is independent from our method which relates the star to the properties of the SNR. One advantage of our method is that it does not require there to be a known associated pulsar. Our Bayesian method could be altered to include stellar radial velocities and pulsar properties. The radial velocities would be an additional constraint on the model, the pulsar parallax could provide a more accurate distance to the SNR, and the pulsar proper motion combined with a time since the SN would set the location of the progenitor binary at the time of the SN. *Gaia* is aiming to provide radial velocities for a bright subset of the main photometric and astrometric sample; it is estimated that for a B1V star with apparent magnitude  $V = 11.3$  the end-of-survey error on the radial velocity<sup>5</sup> will be  $15 \text{ km s}^{-1}$ , which is sufficiently precise for tight constraints to be placed on runaway candidates.

A requirement of our Bayesian framework is the probability of a SNR to have a runaway companion. Accounting for single stars, merging stars, binaries that remain bound post-supernova and runaways that themselves go supernova, we find that one third of core-collapse SNRs should have a runaway companion. In agreement with this result, we find four runaway candidates from the ten SNRs considered.

As mentioned previously, Kochanek (2017a) ruled out runaway companions of the Crab, Cas A and SN 1987A SNRs with initial mass ratios  $q \gtrsim 0.1$ . Including this null result for these three SNRs does not change our conclusion that the number of runaway candidates is consistent with the expected number of runaways, but if our two weaker candidates (TYC 2688-1556-1 and HD 261393) are subsequently ruled out a significant tension could arise. The SNRs considered by Kochanek (2017a) are all younger ( $t_{\text{SNR}} < 1 \text{ kyr}$ ) and more distant ( $d_{\text{SNR}} > 2 \text{ kpc}$ ) than our SNR sample, making the two works complementary. The advantage of considering young SNRs is that a runaway companion is constrained to be much nearer to the centre

<sup>5</sup> <https://www.cosmos.esa.int/web/gaia/science-performance>

of the SNR, which limits the region that must be searched. The main disadvantage is the lack of parallaxes for distant stars which makes it harder to exclude candidates because of the degeneracy between distance, reddening and photometry. In terms of method Kochanek (2017a) used PARSEC isochrones to carry out a pseudo-Bayesian fit to the photometry of each star while accounting for the distance and extinction to the SNR, which we would categorize as a middle ground between our simple and fully Bayesian approaches. Kochanek (2017a) noted that a full simulation of binary evolution was beyond the scope of their work. It is the integration of binary evolution with a fully Bayesian method which is the main advance of this work. We will be able to apply our fully Bayesian method to both the Crab and Cas A SNRs with *Gaia* DR2.

## 2.7 SUMMARY

In this Chapter, I have presented a Bayesian framework designed to search for the runaway former companions of supernovae; this framework makes full use of the available photometry, incorporates 3D dust-maps, is explicit about our expectation that most but not all runaways are OB type, and is statistically rigorous. The framework can be applied easily and uniformly to all SNRs and thus fully automates the task of identifying such companions. When the framework is applied to *Gaia* DR2, and later *Gaia* releases, the millimagnitude precision of the photometry will remove poorly measured stars as contaminants, while the milliarcsecond precision of the parallaxes will remove high proper-motion foreground stars. The final *Gaia* data release aims to be complete down to  $G \approx 20.5$  and at that completeness I will be able to test the existence of a runaway companion for many tens of Galactic SNRs. The few tens of runaway star-SNR pairs that are found will open an entirely new route to studying the late-stage evolution of massive binary stars and thus greatly advance our understanding of core-collapse supernovae. I have not provided a definitive answer to the open question I posed in the Introduction: do the nearby core-collapse supernova remnants contain runaway companions? I have, however, provided a definitive solution.

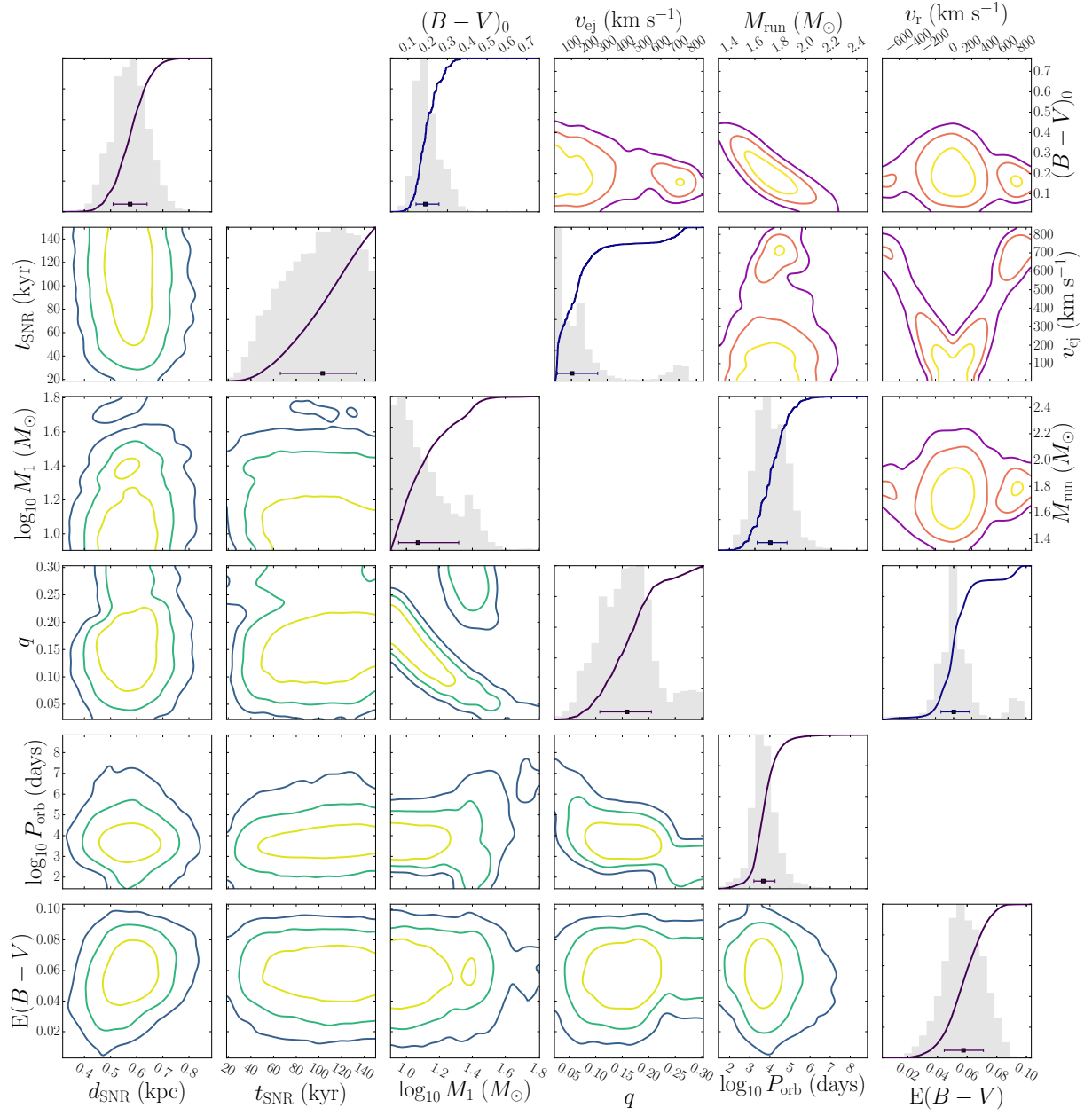


Figure 2.7: Corner plots of the posterior samples from the model of TYC 2688-1556-1 in Go74.0-08.5 with  $1\sigma$ ,  $2\sigma$  and  $3\sigma$  contours. The 1D histograms include the CDF of that parameter and the error bars indicate the median and  $1\sigma$  errorbars of each mode. **Bottom left:** A corner plot showing the model parameters, excluding the five parameters related to the position and peculiar velocity of the SNR which did not have covariances with the other parameters. **Top right:** A corner plot showing a selection of the derived parameters which are functions of the model parameters.

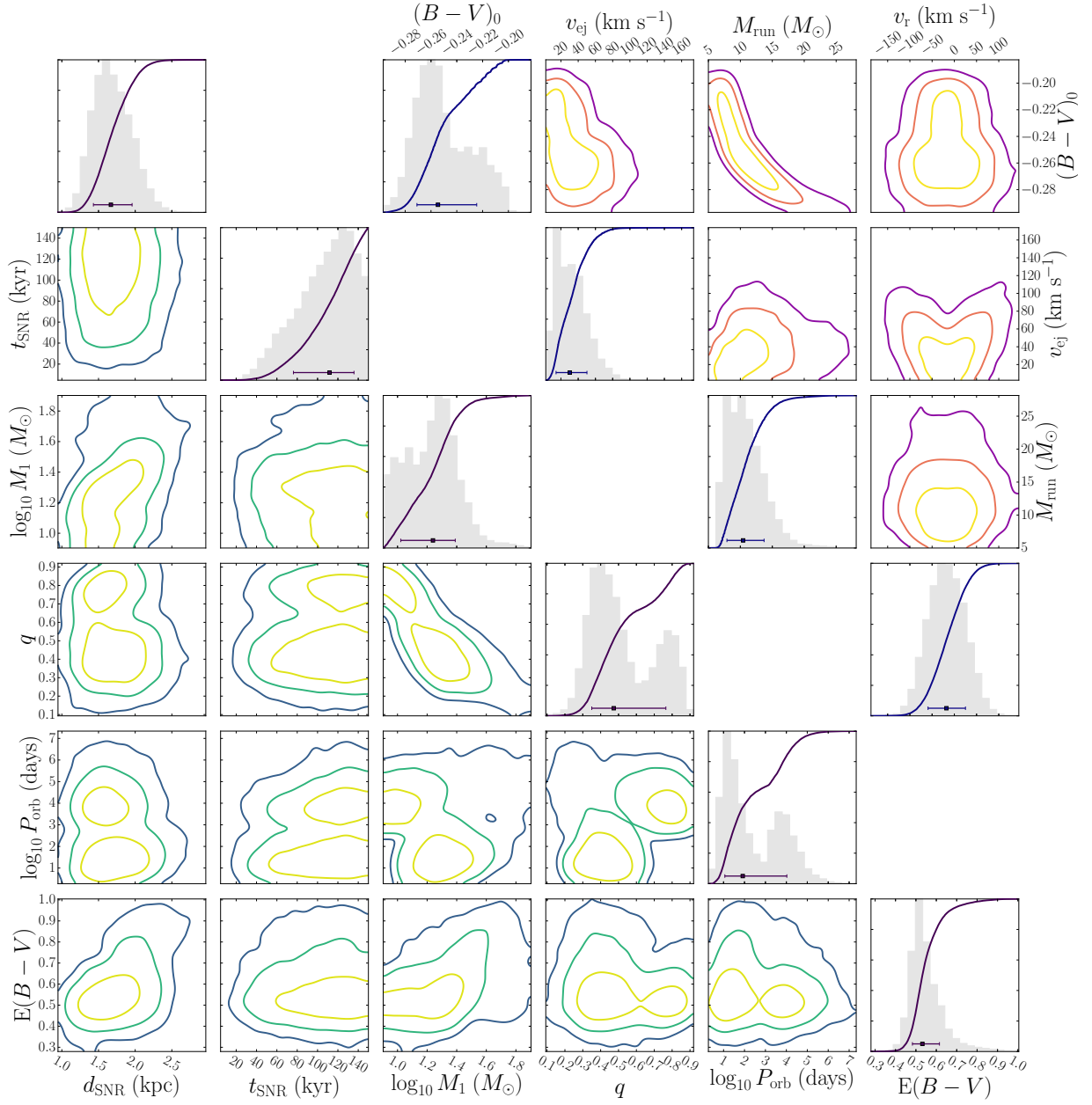


Figure 2.8: As Fig. 2.7 but for the candidate BD+50 3188 in Go89.o+04.7.

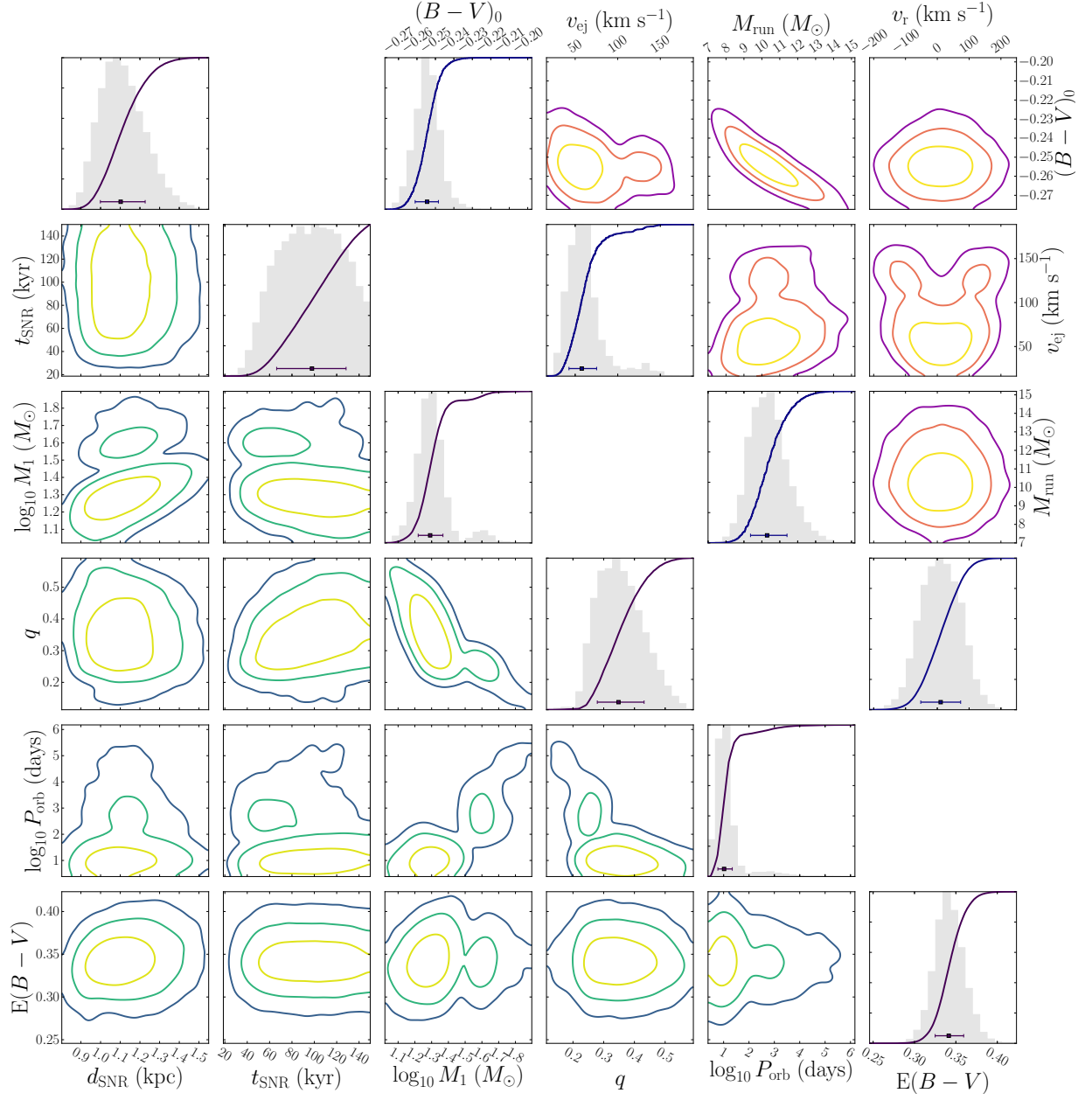


Figure 2.9: As Fig. 2.7 but for the candidate HD 37424 in G180.0-01.7.



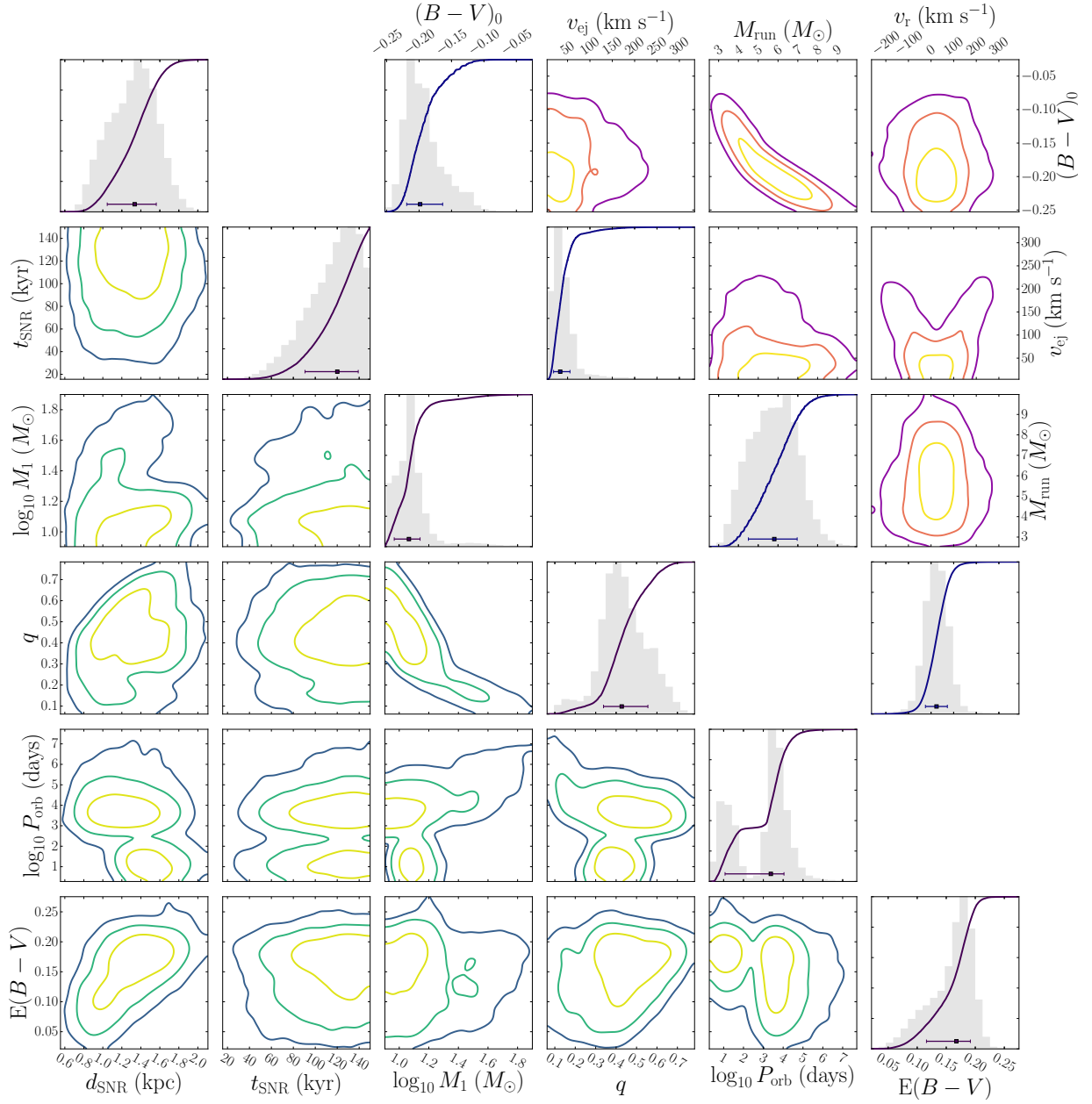


Figure 2.10: As Fig. 2.7 but for the candidate HD261393 in G205.5+00.5.



## ON THE CONNECTION OF THE RUNAWAY BE STARS TO THE BE STAR PHENOMENON

*Based on work originally published in Boubert and Evans (2018).<sup>1</sup>*

In the previous chapter I conducted a search of ten nearby Galactic supernova remnants for the runaway former companion of the progenitor star. Four candidates in four remnants were identified, one of which, BD+50 3188 in remnant HB 21, was found to be a Be star. I argued that this was circumstantial evidence both for the runaway candidacy of the star and for the post-mass-transfer model of Be stars in general. This discovery raises the possibility that with *Gaia* astrometry it may be possible to answer the open question put forward in the Introduction: do the numbers of runaway Be stars support a mass-transfer origin for all Be stars? In this chapter I test that possibility using data in the *Tycho-Gaia* Astrometric Solution (TGAS) from *Gaia* DR1.

Whilst the fraction of runaways among the Be stars is unknown, the fraction of runaway B stars has long been established to be  $\approx 2.5\%$  for stars of type B0–0.5 and declining to  $\approx 1.5\%$  for stars of type B1–B5 (Blaauw, 1961). It is important to note that there is a difference in terminology between theory and observations when it comes to runaway stars. Runaways fractions are calculated observationally by classifying any star with a peculiar velocity greater than  $40 \text{ km s}^{-1}$  to be a runaway star, while theoretically any star ejected from a binary by the supernova explosion of the companion can be called a runaway star with the majority having ejection velocities below this value.

There are several other recent works which lend support to the post-mass-transfer model. Chernyakova et al. (2017) studied the Be-X-ray binary LSI +61° 303, which has an eccentricity  $e > 0.5$ . They argue that the superorbital variability seen in this system is due to the compact remnant passing through different regions of the Be star disc and so probing material of varying densities. One origin for this large eccentricity could be that the compact remnant was formed in a supernova and received a large natal kick. Another way to produce

<sup>1</sup> I conceived this project after identifying the Be star BD+50 3188 as a possible runaway of the supernova remnant HB 21. I was responsible for the implementation and analysis. My supervisor, N. Wyn Evans, made an invaluable contribution by both sanity-checking my results and substantially re-formatting my first draft into a logical presentation of scientific results. This work was aided by discussion with Robert Izzard and Jason Sanders.

an eccentric binary is through capture in a dense stellar system, but LSI +61° 303 does not appear to be situated in such an environment. González-Galán et al. (2018) studied SXP 1062, a Be-X-ray binary located in the Small Magellanic Cloud, which is likely associated with the supernova remnant MCSNR J0127-7332. SXP 1062 is the first Be-X-ray binary that is likely residing in its parental supernova remnant. Nazé, Rauw, and Cazorla (2017) examined  $\pi$  Aquarii, a 14 solar mass Be star orbited by a 3 solar mass main-sequence companion at 1 AU separation. This system could arise if it was originally a triple and the inner binary merged to form what is now the Be star. The merging could have occurred during common envelope evolution, the compact remnant of the binary might have been kicked into the companion or the inner binary could have remained bound post-supernova and merged at a later point.

I assemble the largest catalogue of Be stars with full six-dimensional kinematics in Sec. 2, exploiting the remarkable precision of the TGAS astrometric catalogue. I predict the runaway velocity distribution for Be stars based on simulations of binary star evolution in Sec. 3, accounting for the observational bias of the catalogue. In Sec. 4, I formulate a Bayesian approach to the problem of estimation of the fraction of Be stars that are runaways from binary supernova. I present the main result that around 13% of the Be stars in our catalogue are consistent with being runaway stars in Sec. 5, and list the 40 most probable examples. Finally, in Sec. 6, I discuss whether my results are consistent with all Be stars originating through the post-mass-transfer channel, and show that I can explain the puzzling lack of Be stars in the high-latitude sample of runaway B stars of Martin (2006). Finally, in the Conclusion, I argue that I can resolve the true number of Be star runaways by applying the Bayesian methodology introduced in Sec. 3.3 to the second data release of the *Gaia* satellite.

### 3.1 DATA

Extracting constraints on the origin of Be stars requires well-measured radial velocities, proper motions and distances. We consider three datasets which satisfy this requirement. The first is from Berger and Gies (2001), the second is a cross-match between the Be Star Spectra database (BeSS) with SIMBAD and the *Tycho-Gaia* Astrometric Solution (TGAS), and the third is a cross-match of the Be catalogue of Hou et al. (2016) from the Large Sky Area Multi-Object Fibre Spectroscopic Telescope (LAMOST) with TGAS. We then combine and clean these datasets by removing any duplicates, as well as stars with anomalously high radial velocities.

### 3.1.1 The Berger & Gies sample

The Berger and Gies (2001) sample contains 344 stars. We first obtain positions and updated radial velocities by querying SIMBAD using the identifiers listed by Berger and Gies (2001). Note that the identifier of the thirteenth star in this sample, CSI+6101449, does not have a cross-match in SIMBAD, but querying VizieR returned the valid identifier HD 10664. For 262 stars the error on the radial velocity recorded in SIMBAD is smaller than in Berger and Gies (2001). For 320 stars the radial velocities are consistent within the reported error in the two catalogues. For the other 24 stars we checked the source of the radial velocity in SIMBAD. Only for HD 120991, where the radial velocity reference was Wilson (1953), did we judge the SIMBAD radial velocity to be less reliable than the Berger and Gies (2001) value. In all other cases, we took whichever radial velocity measurement had the smallest error. A majority of the new radial velocities came from Gontcharov (2006) and Kharchenko et al. (2007). Using the positions, we cross-match with TGAS and obtain more accurate parallaxes and proper motions for 163 of the stars. In Fig. 3.1 we illustrate the effect of the updated measurements on the peculiar velocity distribution. Note that the peculiar velocities for Berger and Gies (2001) are taken from that work and use a solar radius  $R_{\odot} = 8.5$  kpc, a local circular speed  $v_{\text{disc}} = 220$  km s<sup>-1</sup> and a solar peculiar velocity  $(U, V, W)_{\odot} = (10.0, 5.25, 7.17)$  km s<sup>-1</sup>. For the peculiar velocities in this work, we use the more recent values stated in Sec. 3.3.

### 3.1.2 Be Star Spectra database

The Be Star Spectra database (BeSS) claims to be a complete catalogue of classical Be stars and Herbig Ae/Be stars. It contains information on 2265 Be stars and reports radial velocities for 856 and radial velocity errors for 759. After collating this information, we queried SIMBAD to obtain radial velocities, parallaxes and proper motions. SIMBAD provides the proper motion errors in terms of an error ellipse with a major axis A, minor axis B and position angle P. We convert these to uncertainties in the individual components following the recommended method<sup>2</sup> and neglect the implied covariances. We then carry out a 1 arcsec nearest neighbour cross-match with TGAS to obtain parallaxes and proper motions. To select whether to use the radial velocity from BeSS or SIMBAD, we pick whichever had the smallest associated error. If the two radial velocities differ by more than  $1\sigma$  with respect to their errors added in quadrature, we look at

<sup>2</sup> <http://simbad.u-strasbg.fr/Pages/guide/errell.htm>

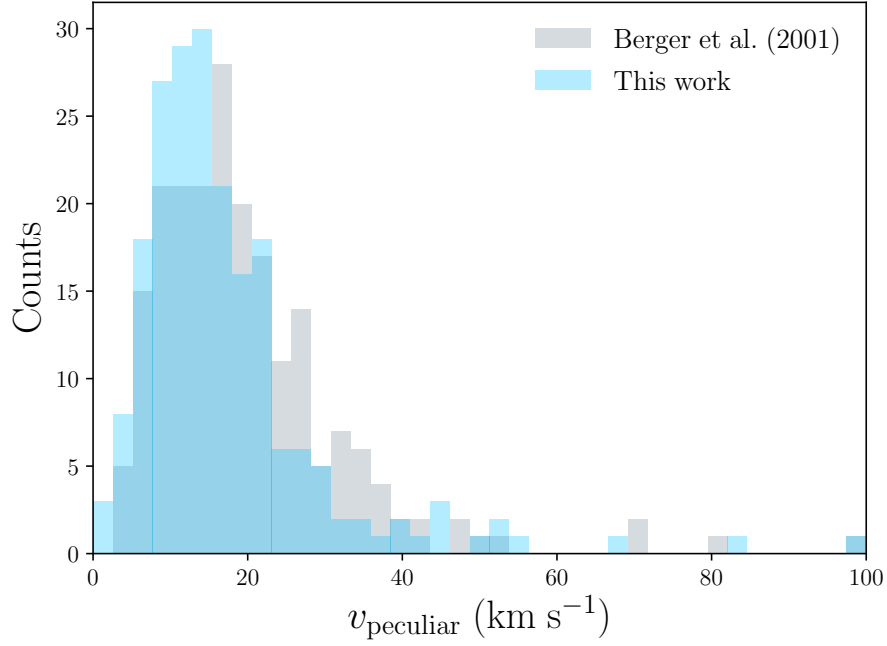


Figure 3.1: Median peculiar velocities relative to the Milky Way disc of an identical sample of stars using the kinematics from either Berger and Gies (2001) or the catalogue assembled in this work. Thanks to TGAS the kinematics in our catalogue are more accurate and this produces a significant tightening in the distribution.

the origin of both measurements and in all cases prefer the radial velocity quoted through SIMBAD. In almost all cases it was possible to trace the velocity quoted in BeSS back to the General Catalogue of Stellar Radial Velocities and its revision (Evans, 1967; Wilson, 1953). These velocities have been superseded.

### 3.1.3 The LAMOST Sample

LAMOST is carrying out a 5 year spectroscopic survey of 10 million Milky Way stars in the Northern hemisphere down to 20.5 mag. Hou et al. (2016) presented a catalogue of 10,436 early-type emission-line stars which are in LAMOST. This catalogue is available as a value-added catalogue of LAMOST DR2<sup>3</sup>. We carry out a 1 arcsec nearest neighbour cross-match with the LAMOST DR2 stellar catalogue to obtain the reported radial velocities with errors and with TGAS to obtain the parallax  $\varpi$  and proper-motions ( $\mu_{\alpha*}$ ,  $\mu_{\delta}$ ). This results in a total of 12 stars. We add  $6.76 \text{ km s}^{-1}$  to correct for the offset found between LAMOST and SDSS SEGUE radial velocities (Jing et al., 2016).

<sup>3</sup> <http://dr2.lamost.org/doc/vac>

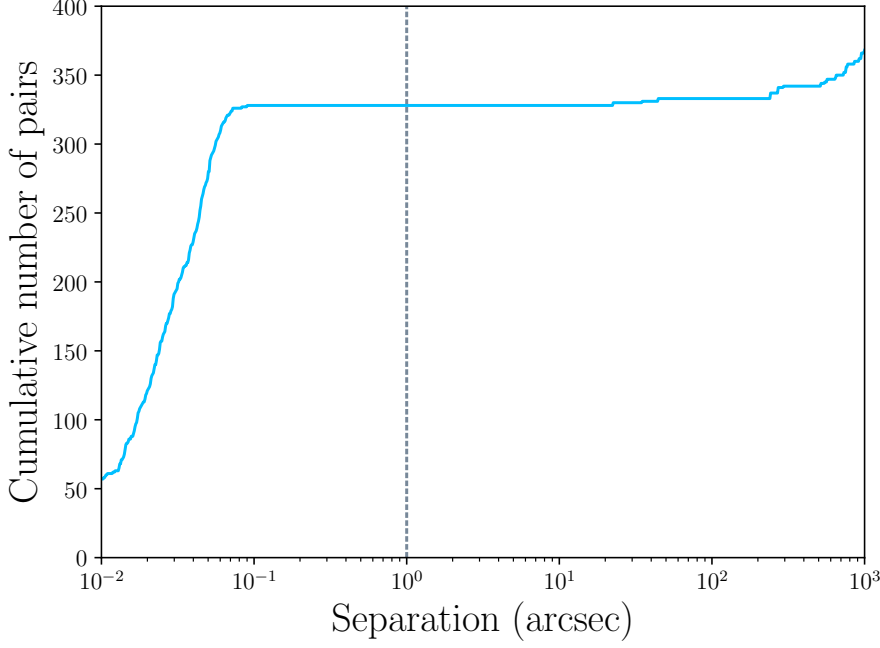


Figure 3.2: Cumulative number of pairs of stars with a separation less than a given bound. The dashed line is our criterion for a duplicate star and it cleanly divides duplicate stars from true close stellar pairs.

#### 3.1.4 The Combined Catalogue

We combine all three sources into one dataset and find there is a large cross-over between the Berger and Gies (2001) and BeSS datasets. We project each star onto the unit sphere and use those 3D positions to construct a  $k$ -dimensional tree. We call a duplicate any pair of stars in the combined dataset that are separated by less than 1 arcsec. There are 328 pairs that meet this criterion. As Fig. 3.2 shows, there are no additional pairs in the range 1–10 arcsec and thus there is no blurring between the duplicate population and the population of close stars that exist in binaries or dense clusters.

We find that three of the stars in our sample have unusually high radial velocities; CPD-32 2038 at  $912.11 \pm 97.922 \text{ km s}^{-1}$ , HD 152979 at  $-588.45 \pm 51.38 \text{ km s}^{-1}$ , and HD 165783 at  $-507.353 \pm 66.777 \text{ km s}^{-1}$ . These velocities are from RAVE DR3 and DR4. In all three cases, the RAVE velocity measurements are the only ones that exist for these stars. All other stars in our sample have velocities  $|v_{\text{rad}}| < 200 \text{ km s}^{-1}$ , thus these are very likely to be spurious measurements. We remove all three stars from our sample. There are a further two stars, HD 306989 and CD-61 4751, whose only reported radial velocity from Reed (2003) has no associated radial velocity error and so these are also removed. This leaves us with a final sample of 632 stars. Their all-sky distribution in Galactic coordinates and median peculiar velocity distribution are shown in Figs. 3.3 and 3.4 respectively.

The Be star sample described above is a biased subset of all Be stars, partly due to the diversity of sources from which it has been drawn. The most significant bias is over-representation of early-type, giant stars, because our sample is flux-limited rather than volume-limited. We quantify this bias by using the spectral types and luminosity classes of the sample obtained from SIMBAD. Among the 632 stars, 599 have an associated spectral type and 532 also have a luminosity class. Multiple stars in the catalogue have a luminosity class of I or II, which contradicts the standard definition of a Be star and thus suggests that there is a degree of uncertainty in the luminosity classes. Similarly, there must be uncertainty in the stellar types because 38 stars are classified as Be stars but do not have a B spectral type. We choose to trust the Be star identification over the spectral type or luminosity class and thus include all 632 stars in our analyses in later sections.

We bin the stars in the two dimensional space of their spectral type  $\{O0, O1, \dots, G0\}$  and luminosity class  $\{I, II, III, IV, V\}$ . Note that the spectral type or luminosity class can indicate a range of possible classifications. In this case, we divide up the contribution of that star to the histogram between all possible combinations of spectral type and luminosity class (i.e. a star whose classification was  $B1/2Iab/II$  would contribute a quarter to each of the bins  $B1I$ ,  $B1II$ ,  $B2I$  and  $B2II$ ). We then apply a Kernel Density Estimation to this histogram with a bandwidth of 0.2322 (estimated using the rule of Scott, 2015 and assuming that each bin has unit length and width) which acts to smooth the histogram and reduce shot noise. This smoothed distribution is shown in Fig. 3.5. We make the assumption that this distribution adequately describes the selection function of the entire 632 stars. This assumption is well-motivated; the distribution of spectral types does not change significantly if we include the 67 stars which have spectral types, but not luminosity classes. Notably, Fig. 3.3 demonstrates that the stars which do not have these classifications are found preferentially in the Southern hemisphere, presumably due to an historical bias in the geographical distribution of telescopes. This bias further motivates the inclusion of all 632 stars in order to avoid spatial bias in our catalogue.

### 3.2 THE POST-MASS-TRANSFER CHANNEL FOR BE STARS

The aim of this section is to use binary stellar population synthesis to predict the population properties of Be stars if they originate through the post-mass-transfer model, and in particular to quantify the expected fraction of runaway Be stars.

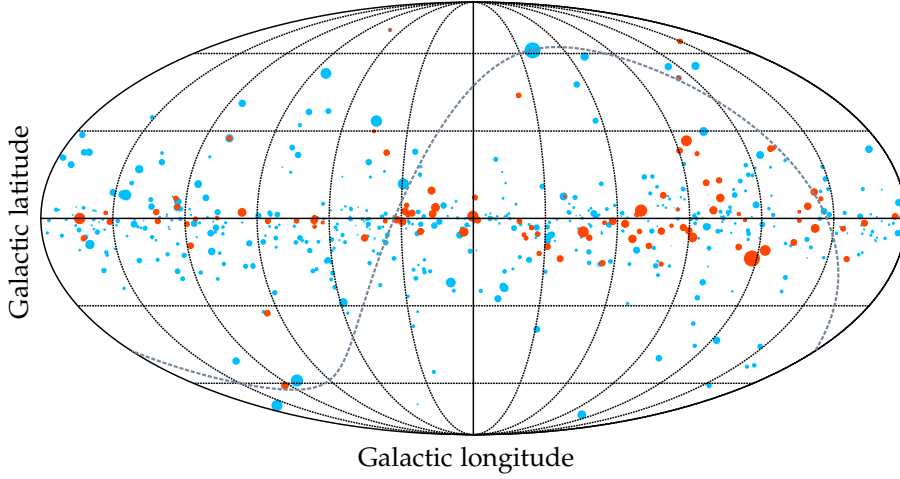


Figure 3.3: Distribution of Be stars in our combined catalogue across the sky. The size of each point is proportional to the parallax. The Galactic centre is at the centre of this image and the celestial equator is shown as a grey dashed line. A subset of the points are coloured orange to indicate stars which do not have an associated spectral type and luminosity class. Such stars are preferentially found in the Southern hemisphere.

### 3.2.1 Be stars from binary population synthesis

Be stars produced through the post-mass-transfer route have interacted with their companion in the past. The runaway velocity is strongly dependent on their past evolution and is imprinted in their present day velocities. We model the evolution of binaries across a grid in parameter space using the `BINARY_C` population-synthesis framework<sup>4</sup>, described in more detail in Appendix A.2. The primary mass  $M_1$ , mass ratio  $q$  and period  $P$  have the ranges

$$\begin{aligned} 1.0 &\leq M_1/M_\odot \leq 80.0, \\ 0.1 M_\odot/M_1 &\leq q \leq 1, \\ -1.0 &\leq \log_{10}(P_{\text{orb}}/\text{days}) \leq 10.0. \end{aligned} \quad (3.1)$$

We assume the primary mass has the Kroupa, 2001 IMF,

$$N(M_1) \propto \begin{cases} M_1^{-0.3}, & \text{if } 0.01 < M_1/M_\odot < 0.08, \\ M_1^{-1.3}, & \text{if } 0.08 < M_1/M_\odot < 0.5, \\ M_1^{-2.3}, & \text{if } 0.5 < M_1/M_\odot < 80.0, \\ 0, & \text{otherwise.} \end{cases} \quad (3.2)$$

We assume a flat mass-ratio distribution for each system over the range  $0.1 M_\odot/M_1 < q < 1$ . We use the hybrid period distribution

<sup>4</sup> We use version 2.opre28, SVN 5018.

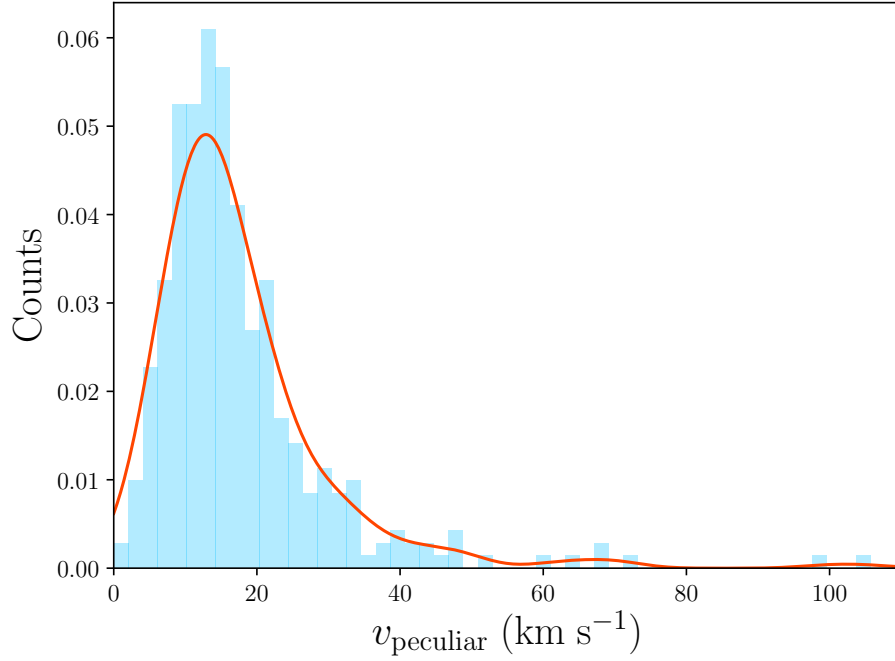


Figure 3.4: Median peculiar velocity distribution of Be stars in our combined catalogue. Overplotted is a kernel density estimate.

from Izzard et al. (2018) which gives the period distribution as a function of primary mass and bridges the log-normal distribution for low-mass stars (Duquennoy & Mayor, 1991) and a power law (Sana et al., 2012) distribution for OB-type stars. The grid is set at solar metallicity because Be stars have short lifetimes of less than 1 Gyr, despite rejuvenation through mass-transfer extending the life of Be stars through the post-mass-transfer route by up to several 100 Myr. `BINARY_C` has previously been used to consider the origins of Be stars by de Mink, Langer, Izzard, Sana, and de Koter (2013) in their investigation of the rotation rates of massive stars. They concluded that the 24.1% of their simulations that resulted in mass gain by the companion or a merger with the primary is consistent with the 20 – 30% of early B type stars which are found to be Be stars (Zorec & Briot, 1997).

An important aspect of this work is that `BINARY_C` does not carry out full stellar structure integration, instead opting for prescriptions that permit the rapid evolution of a large number of binary stars. This simplification allows for rapid population synthesis studies and places `BINARY_C` in the class of synthetic binary stellar evolution codes (see Table 2 of De Marco and Izzard, 2017, for a list of synthetic and detailed binary stellar evolution codes). Similar studies to the present one have been carried out with detailed binary stellar evolution codes, for instance by van Rensbergen, Vanbeveren, and De Loore (1996) and more recently by Eldridge et al. (2011).

Be stars are dwarf or giant B type stars with emission-lines in their spectra. However, the atmospheres of stars are not modelled in detail



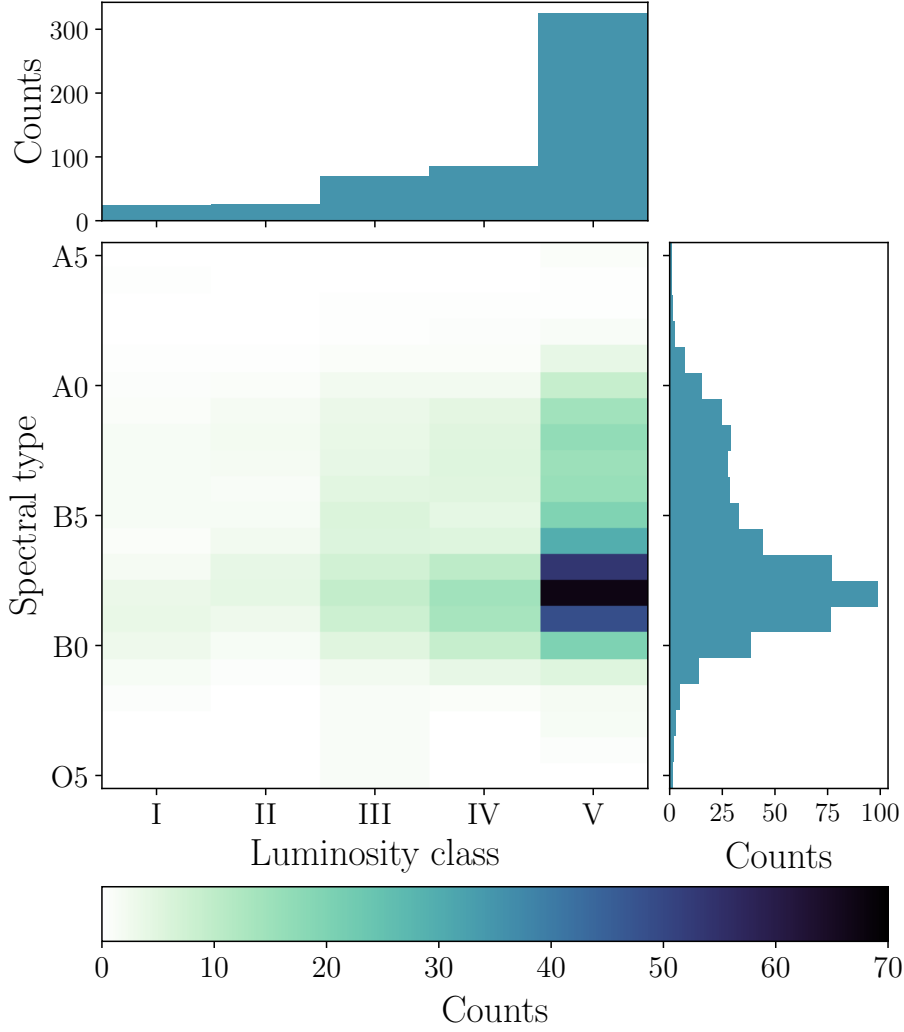


Figure 3.5: Distribution of the 632 Be stars which have both spectral types and luminosity classes. The counts have been convolved with a Gaussian kernel of width 0.2322 to smooth out shot noise. There is a clear observational bias towards earlier types, while 38 stars are classified as Be stars but do not have a B spectral type.

by `BINARY_C`. We thus require a definition of a Be star based on the dynamic properties of the star; the natural expression is in terms of the ratio  $R_{\text{eq}}$  of the equatorial velocity  $v_{\text{eq}}$  to the critical equatorial velocity for break-up  $v_{\text{eq,crit}}$ . Townsend, Owocki, and Howarth (2004) note that, while the canonical value for this ratio is  $R_{\text{eq}} \simeq 0.7 - 0.8$  based on measurements of the rotation of Be stars, this earlier work neglected the effect of equatorial gravity darkening. They postulate that this effect could lead to the Be star rotation rate being underestimated by tens of percent and that a value of  $R_{\text{eq}} \simeq 0.95$  is not ruled out. This near-critical rotation is in better agreement with the scenario first described by Struve (1931), in which material leaks out from the equator of a star spinning near breakup. To illustrate this point, Townsend et al. (2004) note that to launch material ballistically into orbit from the surface of a star spinning at  $R_{\text{eq}} \simeq 0.7$  requires

an additional  $100 \text{ km s}^{-1}$  over one where  $R_{\text{eq}} \simeq 0.95$ . Rivinius et al. (2013) reviewed the observational evidence and concluded that the minimum ratio for a B star to become a Be star is around 0.7 and that the lower limit of the mean ratio of the Be stars is around 0.8. For instance, Rivinius, Štefl, and Baade (2006) found  $R_{\text{eq}} = 0.75 \pm 0.14$  as a lower limit without including gravity darkening. For this work, we consider the range  $R_{\text{eq}} \in (0, 1)$  but focus on the set of plausible values  $R_{\text{eq}} \in \{0.65, 0.75, 0.85, 0.95\}$ . Based on the considerations above and results presented in Sec. 3.2.2, we choose the fiducial value  $R_{\text{eq}} = 0.85$  to use in Sec. 3.3 onwards. The properties of the Be stars appear to be robust to the precise choice of  $R_{\text{eq}}$ .

Another consideration is that, if a binary remains bound post-supernova, its centre of mass experiences a kick (Nelemans, Tauris, & van den Heuvel, 1999). This kick is not included at present in BINARY\_C. However, Berger and Gies (2001) find that for a typical Be star scenario the systematic kick is  $8(\Delta M/M_{\odot}) \text{ km s}^{-1}$ , where  $\Delta M$  is the mass lost by the primary in the supernova. They further note that this mass ratio is of order unity and thus that high velocity runaway binaries containing Be stars are not expected in general. In agreement with this theoretical expectation, observations of Be star - X-ray binaries in the Galaxy find that they have low peculiar velocities of  $15 \pm 6 \text{ km s}^{-1}$  (van den Heuvel, Portegies Zwart, Bhattacharya, & Kaper, 2000), broadly similar to the velocity dispersions of a population of B stars containing no runaways (e.g. Aumer and Binney, 2009).

### 3.2.2 *Properties of the simulated Be star population accounting for selection effects*

The relationship between equatorial rotation and runaway velocity is central to understanding the post-mass-transfer model for the Be star phenomenon. First, mass transfer from the primary to the secondary shrinks the binary and accelerates the orbital velocity, and the orbital velocity is the principal contributor to the post-supernova runaway velocity. This mass transfer spins up the secondary, implying that high velocity runaways will also be rapidly rotating. Second, two massive stars in a close orbit tidally lock. This has the effect of breaking the relation between runaway velocity and rotation velocity for close binaries, which correspond to very fast runaways. This balance between mass transfer spinning up and tidal locking spinning down companions is demonstrated by a plot of runaway velocity  $v_{\text{run}}$  versus equatorial rotation velocity  $v_{\text{eq}}$  for all the simulated, runaway B stars (see Fig. 3.6), where there is a clear uptick in the equatorial velocity of the population over the range  $30 \lesssim v_{\text{ej}} \lesssim 70 \text{ km s}^{-1}$ . The

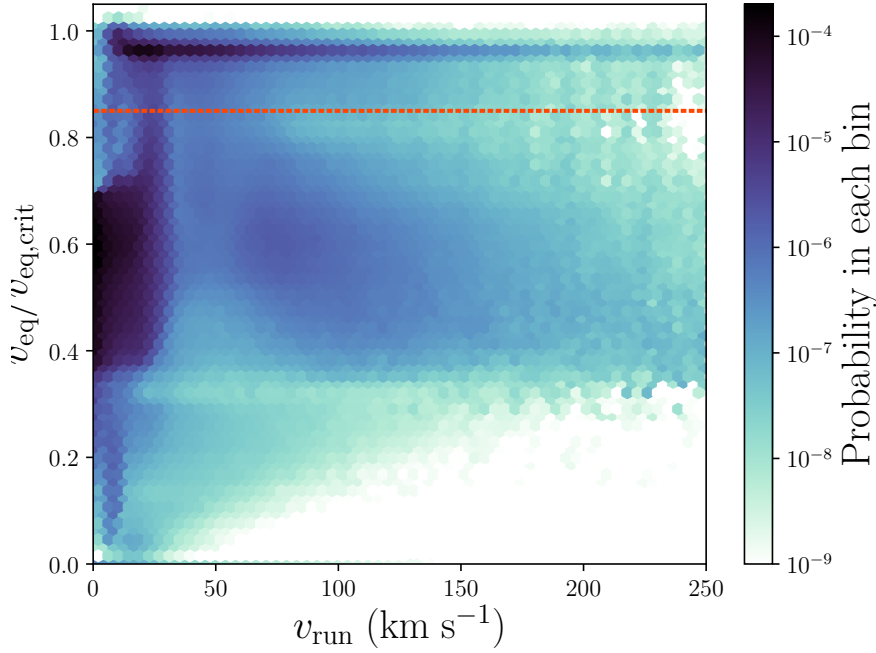


Figure 3.6: Predicted probability distribution for the runaway velocity and critical equatorial velocity ratio of runaway B stars. The dashed line indicates our fiducial value  $R_{\text{eq}} = 0.85$ .

structure of Fig. 3.6 is sensitive to the details of the binary evolution simulation, but in broad terms stars start on the left hand edge with a range of velocities. Some experience mass transfer from the primary which both spins them up and increases the orbit velocity. If the star is spun up to  $v_{\text{eq}}/v_{\text{eq,crit}} > 1$ , then material is lost from the equator until it returns below the critical value. The star remains as a Be star unless mass transfer from the primary shrinks the orbit to the point where the timescale for tidal locking becomes short, in which case the star is spun down. Note that the separation, and hence runaway velocity, at which tidal locking becomes effective is a function of the masses of both components. This is the reason for the broad range of orbital velocities at which the companion is spun down.

The predicted properties of Be stars discussed in the remainder of this section assume a steady-state in which there has been a constant star formation rate for longer than the age of the longest lived B star. These distributions are predictions for the observable population rather than for the stars produced in a single starburst. At each timestep of the binary evolution, we check whether either component of the binary is a B star. If so, we tabulate both the properties of the binary and the probabilistic weight of the system given by the length of the timestep  $dt$  multiplied by the probability of the progenitor binary  $P(M_1, q, P_{\text{orb}})$ .

The frequency of Be stars among the simulated B stars monotonically depends on our choice of  $R_{\text{eq}}$ . Across spectral types B0-B9 and

luminosity classes V-III, we find that the frequency of Be stars is 7.9% for  $R_{\text{eq}} = 0.65$  and declines to 1.9% for  $R_{\text{eq}} = 0.95$ . These frequencies are lower than are observed (e.g. Zorec and Briot, 1997). However, these predicted frequencies are sensitive to uncertain prescriptions for the birth rotation velocities and rotational evolution of the simulated stars. For instance, the birth rotation velocities in the fiducial model are given by an empirically-derived formula from Hurley, Pols, and Tout (2000). If this prescription under-predicts the birth rotation velocities, then this will lead to a lower frequency of Be stars. We investigate this by setting the birth rotation velocity of each star to be the critical rotation velocity. In this extreme case, we find a Be star frequency of 81.7% for  $R_{\text{eq}} = 0.65$  which declines to 3.3% for  $R_{\text{eq}} = 0.95$ . Based on considerations in the previous section, a value  $R_{\text{eq}} = 0.85$  seems most plausible, in which case our fiducial model gives a frequency of 3.1% while the extreme model gives 25.5%. These numbers bracket the observed frequency of Be stars and thus we conclude that an adjustment to the prescriptions for the birth rotation velocities and rotational evolution could bring our prediction in line with observations. While the extreme model boosts the abundance of Be stars by making an unphysical assumption, it does not substantially alter the properties of the resulting Be star population. Thus the predictions made for the properties of Be stars are robust to the adjustments necessary to replicate the observed Be star frequency.

Mass transfer can spin the companion up and cause the Be star phenomenon, but it also decreases the orbital separation and thus increases the velocity of the subsequent runaway Be star. One consequence is that, in rough terms, the longer the mass transfer continues, the more rapidly rotating the companion star and the faster the runaway velocity, implying that the frequency and velocity distribution of runaway stars amongst the Be star population depend on  $R_{\text{eq}}$ . Additionally, the distribution of runaway star velocities is conditional on the mass of the star (for instance, see Fig. 2.2 in Ch. 2) and this should hold for Be stars. An observable proxy for mass is the spectral type of the star and thus we can re-phrase the velocity distributions as being conditional on the spectral type. However, we established in Section 3.1 that our catalogue of Be stars is biased towards early-type Be stars. The implication is that the prediction for the runaway frequency and velocity distribution of the Be stars obtained through simulation is not directly comparable with our Be star catalogue. We account for this selection bias by re-weighting the simulated Be star population to match the observed luminosity class and spectral type distribution. Note that each choice of  $R_{\text{eq}}$  defines a different Be star

population, and thus the re-weighting is carried out for each value of this parameter.

Weighting the simulation outcomes by the observed luminosity class and spectral type distribution has a large effect both on the runaway star sub-population (Fig. 3.7) and on the Be star population in general (Fig. 3.8). We refer to our Be star population from the synthesis as our full model population, while that with all known selection effects included will be referred to as the model population with selection effects.

1. The predicted frequency of runaway stars amongst the model Be star population is increased, as shown in Fig. 3.7a. Earlier stellar types tend to have a greater runaway fraction (e.g. Blaauw, 1961) and the re-weighting increases the weight given to early-type Be stars. Fig. 3.7a shows that choices of larger  $R_{\text{eq}}$  are correlated with greater runaway fractions. One possible reason is that stars which are closer to critical-rotation have experienced more mass-transfer, and thus tend to have a more massive partner whose core-collapse supernova would more easily disrupt the binary.
2. The re-weighting alters the predicted runaway velocity distribution by increasing the contribution of early-type Be stars (Fig. 3.7b). Interestingly, the mean accounting for selection effects is almost independent of the choice of  $R_{\text{eq}}$ , making this mean robust to our fiducial choice of  $R_{\text{eq}} = 0.85$ .
3. Under the assumption of  $R_{\text{eq}} = 0.85$ , the median Be star age drops from 261.7 Myr to 35.4 Myr (Fig. 3.8a). The drastic difference can be explained by the steepness of the mass-main sequence lifetime relation  $\tau_{\text{MS}} \propto M^{-2.5}$  (e.g. Hansen, Kawaler, and Trimble, 2004).
4. Pols et al. (1991) point out that the majority of Be stars formed through the post-mass-transfer scenario are still bound to their companion, because the primary normally transfers sufficient mass to the secondary to either avoid the supernova or for the reduced mass loss in the supernova to not unbind the system. These companions are white dwarfs, neutron stars and black holes. The re-weighting changes both the fraction of the observed Be star population predicted to be in binaries and the stellar types of those companions (Fig. 3.8b). Assuming  $R_{\text{eq}} = 0.85$ , our simulation predicts that more than 90% of all Be stars are in binaries, but that among our observed sample only 77.1% are in binaries. Furthermore, the observed binaries are less than

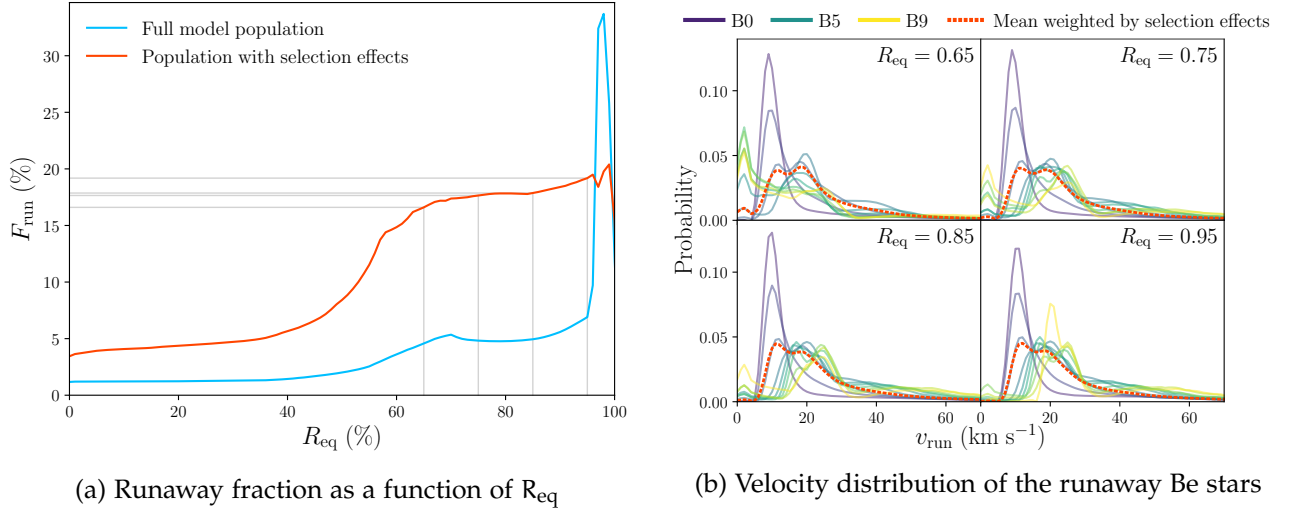


Figure 3.7: Both selection effects and the uncertainty in the choice of  $R_{\text{eq}}$  (the minimum fraction of the critical rotation velocity for a star to be classed as a Be star) can lead to dramatically different simulated populations of runaway Be stars. **Left:** The runaway fraction among Be stars as a function of  $R_{\text{eq}}$  with and without accounting for the observational selection effect. The grey lines indicate the resulting runaway fraction associated with each choice of  $R_{\text{eq}}$  shown in the lower panel. **Right:** The choice of  $R_{\text{eq}}$  changes the velocity distribution of the runaway Be stars as a function of spectral type. In each panel, we show the velocity distribution for each spectral type from B0 to B9, in addition to the mean accounting for the selection effect. Note that as  $R_{\text{eq}}$  increases the effect of Poisson noise also increases because we are defining fewer stars to be Be stars.

half as likely to contain a Be star with a white dwarf companion. The companion that transfers mass to form the Be star must be low-mass in order for the remnant to be a white dwarf, thus the companion Be star must itself be low-mass and so late-type. The high fraction of Be stars residing in binaries with neutron stars or black holes agrees qualitatively with observations of high mass X-ray binaries (HMXBs) in the Magellanic Clouds. In fact, 33 of the 40 HMXBs in the Large Magellanic Cloud (Antoniou & Zezas, 2016) and 69 of the 70 HMXBs in the Small Magellanic Cloud (Antoniou & Zezas, 2016) have Be star companions. Curiously, these authors note that the star formation efficiency of HMXBs in the Large Magellanic Cloud is 17 times smaller than in the Small Magellanic Cloud and argue that this is due to the difference in age and metallicity of the two stellar populations. The effect of varying metallicity on our predictions is an interesting avenue for future work.

### 3.2.3 Compact object natal kick uncertainty

There are several aspects of binary stellar physics that are poorly constrained observationally and must be prescribed when doing population synthesis. Three examples of relevance to the study of runaway

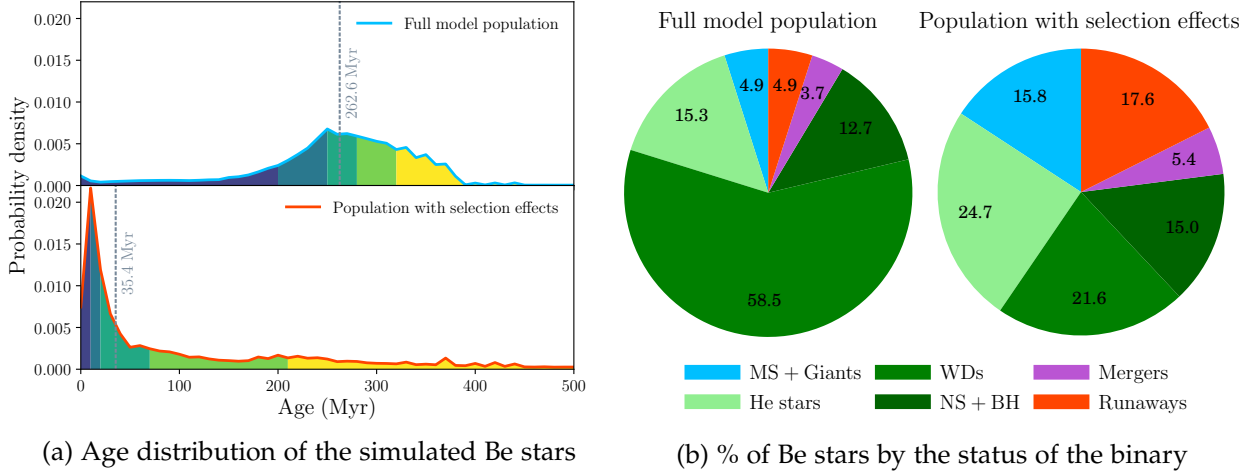


Figure 3.8: The inclusion of observational biases dramatically changes the predicted population of Be stars, under the assumption of  $R_{\text{eq}} = 0.85$ . **Left:** The two panels show the distribution of ages of the Be stars with and without accounting for the observational bias towards early-type Be stars. The grey dashed lines indicate the median age and the coloured regions each account for 20% of the probability. **Right:** Each pie chart gives the proportions of the Be stars for which the progenitor binary is intact, merged or split. If the binary is intact then the stellar type of the companion is given. MS = Main Sequence, WDs = White Dwarf, NS = Neutron Star, BH = Black Hole.

stars are common envelope evolution, natal kicks of compact objects and fallback of material onto black holes. We attempt to quantify how different prescriptions alter our results by generating a population of binary stars with each prescription. However, common envelope evolution is sufficiently poorly understood that there are whole families of alternative prescriptions, so that an investigation of this uncertainty is beyond the scope of this paper. In contrast, for natal compact object kicks, we need only define the probability distribution of kicks  $P(v_{\text{kick}})$ . There are several distributions in the literature that are fits of analytic models to data (a sample of the most popular distributions is shown in Fig. 1.2, including our fiducial choice of the Maxwellian distribution from Hansen and Phinney (1997)). A distribution with a large number of low-velocity compact objects predicts a high fraction of runaways with compact companions.

To explore the impact of the choice of distribution, we simulate a population of binary stars using the Hartman (1997) distribution. This distribution has about 20% of neutron stars receiving a kick less than  $100 \text{ km s}^{-1}$  and thus we expect more binaries to survive the supernova of the primary. The most direct outcome of switching to the Hartman (1997) prescription is that in the full model population, 0.6% fewer Be stars are runaways and 0.6% more are in binaries with neutron stars or black holes. In the population with selection effects included, this trend still holds true, with 15.3% Be star runaways and 17.6% Be stars in compact object binaries. Another trend



is a slight move in the runaway velocity distribution to slower velocities by roughly  $0.5 \text{ km s}^{-1}$ , which is a consequence of both the slower speeds of the neutron stars and the fact that energy is proportional to velocity squared; even if two objects are unbound they still lose speed while escaping, and the speed lost is greater if the two objects have a smaller relative velocity.

Fallback of material onto a black hole in the seconds after the supernova can damp the birth kick and potentially lead to binaries surviving supernovae. One prescription for this fallback was presented in Fryer et al. (2012), who noted that it can alter the predicted number of  $2 - 5 M_{\odot}$  black holes in X-ray binaries by tens of percent (Be stars are frequently found in X-ray binaries). We have not included this fallback in our fiducial model because the uncertainty inherent in the fallback prescription couples to the uncertainty in both the mass of the compact remnant after a supernova (i.e. whether the remnant is a neutron star or a black hole) and the natal kick distribution. Exploring the full space of possible prescriptions is beyond the scope of this paper. However, we believe that including fallback should cause a change in the Be star runaway fraction comparable to changing the natal kick distribution to that of Hartman (1997).

We conclude that the uncertainty in the distribution of natal kicks of compact objects does not greatly impact our results, aside from decreasing the expected Be star runaway fraction by a few percent. One reason for the small scale of the change is that whether a binary is disrupted by a supernova is principally determined by whether the primary loses more than half its mass (Blaauw, 1961), and the kick on the compact object is only a second order effect. The uncertainty in the fallback of material onto a black hole remnant could couple with the natal kick uncertainty, however, and the Be star runaway fraction predicted for the observed catalogue could be as low as 10%.

### 3.3 BAYESIAN FRAMEWORK

We now ask what fraction of the observed Be stars are runaway stars, which is closely related to the question of what fraction can have their origins with the post-mass-transfer model. This is a more subtle question than simply looking for Be stars with peculiar velocities greater than  $40 \text{ km s}^{-1}$ , as done by Berger and Gies (2001), because Fig. 3.7b shows that the median runaway velocity of our simulated Be runaway stars (accounting for observational biases) is only  $19.6 \text{ km s}^{-1}$ . Aumer and Binney (2009) used *Hipparcos* astrometry and photometry and Geneva-Copenhagen radial velocities to calculate the velocity dispersion as a function of colour of 15,000 nearby main-sequence and



subgiant stars. For blue stars with  $B - V < 0$ , they find that the total velocity dispersion is less than  $20 \text{ km s}^{-1}$ . We would thus expect only a small fraction of Be star runaways to have a peculiar velocity in excess of  $40 \text{ km s}^{-1}$ . Another factor is that, in the post-mass-transfer scenario, most Be star producing binaries either evade the supernova through mass transfer or remain bound post-supernova. Thus, most Be stars are found in binaries with white dwarfs, neutron stars or black holes (Fig. 3.8b). This means that only a few percent of all Be stars need have peculiar velocities in excess of  $40 \text{ km s}^{-1}$  in order to imply that all Be stars are produced through the post-mass-transfer channel.

### 3.3.1 Bayesian Mixture Model for the Kinematics

The null hypothesis for a young star in the Milky Way disc is that the velocity is well described by the disc rotation plus velocities drawn from a velocity ellipsoid centred on zero with dispersions  $(\sigma_R, \sigma_\phi, \sigma_z)$ . The velocity dispersions increase with the age on timescales of the order of 1 Gyr. We can reasonably neglect the age dependency and thus assume the dispersions are constant.

We construct a model for a population of stars in the thin disc built from three sub-populations. A fraction  $F_{\text{disc}}$  are well-described by the null hypothesis, a fraction  $F_{\text{run}}$  are runaways and have an additional randomly oriented velocity  $v_{\text{run}}$ , and a fraction  $F_{\text{out}}$  are outliers and have a different randomly oriented velocity  $v_{\text{out}}$ . One physical interpretation of any outliers is that they are stars that have under-gone the two-step-ejection scenario of Pflamm-Altenburg and Kroupa (2010), in which a massive binary is ejected from a cluster by a dynamical interaction and the companion is later accelerated a second time by the supernova of the primary. There are only two free parameters that describe these fractions because they sum to unity and so form a simplex. We assume that every point in this simplex is equally likely, which can be implemented as a flat Dirichlet prior. The probability of observing a star with observables  $\mathbf{x}$  under this composite model is simply a linear combination of the three probability density functions,

$$P(\mathbf{x}) = F_{\text{disc}}P(\mathbf{x}|\text{disc}) + F_{\text{run}}P(\mathbf{x}|\text{runaway}) + F_{\text{out}}P(\mathbf{x}|\text{outlier}). \quad (3.3)$$

The motivation for including an outlier population is that, in Sec. 3.1.4, we removed three stars which had obviously erroneous radial velocities  $|v_{\text{rad}}| > 500 \text{ km s}^{-1}$ . However, some spuriously large velocities may remain and boost the inferred runaway fraction. The functions

$P(\mathbf{x}|\text{model})$  are the priors for the model parameters multiplied by the likelihood of the data with those model parameters.

The observable properties of each star are the parallax  $\varpi$ , proper motions  $(\mu_{\alpha*}, \mu_{\delta})$  and radial velocity  $v_{\text{rad}}$ . The quantities we have are imperfect measurements of the true parallax  $\tilde{\varpi}$ , the true proper motions  $(\tilde{\mu}_{\alpha*}, \tilde{\mu}_{\delta})$  and the true radial velocity  $\tilde{v}_{\text{rad}}$ . The true heliocentric distance  $\tilde{d}$  is then  $1/\tilde{\varpi}$  and, independently, the true Galactocentric velocities  $(\tilde{v}_R, \tilde{v}_{\phi}, \tilde{v}_z)$  can be found using the equations in Johnson and Soderblom (1987). Both these transforms are bijective, thus we are free to express our model in either the distance or parallax and with either of the sets of the velocities. Note that the bijectivity is conditional on the other nuisance parameters having been fixed, such as the Solar position  $R_{\odot}$ . Theoretically, the choice does not change the result of the Bayesian inference and only switches our priors and likelihoods. However, for practical reasons discussed later, it is advantageous to pick the parameters which give the tightest prior. We choose to express our prior in the parameters  $(\tilde{d}, \tilde{\mu}_{\alpha*}, \tilde{\mu}_{\delta}, \tilde{v}_{\text{rad}})$  and thus the likelihood in the parameters  $(\tilde{\varpi}, \tilde{v}_R, \tilde{v}_{\phi}, \tilde{v}_z)$ . We include the necessary Jacobian  $k^2$ , where  $k \approx 4.74057$  is the conversion factor between  $\text{AU yr}^{-1}$  and  $\text{km s}^{-1}$ .

### 3.3.2 The Priors

Consider a model that has parameters  $\theta$  that makes a prediction for some observable data  $\mathbf{x}$ . If we have a function  $\text{Prior}(\theta)$  that describes our prior expectation of the values that the parameters can take and a function  $\text{Likelihood}(\mathbf{x}|\theta)$  that says how likely the data  $\mathbf{x}$  is given a specific choice of the parameters, then our posterior knowledge of the parameters after measuring the data is specified through the distribution

$$\text{Posterior}(\theta|\mathbf{x}) \propto \text{Prior}(\theta) \text{Likelihood}(\mathbf{x}|\theta). \quad (3.4)$$

If new data are subsequently taken, then this posterior distribution should be used as the prior when incorporating the new data. Through this iterative process our knowledge of the parameters converges on their true values.

The parameters can be split into global parameters  $\theta^g$  of the entire population and local parameters  $\theta^l$  of each star. The global parameters only appear once in the prior. However, if the model is applied to  $N$  stars then  $N$  independent copies of the local parameters must be included and are labelled as  $\theta^i$ .

### 3.3.2.1 Global Parameters

The peculiar velocity of the population at birth is assumed to be Gaussian in each of the radial, azimuthal and vertical directions, centred on zero and with independent dispersions  $(\sigma_R, \sigma_\phi, \sigma_z)$ . We place a weakly informative Gaussian prior centred on  $10 \text{ km s}^{-1}$ , with a  $10 \text{ km s}^{-1}$  dispersion and bounded below at zero on each of these dispersions. An additional hyper-parameter is the characteristic length-scale  $L$  of the population, for which we assume a weakly informative Gaussian prior centred on  $0.5 \text{ kpc}$ , with a  $0.5 \text{ kpc}$  dispersion and bounded below at zero. Astraatmadja and Bailer-Jones (2016) found  $L \approx 1.35$  for a simulation of the contents of the full *Gaia* catalogue and thus the prior of  $L$  was motivated by the lower magnitude limit of TGAS. There are five nuisance parameters whose priors are Gaussians centred on their measured value and with a dispersion given by the measurement error: the rotation of the Galactic disc  $V_c$ , the Galactocentric radius of the Sun  $R_\odot$ , and the peculiar velocities of the Sun  $(U_\odot, V_\odot, W_\odot)$ . We assume that the Milky Way disc rotates with a flat circular velocity of  $V_c = 238 \pm 9 \text{ km s}^{-1}$  and that the Sun orbits at the Galactocentric radius  $R_\odot = 8.27 \pm 0.29 \text{ kpc}$  with a peculiar velocity  $(U_\odot, V_\odot, W_\odot) = (11.1 \pm 0.75 \pm 1, 12.24 \pm 0.47 \pm 2, 7.25 \pm 0.37 \pm 0.5) \text{ km s}^{-1}$  (Schönrich, 2012; Schönrich et al., 2010).

### 3.3.2.2 Local Parameters

For the true heliocentric distance  $\tilde{d}$ , we use the exponentially decreasing volume density prior of Bailer-Jones (2015)

$$P(\tilde{d}) = \begin{cases} \frac{\tilde{d}^2}{2L^3} \exp(-\tilde{d}/L), & \text{if } \tilde{d} > 0, \\ 0, & \text{otherwise,} \end{cases} \quad (3.5)$$

where  $L$  is the characteristic length scale hyper-parameter. We remark that this can be equivalently stated in terms of the Gamma distribution as  $\text{Gamma}(3, L)$ . For the true proper motions and radial velocity, the prior is a Gaussian centred on the measured value and with a dispersion given by the measurement error. Both the runaway and outlier populations have an additional velocity described by a speed and a unit vector. The unit vector of ejection  $\mathbf{x}_{ej}$  is assumed to be uniformly distributed on the unit sphere. The runaway speed  $v_{\text{run}}$  is drawn from the analytic distribution obtained in Sec. 3.3.4. The outlier speed  $v_{\text{out}}$  is drawn from a Gaussian centred on zero and with a  $500 \text{ km s}^{-1}$  dispersion. Both speeds are constrained to be greater than zero.

In summary, the prior is

$$\text{Prior}(\theta) = \text{Global}(\theta^g) \prod_i \text{Local}(\theta^i), \quad (3.6)$$

where

$$\begin{aligned} \text{Global}(\theta^g) = & \text{Simplex}(F_{\text{disc}}, F_{\text{run}}, F_{\text{out}}) \text{Normal}(\sigma_R, \sigma_\phi, \sigma_z) \\ & \times \text{Normal}(L) \text{Normal}(V_c, R_\odot, U_\odot, V_\odot, W_\odot), \end{aligned} \quad (3.7)$$

and

$$\begin{aligned} \text{Local}(\theta^i) = & \text{Gamma}(\tilde{d}) \text{Normal}(\tilde{\mu}_{\alpha*}, \tilde{\mu}_\delta, \tilde{v}_{\text{rad}}) \\ & \times \text{DLN}(v_{\text{run}}) \text{Normal}(v_{\text{out}}) \text{UnitVector}(\mathbf{x}_{\text{ej}}). \end{aligned} \quad (3.8)$$

All parameters except the fractions ( $F_{\text{disc}}, F_{\text{run}}, F_{\text{out}}$ ) and the three components of the unit vector  $\mathbf{x}_{\text{ej}}$  are independent and the groupings have only been made to simplify the notation. The function  $\text{DLN}(\cdot)$  indicates the double log-normal fit to the numerical runaway velocity distribution discussed in Sec. 3.3.4.

### 3.3.3 The Likelihood

The likelihood gives the probability of observing the data  $\mathbf{x}$  given the model parameters  $\theta$ . Note that in this problem the data can be broken down into a set of local data  $\mathbf{x}^i$  for each star whose likelihood only depends on the global parameters  $\theta^g$  and the local parameters  $\theta^i$  of that star. Continuing the notation above, we use  $\mathbf{x}^i$  and  $\theta^i$  to label the local data and parameters of a specific star  $i$ . The likelihood is the product of the likelihoods of each star with each individual likelihood containing four terms. The first states how likely the observed parallax  $\varpi$  is given the true parallax  $\tilde{\varpi}$  and is a Gaussian centred on the true parallax with the measurement error on the parallax as the dispersion. The remaining three terms give the likelihood of the peculiar velocity and are Gaussians centred on zero and with dispersions given by the parameters  $(\sigma_R, \sigma_\phi, \sigma_z)$ . In summary the likelihood is,

$$\text{Likelihood}(\mathbf{x}|\theta) = \prod_i \text{Likelihood}(\mathbf{x}^i|\theta^g, \theta^i), \quad (3.9)$$

where

$$\begin{aligned} \text{Likelihood}(\mathbf{x}^l | \boldsymbol{\theta}^g, \boldsymbol{\theta}^l) = k^2 \text{Normal}(\boldsymbol{\omega}) & \left[ F_{\text{disc}} \text{Normal}(\tilde{v}_R, \tilde{v}_\phi, \tilde{v}_z) \right. \\ & + F_{\text{run}} \text{Normal}(\tilde{v}_R - v_{\text{run},R}, \tilde{v}_\phi - v_{\text{run},\phi}, \tilde{v}_z - v_{\text{run},z}) \\ & \left. + F_{\text{out}} \text{Normal}(\tilde{v}_R - v_{\text{out},R}, \tilde{v}_\phi - v_{\text{out},\phi}, \tilde{v}_z - v_{\text{out},z}) \right]. \end{aligned} \quad (3.10)$$

The groupings are only made to simplify the notation and the  $k^2$  is the Jacobian of the transformation.

### 3.3.4 Analytic Fit to Runaway Velocity Distributions

The final ingredient that we need before application of Hamiltonian Monte Carlo techniques in the subsequent section is an analytic fit to the numerical distribution of simulated runaway velocities from Sec. 3.2. We specifically refer to the runaway velocity distribution for the model Be star population defined by  $R_{\text{eq}} = 0.85$  accounting for the observational selection effect, after averaging across the different stellar types. This step is necessary as the derivatives of the posterior with respect to the parameters need to be calculable, as this is a requirement of our method in the proceeding section.

We opt to use the log-normal distribution, defined by the probability density function,

$$P(x | \mu, \sigma) = \begin{cases} \frac{1}{x\sigma\sqrt{2\pi}} \exp\left(-\frac{(\ln x - \mu)^2}{2\sigma^2}\right), & \text{if } x > 0, \\ 0, & \text{otherwise,} \end{cases} \quad (3.11)$$

and with cumulative density function,

$$F(x | \mu, \sigma) = \begin{cases} \frac{1}{2} + \frac{1}{2} \text{erf}\left[\frac{\ln x - \mu}{\sqrt{2}\sigma}\right], & \text{if } x > 0, \\ 0, & \text{otherwise.} \end{cases} \quad (3.12)$$

The log-normal distribution has several properties which make it appropriate for modelling a runaway velocity distribution:

1. log-normals are constrained to be non-zero only for positive  $x$ ,
2. the mode is given by

$$\exp(\mu - \sigma^2)$$

and thus for  $\mu \ll \sigma^2$  a log-normal can approximate a decay,

3. the skewness is given by

$$(\exp \sigma^2 + 2) \sqrt{\exp \sigma^2 - 1}$$

and so for small  $\sigma$  a log-normal can be used to approximate a symmetric distribution offset from the origin.

We fit a mixture of two log-normal distributions to the numeric runaway velocity distribution using the implementation of non-linear least squares in `SciPy`. We found that the fit was best performed using the cumulative density function. In Fig. 3.9 we show a comparison between the probability density functions of our numeric distribution compared to the sum of the two log-normal distributions, as well as a fit containing a single log-normal distribution to illustrate the improvement. The double log-normal does not capture the bimodality near the peak of the distribution, but does trace the tail to large velocities.

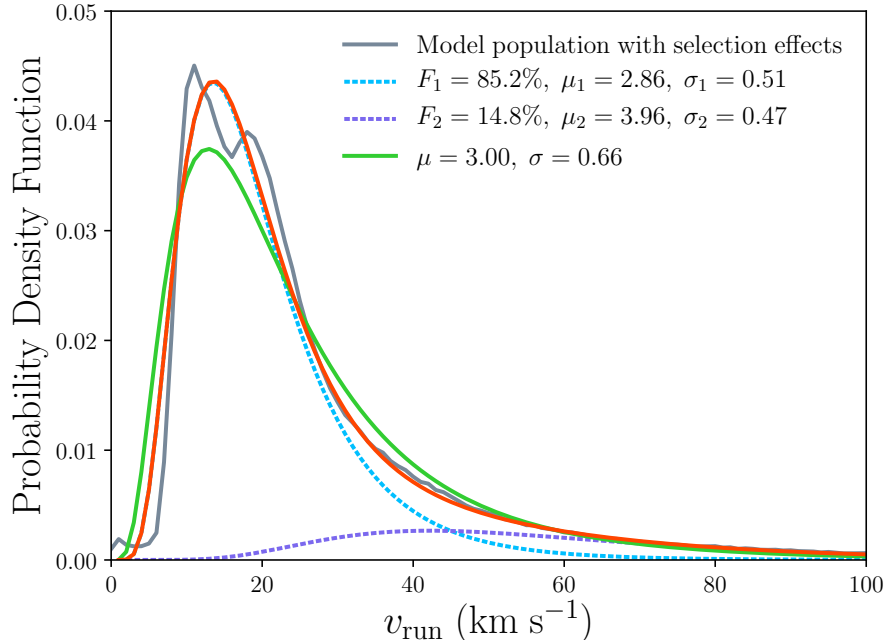


Figure 3.9: Fits of one and two log-normal distributions to the numerical predicted runaway velocity distribution calculated in Section 3.2. In the legend, the  $\mu$  and  $\sigma$  give the parameters of each log-normal distribution and  $F_1$  and  $F_2$  are the fraction of the probability assigned to each component of the double log-normal fit.

### 3.4 THE FRACTION OF BE RUNAWAYS

#### 3.4.1 Preliminaries

363 of the 632 stars in our observed sample have TGAS astrometry and thus have a published covariance matrix between their position,

parallax and proper motions. We neglect the off-diagonal covariances here due to the proof-of-concept nature of this work, but they will be included in the application of our method to the second *Gaia* data release. Positions in TGAS are measured with milliarcsecond accuracy which at a distance of 1 kpc corresponds to a spatial accuracy of 5  $\mu$ pc. The distance over which the properties of the Galaxy vary is much larger than this and thus we fix the coordinates of each star.

Note that, in principle, we could condition the runaway velocity distribution for individual Be stars on their stellar type. However, there are two main arguments against this. First, the individual runaway velocity distributions are subject to greater Poisson noise than their weighted mean. Second, the spectral types for the Be stars in our sample were queried from SIMBAD and thus have a variety of provenances. Taken as a whole, they likely give a good summary of the spectral type distribution of the sample. However, each individual spectral type has a different and unknown uncertainty. If the sample had measured effective temperatures and luminosities with uncertainties, then it would be sensible to condition the runaway velocity distribution of individual Be stars on these physical properties. Such an approach will become viable with the second *Gaia* data release.

When our model is applied to the 632 stars in our observed Be star database we have 5067 free parameters. These are broken down into eleven global parameters which describe the entire sample and eight local parameters for each star. We used the Bayesian inference platform STAN (Carpenter et al., 2017), accessed through CMDSTAN<sup>5</sup>, to obtain the posterior for the model. STAN includes a Hamiltonian Markov chain Monte Carlo sampler which incorporates No-U-Turn Sampling (Hoffman & Gelman, 2011) and so is well suited to high-dimensional problems. We ran four chains and computed the potential scale reduction statistic  $\hat{R}$  (Gelman & Rubin, 1992) across the chains to assess convergence. We used an equal number of warm-up and sampling iterations and doubled the number of iterations until the model converged. The four chains were then merged and used to calculate the statistics.

### 3.4.2 Retrieval of simulated data

A minimum requirement of a successful Bayesian model is the ability to retrieve the input model parameters of simulated data. This is equivalent to saying that if our model of Be star kinematics is correct and complete, then the parameters we retrieve should be close to

<sup>5</sup> Stan Development Team. 2017. CmdStan: the command-line interface to Stan, Version 2.16.0. <http://mc-stan.org>

the true values. One common reason for this not to be true is the existence of a degeneracy between two parameters which the data are not precise enough to break. For our Be star model we expect there to be a strong degeneracy between the three velocity dispersions and the runaway fraction, and thus it is essential that we investigate whether the uncertainties on our data are sufficiently small to allow this degeneracy to be broken.

We generate a test set of stars assuming known  $F_{\text{run}} = 17.5\%$  and  $(v_R, v_\phi, v_z) = (12, 10, 4) \text{ km s}^{-1}$ . We draw a random set of  $(V_c, R_\odot, U_\odot, V_\odot, W_\odot)$  from within their uncertainties to act as the ‘truth’ of the fake catalogue. We create the fake stars in a one-to-one correspondence with the real catalogue, taking both the positions and uncertainties from the true stars. The size of the uncertainties roughly correlates with the distance to the star, so to sample a realistic distance to each fake star, given the uncertainties, we draw from the posterior for the distance to the real star  $\text{Gamma}(0, L) \text{ Normal}(\omega, \sigma_\omega)$ , where we fix  $L = 0.2 \text{ kpc}$  and  $(\omega, \sigma_\omega)$  refer to the parallax and uncertainty of the real star. To generate the radial velocities and proper motions, we first draw three random velocities from the velocity dispersion distributions, add on a randomly oriented ejection velocity for the randomly selected subset of runaway stars, and then transform to the equatorial frame. Finally, the parallaxes, radial velocities and proper motions are convolved with the uncertainties. Note that we do not include an outlier population.

Our principal model is the one introduced in Sec. 3.3, which has contributions from disc, outlier and runaway populations and which uses the double log-normal fit to the runaway velocity distribution. We present the posterior for this model when applied to the fake catalogue in Fig. 3.10, with the true values shown in purple. The interpretation of this plot is that the uncertainties on the current set of Be stars are too large to wholly break the degeneracy between  $F_{\text{run}}$  and the velocity dispersions. However, given the width of the priors on these parameters, the retrieved values are remarkably in agreement with the true values.

While our chief concern is the runaway fraction among the entire Be star population, it is interesting to consider whether our method is successful at classifying individual stars. We expect that stars are only successfully classified as runaways if they are travelling sufficiently rapidly, but not so rapidly as to be misclassified as outliers. Our method does not classify stars directly, but does return the probability of membership of each class. An obvious classification scheme is that if the probability of being a runaway star is greater than  $x\%$ , then the star is classed as a runaway. One common metric to decide



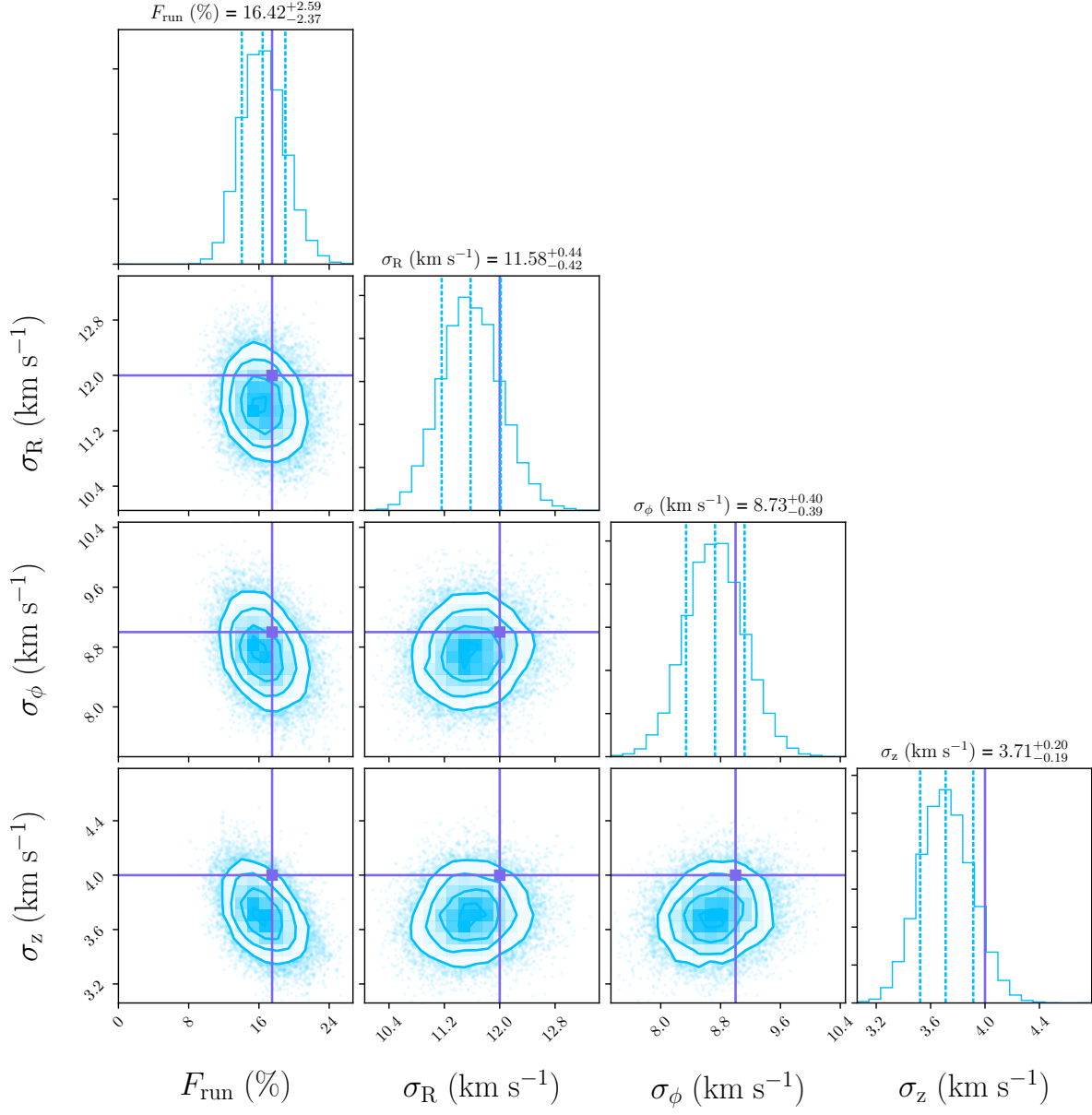


Figure 3.10: Corner plot of the posterior for the retrieval.

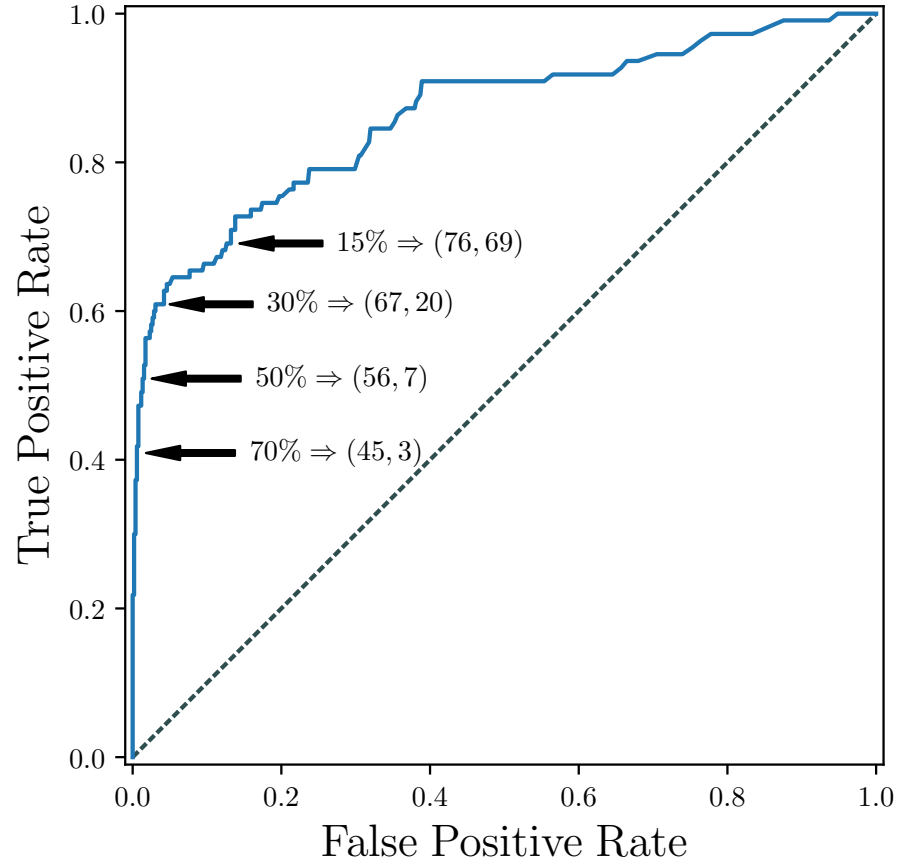


Figure 3.11: The receiver operating characteristic curve for the classification of runaway stars based on the mean of the posterior probability of being a runaway star being greater than  $x\%$ . The grey dashed line corresponds to a classifier that randomly guesses and which our classification far out-competes. The annotations are of the form ' $x\% \Rightarrow (\# \text{ of True Positives}, \# \text{ of False Positives})$ '.

what value of  $x$  to use is the receiver operating characteristic curve (Fig. 3.11), where the true positive rate and false positive rate are plotted as a parametric function of  $x$ . A classification scheme where any star with a probability of being a runaway star greater than 50% is classed as a runaway star performs well, because it can pick out more than half the true runaway stars with only 10% contamination.

We conclude both that our method can accurately retrieve the fraction of runaway stars and the velocity dispersions, as well as produce a low-contamination list of runaway stars.

### 3.4.3 Principal model

We now apply the model to the true catalogue of Be stars described in Section 3.1. In Fig. 3.12, we show the posterior for the runaway fraction  $F_{\text{run}}$  and the velocity dispersions of the population. The outlier fraction is only  $F_{\text{out}} = 0.36^{+0.35}_{-0.22}\%$  which means that the high velocity

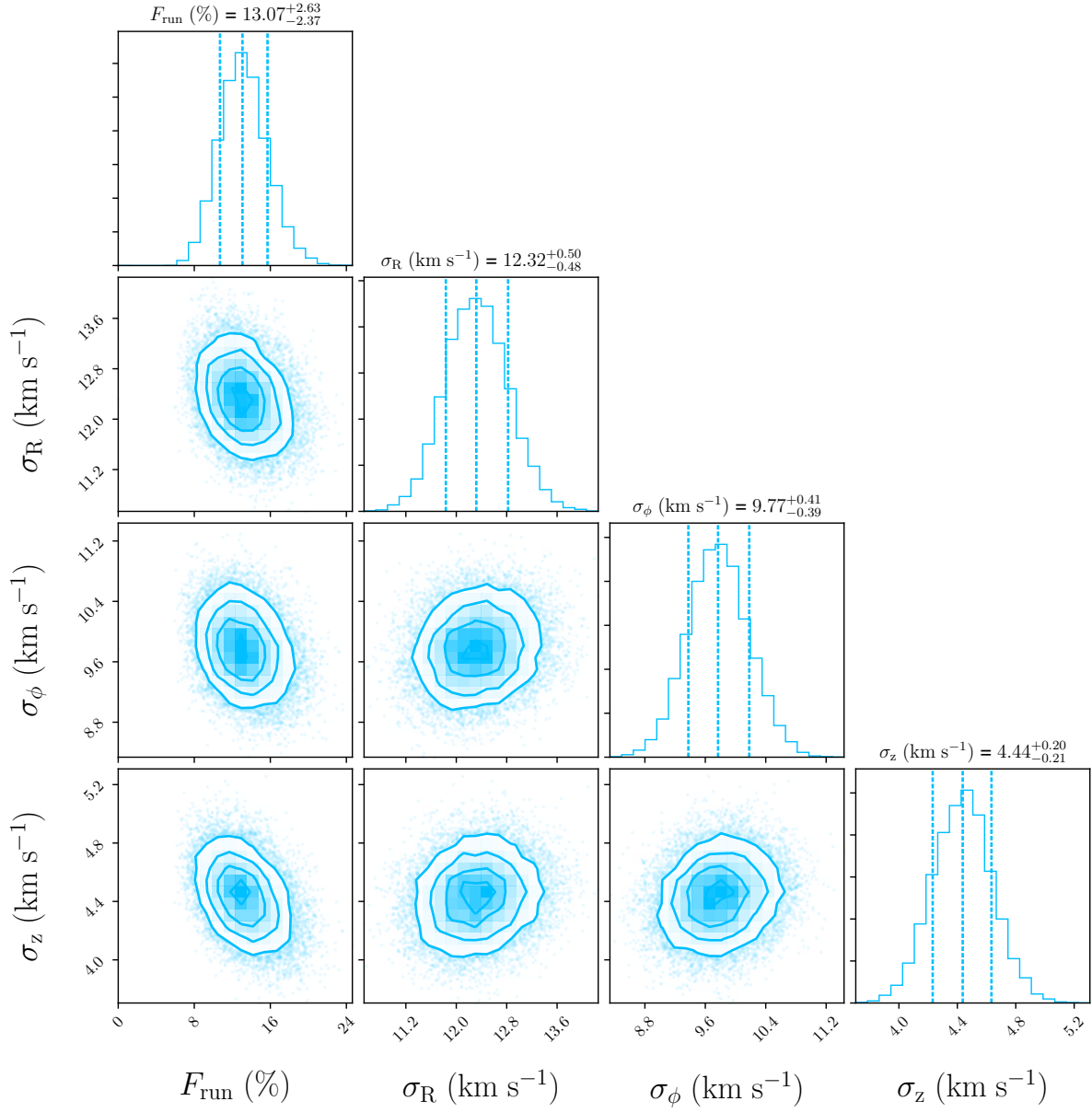


Figure 3.12: Corner plot of the posterior for the principal model.

stars are sufficiently well described by the runaway model. The posterior runaway fraction is about  $13.1^{+2.6}_{-2.4}\%$ . Using the classification scheme from Sec. 3.4.2, 40 stars are classified as runaway stars and they are given in Table 3.1. 7 of these stars were classed as high peculiar space velocity stars by Berger and Gies (2001) and this subset are indicated in Table 3.1. We perform a brief search of SIMBAD to look for particularly interesting cases:

- **Menkib:** There are only 313 IAU-approved<sup>6</sup> named stars and so it is perhaps surprising that one should appear in this work. Menkib is a previously known runaway star (Hoogerwerf, de Bruijne, & de Zeeuw, 2001) in the constellation of Perseus and associated with the  $2.5^\circ$  bowshock nebula NGC 1499 (otherwise known as the California Nebula).
- **Eclipsing binaries:** W Del is a member of an Algol eclipsing binary, while V716 Cen and RY Sct are members of Beta Lyrae eclipsing binaries. Both these classes of eclipsing, semi-detached binaries contain one main sequence and one giant star, in which the giant is transferring mass onto the main sequence star. This mass transfer could plausibly spin up the companion and produce a Be star, which explains the occurrence of three of these rare binaries in the list. That these three systems are binaries does not necessarily imply they are not runaway stars; semi-detached binaries are necessarily close and thus it is plausible for these systems to have originated in a triple system which was unbound in the supernova of the third, most-massive star. Mass transfer from the third star onto these binaries may indeed have lead to these systems being so close by causing an in-spiral due to gas drag. Runaway binaries from massive triple systems would have modest runaway velocities because there is necessarily a limit to how close they can be to the primary. Conversely, it is also possible that these binaries could have been ejected from the core of a young cluster through dynamical interactions. Dynamical ejection has been suggested as the more likely source of binary runaway stars, although the triple supernova mechanism should produce some number of runaway binaries (Perets, 2009).
- **Z Her:** Harmanec, Koubský, and Krpata (1972) conclude that this system is composed of a  $5.4 M_\odot$  Be star with a  $0.66 M_\odot$  companion. However, Popper (1988) conclude that this is instead an AM Canus Venaticorum variable with masses  $1.61 + 1.31 M_\odot$ , which is the classification reported by SIMBAD.

<sup>6</sup> [https://www.iau.org/public/themes/naming\\_stars/](https://www.iau.org/public/themes/naming_stars/), accessed 12/03/2018.

One aspect of runaway stars kinematics not included in our model is that runaway B stars are found at greater altitudes above the disc than a typical B star. Reassuringly, the 40 most probable runaway stars have a greater spread in altitudes than the rest of the sample (standard deviations 0.23 kpc and 0.10 kpc). Aside from the resulting slightly broader distribution of Galactic latitudes, the 40 runaway stars are otherwise distributed similarly across the sky to the rest of the catalogue.

Suppose we now change the principal model by setting the runaway fraction to zero. Then we obtain a significant outlier fraction of  $F_{\text{out}} = 2.85^{+0.78}_{-0.66}\%$ , implying that around 18 stars of the 632 Be stars in the dataset would need an alternative explanation for their velocity. In this case, the posterior also favours somewhat higher velocity dispersions, closer to the values for a 250 Myr old population of stars. Given that the Be stars in our simulated binary evolution have a median age of 35.4 Myr, this seems unlikely.

Another simple change to the principal model is to replace the runaway velocity distribution with the single log-normal fit from Sec. 3.3.4, and for this modified model we obtain

$$F_{\text{run}} = 12.9^{+2.6}_{-2.3}\%,$$

$$(\sigma_R, \sigma_\phi, \sigma_z) = (12.3, 9.8, 4.5) \pm (0.5, 0.4, 0.2) \text{ km s}^{-1}. \quad (3.13)$$

The results are entirely consistent with the double log-normal case, which is perhaps not surprising since the PDFs for both distributions are within a factor of two at almost all velocities (see Fig. 3.9). The motivation for mentioning this possibility is that a single log-normal is easier to work with both analytically and computationally, and that it provides a benchmark for the subsequent section.

#### 3.4.4 A Free Log-normal

The runaway velocity distribution obtained through binary evolution in Sec. 3.2 has systematic errors due to gaps in our understanding of the physics of interacting, massive binary stars as well as the ad hoc definition of a Be star. This uncertainty can be quantified by loosening the requirement that the runaway velocity distribution is precisely the double log-normal obtained by our fit. Instead, we assume that the runaway velocity distribution is described by a log-normal distribution with two hyperparameters  $\mu$  and  $\sigma$ . These hyperparameters have priors  $\mu \sim \text{Normal}(0, 10)$  and  $\sigma \sim \text{Normal}(0.5, 0.5)$ . Note, however, that the data are sufficiently informative that the choice of these

Table 3.1: List of stars identified as highly-likely runaway stars by the method described in Sec. 3.4.3.  $P_{\text{run}}$  is the probability that the star is a runaway,  $v_{\text{run}}$  is the posterior runaway velocity and  $d$  is the posterior distance inferred from the parallax. All of the names are resolvable by Simbad. The starred entries are high-peculiar space velocity stars mentioned by Berger and Gies (2001). Based on Fig. 3.11, we should expect around 4 of these stars to be false positives.

$P_{\text{run}}(\%)$	Name	$v_{\text{run}} (\text{km s}^{-1})$	$d (\text{pc})$	$z (\text{pc})$
99.8	CD-30 850	$28.0^{+7.5}_{-6.2}$	$704^{+294}_{-206}$	$-660^{+193}_{-276}$
99.3	W Del	$32.5^{+10.2}_{-9.2}$	$835^{+191}_{-141}$	$-196^{+33}_{-45}$
99.1	HD 20340*	$36.8^{+10.7}_{-8.1}$	$408^{+149}_{-97}$	$-335^{+80}_{-122}$
99.0	HD 30677	$25.3^{+7.4}_{-6.5}$	$1005^{+277}_{-206}$	$-380^{+78}_{-105}$
98.9	HD 195407*	$59.1^{+11.6}_{-12.3}$	$1063^{+261}_{-182}$	$-23^{+4}_{-6}$
98.8	HD 127617	$40.2^{+16.3}_{-12.4}$	$703^{+231}_{-170}$	$640^{+210}_{-155}$
98.7	HD 137387	$56.9^{+12.1}_{-11.9}$	$384^{+41}_{-35}$	$-93^{+8}_{-10}$
98.4	HD 57682	$48.4^{+13.2}_{-10.5}$	$551^{+170}_{-113}$	$25^{+8}_{-5}$
98.1	Menkib	$54.9^{+12.8}_{-13.5}$	$411^{+101}_{-70}$	$-93^{+16}_{-23}$
98.0	HD 216044	$50.6^{+13.0}_{-14.4}$	$1428^{+412}_{-320}$	$-91^{+20}_{-26}$
97.7	HD 194057	$58.1^{+13.0}_{-13.6}$	$1616^{+412}_{-304}$	$128^{+33}_{-24}$
96.7	V2123 Cyg	$76.4^{+12.7}_{-12.7}$	$1034^{+250}_{-183}$	$-89^{+16}_{-21}$
95.7	HD 107348*	$32.1^{+13.8}_{-11.5}$	$114^{+11}_{-9}$	$74^{+7}_{-6}$
94.6	HD 205618*	$31.6^{+16.0}_{-11.5}$	$955^{+242}_{-181}$	$-269^{+51}_{-68}$
94.2	HD 181409	$77.0^{+20.7}_{-20.8}$	$569^{+114}_{-86}$	$92^{+18}_{-14}$
93.2	V716 Cen	$49.5^{+17.1}_{-19.5}$	$267^{+35}_{-28}$	$30^{+4}_{-3}$
93.1	HD 81753	$27.6^{+12.6}_{-9.2}$	$447^{+131}_{-92}$	$120^{+35}_{-25}$
92.7	HD 150288	$78.2^{+20.3}_{-24.9}$	$685^{+296}_{-193}$	$-6^{+2}_{-3}$
92.0	TYC 3146-824-1	$28.1^{+13.2}_{-9.8}$	$836^{+205}_{-145}$	$186^{+46}_{-32}$
90.8	HD 210129*	$88.3^{+15.5}_{-17.6}$	$211^{+32}_{-25}$	$-96^{+11}_{-15}$
89.0	BD+22 3833	$20.4^{+7.3}_{-5.9}$	$186^{+28}_{-22}$	$-7^{+1}_{-1}$
88.5	HD 50658*	$31.8^{+14.6}_{-12.4}$	$273^{+64}_{-43}$	$94^{+22}_{-15}$
87.3	BD-1 3834	$23.3^{+11.4}_{-8.3}$	$1101^{+282}_{-210}$	$-255^{+49}_{-65}$
85.7	TYC 3327-2315-1	$18.9^{+7.4}_{-5.5}$	$190^{+15}_{-13}$	$-18^{+1}_{-1}$
82.9	HD 305560	$29.0^{+11.9}_{-11.5}$	$1627^{+375}_{-289}$	$-38^{+7}_{-9}$
79.4	7 Vul	$25.9^{+11.9}_{-10.0}$	$347^{+67}_{-48}$	$7^{+1}_{-1}$
79.4	BD+23 3183	$26.7^{+17.3}_{-11.0}$	$778^{+200}_{-141}$	$317^{+81}_{-57}$
78.8	CD-42 11983	$20.1^{+8.5}_{-6.5}$	$536^{+266}_{-170}$	$-22^{+7}_{-11}$
68.9	HD 175511	$19.1^{+9.3}_{-6.4}$	$402^{+43}_{-36}$	$158^{+17}_{-14}$
67.0	HD 152505	$21.8^{+14.1}_{-8.4}$	$763^{+178}_{-121}$	$-48^{+8}_{-11}$
64.6	RY Sct	$130.1^{+18.6}_{-111.8}$	$1361^{+387}_{-276}$	$-3^{+1}_{-1}$
61.4	GW Vel	$24.3^{+14.0}_{-10.2}$	$1087^{+273}_{-199}$	$-17^{+3}_{-4}$
61.4	CD-29 5159	$26.1^{+15.7}_{-11.7}$	$1911^{+660}_{-468}$	$-21^{+5}_{-7}$
60.8	Z Her	$24.7^{+14.5}_{-10.6}$	$84^{+2}_{-2}$	$42^{+1}_{-1}$
59.8	HD 37657*	$26.6^{+17.6}_{-12.6}$	$698^{+163}_{-114}$	$83^{+19}_{-13}$
56.9	BD-20 6251	$18.3^{+10.1}_{-6.2}$	$250^{+80}_{-50}$	$-177^{+36}_{-57}$
56.7	PZ Gem	$23.9^{+15.7}_{-10.5}$	$773^{+253}_{-172}$	$21^{+7}_{-5}$
51.9	V442 And	$24.4^{+17.1}_{-11.1}$	$1056^{+280}_{-243}$	$-276^{+64}_{-73}$
51.4	BD+52 2280	$18.9^{+11.1}_{-6.9}$	$322^{+68}_{-44}$	$121^{+26}_{-17}$
50.4	TYC 870-115-1	$24.3^{+19.1}_{-11.0}$	$304^{+54}_{-39}$	$287^{+51}_{-37}$

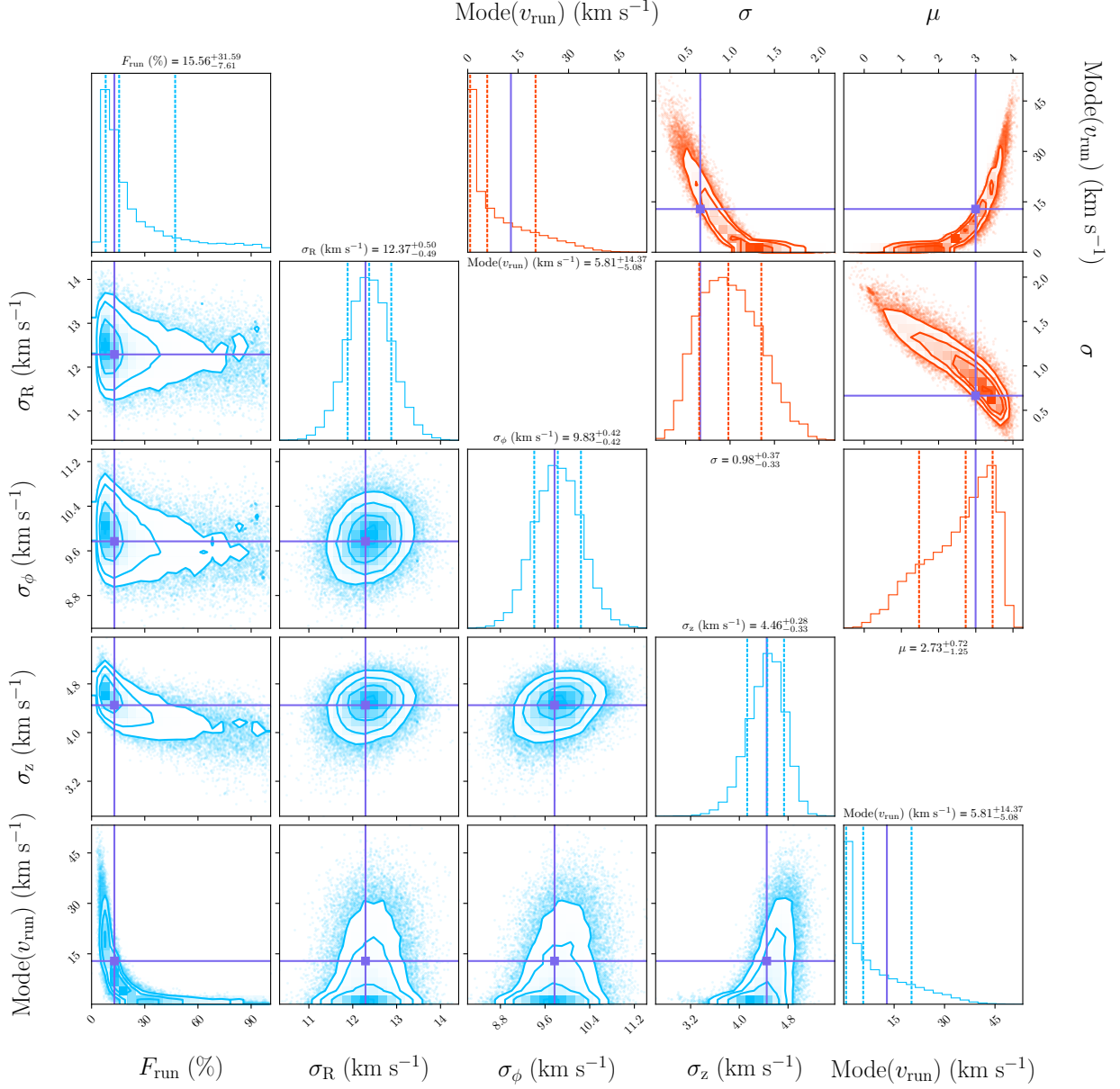


Figure 3.13: The posterior for a model in which the functional form of the runaway velocity distribution is constrained to be a  $\text{LogNormal}(\mu, \sigma)$  distribution, but the  $\mu$  and  $\sigma$  parameters are free to vary. **Upper:** The posterior distributions for  $\mu$  and  $\sigma$  together with the resulting  $\text{Mode}(v_{\text{run}})$ . The green truths indicate the fixed values obtained by fitting a log-normal distribution to the simulated outcomes of binary evolution. **Lower:** The posterior for the runaway fraction and velocity dispersions with the mode of the runaway velocity distribution shown for reference with the upper panel. The green truths indicate the median values obtained from the model where  $\mu$  and  $\sigma$  were fixed as in Sec. 3.3.4.

priors is not dominant. The posterior for this model is shown in the two corner plots of Fig. 3.13.

The mode of the posterior in  $(\mu, \sigma)$  is close to the values which would replicate the single log-normal fit shown in Fig. 3.9. This implies that the runaway velocity distribution predicted in Sec. 3.2 is plausible. One of the key degeneracies in the posterior is between the runaway fraction and the mode of the runaway velocity distribution. A property of the log-normal distribution is that for  $\mu \ll \sigma^2$  the PDF can approximate a decay from the origin, i.e. all the probability is in runaway stars which have a zero runaway velocity, in which case all the Be stars can be runaway stars with no increase in their expected velocity. The existence of this degeneracy demonstrates that the total velocities of the Be stars are well constrained and that the model is simply changing the fraction of these velocities arising from either the velocity dispersion of the disc or the runaway velocity.

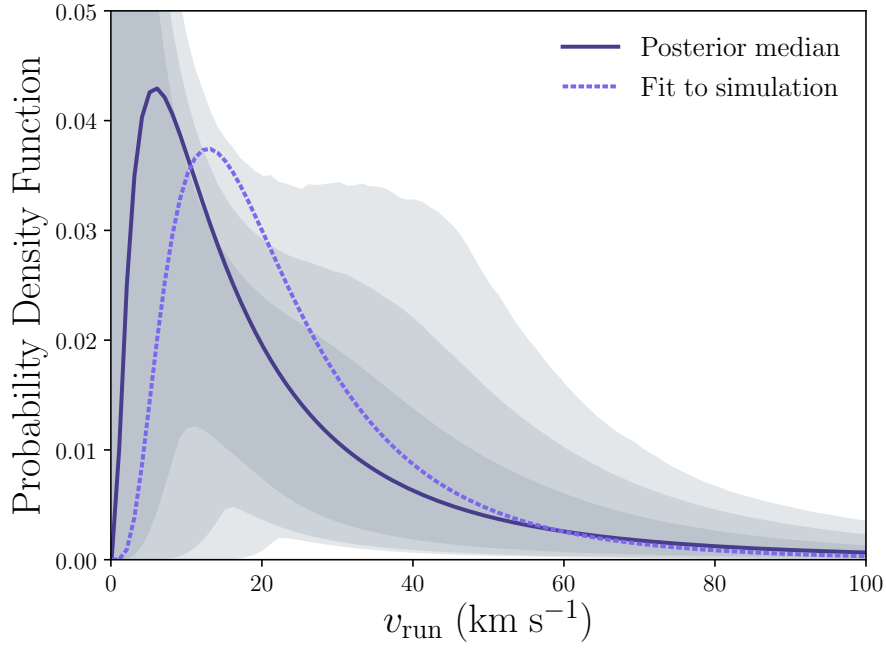
Each sampled point in the posterior corresponds to a different runaway velocity distribution. We take these velocity distributions and compute the 1, 2, and 3 $\sigma$  contours of the probability and cumulative density functions at each value of  $v_{\text{run}}$ , and compare in Fig. 3.14 to the single log-normal runaway velocity distribution shown in Fig. 3.9. The fit single log-normal is not an outlier in these plots which affirms that the runaway velocity distribution predicted by our simulations of binary stars is credible.

### 3.5 DISCUSSION

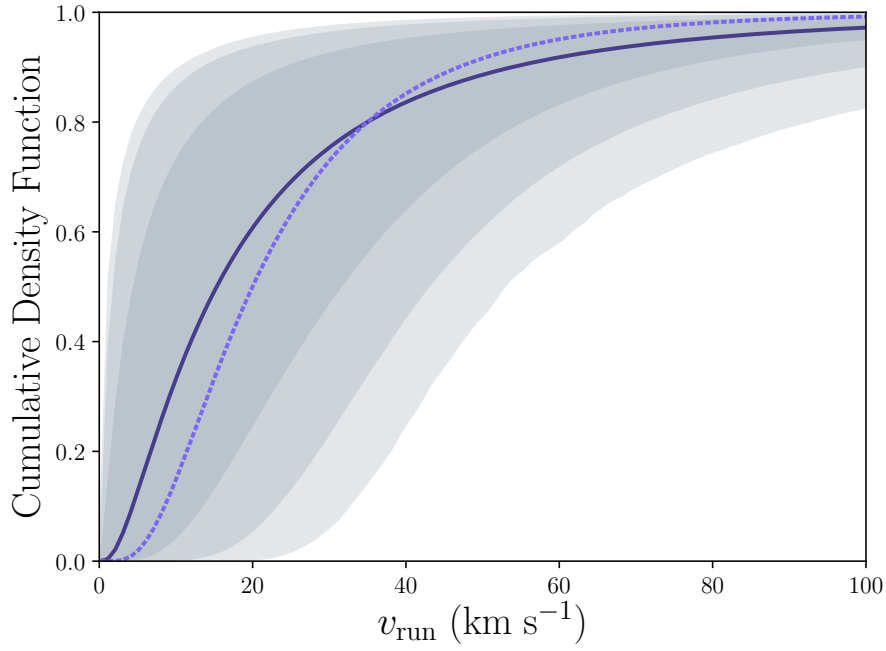
We have constructed the largest catalogue of Be stars with full six-dimensional kinematics to date. This used three sources – namely, the Berger and Gies (2001) survey, the Be Star Spectra database (BeSS) and the catalogue of Hou et al. (2016) from LAMOST – crossmatching with TGAS where necessary to obtain updated proper motions and parallaxes. Our final combined catalogue contains 632 Be stars.

We then modelled the evolution of binaries across a grid in parameter space using the fast `BINARY_C` code (see e.g., Izzard et al., 2009) with a view to testing the post-mass-transfer model of Be stars (Pols et al., 1991). We computed the probability distribution for the runaway velocity and critical equatorial velocity ratio. We developed a criterion based on the equatorial velocity ratio for Be stars and thus obtained the distribution of runaway velocities and a prediction that 5% of all Be stars should be runaways (lower curve in Fig. 3.7a). We then demonstrated that it is vital to account for the observational bias towards early-type Be stars in our catalogue, because this changes our prediction for the population. For instance, we find that a fraction of





(a) Probability density functions.



(b) Cumulative density functions.

Figure 3.14: In grey, we show the 1, 2, and  $3\sigma$  contours of the log-normal distributions implied by the posterior of  $(\mu, \sigma)$  shown in Fig. 3.13. The dark line is the log-normal given by the median of the posterior and the purple dashed line is the single log-normal fit to the simulated runaway velocity distribution shown in green in Fig. 3.9.

17.5% Be stars in our catalogue being runaways is consistent with all classical Be stars originating through mass transfer in binaries, as the rest remain bound post-supernova or miss the supernova phase entirely.

To describe the kinematics of Be stars in our sample, we developed a Bayesian mixture model comprising three populations – thin disc stars, runaways and contaminants. The Bayesian model contained a total of 5067 parameters to represent the kinematics of 632 Be stars. Successfully tackling a Bayesian problem of this scope is a central achievement of this work. It allows us to go beyond fitting a runaway velocity distribution by modelling the distance, velocity dispersions and runaway fraction and velocities simultaneously. We verified that our method is both able to accurately retrieve the input parameters of an artificially-generated test set of stars and individually identify with low contamination the fastest third of the runaway stars. Applying to the true dataset, the posterior runaway fraction of Be stars is  $13.1^{+2.6}_{-2.4}\%$ . This suggests that some Be stars may originate through a process other than the post-mass-transfer scenario. However, caution is needed as there are a number of factors that may have caused us to underestimate the runaway fraction, which we now discuss.

### 3.5.1 *Large uncertainty and wide velocity dispersion priors*

Our weak prior on the global velocity dispersions may allow higher values to be taken at the expense of the number of runaways. Using the relations between age and velocity dispersions of Aumer and Binney (2009), we find that the posterior velocity dispersions imply that the population is around 200 Myr old, while the Be stars in our model population (accounting for selection effects) have a median age of 35.4 Myr. It appears likely that the velocity dispersions are overestimated, with the caveat that it is likely that the Aumer and Binney (2009) velocity dispersions for young stars may be driven by their assumed functional form of the velocity dispersions with age,

$$\sigma(\tau) = v_{10} \left( \frac{\tau + \tau_1}{10 \text{ Gyr} + \tau_1} \right)^\beta \quad (3.14)$$

where  $v_{10}$  and  $\tau_1$  characterize the velocity dispersion at 10 Gyr and at birth and  $\beta$  describes the efficiency of stochastic acceleration. The degeneracy between the velocity dispersions and the number of runaways could be broken either by measuring the velocity dispersion of a population of runaway-free stars coeval to the Be stars or by exploiting the precise astrometry in *Gaia* DR2.

### 3.5.2 *Uncertainty in binary stellar evolution*

An alternative origin for the uncertainty is that the binary evolution simulations rely on a number of uncertain ingredients, some of which we discussed in Section 3.2.3 such as the natal kick distribution of compact objects, the fallback of material onto black holes and common envelope evolution. The use of different prescriptions for these aspects could easily resolve the discrepancy either by decreasing the frequency of runaway Be stars or shifting the runaway velocity distribution to smaller velocities (thus increasing the confusion between true runaways and fast disc stars).

More subtle changes to the binary evolution simulations could also account for part of the difference. For instance, if the prescription for tidal locking requires that the two stars need to be closer than is the case in reality, then the runaway velocity distribution of Be stars will be inflated to faster velocities. The details of the simulated population of Be stars are also sensitive to prescriptions describing mass transfer and rotation, both of which contain their own uncertainties.

Studies of single and binary stars using *Gaia* data over the next few years will drastically constrain these uncertainties in stellar evolution, which in turn will allow for a much keener inference to be made on the runaway fraction among Be stars.

### 3.5.3 *Observational bias against runaway stars*

Be stars are young and thus are typically found at low Galactic latitudes, because they do not live long enough for their vertical velocity to be excited through disc heating. However, runaway Be stars ejected out of the disc could have a large vertical velocity component and thus be found at high latitudes. There will be a trend in which high velocity runaway objects are more common at high latitudes. Considering the 40 high-likelihood runaway stars identified in Table 3.1, which are necessarily the fastest runaway stars in the catalogue, we see that all but two are within 400 pc of the Galactic plane. It is thus possible that our observational bias towards nearby objects may exclude some of the higher velocity Be runaway stars. If the discrepancy were to be entirely explained by this bias, we would need to miss the furthest 25% of runaway Be stars from the disc.

To investigate this possibility, we sample 10,000 Be runaway stars with velocity dispersions given by the posterior in Section 3.4.3 and runaway velocities sampled from the model distribution obtained in Section 3.2.2. We assume the Be stars are born proportionally to the disc density found by Bovy and Rix (2013), noting that with a scale-

height of 400 pc this is likely to over-estimate the number of high-latitude Be stars. The orbits of the sampled Be stars are then followed through the Milky Way using `GALPY` and the included `MWPotential2014` potential (Bovy, 2015). Even with this vertically extended distribution of Be star birth locations, we find that only 20% of runaway Be stars should be found above  $|z| = 0.5$  kpc. Using a more realistic vertical dispersion of 100 pc derived from our observed sample of non-runaway stars, we find that only 3% of Be runaways should be found above  $|z| = 0.5$  kpc and only 0.6% above  $|z| = 1.0$  kpc.

While this bias is not able to resolve the discrepancy, it does answer a long-standing open question which we discuss in the following subsection; Martin (2006) found that there were no Be stars among their 31 high-latitude ( $|z| \gtrsim 1.0$  kpc) B runaway stars.

#### 3.5.4 *Should we find Be stars at high latitude?*

Martin (2006) investigated the origin and evolutionary status of 48 B stars found far from the plane of the Milky Way and, surprisingly, found no Be stars in the sample despite the expectation of at least 10 Be stars based on the incidence of Be stars observed in the field by Zorec and Briot (1997). Previously, Slettebak, Wagner, and Bertram (1997) identified 8 Be stars between  $0.2 < |z| < 0.9$  kpc from the plane, which implies only a small overlap with the Martin (2006) sample covering  $0.5 < |z| < 2.0$  kpc. Martin (2006) provides several arguments that could explain this absence:

1. The short baseline of the data may have missed temporarily inactive Be stars.
2. Magnitude-limited field studies are biased towards younger, brighter stars which have a higher rate of Be stars, i.e. the Be stars aren't missing in this sample, merely overcounted in the field.
3. Based on the  $v \sin i$  distribution and the lack of observed binaries among the dataset, the B stars may be mostly dynamically ejected from a cluster environment. It has been observed that there are fewer Be stars in clusters (although this may be a selection effect).

This list of solutions doesn't consider the possibility that the Be phenomenon might be correlated with the runaway velocity, which could naturally explain the observations if very few Be stars are ejected at high enough velocities to reach high altitudes above the disc. This kinematic selection effect is mentioned by Martin (2006) who found that no star ejected with a velocity less than  $50 \text{ km s}^{-1}$  can make it

to 0.5 kpc above the disc even if the ejection velocity is aligned with the vertical. As we discussed in Section 3.5.3, only 3% of Be runaway stars should be found more than 0.5 kpc from the disc according to our predicted, selection-effect-included runaway velocity distribution, potentially contributing substantially to the solution of this problem.

### 3.6 SUMMARY

In this Chapter, I have shown that the first *Gaia* data release advances our understanding of the Be stars' origin by revealing their kinematics. Although I have not fully resolved the contribution of the post-mass-transfer channel to the Be star population with the TGAS data, I am optimistic about the road ahead. The later *Gaia* data releases will increase the sample of Be stars with accurate kinematics by at least an order of magnitude; for instance, Hou et al. (2016) present a catalogue of 5187 Be stars in LAMOST, all of which will have proper-motions and parallaxes in *Gaia* DR2. *Gaia* DR2 will also eliminate some of the uncertainty discussed above, for instance by enabling a precise determination of the velocity dispersion of young stars as a function of their age. The Bayesian approach developed in this work to tackle the kinematics of a large population lays the foundation for the full exploitation of this future dataset and will allow me to determine whether the numbers of runaway Be stars support a mass-transfer origin for all Be stars.



## HYPERVELOCITY STARS AND THE LARGE MAGELLANIC CLOUD

---

At present, there is no good explanation for the anisotropic distribution of unbound late B-type stars in the halo.

Brown (2015)

A *hypervelocity star* (HVS) is any star whose velocity in the Galactic rest frame exceeds the local escape speed of the Milky Way (MW). As discussed in Sec. 1.3.5 of the Introduction, there are a few dozen late B-type HVSs in the halo which are generally believed to have been ejected from the Galactic centre by the Hills (1988) mechanism. The flaw in this origin story is that the Hills mechanism would predict an even spread of HVSs across the sky, contrary to the anisotropic distribution that is observed. Several attempts have been made to introduce asymmetry into the Hills mechanism, but these were found to be unlikely explanations (see Sec. 1.3.5 or Brown, 2015).

I present in this Chapter my novel explanation of the anisotropy: a majority of the HVSs in the halo originate in the Large Magellanic Cloud (LMC). The clump of HVSs is explained as the tip of a stream of HVSs crossing into the Northern Hemisphere from the LMC. There are several reasons to believe this could be the case:

1. The LMC is lower mass than the MW.  
*It is easier for stars to escape the gravitational potential of the LMC.*
2. The LMC is moving past the MW at  $321 \pm 24 \text{ km s}^{-1}$ .  
*Stars that escape are boosted by the orbital velocity of the LMC.*
3. The escape speed from the MW at the LMC is  $377^{+35}_{-28} \text{ km s}^{-1}$ .  
*Stars kicked ahead of the LMC at  $57^{+42}_{-38} \text{ km s}^{-1}$  will be HVSs.*
4. The LMC is sufficiently massive that it may host an MBH<sup>3</sup>.  
*The Hills mechanism could plausibly be operating in the LMC.*
5. The LMC is forming stars at a comparable rate to the MW<sup>4</sup>.  
*The runaway star mechanisms must be operating in the LMC.*

### *Hills mechanism:*

Hills (1988) theorised that the tidal disruption of a stellar binary during a close encounter with the massive black hole at the centre of the MW could eject one or both of the stars.

---

<sup>1</sup> Kallivayalil et al. (2013)

<sup>2</sup> Williams, Belokurov, Casey, and Evans (2017)

<sup>3</sup> Observations of LMC-mass dwarf galaxies hosting MBHs find a median black hole mass of  $2 \times 10^5 M_{\odot}$  (Reines, Greene, & Geha, 2013).

<sup>4</sup>  $0.2 M_{\odot} \text{ yr}^{-1}$  (Harris & Zaritsky, 2009) versus  $0.68\text{--}1.45 M_{\odot} \text{ yr}^{-1}$  for the MW (Robin et al., 2010).

I have investigated the consequences of these five statements from two directions. In Sec. 4.1, I predict the expected distribution of stars ejected from the LMC if it were to host an MBH and show that this can explain the HVS anisotropy. In Sec. 4.2, I attempt to simulate the occurrence of binary supernova ejections in the LMC over the past 2 billion years as accurately as possible, and show that the production of HVSs arises as a natural consequence. Some other possible origins of unbound LMC stars include stripping from the LMC by a previous passage of the SMC (Besla, Hernquist, & Loeb, 2013), formation in the gas of the leading arm of the LMC (Casetti-Dinescu et al., 2014), or dynamical interactions in a stellar cluster, possibly involving an intermediate mass black hole (Gualandris & Portegies Zwart, 2007).

#### 4.1 HILLS MECHANISM IN THE LMC

*Based on work originally published in Boubert and Evans (2016).<sup>5</sup>*

It is an organic extension of the Hills mechanism to ask where it may occur beyond the Milky Way. Lu, Yu, and Lin (2007) and Sherwin, Loeb, and O’Leary (2008) suggest the central MBHs of M31 and M32 as possible sites; the discovery of a red supergiant runaway candidate of M31 by Evans and Massey (2015) portends that these two possibilities may soon be testable. The LMC is the most massive of the MW’s dwarf satellites and thus there is the potential for the LMC to host a central MBH. The Hills mechanism acting in the LMC could accelerate large numbers of stars to a few  $100 \text{ km s}^{-1}$ , which is above the escape speed from the LMC. The LMC has an orbital velocity of  $321 \pm 24 \text{ km s}^{-1}$  (Kallivayalil et al., 2013), thus alignment of these velocity vectors could result in stars that escape both the LMC and MW. The location of the LMC on the sky and the orientation of its velocity vector could explain the spatial anisotropy in the observed HVSs.

##### 4.1.1 Method

To test the hypothesis that there is a significant number of HVSs ejected from the LMC, we require a prediction for the observables of such a population and a reference population of HVSs from the Galactic Center (GC). A useful starting point is the effort by Kenyon, Bromley, Brown, and Geller (2014) to model the ejection of HVSs from the

<sup>5</sup> I conceived of an LMC origin of the hypervelocity stars and developed this project in collaboration with N. Wyn Evans. I was principally responsible for the implementation and write-up, however N. Wyn Evans both suggested the spherical harmonic analysis and contributed invaluable edits to the text. Prashin Jethwa contributed the LMC orbit used in Sec. 4.1.1.3 and we acknowledged Scott Kenyon for useful and prompt answers to our queries.



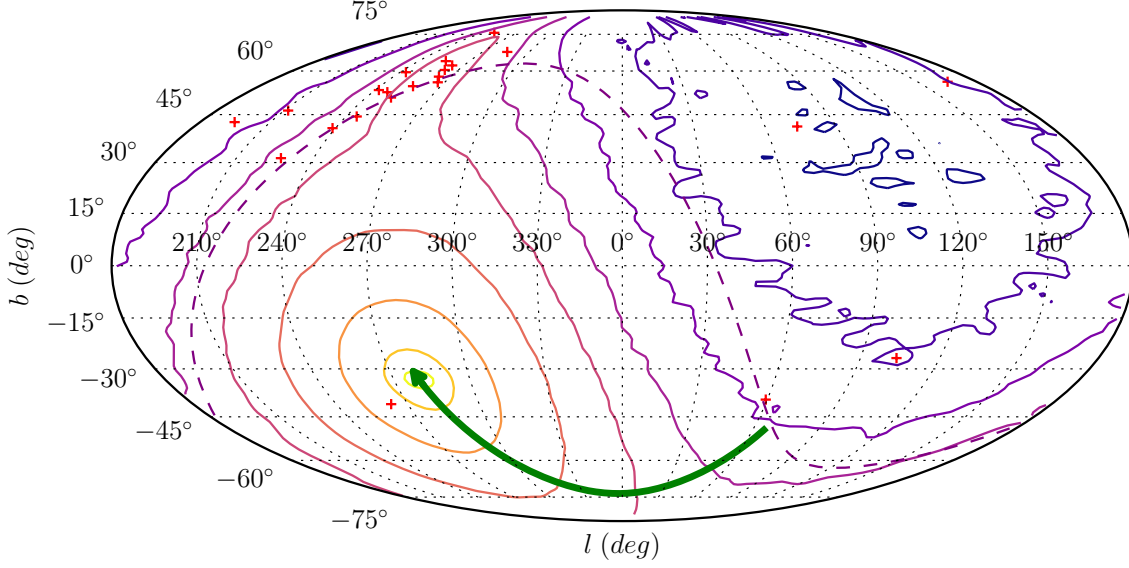


Figure 4.1: Predicted distribution in Galactic coordinates of HVSs from the LMC at a heliocentric distance  $50 < d < 120$  kpc, using the HVLMC-A model from Section 4.1.1. Density contours are spaced  $10^{1/2}$  apart with the yellow contour denoting the highest density, the green arrow marks the path of the LMC over the last 350 Myr, the purple dashed line is the celestial equator, and the red crosses are the HVS candidates denoted HVS1, HVS2, etc. by Brown.

GC; our strategy is to apply their method to LMC ejections. We consider three models; HVGc is a model that produces stars from the GC and is identical to HV3 from Kenyon et al. (2014), HVLMC-A is a population from the LMC, and HVLMC-B is identical to HVLMC-A but has the initial ejection velocity cut by  $200 \text{ km s}^{-1}$  to approximate the escape velocity from the centre of the LMC. All three models consider  $3 M_{\odot}$  HVSs, which have a typical main sequence lifetime of 350 Myr, because we are attempting to replicate the B-type HVSs in the halo (Brown, 2015). We simulate the process of ejection from the centre of the LMC by seeding HVSs along the orbit of the LMC over the past 350 Myr, with a velocity which is the sum of the orbital velocity of the LMC and the ejection velocity due to the Hills mechanism. These stars are then evolved through a potential model of the MW until present day, at which point we record the position and velocity in the Galactic rest frame. To allow for cross-comparisons with Kenyon et al. (2014), we assume that the Sun is at a position  $(x, y, z) = (-R_{\odot}, 0, 0)$  relative to the GC where  $R_{\odot} = 8 \text{ kpc}$ , and is travelling with a velocity  $(v_x, v_y, v_z) = (0, v_{\odot}, 0)$  where  $v_{\odot} = 235 \text{ km s}^{-1}$ .

#### 4.1.1.1 LMC black hole mass

Observations of dwarf galaxy hosts of MBHs were carried out by Reines et al. (2013), who specifically reference these galaxies as be-

ing in the mass range of the LMC. For dwarf galaxies with stellar masses in the range  $10^{8.5} \lesssim M_{\text{star}} \lesssim 10^{9.5} M_{\odot}$  they find MBH masses of  $10^5 \lesssim M_{\text{bh}} \lesssim 10^6 M_{\odot}$ , with a median of  $M_{\text{bh}} \sim 2 \times 10^5 M_{\odot}$ . The mean of the ejection velocity from the Hills mechanism is only weakly dependent on the MBH mass ( $\propto M_{\text{bh}}^{1/6}$ ), see Section 4.1.1.2, and therefore a factor of 10 in MBH mass is only a factor of  $\sim 1.5$  in the mean ejection velocity. Using Equation 4.4 from Section 4.1.1.2, we see that the mean ejection velocity for the binaries with a separation of 0.115 AU is  $\approx 1800 \text{ km s}^{-1}$ , hence MBHs which are  $10^4$  times less massive are still capable of ejecting HVs at velocities of  $\geq 350 \text{ km s}^{-1}$ . We thus assume a fiducial value  $M_{\text{bh}} = 1.7 \times 10^5 M_{\odot}$ , similar to the median of Reines et al. (2013)<sup>6</sup>.

#### 4.1.1.2 Hills mechanism

We first require the initial positions  $\tilde{\mathbf{r}}_0$  and velocities  $\tilde{\mathbf{v}}_0$  of the candidate HVs in a frame co-moving with the MBH from which they were ejected. This Section uses the prescription of Kenyon et al. (2014), itself based on the Hills mechanism algorithm of Bromley et al. (2006), which we briefly describe here to aid clarity. At the time of their ejection the stars are uniformly distributed across the surface of a sphere with radius 1.4 pc centred on the MBH and given an initial outwardly radial trajectory. Thus the only free parameters not yet determined are the magnitude of the velocity  $v_{\text{ej}}$ , the age of the star when it is ejected  $t_{\text{ej}}$ , and the age of the star when it is observed  $t_{\text{obs}}$ .

Suppose that an equal mass binary with separation  $a_{\text{bin}}$  interacts at a closest approach  $r_{\text{close}}$  with a MBH of mass  $M_{\text{bh}}$ . One star of the system will be ejected by the Hills mechanism with probability

$$P_{\text{ej}} = 1 - D/175 \quad (4.1)$$

where

$$D = D_0 \left( \frac{r_{\text{close}}}{a_{\text{bin}}} \right), \quad D_0 = \left[ \frac{2M_{\text{bh}}}{10^6(M_1 + M_2)} \right]^{-1/3}. \quad (4.2)$$

The probability  $P$  that a star is ejected is drawn from a uniform distribution between 0 and 1. If the star is ejected, then following Kenyon et al. (2014), the velocity is drawn from the distribution

$$P(v_{\text{ej}})dv_{\text{ej}} \propto \exp\left(-\frac{(v_{\text{ej}} - v_{\text{ej,H}})^2}{2\sigma_v^2}\right)dv_{\text{ej}}, \quad (4.3)$$

<sup>6</sup> I do not know why I chose precisely this value, however it is conveniently true that it is close to the Reines et al. (2013) median.

where  $\sigma_v = 0.2v_{ej,H}$  and  $v_{ej,H}$  is given by

$$v_{ej,H} = 1760 \left( \frac{a_{bin}}{0.1 \text{ AU}} \right)^{-1/2} \left( \frac{M_1 + M_2}{2 M_\odot} \right)^{1/3} \times \left( \frac{M_{bh}}{3.5 \times 10^6 M_\odot} \right)^{1/6} f_R \text{ km s}^{-1}. \quad (4.4)$$

We only consider equal mass binaries so  $M_1 = M_2$ . Note that  $f_R$  is a normalisation factor (Kenyon et al., 2014)

$$f_R = 0.774 + (0.0204 + (-6.23 \times 10^{-4} + (7.62 \times 10^{-6} + (-4.24 \times 10^{-8} + 8.62 \times 10^{-11} D)D)D)D)D. \quad (4.5)$$

Since we are interested in all possible equal mass binary systems that can result in an ejection we sample from distributions of  $a_{bin}$  and  $r_{close}$ . The separation of the binary  $a_{bin}$  is drawn from

$$P(a_{bin})da_{bin} \propto \frac{1}{a_{bin}}da_{bin}, \quad (4.6)$$

where  $a_{bin,min} = 0.115 \text{ AU}$  for stars of mass  $3 M_\odot$  and  $a_{bin,max} = 4 \text{ AU}$ . The closest approach  $r_{close}$  has

$$P(r_{close})dr_{close} \propto r_{close}dr_{close}, \quad (4.7)$$

where  $r_{close,min} = 1 \text{ AU}$  and  $r_{close,max} = 175a_{bin,max}/D_0$ .

Both the age of the star at the time of ejection  $t_{ej}$  and observation  $t_{obs}$  are drawn from the uniform distribution

$$P(t)dt \propto dt, \quad (4.8)$$

where  $t_{min} = 0 \text{ Gyr}$  and  $t_{max} = t_{ms}$  and the main sequence lifetime  $t_{ms} = 0.35 \text{ Gyr}$  for stars of mass  $3 M_\odot$ . The time of flight of the star from ejection to observation is then defined by  $t_f = t_{obs} - t_{ej}$ .

We discard any sampled star that does not satisfy  $P_{ej} \geq P$ ,  $v_{ej} \geq v_{ej,min}$  and  $t_{ej} < t_{obs}$ . Note that  $v_{ej,min}$  is chosen to minimise the computation time spent on stars that will be difficult to observe. For the HVGC model this corresponds to stars that will remain in the GC so  $v_{ej,min} = 600 \text{ km s}^{-1}$ . For stars in the HVLMC-A and HVLMC-B models, we choose  $v_{ej,min} = 200 \text{ km s}^{-1}$  to ensure we only include stars that escape the LMC.

#### 4.1.1.3 Large Magellanic Cloud orbit

For stars ejected from the centre of the MW, the position  $\mathbf{r}_0$  and velocity  $\mathbf{v}_0$  vectors in the Galactic rest frame satisfy  $\mathbf{r}_0 = \tilde{\mathbf{r}}_0$  and  $\mathbf{v}_0 = \tilde{\mathbf{v}}_0$ . However, for stars ejected from the LMC

$$\mathbf{r}_0 = \tilde{\mathbf{r}}_0 + \mathbf{r}_{\text{LMC}}(t_f), \quad \mathbf{v}_0 = \tilde{\mathbf{v}}_0 + \mathbf{v}_{\text{LMC}}(t_f), \quad (4.9)$$

where  $\mathbf{r}_{\text{LMC}}(t_f)$  and  $\mathbf{v}_{\text{LMC}}(t_f)$  are the position and velocity vectors of the LMC  $t_f$  years ago.

These definitions require knowledge of the position and velocity of the LMC over the past 350 Myr, for which we use an orbit of the LMC around the MW taken from Jethwa, Erkal, and Belokurov (2016), who rewound the orbit of the LMC from the present position including the effect of dynamical friction. The potential used by Jethwa et al. (2016) for the MW is an Navarro, Frenk, and White (1997, hereafter NFW) halo with mass  $10^{12} M_\odot$  and concentration 7.328 and a Miyamoto and Nagai (1975) disc with radial scale-length 3 kpc and vertical scale-length 0.28 kpc and a mass chosen to give the solar circular velocity at the position of the sun. The LMC has an NFW halo with mass  $2 \times 10^{10} M_\odot$  and concentration 9.450 and a Plummer bulge with scale-length 3 kpc and a mass chosen to satisfy the mass constraint of van der Marel (2015).

#### 4.1.1.4 Milky Way potential

For the MW, we use the potential from Kenyon, Bromley, Geller, and Brown (2008), which was optimised to reproduce the Galactic potential at both parsec scales near the MBH Sgr A\* and at scales of tens of kiloparsecs in the halo. This potential consists of four components

$$\phi_G = \phi_{\text{bh}} + \phi_{\text{b}} + \phi_{\text{d}} + \phi_{\text{h}} \quad (4.10)$$

where

$$\phi_{\text{bh}}(r) = -GM_{\text{bh}}/r \quad (4.11)$$

is the Keplerian potential of the central MBH with  $M_{\text{bh}} = 3.5 \times 10^6 M_\odot$ ,

$$\phi_{\text{b}}(r) = -GM_{\text{b}}/(r + a_{\text{b}}), \quad (4.12)$$

is the Hernquist (1990) potential of the bulge with  $M_{\text{b}} = 3.76 \times 10^9 M_\odot$  and  $a_{\text{b}} = 0.1$  kpc,

$$\phi_{\text{d}}(R, z) = -GM_{\text{d}}/\sqrt{R^2 + \left[ a_{\text{d}} + (z^2 + b_{\text{d}}^2)^{1/2} \right]}, \quad (4.13)$$

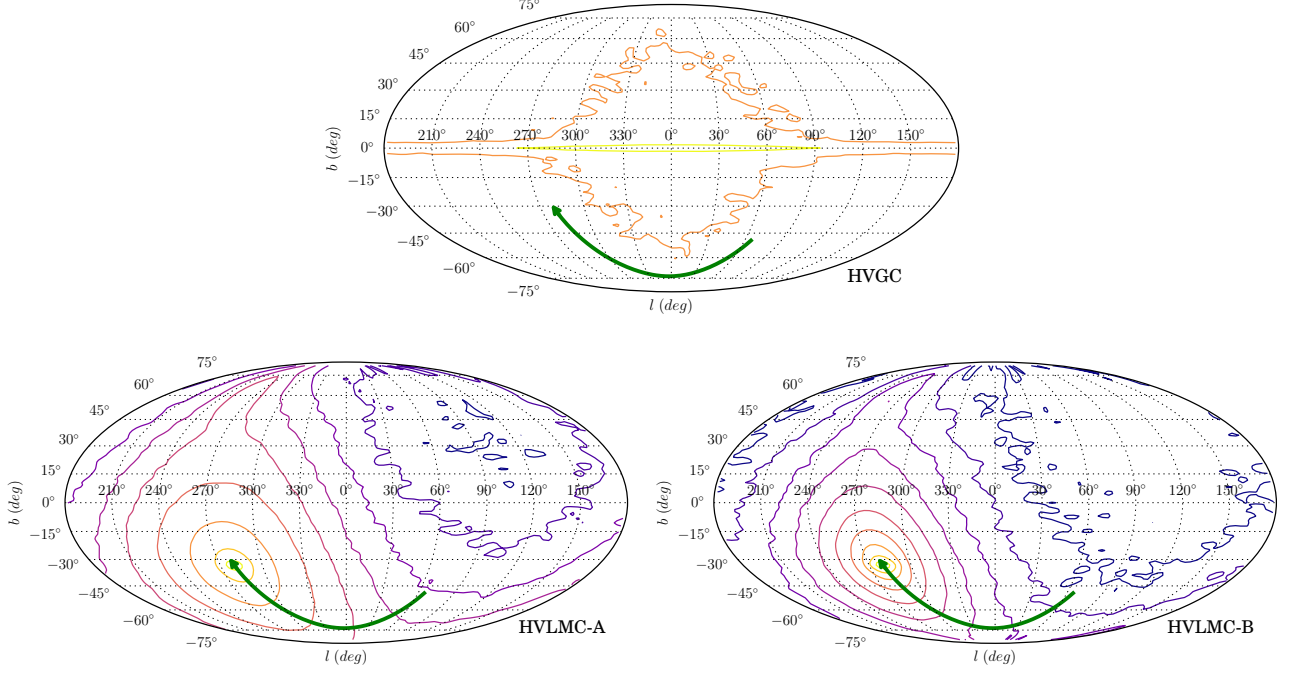


Figure 4.2: Density contours in Galactic coordinates for the stars from the three models with heliocentric distance  $50 \leq d \leq 120$  kpc.

is the Miyamoto and Nagai (1975) potential of the disc with  $M_d = 6 \times 10^{10} M_\odot$ ,  $a_d = 2.75$  kpc and  $b_d = 0.3$  kpc, and

$$\phi_h(r) = -GM_h \ln(1 + r/r_h)/r, \quad (4.14)$$

is the NFW potential of the dark matter halo with  $M_h = 10^{12} M_\odot$  and  $r_h = 20$  kpc. The values for each parameter are from Kenyon et al. (2014).

#### 4.1.2 Discussion

##### 4.1.2.1 All sky density plots

The density distribution of HVs can be illustrated by an all-sky plot in Galactic coordinates, using the equal-area Mollweide projection. We consider only stars with heliocentric distance  $50 < d < 120$  kpc, since the distance of the LMC is  $50.1 \pm 2.5$  kpc (van der Marel, 2015) and this range covers the clustering of HVs near the constellations of Leo and Sextans reported by Brown et al. (2009), however the kinematics in the distance bin  $0 < d < 50$  kpc are broadly similar. Figure 4.2 suggests that the expected distribution of LMC HVs on the sky is a dipole, which contrasts with the monopole shown by HVs from the GC. Note that for the HVGC model the first few contours aren't shown, because there are HVs from the GC in our population across the entire sky.

We emphasise that the density contours are not normalised to the ejection rate from either MBH. Brown (2015) justifies an ejection rate of  $10^{-4} \text{ yr}^{-1}$  for the MW MBH, but the ejection rate from a MBH at the centre of the LMC will depend significantly on the internal dynamics and star formation rate of the LMC as well as the mass of the MBH. We speculate that the large contribution of the orbital velocity makes an observable signal of LMC HVSs plausible.

In the discovery paper of HVS11, Brown et al. (2009) commented that that star was within  $3.9^\circ$  of the Sextans dwarf galaxy while the typical angular separation of HVSs from Local Group dwarf galaxies is  $10^\circ - 20^\circ$ . Brown et al. (2009) ruled out an association with Sextans based on the  $260 \text{ km s}^{-1}$  relative velocity of HVS11 towards Sextans, however the initial instinct that coincidence on the sky is a requirement for association is challenged by Figure 4.2. The LMC HVSs are distributed across a wide region of the sky.

Figure 4.1 highlights an intriguing extension of the distribution that leads the LMC and is coincident with the clump observed by Brown et al. (2009). This is the only area of the sky which is both densely populated in our LMC HVSs models and well-covered by HVS surveys, since almost all of these surveys have covered solely the northern hemisphere, partially due to the footprint of SDSS. The one HVS plotted in Figure 4.1 that lies in the southern celestial hemisphere is HE 0437-5439 (HVS3) which was discovered by Edelmann et al. (2005), who noted that the flight time was longer than the main sequence lifetime for the star and hence either it is a blue straggler and was ejected as a binary from the GC or has its origin in the LMC. The possible LMC origin of this star is revisited in Sec. 5.2.

As mentioned in Sec. 1.3.5 of the Introduction, there are other possible explanations of the anisotropy, including selection effects, contamination by runaway companions to supernovae, tidal debris from disruption of a dwarf galaxy, temporary intermediate mass black hole companions to the central MBH of the MW, and interactions between two stellar discs near the central MBH which imprint their geometry on the ejected HVSs. An LMC origin is attractive compared to the other possibilities because the anisotropy is an unavoidable consequence of the LMC's orbit, i.e. the model requires no fine-tuning.

#### 4.1.2.2 *All sky velocity plots*

In Figure 4.3 we show contours of the mean heliocentric radial velocity in each bin, where the standard deviation in each plot is a couple  $100 \text{ km s}^{-1}$ . The remaining two velocity dimensions are summarised in Figure 4.4, where we plot contours of the mean proper motion in each bin in both equatorial and Galactic coordinates with a typical

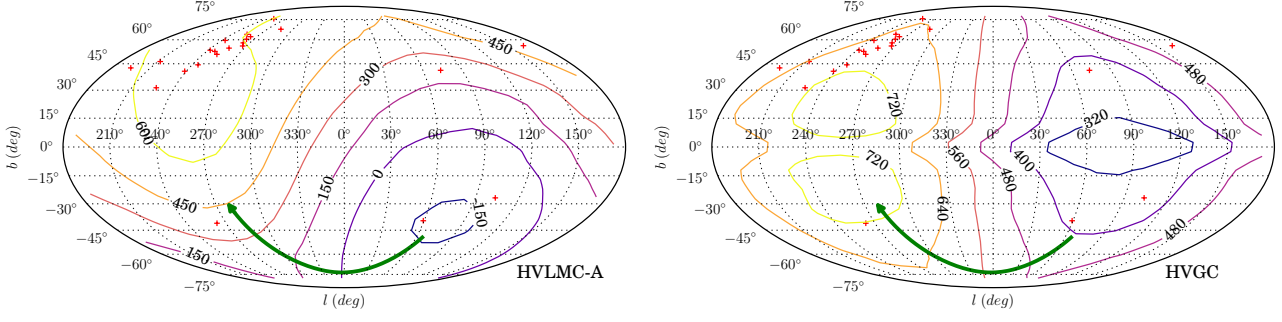


Figure 4.3: Mean heliocentric radial velocity for stars at distance  $50 < d < 120$  kpc.

standard deviation of  $0.5 \text{ mas yr}^{-1}$ . For the HVLMC-A model the contours demonstrate the imprint of the orbital velocity of the LMC in the kinematics of the HVSs, while for the HVGC stars the dominant effect is the solar rotation.

Considering Figures 4.3 and 4.4, we see that at the locations on the sky of the currently observed B-type HVSs the velocity distributions of HVSs in the HVGC and HVLMC-A models are coincident. Each model has a standard deviation of  $0.5 \text{ mas yr}^{-1}$  and the current proper motions for these stars have a typical error of  $0.5 \text{ mas yr}^{-1}$  (Brown et al., 2015), therefore it will not be possible to test our hypothesis using the current sample of HVSs. This situation should be resolved by *Gaia*, which will give proper motions for HVSs in regions on the sky where the two models differ by up to  $0.7 \text{ mas yr}^{-1}$ . To illustrate this point, the first and third quartile ranges of the magnitude of the proper motions for stars at a distance  $50 < d < 75$  kpc are  $0.53 < \mu < 0.82 \text{ mas yr}^{-1}$  in the HVGC model and  $1.28 < \mu < 1.88 \text{ mas yr}^{-1}$  in the HVLMC-A model. Comparing these ranges to end-of-mission proper motion errors for *Gaia*<sup>7</sup> of around  $450 \text{ } \mu\text{as yr}^{-1}$  for B1V stars with apparent magnitude  $V = 20$  mag, corresponding to stars at about 100 kpc, it may be possible for *Gaia* to distinguish between the two populations.

#### 4.1.2.3 Spherical harmonics

One method of quantifying the relative spatial distributions of HVSs from the centre of the Galaxy and the LMC is to consider the power in each mode of the spherical harmonic power spectrum of the density. For spherical harmonics defined by

$$Y_{\ell}^m(\theta, \varphi) = \sqrt{\frac{(2\ell+1)(\ell-m)!}{4\pi(\ell+m)!}} P_{\ell}^m(\cos \theta) e^{-im\varphi}, \quad (4.15)$$

<sup>7</sup> <http://www.cosmos.esa.int/web/gaia/science-performance>



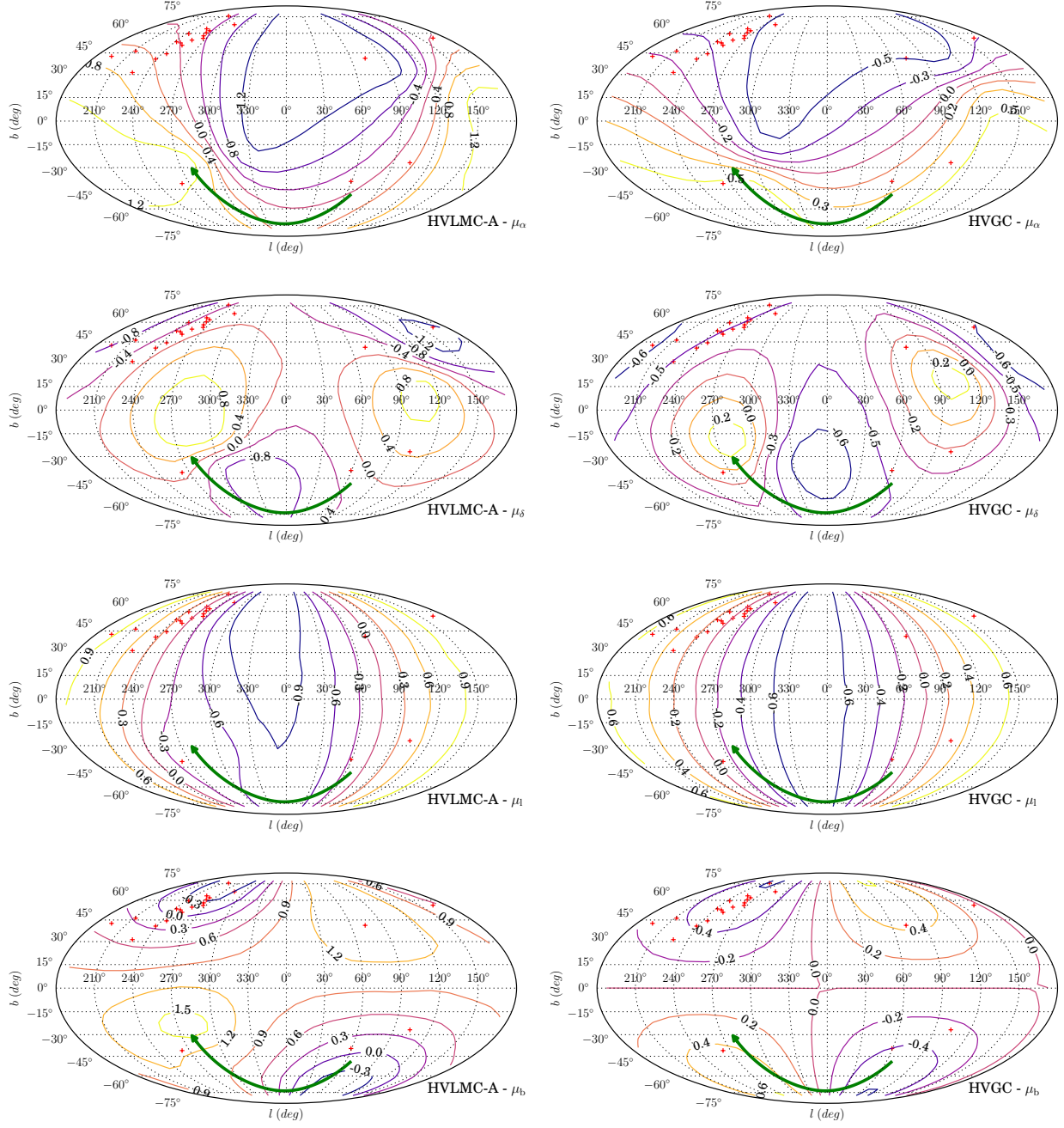


Figure 4.4: Mean equatorial proper motions ( $\mu_\alpha, \mu_\delta$ ) and Galactic proper motions ( $\mu_l, \mu_b$ ) for stars at distance  $50 < d < 120$  kpc.



where  $\theta$  and  $\varphi$  are the colatitudinal and longitudinal coordinates, we can expand any function  $f(\theta, \varphi)$  that is square-integrable on the unit sphere as

$$f(\theta, \varphi) = \sum_{\ell=0}^{\infty} \sum_{m=-\ell}^{\ell} f_{\ell}^m Y_{\ell}^m(\theta, \varphi). \quad (4.16)$$

Using the orthonormality property of our chosen definition of the spherical harmonics we can then write

$$f_{\ell}^m = \int_0^{2\pi} d\varphi \int_0^{\pi} d\theta \sin \theta f(\theta, \varphi) Y_{\ell}^{m*}(\theta, \varphi). \quad (4.17)$$

For our purposes, the function  $f$  is a sum of delta functions on the unit sphere at the locations  $(l_i, b_i)$  of each of the simulated HVSSs:

$$f(b, l) = \sum_i \delta(b - b_i, l - l_i). \quad (4.18)$$

Noting that  $b = \frac{\pi}{2} - \theta, l = \varphi$ , this sum of delta functions transforms Equation 4.17 into a sum over the HVSSs,

$$f_{\ell}^m = \sum_i \cos b_i Y_{\ell}^{m*} \left( \frac{\pi}{2} - b_i, l_i \right). \quad (4.19)$$

The angular power spectrum of  $f$  is then given by

$$S(\ell) = 4\pi \sum_{m=-\ell}^{\ell} |f_{\ell}^m|^2, \quad (4.20)$$

and are plotted for our populations of HVSSs in Figure 4.5.

Almost all of the power for the HVGC stars in this distance range is in the monopole, which we expect as the highest velocity stars are ejected along essentially straight lines from the GC, and at  $d > 50$  kpc the difference between the the observer being located at the sun or the GC is minimal. The HVLMC-A model has a peak in power in the dipole/quadrupole, with a long tail that is caused by the fast stars ejected ahead of the LMC and slow stars lagging behind. The distinguishing features between the two models are

1. a strong monopole in the HVGC model versus a strong dipole/quadrupole in the HVLMC-A model,
2. a large amount of power at high  $\ell$  in the HVLMC-A model.

The HVLMC-B model has a large section of the sky where there are no HVSSs, thus is not well-approximated by a dipole. The power is then spread across a large number of modes since no one mode is a good approximation. Our proposed spherical harmonic analysis

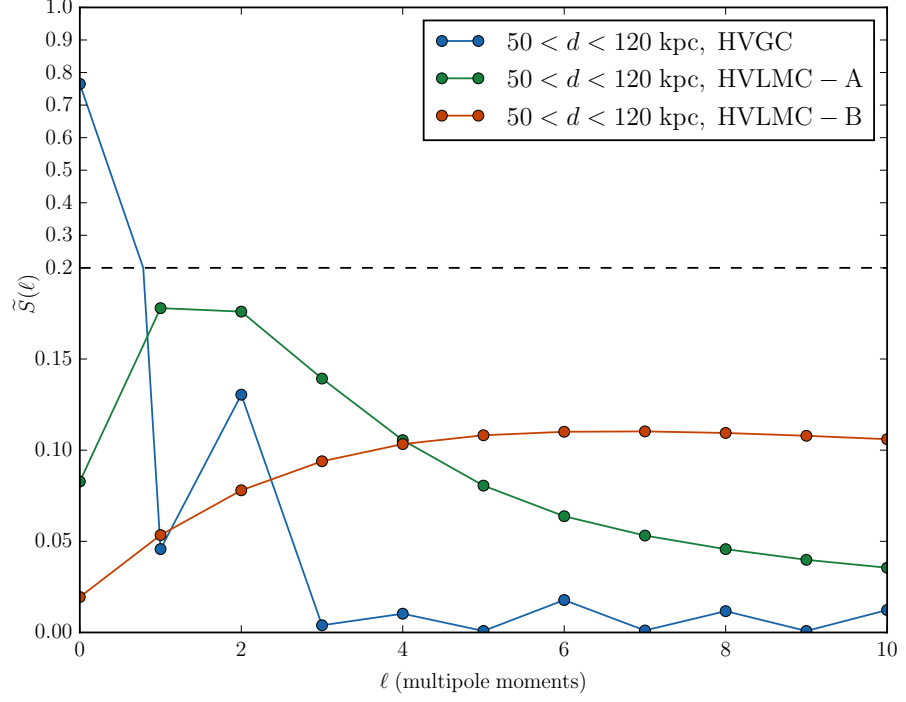


Figure 4.5: Spherical harmonics for the distance bin  $50 < d < 120$  kpc. The power spectrum  $S(\ell)$  has been normalised by the total power for each model to give  $\tilde{S}(\ell)$ , since we are primarily interested in the relative power in each mode between models.

is capable of distinguishing between hypervelocity populations in a quantitative way, and may become a vital tool when larger and more complete hypervelocity populations are discovered.

#### 4.1.3 Summary

I have established that hypervelocity stars (HVSs) created in the Large Magellanic Cloud (LMC) should be found across most of the sky, breaking our intuition that coincidence on the sky is a necessary requirement for association with a Local Group dwarf galaxy. The LMC, and perhaps other satellites of the MW, may well have imprinted distinctive signatures on the distribution of HVSs right across the sky. HVSs with an LMC origin could provide a natural solution to the clustering of HVSs in the direction of Leo and Sextans found by Brown et al. (2009). Uniquely, this area of the sky is densely populated by LMC origin models and is well-covered by current HVS surveys. If the HVSs are from the LMC, then the clump in Leo and Sextans is only the tip of a stream that stretches across much of the Southern hemisphere. The implication of an LMC origin for the known hypervelocity stars is that there must be hundreds or thousands more HVSs in the Southern skies. The recently released *Gaia* DR2 will allow for a direct test of this prediction and work to conduct that test is under-

way. If I fail to find a significant number of HVSs near the LMC, then the model will be falsified. A possible reason for failure is that the LMC does not host a significant black hole. However, my choice of the Hills mechanism as the production route was solely due to its proposed dominance in the MW (Brown, 2015).

The geometry and the dynamics of the ejections can be translated to the other production routes which will be active in the disc of the LMC, such as runaway companions of supernovae and three-body dynamical interactions. The orbital velocity of the LMC can provide  $321 \pm 24 \text{ km s}^{-1}$  (Kallivayalil et al., 2013), and thus stars from these two mechanisms could be ejected with sufficient speed to be HVSs. I investigate the possibility of runaway companions of supernovae escaping the LMC in the following section.

#### 4.2 RUNAWAY STARS FROM THE LMC

*Based on work originally published in Boubert, Erkal, et al. (2017).<sup>8</sup>*

The Large Magellanic Cloud (LMC) is star-forming ( $0.2 \text{ M}_{\odot} \text{ yr}^{-1}$ , Harris and Zaritsky, 2009) and so must contain massive binary stars; if there are massive binary stars, then the binary supernova runaway scenario described by Blaauw (1961) must be occurring. In this Section, I explore the consequences of the production of runaway stars in the LMC. As described in the introduction to this Chapter, it is plausible that runaway stars from the LMC could contribute a meaningful proportion of the Galactic HVSs. To avoid the confusion of referring to stars which escape the LMC as HVSs with respect to the LMC, I will use the terms LMC remainers/escapers to refer to stars which are bound/unbound to the LMC.

In Section 4.1.1, I describe the method I used to generate runaways and then follow their stellar evolution and orbit in an LMC-MW potential. There are many observables associated with runaway stars which escape the LMC and I discuss these in Section 4.2.2. My conclusion is that runaway stars escaping the LMC must contribute to the Milky Way hypervelocity star population, but that the stellar types

---

<sup>8</sup> I lead this project and was responsible for a majority of the implementation and analysis. N. Wyn Evans heavily influenced the direction of the work and was primarily responsible for the section investigating microlensing. Rob Izzard consulted on the use of his binary population synthesis code `BINARY_C` and made innumerable edits to the text. After I had generated initial conditions for the runaway stars, Denis Erkal was responsible for integrating their orbits in a MW-LMC potential. Denis Erkal acknowledged that research leading to these results received funding from the European Research Council under the European Union's Seventh Framework Programme (FP/2007- 2013)/ERC Grant Agreement no. 308024. Robert G. Izzard thanked the STFC for funding his Rutherford fellowship under grant ST/L003910/1 and Churchill College, Cambridge for his fellowship.

and distribution of these hypervelocity runaways are dependent on the assumed binary evolution model.

#### 4.2.1 LMC runaway ejection model

There are several ingredients required for a model of the ejection of runaway stars from the LMC. Assuming a metallicity and star formation history for the LMC, we evolve a synthetic population of single and binary stars and identify the runaway stars. The runaways are then initialised in the LMC disc and their subsequent orbits integrated through an evolving N-body potential of the LMC and the Galaxy. The outcomes of the stellar evolution of these runaway stars and their kinematics are then transformed into observable properties.

##### 4.2.1.1 Star Formation History of the LMC

Our method requires knowledge of the time dependent star-formation rate (SFR) and metallicity of the LMC. Harris and Zaritsky, 2009 found that the star formation rate of the LMC over the past 5 Gyr has been constant at  $0.2 \text{ M}_{\odot} \text{ yr}^{-1}$  within a factor of two. However, this period of constancy was preceded by a quiescent epoch between 5 and 12 Gyr ago. We thus assume a constant star formation rate over the entire 1.97 Gyr we simulate.

Piatti and Geisler, 2013 investigated the age-metallicity relation for the LMC using photometry across 21 fields. They derived an approximate scaling,

$$[\text{Fe}/\text{H}] = C + \left( \frac{\partial[\text{Fe}/\text{H}]}{\partial t} \right) t + \left( \frac{\partial[\text{Fe}/\text{H}]}{\partial \alpha} \right) \alpha, \quad (4.21)$$

with  $C = -0.55 \pm 0.02 \text{ dex}$ ,  $\partial[\text{Fe}/\text{H}]/\partial t = -0.047 \pm 0.003 \text{ dex Gyr}^{-1}$  and  $\partial[\text{Fe}/\text{H}]/\partial \alpha = -0.007 \pm 0.006 \text{ dex degree}^{-1}$ , where  $\alpha$  is the de-projected angular distance from the centre of the LMC. The dependency on the angular distance is argued by Piatti and Geisler, 2013 to be negligible, because under the assumption of an LMC distance of 50 kpc it corresponds to a gradient of  $-0.01 \pm 0.01 \text{ dex kpc}^{-1}$ . Thus, we assume a constant metallicity throughout the LMC star-forming regions. Over the 1.97 Gyr of our simulations even the temporal gradient is mostly negligible, producing a change in  $[\text{Fe}/\text{H}]$  of  $-0.093 \pm 0.006 \text{ dex}$ , therefore we form stars at a constant metallicity of  $Z = 0.008$ .

Most stars form in clusters (Lada & Lada, 2003), but this does not mean that star formation in the LMC is clumpy. The currently most prominent star-forming region in the LMC is 30 Doradus, also known as the Tarantula Nebula. De Marchi et al. (2011) found the star forma-

tion rate to be of the order  $200 \text{ M}_{\odot} \text{ Myr}^{-1}$  over at least the last 30 Myr for objects in the mass range  $0.5 - 4.0 \text{ M}_{\odot}$ . This is consistent with the more recent work of Cignoni et al. (2015) who, as part of the Hubble Tarantula Treasury Project, found that the star formation rate (SFR) in 30 Doradus has exceeded the average LMC SFR for the last 20 Myr. While 30 Doradus is one of the most active star formation regions in the Local Group, comparing its rate  $200 \text{ M}_{\odot} \text{ Myr}^{-1}$  to the rate for the entire LMC  $0.2 \text{ M}_{\odot} \text{ yr}^{-1}$  reveals that 30 Doradus makes up only 0.2% of the recent star formation activity of the LMC. We are thus well justified in forming stars directly proportional to the density of the assumed LMC disc potential and neglecting any inhomogeneities due to star forming clusters. We note that if this assumption does break down, it would reveal itself as a skewed density distribution of the ejected stars on the sky. This is because the location from which runaway stars are ejected is encoded in the velocity of those runaways through the contribution of the LMC disc rotation at the location of ejection.

#### 4.2.1.2 Binary Evolution

A standard prescription for the distribution of runaway star ejection velocities  $v_{\text{ej}}$  is an exponential law in the form  $\exp(-v_{\text{ej}}/v_s)$ , where  $v_s \approx 150 \text{ km s}^{-1}$  is a characteristic velocity which sets the width of the distribution (used by Bromley, Kenyon, Brown, and Geller 2009 and Kenyon et al. 2014 who matched to binary star simulations of Portegies Zwart 2000). However, this velocity distribution is simplistic because the highest ejection velocities require close binaries. Close binaries interact, making the ejection velocities of runaways a sensitive function of the binary initial conditions. Given that the magnitude and colour of stars can be thought of broadly as a proxy for their mass and that one of the most important parameters in binary interaction is the ratio of masses  $q$ , the colour and ejection velocity of a runaway star must be interdependent.

We form stars in bursts every 1 Myr. This is driven by a computational consideration to allow for a simple implementation of star formation in which we sample single and binary stars from analytic distributions until we have formed the required mass of stars. A SFR of  $0.2 \text{ M}_{\odot} \text{ yr}^{-1}$  means we are thus forming starbursts with a total mass of  $2 \times 10^5 \text{ M}_{\odot}$ . Only a small fraction of this mass is used to form runaways. Our model population consists of both single stars and binaries, but no higher-order multiples are considered. To generate the population, we sample in the primary mass and, for binaries, in the mass ratio and initial period. We sample systems one-by-one until we have formed the required total mass of stars in a timestep.

We first sample the primary mass of each system from the Kroupa, 2001 IMF,

$$N(M_1) \propto \begin{cases} M_1^{-0.3}, & \text{if } 0.01 < M_1/M_\odot < 0.08, \\ M_1^{-1.3}, & \text{if } 0.08 < M_1/M_\odot < 0.5, \\ M_1^{-2.3}, & \text{if } 0.5 < M_1/M_\odot < 80.0, \\ 0, & \text{otherwise.} \end{cases} \quad (4.22)$$

We calculate the binary fraction as a function of primary mass. Arenou, 2010 provides an analytic empirical fit to the observed binary fraction of various stellar masses,

$$F_{\text{bin}}(M_1) = 0.8388 \tanh(0.079 + 0.688M_1). \quad (4.23)$$

We validate this formula by comparing to the data of Raghavan et al. (2010), who provide the binary fraction as a function of spectral type. The binary fraction has only been well studied in the Milky Way and it is possible that the lower metallicity stars in the LMC could exhibit a different dependency on the primary mass. Our results turn out not to be overly dependent on the exact form assumed for the dependency of the binary fraction on the primary mass. This is because in our grid of evolved binary systems most runaways come from high-mass systems in which the binary fraction is close to unity in all prescriptions. We assume a flat mass-ratio distribution for each system over the range  $0.1 M_\odot/M_1 < q < 1$ . The period distribution is taken from Duquennoy and Mayor (1991) and is a normal distribution in  $\log_{10}(P/\text{days})$  with a mean of 4.8 and a standard deviation of 2.3, truncated to lie between -2.0 and 12.0. The observed period distribution of OB-type stars is closer to being log-uniform (Öpik, 1924; Sana et al., 2012), however the error incurred by this choice is subdominant to the uncertainty in the outcome of the common-envelope phase.

We model the properties of stars ejected from binary systems in which one component goes supernova using the `BINARY_C` population-synthesis framework<sup>9</sup>, described in more detail in Appendix A.2.

The initial conditions of the binaries sampled are compared to a binary grid and we identify all runaways which are formed by this pop-

<sup>9</sup> We use version 2.0pre22, SVN 4585.

ulation. We pre-compute this binary grid of 8,000,000 binaries with primary mass  $M_1$ , mass ratio  $q$  and period  $P$  having the ranges,

$$\begin{aligned} 8.0 &\leq M_1/M_\odot \leq 80.0, \\ 0.1 M_\odot/M_1 &\leq q \leq 1, \\ -2.0 &\leq \log_{10}(P/\text{days}) \leq 12.0. \end{aligned} \tag{4.24}$$

The distribution of runaway ejection velocity  $v_{\text{ej}}$  and  $B - V$  colour at the time of ejection from the progenitor binary is shown in Fig. 4.6. The distribution can be divided into two regions. The slower runaways with  $v_{\text{ej}} < 30 \text{ km s}^{-1}$  are the classical runaways in which the progenitor binary does not interact prior to the supernova. Conversely, runaways with  $v_{\text{ej}} > 30 \text{ km s}^{-1}$  are those whose progenitor binary did interact. When the primary evolves to the giant branch, it overflows its Roche-lobe onto the companion, provided the companion is sufficiently close (De Marco & Izzard, 2017). Mass transfer from a higher mass star to a lower mass star shrinks the binary orbit and increases the rate of mass transfer. This process is self-reinforcing and leads to common envelope evolution and further shrinkage of the binary. If the common envelope is dissipated before the stars merge, the binary is left in a close orbit. When the primary does go supernova shortly afterwards the natal kick on the remnant may be sufficient to unbind this close binary. In this case the rapid orbital velocity of the companion prior to the explosion results in a fast runaway. The impulse of the supernova ejecta impacting on the companion can contribute to the ejection velocity, but for almost all the runaways considered this was a negligible effect. The structure in this plot simply reflects the different channels that this behaviour can follow, together with the dependency on the mass and evolutionary state of the companion. The sideways chevron with  $v_{\text{ej}} = 400\text{--}800 \text{ km s}^{-1}$  and  $B - V \sim 0$  corresponds to cases in which the companion is so massive initially that the binary is close to being equal-mass. When a more massive star transfers mass to a lower-mass companion, the orbit shrinks. The converse is that when a less massive star transfers mass to a higher mass companion, the orbit grows. Thus, sustained mass transfer causes the companion to first approach and then retreat from the primary. The fastest runways are those in which the stars are closest prior to the common-envelope phase and thus the tip of the chevron represents systems in which the binary is equal-mass prior to the common-envelope.

The binary origin of the runaway stars which escape the LMC influences their subsequent evolution because prior to ejection more than 90% experience mass transfer from the primary. The transferred



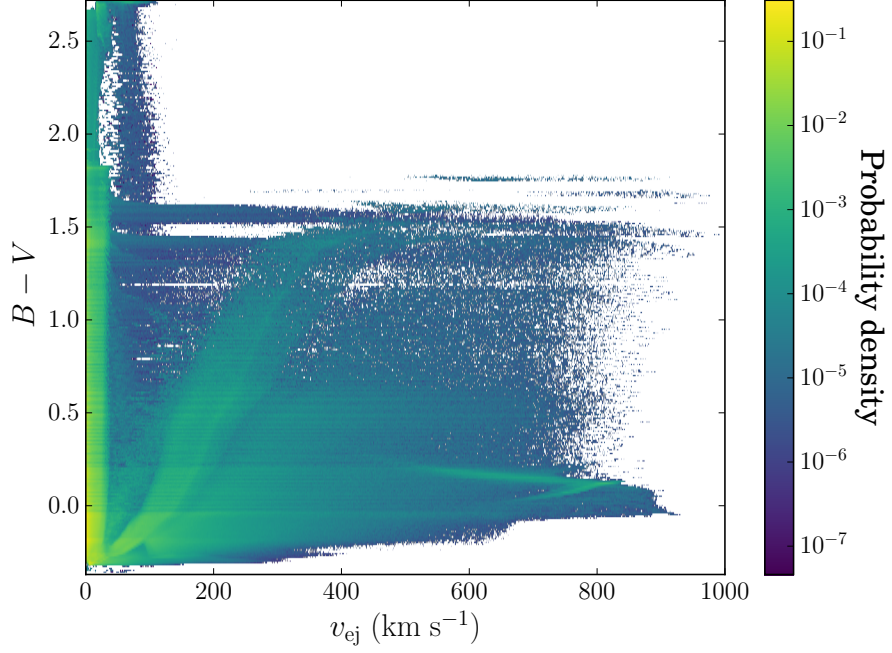


Figure 4.6: Probability density distribution in velocity-colour space at the time of ejection from the progenitor binary of the runaways produced by our binary evolution grid assuming LMC metallicity  $Z = 0.008$  and common-envelope ejection efficiency  $\alpha_{\text{CE}} = 1.0$ .

mass can be up to several  $M_{\odot}$  in extreme cases. Thus the runaways in our simulation would appear as blue stragglers in comparison to their progenitor population, i.e. would be bluer than a single star of equivalent age and initial mass.

A finite but non-negligible time elapses between the formation of a binary and the ejection of a runaway (Zapartas, de Mink, Izzard, et al., 2017), typically between 1–50 Myr. We bin the emission time of our runaways to the nearest 10 Myr because that is the frequency of snapshots in the N-body simulation. Once we have the time of ejection, we evolve each system which produces a runaway to the present day to ascertain the current observable properties. We record the stellar type, the mass, the Johnson-Cousins UBVRIJK magnitudes, the Sloan Digital Sky Survey ugriz magnitudes and the *Gaia* G, GBP, GRP and GRVS magnitudes. Because most of our binaries are B-type stars evolved on Gyr timescales, more than 70% of our runaways cease nuclear burning before the present day. If there is a supernova, we record the time that it occurred so we can later extract its location from the N-body model. We sample from a Maxwellian distribution of kick velocities for the neutron star and black hole remnants of Type II supernova progenitors (discussed in more detail in Section 4.2.2.5) and run a second N-body integration to compute the final location of these compact remnants.



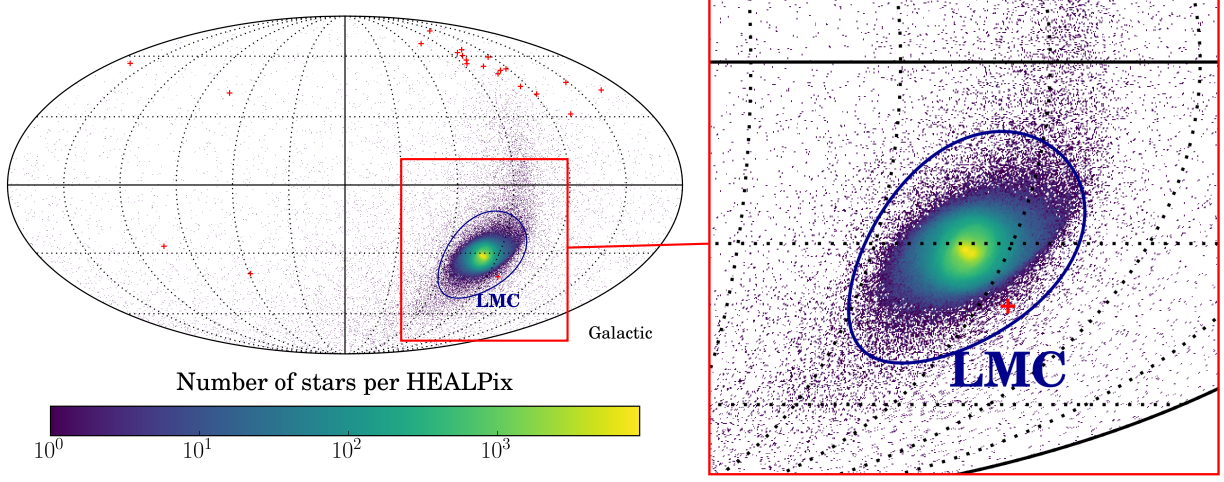


Figure 4.7: **Left:** All-sky present day distribution of runaways produced by our model of the LMC. The blue circle corresponds to the assumed tidal radius of the LMC of 20 kpc. The red crosses are the observed population of B-type HVSSs. **Right:** Zoom-in at higher resolution to illustrate the structure of our LMC disc. An animation of the evolution of this plot through each snapshot of our simulation is available at <https://youtu.be/eE-1JXBP1J8>.

#### 4.2.1.3 *N-body MW/LMC Model*

To model the runaways produced by the LMC, we use an N-body simulation of the LMC and the Milky Way galaxies. The LMC is modelled with two components (disc and dark matter halo) while the Galaxy is modelled with three components (disc, bulge and dark matter halo). The initial conditions are chosen such that the relative position of the Galaxy to the LMC matches their present day value within  $2\sigma$  (see Sec. 4 of Mackey et al., 2016 for more details on the simulations). Our simulations are evolved with the N-body part of GADGET-3. This is similar to GADGET-2 (Springel, 2005) but modified in two critical ways. First, we track the location of the centre of mass of the LMC by using a shrinking sphere algorithm on the inner 10 kpc at each timestep. As a consistency check, the potential minimum of LMC particles is computed every 49 Myr and we find no significant jumps in the LMC position. Second, the code is modified to release massless tracer particles with a given offset in position and velocity from the LMC. These are used to model the runaways. Before injecting any tracers, the simulation is evolved for 1.97 Gyr to the present and we record the LMC disc rotation curve, radial density profile, vertical density profile, orientation, position and velocity as a function of time. Fits to these properties, along with the extra velocity components of runaways (described below), are used to generate the initial conditions for the final simulation in which, as the LMC evolves in time, tracer particles are released representing the runaways.

The velocity vector of stars ejected from the LMC has three major components: the orbital velocity of the LMC, the rotation of the LMC disc and the ejection velocity of the runaway. The velocity is dominated in most cases by the  $321 \text{ km s}^{-1}$  orbital velocity of the LMC (Kallivayalil et al., 2013). We initialise our runaways by sampling in cylindrical coordinates  $(R, z, \phi)$  with a weighting factor  $\rho(R, z, \phi)$  which accounts for the density of the LMC disc at each location. From the N-body simulation, we find distributions of the tangential, radial and vertical velocities of the stars in the LMC disc at each point in the disc and at various times spaced at 10 Myr. We sample in these to determine the location and velocity of the progenitor binary at the moment of the supernova. We then add the ejection velocity by multiplying the ejection speed with a randomly-oriented unit vector. The position and velocity are then converted into the rest frame of the Galaxy.

Runaways are initialised in the simulation as massless particles every 10 Myr as described in Section 4.2.1.2 and their orbits integrated to the present day. It is important to note that we sample in a large number of parameters and the number of generated runaways is relatively small. Thus, the extreme outliers of our population are subject to small-number statistical uncertainties.

#### 4.2.1.4 Observables

We calculate heliocentric observables for each of our runaways by assuming that the Sun is at  $R_{\odot} = 8.5 \text{ kpc}$  and the Milky Way's disc rotation speed  $v_{\text{disc}} = 240 \text{ km s}^{-1}$  with a solar peculiar velocity of  $(U_{\odot}, V_{\odot}, W_{\odot}) = (11.1, 12.24, 7.25) \text{ km s}^{-1}$  (Schönrich et al., 2010). We define those stars whose present location is 20 kpc from the LMC to have escaped the LMC. This is similar to the observed  $22.3 \pm 5.2 \text{ kpc}$  tidal radius of the LMC (van der Marel & Kallivayalil, 2014). A subset of the LMC escapers will also be hypervelocity with respect to the Milky Way. We define stars which are Galactic HVs to be those with a Galactic rest frame velocity greater than

$$v_{\text{esc}}(x) = (624.9 - 9.41543x + 0.134835346x^2 - 1.292640 \times 10^{-3}x^3 + 6.5435315 \times 10^{-6}x^4 - 1.3312833 \times 10^{-8}x^5) \text{ km s}^{-1} \quad (4.25)$$

where  $x = r/1 \text{ kpc}$  and  $r$  is the spherical Galactocentric radius. We take this escape velocity curve from Brown et al., 2014 who calculated it for a three-component potential which approximates sufficiently well our live Milky Way Galaxy. We then take the magnitudes from Section 4.2.1.2, redden them using the Schlegel et al., 1998 dust

map and correct them to heliocentric apparent magnitudes. We use the present day Cartesian coordinates of the stars to calculate the heliocentric kinematic observables of each star including equatorial coordinates, distance, line-of-sight velocity and proper motions.

#### 4.2.2 *Properties of LMC Runaways*

The natural consequence of binary evolution in the LMC is a population of runaway stars with extreme properties. In our simulation, tens of thousands of stars escape the LMC with thousands surviving as main-sequence stars at the present day. Their spatial properties and kinematics are discussed in Section 4.2.2.1. If the LMC is as massive as recent work suggests (e.g. Jethwa et al., 2016; Kallivayalil et al., 2013; Peñarrubia, Gómez, Besla, Erkal, & Ma, 2015) and as is assumed in our orbital integration, then the LMC is only marginally bound to the Galaxy and is on its first pericentre passage. A significant fraction of the stars which are LMC escapers are also unbound from the Galaxy, and so are HVSs. We discuss this possibility and compare to the known population of HVSs in Section 4.2.2.2. Existing observations of a number of populations of stars in the outskirts of the LMC lend indirect evidence to our hypothesis, as outlined in Section 4.2.2.3. The prospects for detecting an escaping LMC runaway population are discussed in Section 4.2.2.4. Lastly, a substantial fraction of our runaway stars go supernova resulting in a host of more exotic observables which we consider in Section 4.2.2.5. These include Type II supernovae far out in the LMC halo, pulsars tens of kiloparsecs from the nearest site of recent star formation and microlensing by compact remnants.

##### 4.2.2.1 *Spatial Distribution and Kinematics*

The most notable feature is the extreme anisotropy of the LMC runaway distribution on the sky, which is aligned along the orbit of the LMC (Fig. 4.7). The stars we see at a particular point on the sky are a combination of stars which were ejected slowly a long time ago and stars which were ejected rapidly but more recently. The orbit of the LMC varies in heliocentric distance and so a magnitude-limited survey will miss both low-mass recent ejections and high-mass, high-velocity runaways that have travelled far enough to be beyond the detection limit. We find a range of stellar types for both LMC escapees and Milky Way HVSs (Table 4.1). At the present day, most of our runaways are remnants which reflects the skew in the runaway mass distribution introduced by the preference for high mass primaries to host high mass companions. The lower HVS fraction of

white dwarfs is because these are the remnants of the more massive of our runaways and higher mass stars are, to first order, ejected at lower velocities. This can be shown by considering the simple case of a circular binary where, if the mass of the primary and the separation are held constant, the orbital velocity of the secondary  $v_2$  only exhibits a dependency on the total mass of the system  $M$  through  $v_2 \propto M^{-1/2}$ . Increasing the mass of the secondary thus decreases its orbital velocity, which in most cases is the dominant contributor to the ejection velocity. The lack of helium white dwarfs is to be expected. Helium white dwarfs can only be formed if the ignition of helium can be avoided, and therefore they can only be produced from the evolution of low-mass stars over a Hubble time or if a more massive star has its hydrogen envelope stripped by a companion (e.g. Althaus & Benvenuto, 1997). Because we specifically consider the scenario in which the companion escapes after the explosion of the primary, the companion does not have a chance to evolve to the giant branch and then experience mass transfer. Conversely, if the companion remains bound to the primary post-SN, it could then experience mass-loss as it evolves. Observed counterparts of this channel are the well known pulsar – helium white dwarf binaries (e.g. Backer, 1998). The observed single, low-mass, helium white dwarfs are instead thought to be the remnants of giant-branch donor stars whose envelope was stripped when their companion exploded as a SN Ia (Justham et al., 2009).

The orbit of the LMC is close to being polar and thus the Galactic latitude of an LMC runaway star approximately determines its kinematics. In Fig. 4.8, we plot the kinematics of the predicted LMC runaway population against Galactic latitude. We also plot the known HVs and several observed populations of OB-type stars near the LMC which are discussed further in Sections 4.2.2.2 and 4.2.2.3, respectively.

A convenient benefit of simulating runaway stars from a galaxy is that it enables the calculation of the escape velocity curve, which at each distance from the centre of a galaxy gives the minimum speed required for a star at that location to be unbound. We take the initial velocities and radii in the frame of the LMC for those stars which we know subsequently escape to beyond 20 kpc from the LMC. Because these occur sufficiently frequently at all radii within the LMC, we estimate the escape velocity by finding the curve that bounds these stars from below in the  $r_{\text{init}} - v_{\text{init}}$  plane. This is complicated by the presence of stars which escape the LMC through the Lagrange points, so in practice we bin the stars radially and find the first percentile in

Type	LMC remainers	LMC escapers	MW HVSS
LM-MS	86577	1227	77.1%
MS	245486	7485	65.2%
HG	1112	31	64.5%
GB	1753	79	76.0%
CHeB	23533	487	66.7%
EAGB	678	12	83.3%
TPAGB	320	8	75.0%
HeMS	15	0	—
HeHG	2	0	—
HeGB	0	0	—
HeWD	0	0	—
COWD	510338	5233	57.0%
ONeWD	202206	436	43.3%
NS	146323	398527	82.9%
BH	162646	445562	83.0%
Total	1380989	858997	82.6%

Table 4.1: Summary of stellar types at the present day by number of stars which either remain bound to or escape the Large Magellanic Cloud, and the fraction of the latter which are hypervelocity stars with respect to the Milky Way. **Key:** LM-MS - *Low Mass Main Sequence*, MS - *Main Sequence*, HG - *Hertzsprung Gap*, GB - *Giant Branch*, CHeB - *Core Helium Burning*, EAGB - *Early Asymptotic Giant Branch*, TPAGB - *Thermally Pulsating Asymptotic Giant Branch*, HeMS - *naked Helium Main Sequence*, HeHG - *naked Helium Hertzsprung Gap*, HeGB - *naked Helium Giant Branch*, HeWD - *Helium White Dwarf*, COWD - *Carbon-Oxygen White Dwarf*, ONeWD - *Oxygen-Neon White Dwarf*, NS - *Neutron Star*, BH - *Black Hole*.

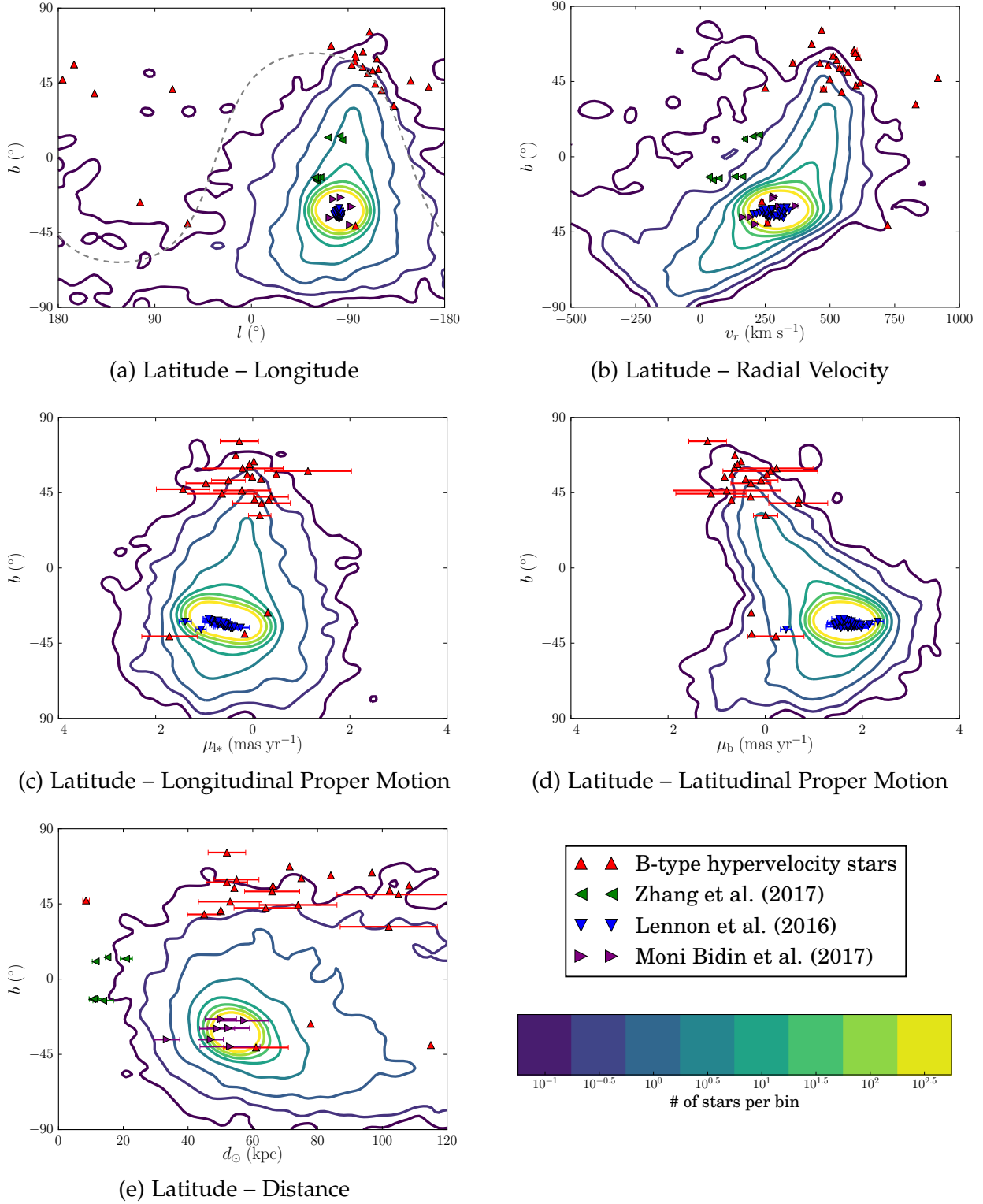


Figure 4.8: Predictions of the kinematics of our LMC runaway model plotted as logarithmically-spaced contours of the number of stars in each bin. The bins are defined by a  $100 \times 100$  grid over the range of each plot. Also shown are observations of OB-stars near the LMC in the literature: the known B-type hypervelocity stars, stars which may have formed from the gas in the leading arm (Zhang et al., 2017), candidate runaways in the LMC (Lennon, van der Marel, Lerate, O’Mullane, & Sahlmann, 2016) and young stars in the outskirts of the LMC (Moni Bidin et al., 2017). The distances for the stars from Zhang et al. (2017) and Moni Bidin et al. (2017) are calculated from distance moduli, proper motions were only available for the Lennon, van der Marel, Lerate, O’Mullane, and Sahlmann (2016) stars and a subset of the hypervelocity stars, and the Lennon, van der Marel, Lerate, O’Mullane, and Sahlmann (2016) stars only have distances by association with the LMC. The grey dashed line marks the celestial equator and SDSS photometry only covers the region above this line.

velocity in each bin after removing outliers with  $v_{\text{esc}} \leq 90 \text{ km s}^{-1}$ . We fit a fifth order polynomial through these values and obtain,

$$v_{\text{esc}}(x) = (252.1 - 26.74734x + 2.44534040x^2 - 0.164199176x^3 + 6.24490163 \times 10^{-3}x^4 - 9.04817931 \times 10^{-5}x^5) \text{ km s}^{-1}, \quad (4.26)$$

where  $x = r/1 \text{ kpc}$  and  $r$  is the spherical radius from the LMC centre, which we plot in Fig. 4.9. Note that because we have a lower initial density of stars at large radii, the escape velocity curve is less accurate at these distances and we would not advocate using it outside 15 kpc. Eqn. 4.26 is the escape velocity curve of the LMC in isolation. The LMC has been truncated by the Milky Way at the tidal radius by the present day and thus the escape velocity currently is lower than over the previous 1.97 Gyr.

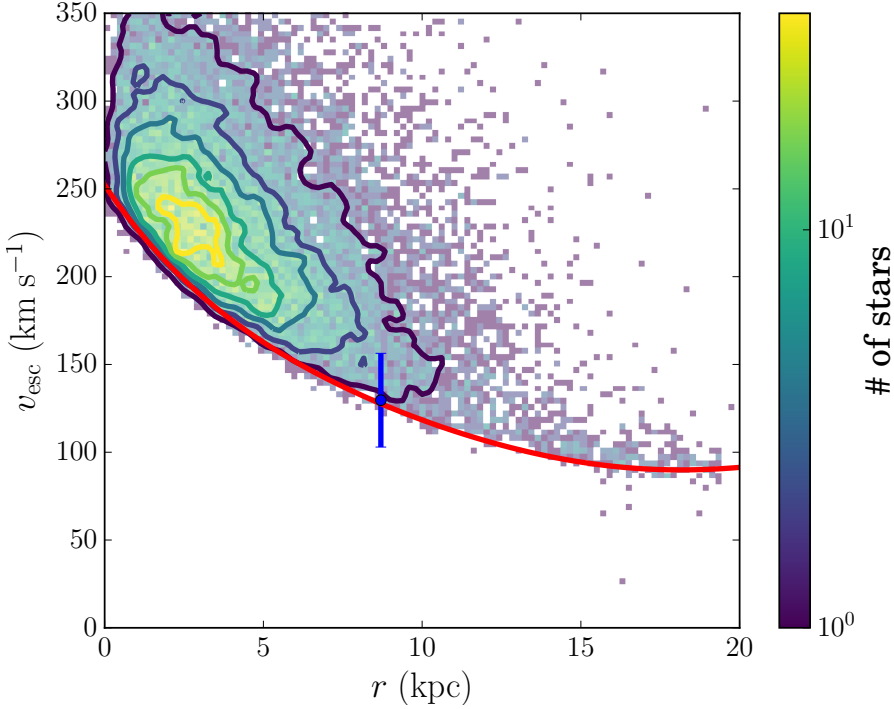


Figure 4.9: The escape velocity curve of our modelled LMC potential (see Section 4.2.2.1). The contours illustrate the distribution of our LMC escapers, the red line is our estimated escape velocity curve and the blue point is the mass constraint for the LMC  $M(8.7 \text{ kpc}) = (1.7 \pm 0.7) \times 10^{10} M_{\odot}$  (van der Marel & Kallivayalil, 2014) converted to escape velocity with  $v_{\text{esc}} = \sqrt{2GM/r}$ , where  $G$  is the gravitational constant and  $r$  is the spherical radius.

#### 4.2.2.2 Hypervelocity Stars (HVSs)

An LMC origin had previously been explored for the one HVS in the southern hemisphere, HE 0437-5439, which was discovered by Edel-



mann et al., 2005). The flight time is longer than the main-sequence lifetime of the star and hence either it is a blue straggler, and was ejected as a binary from the Galactic Centre, or it has its origin in the LMC. The mechanism that ejected HE 0437-5439 from the LMC has been suggested to be either interactions with a black hole more massive than  $10^3 M_{\odot}$  (Gualandris & Portegies Zwart, 2007) or dynamical ejection from a cluster (Przybilla et al., 2008).

In this Section, we consider the population of HVs produced by the binary supernova runaway mechanism operating in the LMC, which Table 4.1 demonstrates is substantial. However, we find that our model LMC runaway HVs which make it into the footprint of SDSS are inconsistent with the observed HVs, being in the mass range  $1.6 M_{\odot} < M < 3.0 M_{\odot}$  rather than the  $M > 3.0 M_{\odot}$  of the B-type HVs. The reason for this is clear from Fig. 4.6. Those stars that make it into the footprint of SDSS have  $v_{ej} \gtrsim 200 \text{ km s}^{-1}$  and there is a distinctly low probability density of runaways at these speeds with  $B - V < 0$ . There are three possibilities that either dismiss or resolve this discrepancy:

1. The observed B-type HVs do originate in the Milky Way galaxy from one of the processes discussed above and the anisotropy indicates a symmetry-breaking in these processes. One example would be if the binary stars which interact with Sgr A\* are scattered from a disc in the Galactic nucleus rather than coming from a spherically-symmetric population.
2. The observed B-type HVs originate in the LMC, but are ejected by a process which has a higher typical ejection velocity than runaways – either the Hills mechanism or dynamical ejection from a cluster.
3. Our prescription for the common-envelope evolution of binary stars is inaccurate. We follow Hurley, Tout, and Pols (2002) and set  $\alpha_{CE} = 1.0$ , where  $\alpha_{CE}$  is the efficiency with which the orbital energy of the binary can be used to remove the common envelope, but this parameter is not well-constrained observationally. If we instead set  $\alpha_{CE} = 0.1$ , we find a high-velocity distribution where the HVs would be predominantly of A and B type. There is additional uncertainty in the fraction  $\lambda_{CE}$  of the binding energy of the envelope which is required to eject the envelope. We use a fit to tabulated numerical results which is implemented in `BINARY_C` (Dewi & Tauris, 2000; Tauris & Dewi, 2001). However, the tabulated  $\lambda_{CE}$  were calculated at solar metallicity. The parameters  $\alpha_{CE}$  and  $\lambda_{CE}$  appear together in the  $\alpha$ -prescription and so it is the combination  $\alpha_{CE}\lambda_{CE}$  which



sets the post-common-envelope separation. An error in either parameter could explain the possible discrepancy between the observed HVSs and our LMC runaway model.

We can evaluate whether the observed HVSs originate in the LMC, whilst being agnostic about the mechanism, by considering the runaway stars in our model to be tracer particles of the kinematic distribution of stars ejected from the LMC. When discussing the known HVSs we specifically refer to the candidates discovered by the HVS surveys (Brown et al., 2009, 2012, 2014; Brown et al., 2005, 2006a, 2006b; Brown et al., 2007a, 2007b) in addition to HE 0437-5439 (Edelmann et al., 2005) and US 708 (Hirsch et al., 2005), with recent updated proper motions from the Hubble Space Telescope (Brown et al., 2015). Fig. 4.8 demonstrates that the 6D kinematics of the known HVSs are consistent with the expectations for an LMC origin. The agreement in proper motions and distance is not surprising. The known HVSs were found in observation campaigns (Brown et al., 2009; Brown et al., 2006a, 2006b) that selected for distant B-type stars in the footprint of SDSS, and thus most have  $\delta > 0^\circ$  and are at distances  $50 < d < 120$  kpc. At these distances, the proper motion projects to nearly zero independent of whether the star originates in the Galaxy or LMC. It is surprising, however, that an LMC origin can reproduce the clustering in the  $b-l$  and  $b-v_r$  plots, neither of which can be explained by a spherically-symmetric ejection from the Galactic Centre by the Hills mechanism. In Fig. 4.8 (a), we include a dashed line equivalent to  $\delta = 0^\circ$  which corresponds to the lower edge of the region of the sky which has been thoroughly searched for HVSs. The current searches for HVSs using SDSS are in the wrong part of the sky for the majority of an LMC escaping distribution. The other populations of OB stars shown in Fig. 4.8 are from comparatively shallow surveys down to magnitudes around  $V = 16$  mag, while the known HVSs have SDSS magnitudes in the range  $17.5 < g_0 < 21.0$ . If the observed HVS population does originate in the LMC, then the final *Gaia* catalogue, complete down to  $G \approx 20.7$  mag, could contain hundreds or even thousands of stars which have escaped the LMC, the majority of which would be HVSs.

#### 4.2.2.3 Observations of Outer LMC Populations

Zhang et al., 2017 reported high-resolution spectra of eight previously claimed candidates (Casetti-Dinescu et al., 2014; Casetti-Dinescu, Vieira, Girard, & van Altena, 2012) for OB-type stars which have formed from the gas in the Leading Arm of the Magellanic System. They found that for five of these stars their chemistry was consistent with

an LMC origin and that their kinematics appeared to rule out membership of the Milky Way disc. Zhang et al., 2017 concluded that these stars therefore must have formed from the gas in the leading arm. One property of these stars is however quite puzzling: none display a clear signal of radial velocity variation from a binary companion. Zhang et al., 2017 factor in the detection efficiency of their observations and calculate that the probability of their null detection is 14% (8.7%) if the underlying binary fraction is 50% (60%). While this is not statistically significant evidence for an unusually low binary fraction, the null detection of companions is entirely consistent with our prediction of B-type runaway stars from the LMC. Casetti-Dinescu et al. (2014) rejected a Galactic runaway origin for these five B-type stars arguing that their radial velocity dispersion of  $33 \text{ km s}^{-1}$  is too low compared to the  $\sim 130 \text{ km s}^{-1}$  (Bromley et al., 2009) expected for Milky Way runaways, and that an ejection mechanism would need to be “directionally coherent, which is highly unlikely”. However, Casetti-Dinescu et al. (2014) do not consider a runaway origin from the LMC which naturally explains the low velocity dispersion. There is one O6V star, labelled by Zhang et al. (2017) as CD14-Ao8, which Casetti-Dinescu et al. (2014) do consider as originating in the LMC, but they argue it must have formed in-situ from the gas of the Leading Arm since its lifetime is too short (1–2 Myr) for it to have travelled from the LMC at any less than about  $10^4 \text{ km s}^{-1}$ . However, Zhang et al. (2017) argue that CD14-Ao8 is more likely to be a helium-deficient sdO star with  $\log N_{\text{He}}/N_{\text{H}} = -1.69 \pm 0.24$ . Martin, Jeffery, N., and Woolf (2017) discuss the likely production mechanism of subdwarf stars as a function of their helium abundance. Helium-deficient subdwarfs are thought to be produced by close interactions in a binary and have ages between 0.2 and 10 Gyr, allowing CD14-Ao8 to have originated anywhere in the MW or the LMC. Martin et al. (2017) mention the possibility that intermediate-helium sdO/sdB stars are the polluted, runaway companions of SN Ia progenitors, which has previously been used to explain the helium-rich HVS US708 (Geier et al., 2013; Justham et al., 2009). This suggests an intriguing alternative origin for CD14-Ao8 as a runaway from a Type Ia SNe in the LMC, which may be required if more precise data constrain the helium abundance to be in the range  $5\% < n_{\text{He}} < 80\%$  considered by Martin et al. (2017) to be intermediate-helium. In Fig. 4.8, we show the kinematics of the Zhang et al. (2017) sample against the LMC runaway predictions. These stars are consistent with an LMC runaway origin. Their position near the edge of the LMC runaway distribution in radial velocity and distance is a natural consequence of the shallowness of the survey, which only probes the nearest edge of the

distribution in regions where we would predict relatively low radial velocities.

Lennon et al., 2016 combined the precise proper motions of the *Tycho-Gaia* Astrometric Solution (TGAS) with prior radial velocity surveys to search for runaway stars amongst the 31 brightest stars in the LMC. They found that only two of these 31 candidates are outliers in velocity, while the remaining stars are consistent with a rotating disc. In fact, the majority of our runaways would be classed as walkaways, with 65% of runaways having ejection velocities less than  $10 \text{ km s}^{-1}$ , and hence indistinguishable from the disc population. There is also the statistical argument that most massive stars are in binaries, so most of these stars are either runaways or have a companion. Of the two outliers, Sk-67 2 is suggested as a candidate hypervelocity star based on a peculiar velocity of  $359 \text{ km s}^{-1}$  and R 71 could be the evolved product of a slow runaway binary. Note that R 71 is a Luminous Blue Variable (LBV). It was hypothesised by Smith and Tombleson, 2015 that the higher spatial dispersion of LBVs versus O-type and Wolf-Rayet stars in the LMC indicates either that LBVs are merged stars or they are runaway stars that were rejuvenated by mass transfer before being ejected. This contradicts the standard view of LBVs as a necessary transition state of massive stars between core hydrogen burning and the Wolf-Rayet phase. We seek analogues of the runaway candidates of Lennon et al., 2016 in our simulation, assuming they lie at a distance of  $50.1 \pm 3.0 \text{ kpc}$ , and find that most are consistent with a runaway origin (Fig. 4.8). We are hindered because we compare the brightest stars between observations and our model LMC runaway population. Small number statistics dominate and it is difficult to quantify whether any particular star is inconsistent with our model. The hypervelocity candidate Sk-67 2 is the clear outlier from the other candidates of Lennon et al. (2016) in Fig. 4.8 (d) where we plot  $b - \mu_b$ . It is possible that the Hills mechanism or dynamical ejection is required to explain this star. The other outlier in Fig. 4.8 (c) is Sk-71 42 which Lennon et al. (2016) note as having a large `astrometric_excess_noise` parameter in TGAS and stated that further data would be necessary before they could speculate on the nature of the star.

It is interesting to note the similarities between Sk-67 2 and a previous discovery by Evans and Massey (2015) of a  $12\text{--}15 \text{ M}_{\odot}$  runaway red supergiant J004330.06+405258.4 at a projected distance of 4.6 kpc from the plane of M31's disc. Evans and Massey (2015) mention that J004330.06+405258.4 may be a high-mass analogue of the MW HVSs since it is likely unbound from M31. Both stars are supergiants and both are discrepant with their host galaxies' kinematics

by  $\sim 300 \text{ km s}^{-1}$ . Evans and Massey (2015) mention four previous discoveries of yellow and red supergiants in the LMC, SMC and M33 which have peculiar velocities around  $150 \text{ km s}^{-1}$ . These massive runaways are difficult to reproduce in our current model, however a modification of the common-envelope prescription to produce more early-type stars would likely resolve this problem (Sec. 4.2.2.2). These stars are some of the brightest stars visible in the Local Group and so are obvious candidates for spectroscopic follow-up when they are found far from central star formation regions. It is possible that these stars are only the first tracers of a high-velocity runaway population which exists throughout the Local Group.

*Subsequent work by Casetti-Dinescu et al. (2018) confirmed my prediction by showing with Gaia DR2 proper motions that two of the six stars are runaways from the centre.*

Moni Bidin et al. (2017) searched for star formation on the periphery of the LMC disc between  $6^\circ$  and  $30^\circ$  from the centre. They found six recently formed stars well away from the central star formation in the LMC, with  $V < 16$ , separation  $7^\circ$ – $13^\circ$  and ages between 10 and 50 Myr. They argued that if their tangential velocity is only as discrepant from the LMC disc tangential velocity as their radial velocity component, these stars cannot have travelled to their current location within their lifetimes. However, in our simulation, analogues of these stars do exist with similar ages because the assumption of equally discrepant velocity components does not hold. The existence of a ring-like structure is a natural consequence of sampling a small number of stars from a population which rapidly decreases in number with radius and is truncated at  $6^\circ$  from the LMC.

#### 4.2.2.4 Prospects with Gaia

The *Gaia* satellite is predicted to be complete down to  $G \approx 20.7$ , hence will be the first survey covering the Southern hemisphere which is sensitive to the population of runaway stars which may have escaped the LMC. We compare the predicted observable properties of the LMC runaways to the expected  $\pm 1\sigma$  end-of-mission radial velocity and proper motions errors for *Gaia* in Fig. 4.10. The proper motion errors are the predicted sky-average errors for an unreddened G2V star<sup>10</sup>. The radial velocity errors are calculated for an unreddened GoV star using a standard performance model<sup>11</sup> which is valid down to  $G_{\text{RVS}} \sim 16$ , where we used the colour-colour relations calculated by Jordi et al. (2010) to convert  $G$  to Johnson  $V$  and  $G_{\text{RVS}}$ . The mean mass of the LMC escapers is  $1.35 M_\odot$  which justifies the choice of GoV/G2V to illustrate the errors, however there are a range of LMC escaper masses. More (less) massive stars will have larger (smaller) errors. The radial velocities measured by *Gaia* are unlikely to have

<sup>10</sup> <https://www.cosmos.esa.int/web/gaia/sp-table1>

<sup>11</sup> <https://www.cosmos.esa.int/web/gaia/science-performance>

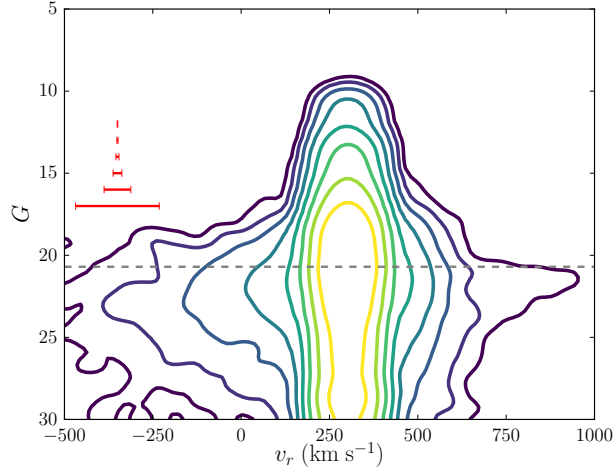
the necessary precision to detect the population of escaping LMC runaways (Fig. 4.10 (a)), with the possible exception of the bright  $G = 15\text{--}16$  and fast  $v_r \approx 500 \text{ km s}^{-1}$  stars. Figures 4.10 (b) and (c) show that the  $\mu\text{as}$  astrometric precision of *Gaia* should result in the detection of high velocity runaways purely by their proper motion. The uncertainties on the parallax measurements by *Gaia* rule out the possibility of a significant detection of parallax in LMC runaway stars. Distances would need to be obtained photometrically to validate any candidates. The LMC escapers will also be distinct from the LMC in their position on the sky and thus we conclude that *Gaia* will observe such a population if it exists. A change in the common envelope prescription to produce more early-type stars (Sec. 4.2.2.2) would not change this conclusion because the small increase in the astrometric uncertainties at fixed  $G$  is more than cancelled by the shift of the distribution to brighter  $G$  magnitudes.

#### 4.2.2.5 *Exotica: Runaway Supernovae, Pulsars and Microlensing*

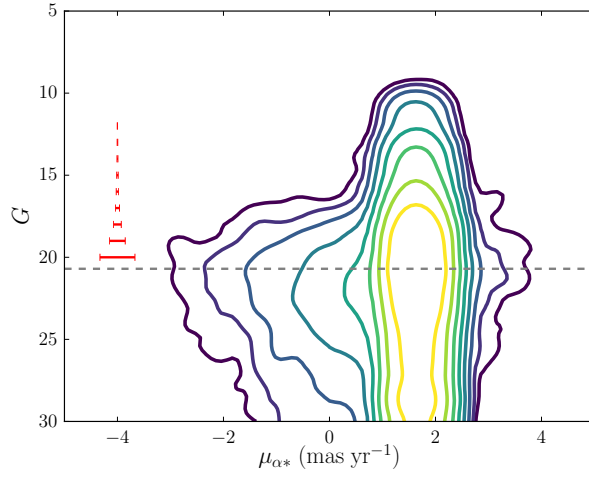
##### *Runaway Supernovae and Pulsars*

In our model, a substantial fraction of runaways (51.0%) have experienced a core-collapse supernova before the present day, at a rate of  $5.9 \times 10^{-4} \text{ yr}^{-1}$ , leaving behind a compact neutron star or black hole remnant. The compact remnants experience a kick which we prescribe to be Maxwellian-distributed with a dispersion of  $190 \text{ km s}^{-1}$  (Hansen & Phinney, 1997). However, the fact that pulsars exist in globular clusters suggests that a fraction of neutron stars could receive almost no kick at birth (Podsiadlowski, Pfahl, & Rappaport, 2005). Several authors have found that a bimodal Gaussian is required to describe the observed pulsar velocity distribution (Cordes & Chernoff, 1998; Fryer, Burrows, & Benz, 1998), but these studies differ on the required properties of such a distribution. Given that the runaway velocity distribution is itself uncertain, we feel justified in preferring the simplicity of a unimodal distribution in this study. The SN kick, in most cases, dominates the velocity of the remnant. The majority of these remnants subsequently escape the LMC and most of those are unbound from the Galaxy (Fig. 4.11). Despite the high kick dispersion, the distribution on the sky preserves the signal of their LMC origin and thus, if they are observable, their origin is unambiguous. There are few accessible observables associated with single, compact remnants at tens of kiloparsecs. However, for the first few tens of millions of years, neutron stars manifest themselves as pulsars.

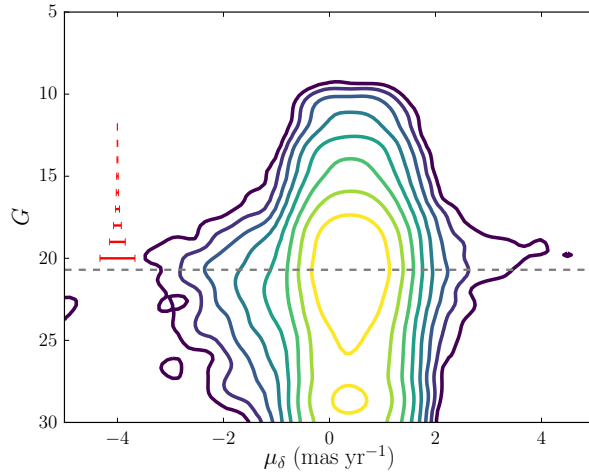
The Australia Telescope National Facility Pulsar Catalogue (Manchester, Hobbs, Teoh, & Hobbs, 2005, available at <http://www.atnf.csiro.au/research/pulsar/psrcat>) reveals there are 29 pulsars currently as-



(a) Apparent Magnitude – Radial Velocity



(b) Apparent Magnitude – Longitudinal Proper Motion



(c) Apparent Magnitude – Latitudinal Proper Motion

Figure 4.10: Predicted properties of LMC runaways which would be observed by *Gaia* plotted as logarithmically-spaced contours of the number of stars in each bin (see Fig. 4.8 for the colourbar). The kinematics are heliocentric and  $G$  is the unreddened apparent magnitude. The grey dashed line indicates the  $G \approx 20.7$  completeness limit for *Gaia* and the red error bars represent the  $\pm 1\sigma$  predicted end-of-mission radial velocity and proper motion errors as a function of  $G$  (described in detail in Sec. 4.2.2.4).



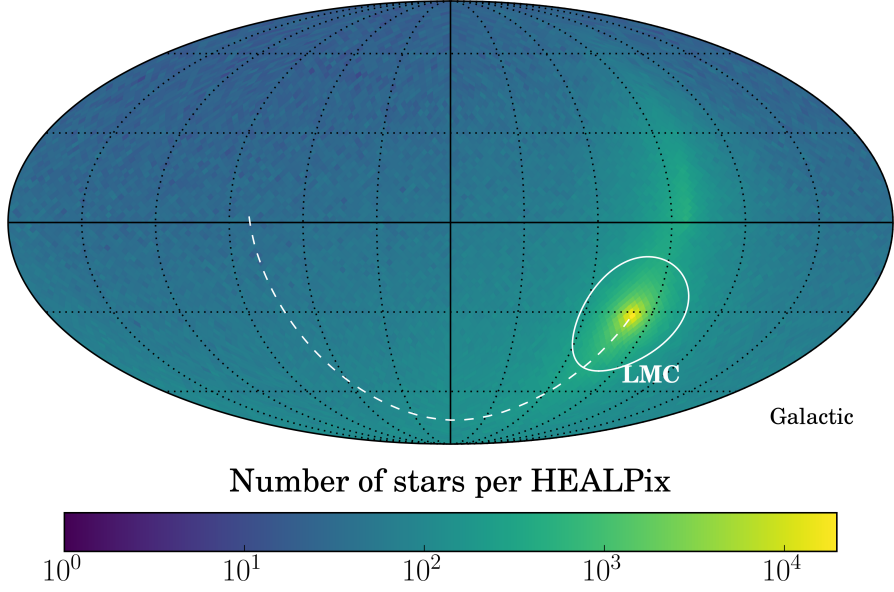


Figure 4.11: All sky distribution of remnants produced by runaway supernovae in our models (Sec. 4.2.2.5). The white solid line indicates the 20 kpc tidal radius of the LMC and the white dashed line is the orbit of the LMC over the last 1.97 Gyr in the frame where the Sun is fixed at  $(x, y, z) = (-R_{\odot}, 0, 0)$ .

sociated with the LMC or SMC. We cannot accurately estimate the distance to these pulsars except through their plausible association with the Magellanic Clouds. For pulsars too far away for parallax measurements, the primary distance estimate is found by relating the dispersion measure to the integrated electron column density along the line of sight. This method is only reliable out to distances of  $\sim 20$  kpc. For example, the most recent electron density maps made by Yao, Manchester, and Wang, 2017 return a maximum distance of 25 kpc to any pulsar with an anomalously high dispersion measure. There are 75 pulsars in our simulation closer than this upper limit. However, the completeness of the existing pulsar surveys is patchy at these distances, and all but one of the pulsars estimated to lie beyond 20 kpc are in the direction of the well-studied Galactic bulge. The wide field of view and high sensitivity of the Square Kilometre Array will enable the discovery of 20,000 new pulsars (Smits et al., 2009). This is an order of magnitude increase in sample size and will provide a test of our model. The possibility that hundreds of thousands of neutron stars have been ejected from the LMC and are now populating the local IGM was mentioned by Ridley and Lorimer, 2010 in the context of single star evolution.

### *Microlensing*

Photometric microlensing towards the LMC by an intervening population of dark objects was thought to be a straightforward test of the

existence of massive compact halo objects (MACHOs), which may comprise some of the dark matter (Paczynski, 1986). When the experiment was carried out, 40% of the microlensing optical depth was indeed unexplained by Galactic populations, such as the thick disc and halo. However, this signal is too small to be caused by MACHOs if they comprise the entirety of the Milky Way's dark matter halo. Several authors attempt to explain this excess with stellar populations at various points along the line of sight to the LMC (Evans & Kerins, 2000; Zhao, 1998), though the viability of this explanation has also been disputed (Gould, 1997, 1999). Besla et al. (2013) modelled the interaction of the LMC with the SMC and found that the microlensing might be explained by clumpy tidal debris from the SMC being microlensed by the LMC disc. Here, we consider whether our substantial population of neutron stars and black holes contributes to the microlensing optical depth to the LMC. We use the formula of Gould, 1999 for the required surface mass density  $\Sigma$  to contribute lensing optical depth  $\tau_p$ ,

$$\Sigma = 47 \left( \frac{\tau_p}{2.9 \times 10^{-7}} \right) \left( \frac{\hat{D}}{10 \text{ kpc}} \right)^{-1} M_{\odot} \text{ pc}^{-2}, \quad \hat{D} \equiv \frac{d_{ol} d_{ls}}{d_{os}}, \quad (4.27)$$

where  $d_{ol}$ ,  $d_{ls}$  and  $d_{os}$  are the respective observer-lens, lens-source and observer-source distances. We find that our remnants contribute 0.0035% to the observed microlensing optical depth. In our calculations, we only include those remnants in front of the LMC and within three degrees of the sightline between the observer and the centre of the LMC.

Less familiar than photometric microlensing is the accompanying astrometric effect, in which the light centroid of the source is deflected by the presence of the foreground lens. Belokurov and Evans (2002) calculated the all-sky photometric and astrometric microlensing optical depths detectable by *Gaia* and found that the astrometric optical depth was two orders of magnitude larger than the photometric optical depth. We calculate the astrometric optical depth  $\tau_a$  for our neutron star and black hole population using Equation 14 from Belokurov and Evans (2002),

$$\tau_a = 4 \sqrt{\frac{G}{c^2}} d_{os} \langle M^{-1/2} \rangle \sqrt{\frac{T_{\text{life}}^3 v^3}{5\sqrt{2}\sigma_a}} \int_0^1 \rho(x) \sqrt{1-x} dx, \quad (4.28)$$

where  $G$  is the gravitational constant,  $c$  is the speed of light,  $\langle M^{-1/2} \rangle$  is the mean of the inverse square-root of the masses of the compact remnants,  $T_{\text{life}} = 5 \text{ yr}$  is the estimated lifetime of *Gaia*,  $\sigma_a = 390 \mu\text{s}$  is the predicted mean position accuracy of *Gaia* for sources with  $G =$



18 mag,  $v \sim 140 \text{ km s}^{-1}$  is a characteristic velocity of the lens relative to the LMC disc and  $\rho(x)$  is the mass density at a fraction  $x$  along the line-of-sight to the source. We find  $\tau_a = 1.0 \times 10^{-10}$  which is 15 times greater than the corresponding photometric microlensing optical depth. However, this optical depth is likely still too small to give observable consequences.

#### 4.2.3 Summary

In this Section, we have presented a novel source of hypervelocity stars (HVSs) in the Milky Way (MW) halo. In our model, HVSs originate as runaway stars from the Large Magellanic Cloud (LMC). The known HVSs possess the kinematics expected of stars which have been ejected from the LMC, and thus an LMC origin for some of these stars must be considered a realistic possibility.

There are a number of current observations that support our scenario, albeit indirectly. This includes: (i) a sample of the 31 brightest stars in the LMC which are consistent with runaway expectations except perhaps from one anomalously fast supergiant (Lennon et al., 2016), (ii) young stars in the periphery of the LMC far from star formation regions (Moni Bidin et al., 2017) and (iii) B-type stars in the gaseous leading arm of the LMC with LMC kinematics and chemistry whose anomalous single nature is in line with a runaway origin (Zhang et al., 2017).

The HVSs found in the Sloan Digital Sky Survey footprint are B-type stars with masses exceeding  $3 M_{\odot}$ . In our model, the LMC runaways that end up as hypervelocity in the Sloan footprint have somewhat smaller masses, typically between  $1.6 M_{\odot} < M < 3.0 M_{\odot}$ . However, there is a strong dependency of the mass and colour of the produced HVSs on the common-envelope prescription, with lower common-envelope ejection efficiencies broadly associated with higher mass hypervelocity stars. So, this discrepancy could be resolved by modest changes to the uncertain prescription of common envelope evolution. Alternatively, the observed HVS population may have contributions from multiple processes only one of which is the fast moving LMC runaway stars.

Our model leads to predictions of the spatial and kinematic signatures of HVSs seen by *Gaia* and the hypervelocity pulsars observed by the Square Kilometre Array. We predict that both will be preferentially found along the past and future orbit of the LMC. The final *Gaia* catalogue aims to be complete down to  $G \approx 20.7$  subject to crowding in dense fields. This should detect a large number of hypervelocity runaways from the LMC. We would expect about 200 of

these stars at distances  $30 < d < 120$  kpc and with proper motions around 1 mas. This corresponds to a (heliocentric) tangential velocity of around  $500 \text{ km s}^{-1}$  at the location of the LMC. However, we do not expect either parallax or radial velocities for these stars from *Gaia*, so identification of their nature will rely on photometric distances and spectroscopy.

In investigating the runaway processes in the LMC, we have linked a binary stellar evolution code with an N-body model of the interaction between the Galaxy and the LMC, which enabled us to make powerful predictions. A problem which required bringing together stellar evolution and stellar dynamics has implications for both. LMC runaway stars can provide important constraints on both common-envelope dispersal and the escape velocity of the Milky Way.

Runaway stars are a natural consequence of binary evolution in a star-forming galaxy, and hence they will certainly exist in the LMC. The exceptionally fast runaways, which become HVSs with respect to the Milky Way, are sensitive to the prescription of binary evolution. Changing the binary evolution only seems to modify the properties of those HVSs and not their number or distribution on the sky. Our argument therefore does not rely on the precise details of binary evolution. Furthermore, there are observed counterparts to our evolutionary channel. A pulsar – helium white dwarf binary is left behind if the system is not unbound during the supernova, but is close enough after the end of common-envelope evolution that the companion is stripped before igniting helium. The extreme velocity of the runaways originates in the orbital velocity of such close binaries. We conclude that hypervelocity runaway stars from the LMC, as a consequence of star-formation, are unavoidable. They must contribute to the Galactic HVS population. The only argument is whether this process is dominant or subordinate.

#### 4.3 CONCLUSION

I have presented two channels for the production of hypervelocity stars in the LMC: ejection by a massive black hole or by the supernova of a companion star. An origin in the LMC would naturally explain why hypervelocity stars are predominantly found near the constellations of Leo and Sextans. Either of these channels can replicate the distances, radial velocities and proper motions of the observed hypervelocity stars, however both have caveats. Firstly, there may not be a massive black hole in the LMC. Secondly, our simulation of runaway stars from the LMC was not able to exactly match the stellar masses

of the hypervelocity stars, however it is possible that this is only due to gaps in our understanding of common envelope evolution.

There is emerging evidence that my hypothesis may be correct. Erkal et al. (2018) has proven that HVS3 (HE 0437-5439), an  $8 M_{\odot}$  star, was ejected from the LMC  $21.1^{+6.1}_{-4.6}$  Myr ago at  $870^{+69}_{-66}$  km s<sup>-1</sup> (see Sec. 5.2 for further discussion). Further, we proposed in Sec. 4.2.2.2 that some of the six young stars on the outskirts of LMC discussed by Moni Bidin et al. (2017) were runaways, and with *Gaia* DR2 proper motions Casetti-Dinescu et al. (2018) showed that 2 of these stars are indeed runaway stars. Lennon et al. (2018) confirmed that the massive star VFTS 16, a  $100 M_{\odot}$  star, is an  $80 \pm 11$  km s<sup>-1</sup> runaway from the central cluster of the Tarantula Nebula. Each of these results has used data from *Gaia* DR2, which underlines the importance of that dataset for the study of fast stars.

An additional observable not mentioned in the previous two sections is that the smaller kick required to produce a hypervelocity star from the LMC rather than the MW makes it more likely that the ejected star could retain a stellar or planetary companion. The HVS candidate SDSS J121150.27+143716.2 was shown to be a binary by Németh et al. (2016), who concluded that the usual production routes for HVSs cannot achieve a Galactic rest-frame velocity of 571.3 km s<sup>-1</sup> without disrupting the binary and thus the binary is either an extreme halo object or was accreted from the debris of a destroyed satellite galaxy. While the kinematics of this candidate are inconsistent with the LMC, I speculate that the addition of the orbital velocity of a Local Group dwarf galaxy with the ejection velocity due to a standard HVS production route could explain this HVS binary. Confirmed hypervelocity stars should have their radial velocities monitored to investigate whether they do have companions.

If the hypervelocity stars in the Northern hemisphere originate in the LMC, then there must be a stream containing hundreds or thousands of hypervelocity stars in the Southern hemisphere. That stream would encode the LMC's potential and past orbit and, through the density of stars along its length, the star-formation history. The stream should be distorted by the interaction with the SMC and this would reveal the LMC-SMC interaction history. Even better, there may be a counterpart stream of stars being ejected from the SMC. By studying the velocities, ages, masses, rotation rates and chemistry of the stars in the stream, it should be possible to infer the mechanism which ejected each star. These stars will then be powerful probes of the processes that kicked them from the LMC, and will enable astronomers to both directly study the products of extreme end-stage

binary evolution and to test the existence of an LMC central black hole.

While Sec. 4.1 shows that the hypervelocity stars in the Galactic halo are consistent with an LMC origin, Sec. 4.2 demonstrates that we should expect several thousand hypervelocity stars from the LMC to exist. There is no longer any doubt that the LMC is producing hypervelocity stars; the only question is whether the MW or the LMC is the dominant source.

*Gaia* is a revolutionary mission for Galactic dynamics, but is particularly game-changing in the study of hypervelocity stars. First, *Gaia* will provide the first deep, multi-band photometric survey of the entire sky, enabling the key strategy of the HVS Survey (e.g. spectroscopic follow-up of photometrically selected faint, blue stars, Brown et al., 2006a) to be applied in the Southern hemisphere. Second, *Gaia* will measure precise proper motions of the hypervelocity stars in the halo and thus allow a more constrained determination of their origin. Third, *Gaia* will likely decimate the hundreds of candidate late-type hypervelocity stars in the literature by measuring more accurate distances and proper motions. Fourth, *Gaia* will measure precise distances, proper motions and radial velocities for tens of millions of stars that have never had these measurements, and thus *Gaia* should directly discover new hypervelocity stars (e.g. Marchetti et al., 2018 predicts that *Gaia* DR2 will reveal a few tens of hypervelocity stars). Fifth, *Gaia* will transform our understanding of the Milky Way’s structure and result in a more precise escape speed curve, thus may raise or lower the bar for consideration as a hypervelocity star.

In the remainder of this Chapter, I present a smörgåsbord of early hypervelocity star results with *Gaia* DR2. In Sec. 5.1, I revisit the 532 hypervelocity candidates in the literature and demonstrate that all but one of the late-type candidates are bound to the Galaxy. In Sec. 5.2, I summarise an investigation into the origin of the late-B hypervelocity stars using *Gaia* DR2 proper motions whose primary result was that HV3 originates in the LMC. In Sec. 5.3, I detail my contribution to the discovery of three hypervelocity white dwarfs in *Gaia* DR2, which we interpreted as runaway companions of Type Ia supernovae.

## 5.1 REVISITING THE HYPERVELOCITY STARS

*Based on work originally published in Boubert et al. (2018).<sup>1</sup>*

<sup>1</sup> I conceived and lead this project, and was principally responsible for the data acquisition and analysis of results. James Guillochon and N. Wyn Evans wrote substantial fractions of the text this Section is based on, and James was also heavily involved in the creation of the Open Fast Stars Catalog which has a separate declaration in the Appendix. Warren R. Brown, Saurabh W. Jha, Ken J. Shen, and Angus Williams gave valuable input in the development of the work. Keith Hawkins thanked the Simons Society of Fellows and the Flatiron Institute Center for Computational Astrophysics. Idan Ginsburg was supported in part by Harvard University funds and the Institute

On the release day of *Gaia* DR2, 25 April 2018, there were 524 candidate hypervelocity stars in the literature. We knew this because James Guillochon and I had constructed the Open Fast Stars Catalog (OFSC), an on-line database containing the astrometry, photometry and spectroscopy of every proposed hypervelocity star. The OFSC is described in Appendix A.4. Many types of stars were included in the catalogue, from the late-B dwarfs in the halo to nearby M giants, in addition to two white dwarfs and several subdwarfs. However, a significant fraction of these candidates were quite speculative. As discussed in Sec. 1.3.5, many of the nearby hypervelocity stars rely on a large tangential velocity derived from a photometric distance combined with the proper motion. There is a history of tangential velocity hypervelocity candidates being refuted, for instance the 20 G and K candidates of Palladino et al. (2014) were later disproved with the corrected proper motions derived by Ziegerer et al. (2015). In contrast, the hypervelocity classification of the late B-type hypervelocity stars in the halo was secure, because i) the radial velocity was sufficient to make the star unbound even without adding on the proper motion and ii) a B-type star could only reach the outer halo if it were a hypervelocity star.

If a late-type hypervelocity star near the Sun were to be identified, then it would be transformative for our understanding of the hypervelocity stars' origin. The two different populations of hypervelocity stars would probe different kinematic regimes and could potentially be used to distinguish between the formation scenarios. The question of whether there are any late-type hypervelocity stars lies at the centre of the hypervelocity star mystery.

The objective of this Section is to provide a comprehensive update on the status of the hypervelocity candidates in the literature after *Gaia* DR2. I specifically focus on the nearby, late-type candidates because these are the stars whose status is most likely to change with improved astrometry. In Section 5.1.1, I briefly cover the history of searches for late-type hypervelocity stars. Section 5.1.2 provides an overview of the landscape of hypervelocity star candidates and looks in detail at the one confirmed late-type hypervelocity star.

#### 5.1.1 *History of searches for late-type hypervelocity stars*

Prior to *Gaia* DR2, a number of late-type hypervelocity candidates had been claimed in the literature. We define late-type as stars whose spectral type is F, G, K or M, including both dwarf and giant stars. Many of these identifications were based on cross-matches between

---

for Theory and Computation. Jay Strader acknowledged support from the Packard Foundation.

spectroscopic surveys such as SEGUE (The SDSS-II SEGUE Collaboration et al., 2009) and LAMOST (Cui et al., 2012) together with the SDSS-USNO proper motion catalogues (Munn et al., 2008; Munn et al., 2004). With the addition of photometric parallaxes, this gives the full space motion of the candidate. This motion is compared to a Galactic escape speed curve to determine whether the star is unbound. The radial velocity is usually secure, but photometric parallaxes typically have errors of 15 per cent. Even the most carefully constructed ground-based proper motion catalogues tend to have some erroneous measurements, especially in the high proper motion regime.

As an example, Li et al. (2012) searched through Sloan Digital Sky Survey (SDSS) Data Release 7 and identified 13 F-type hypervelocity star candidates. They used SEGUE spectroscopy and proper motions from the SDSS-USNO (Munn et al., 2004) and argued from orbit integrations that 9 candidates emanated from the Galactic Centre or disc, whilst the remaining 4 had a more exotic origin, such as tidal disruption of dwarf galaxies (Abadi, Navarro, & Steinmetz, 2009). Paladino et al. (2014) also carried out a search in the SEGUE G and K dwarfs sample, again based on proper motions from SDSS+USNO-B (Munn et al., 2004). The fate of these candidates illustrates the pitfalls of such work. Many of the candidates were contested either because they are high-velocity halo stars and therefore bound or because the ground-based proper motions are inflated (Ziegerer et al., 2015).

The LAMOST survey also proved to be a happy hunting ground for late-type hypervelocity star candidates. Li et al. (2015) claimed 19 low mass F, G and K type hypervelocity star candidates from over one million stars found in the first data release of the LAMOST regular survey. They combined LAMOST spectroscopy with SDSS-USNO-B (Munn et al., 2004) proper motions. Their final cleaned candidate list used only stars with reliable proper motions, high quality spectra and trustworthy astrophysical parameters. The candidates had probabilities of being unbound, as judged from Monte Carlo simulations of orbit integrations, in excess of 50 per cent. However, there were 8 high quality candidates with a probability in excess of 80 per cent.

We are not the first to realise the potential of *Gaia* as a purger of late-type hypervelocity candidates. Marchetti et al. (2017) trained a neural network to identify hypervelocity star candidates in *Gaia* DR1 and noticed that one of their candidates HD 5223 had previously been suggested by Pereira et al. (2012). The *Gaia* parallax indicated that it was much closer than previously thought. Given the history of the subject, *Gaia* Data Release 2 proper motions might well be expected to winnow the late-type hypervelocity candidates.

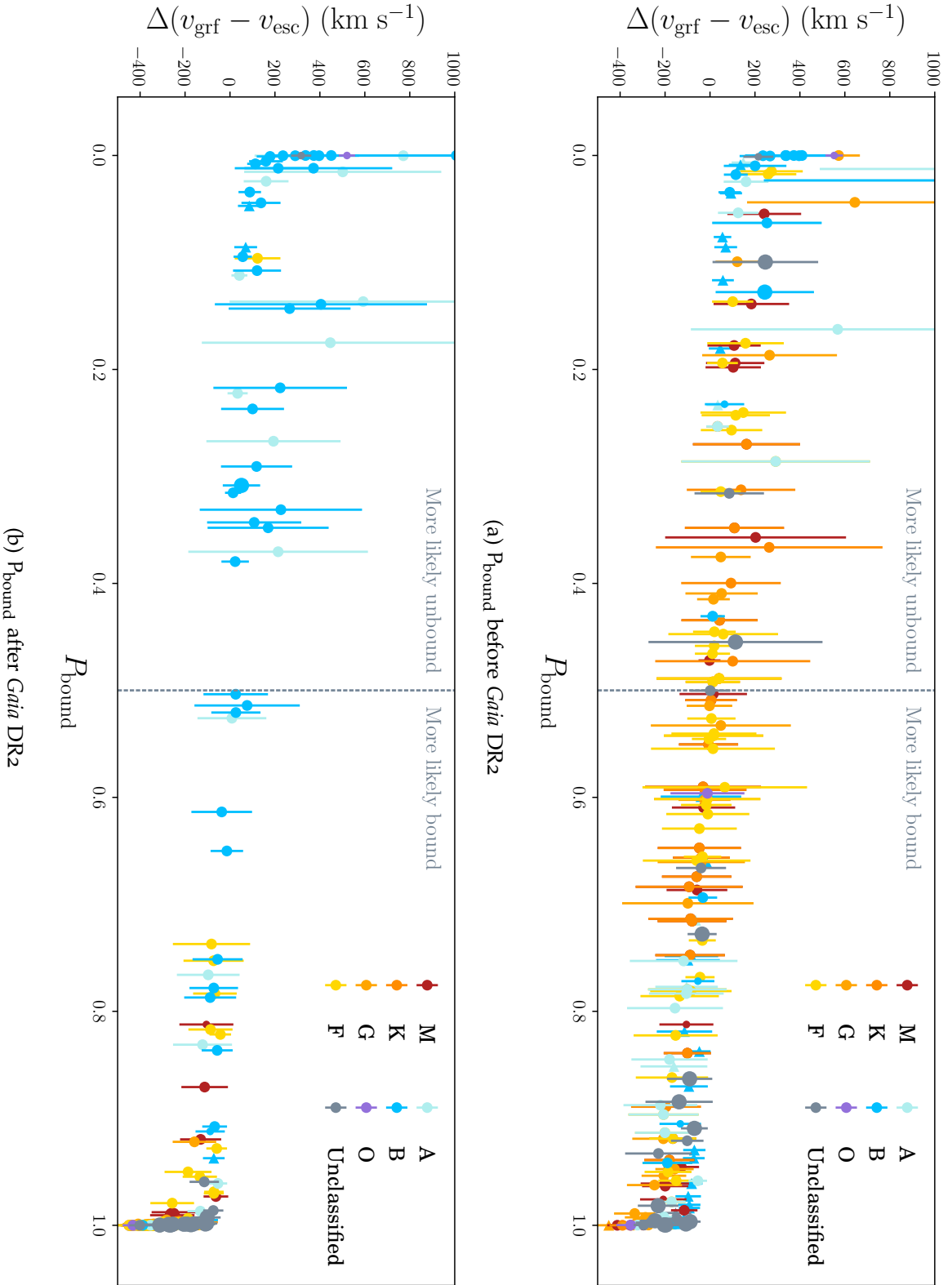


Figure 5.1: The probability of a candidate hypervelocity star being bound to the Galaxy versus the difference between the Galactocentric rest-frame velocity and the escape speed. The error bars incorporate errors and correlations in the distances, radial velocities and proper motions of the stars, as well as the uncertainties in the Solar kinematics and the Milky Way escape velocity (see the Appendix for more detail). Some stars are missing either the radial velocity or proper motions and thus the probability is only an upper limit (these objects are indicated with a triangle). The size of the point reflects whether the star is a giant (large), dwarf (medium) or a white dwarf or subdwarf (small).



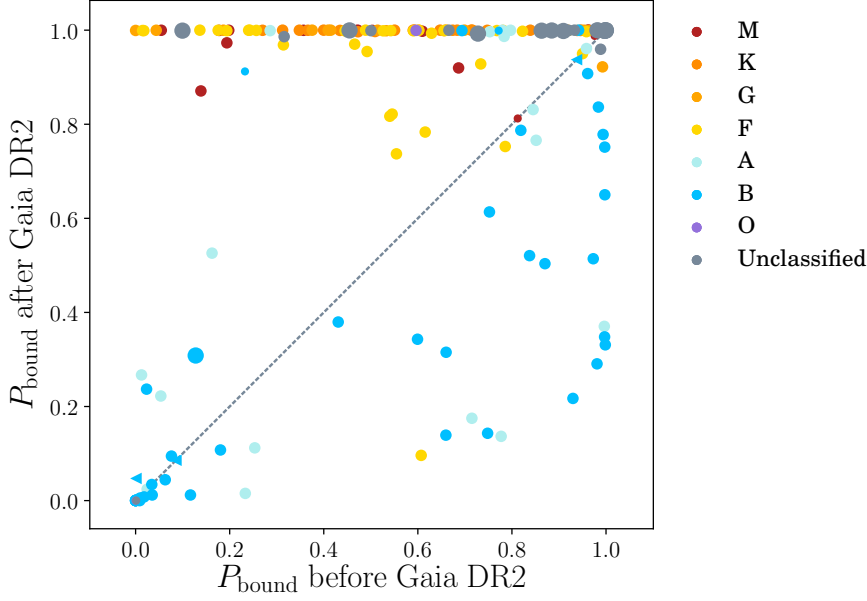


Figure 5.2: Probability  $P_{\text{bound}}$  that each high-velocity candidate is bound to the Milky Way before (x-axis) and after (y-axis) the inclusion of DR2. The shapes of the markers is as in Fig. 5.1.

### 5.1.2 Results

The Open Fast Stars Catalog (presented in detail in Appendix A.4) automatically queries *Gaia* DR2 and calculates the posterior probability that each star is bound  $P_{\text{bound}}$  (the method is described in detail in the Appendix). Of the 524 candidate hypervelocity stars in our catalogue, 514 have *Gaia* photometry and 501 have *Gaia* astrometry in DR2. This compares with only 472 having photometry and 18 having astrometry in *Gaia* DR1. Almost all hypervelocity candidates now have precise proper motions and parallaxes, which transforms the landscape of hypervelocity star research. Before *Gaia* DR2, there were 71 candidates with  $P_{\text{bound}} < 0.5$  and 132 candidates with  $P_{\text{bound}} > 0.5$ . After *Gaia* DR2, these numbers dramatically changed with 41 candidates with  $P_{\text{bound}} < 0.5$  and 464 candidates with  $P_{\text{bound}} > 0.5$ . The increase in the numbers of classified stars is because *Gaia* provides parallaxes for the 321 candidates proposed by Vickers, Smith, and Grebel (2015), who had calculated photometric distances but not published them. We note that 428 hypervelocity candidates have a probability greater than 99% of being bound to Milky Way and thus are ruled out. A caveat is that 5 stars are missing a radial velocity or proper motion in our catalogue and thus the  $P_{\text{bound}}$  is only an upper limit. It is possible that as the Open Fast Stars Catalog becomes more complete some of these candidates could be resurrected. A fur-

*Vickers et al. (2015) have now kindly provided distances for their candidates and these are published in the OFSC.*

<sup>1</sup> <https://faststars.space/sky-locations/>

Table 5.1: The hypervelocity candidates with  $P_{\text{bound}} < 0.5$  subdivided by original discovery survey or paper. The Hypervelocity Star Survey (Brown, Geller, & Kenyon, 2014; Brown, Geller, Kenyon, & Kurtz, 2005; Brown, Geller, Kenyon, Kurtz, & Bromley, 2007b) has remarkably discovered 32 of these 41 stars, while the LAMOST HVS Survey (Huang et al., 2017; Zheng et al., 2014) contributes a further 3.

Survey	#	Names
Hypervelocity Star Survey	32	HVS <sub>1,4-10,12-24</sub> and others
Hirsch, Heber, O'Toole, and Bresolin (2005)	1	US 708 (a.k.a. HVS <sub>2</sub> )
Edelmann, Napiwotzki, Heber, Christlieb, and Reimers (2005)	1	HE 0437-5439 (a.k.a. HVS <sub>3</sub> )
Heber, Edelmann, Napiwotzki, Altmann, and Scholz (2008)	1	HD 271791
Tillich et al. (2009)	1	SDSS J013655.91+242546.0
LAMOST HVS Survey	3	LAMOST-HVS <sub>1-3</sub>
Li et al. (2015)	1	Li10 (F9 dwarf)
Vennes et al. (2017)	1	GD 492 (white dwarf)

ther caveat is that in the following analysis we do not consider the red giant J004330.06+405258.4, which is thought to be a hypervelocity star of M<sub>31</sub> and is at a distance of 760 kpc (Evans & Massey, 2015). J004330.06+405258.4 is shown in Figs. 1.3 and 5.4 for completeness. We also do not consider Li2, the second candidate of Li et al. (2015), because there are two radial velocity measurements in the literature which disagree: LAMOST reports  $-60 \pm 10 \text{ km s}^{-1}$  whilst SDSS reports  $-160.8 \pm 3.4 \text{ km s}^{-1}$ . The simplest explanation is that this star is an unresolved binary and thus the reported radial velocities are not representative of the true systemic velocity.

In Figure 5.1, we show the bound probability versus the difference between the Galactocentric rest-frame velocity and the escape velocity as a function of the spectral type. The overarching trend is for late-type FGKM stars to be assessed as more bound after DR2, while early-type OBA stars become less bound. This trend is made obvious in Fig. 5.2 where we directly compare  $P_{\text{bound}}$  computed before and after *Gaia* DR2; almost all the late-type stars are conclusively bound with DR2, whilst a large number of OBA stars have an increased probability of being unbound (they move to the lower right of this figure).

In Tab. 5.1, we list all candidates which have  $P_{\text{bound}} < 0.5$ . This list of candidates comprises 38 B/A dwarfs, one subdwarf O star, one F9 dwarf and one white dwarf, and we will consider each of these categories in turn.

#### 5.1.2.1 *The early-type B/A candidates*

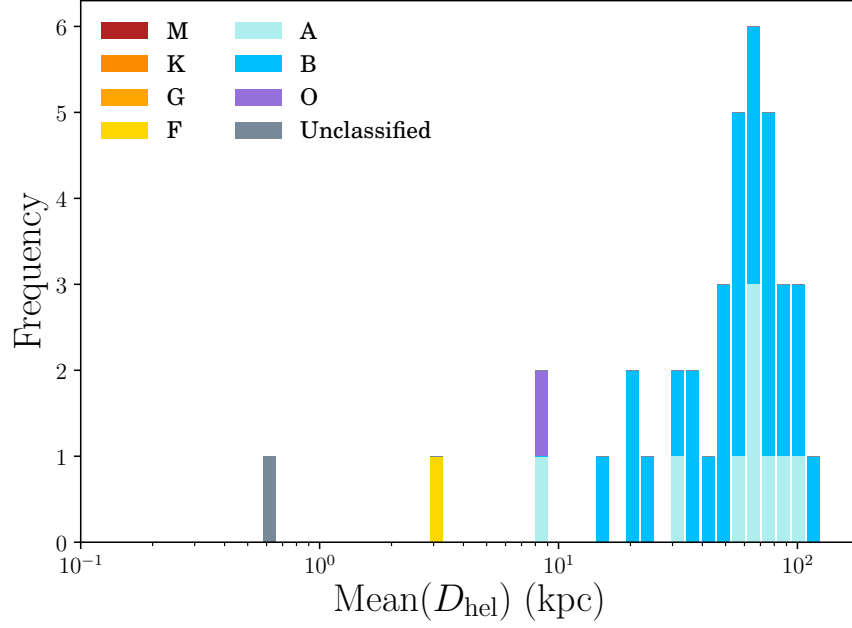
Over the past 13 years the Hypervelocity Star Survey (Brown et al., 2014; Brown et al., 2005; Brown et al., 2007b) has discovered many tens of faint, blue stars in the halo of the Milky Way. These stars were classified as hypervelocity stars based solely on their large radial velocities and thus could not be ruled out by *Gaia* astrometry; by measuring their proper motions *Gaia* was only increasing their Galactocentric rest-frame velocity. This argument extends to most of the early-type stars shown in Fig. 5.1, except for close stars such as HD 271791 at  $21 \pm 4$  kpc (Heber, Edelmann, Napiwotzki, Altmann, & Scholz, 2008) who had previously measured proper motions, and thus explains their trend to being more likely unbound.

As the majority of the remaining hypervelocity candidates are early-type, the distance distribution (see Fig. 5.3) of hypervelocity stars is now dominated by objects in the distance range 10 – 110 kpc, with a modal distance of around 70 kpc. The mean hypervelocity candidate with  $P_{\text{bound}} < 0.5$  is now more distant than the LMC ( $49.97 \pm 1.126$  kpc, Pietrzyński et al., 2013). A further consequence is that the sky distribution is no longer homogeneous within the Northern equatorial hemisphere (see Fig. 5.4). The clump near the centre of the plot is the well-known clustering of early-type hypervelocity stars near the Leo constellation (e.g. Brown et al., 2009). The star located beside the LMC is HVS<sub>3</sub>: an  $8 M_{\odot}$  star thought to have been ejected from the LMC (Edelmann et al., 2005; Erkal et al., 2018; Gualandris & Portegies Zwart, 2007).

We note that the distance distribution shown in Fig. 5.3 is biased by the way that the early-type hypervelocity stars were discovered. The Hypervelocity Star Survey (Brown et al., 2014; Brown et al., 2005; Brown et al., 2007b) selected for blue, faint objects at high latitudes, because a B type star would require a large velocity to reach the halo within its lifetime. Thus by construction our sample of hypervelocity stars is biased towards stars at great distances. The existence or non-existence of early-type hypervelocity stars closer to the Galaxy will allow us to tell whether the hypervelocity stars have a Galactic or extragalactic origin.

#### 5.1.2.2 *Type Ia supernova donors and survivors*

Both US 708 (Hirsch et al., 2005) and GD 492 (Vennes et al., 2017) are thought to be associated with Supernova Ia, as discussed in the Introduction (Sec. 1.3.5). Both are confirmed to be hypervelocity stars. Note that the other white dwarf hypervelocity candidate SDSSJ124043.01+671034.68 (Kepler, Koester, & Ourique, 2016) is confirmed with *Gaia* DR2 to be bound to the Galaxy.



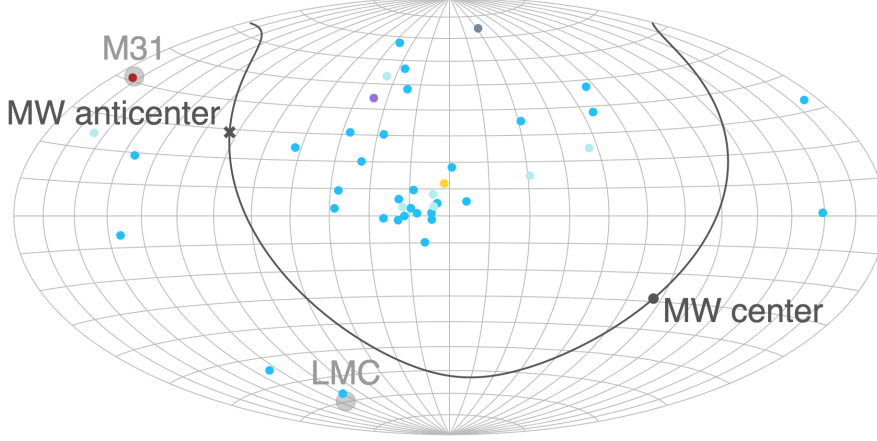


Figure 5.4: Same as Figure 1.3, but for hypervelocity candidates with  $P_{\text{bound}} < 0.5$  (see Tab. 5.1).

Li10 is consistent with having passed through the disc roughly 15 Myr ago, however we note that this is only a small fraction of the main sequence lifetime of an F9 star and thus we cannot use this time as an estimator of the flight time. The possibility of hypervelocity stars arriving in the Milky Way from M31 (Sherwin et al., 2008) or the LMC (Boubert & Evans, 2016; Boubert, Erkal, et al., 2017) has been suggested in the literature. However, the orbit of this star is not aligned with either of these galaxies (see Fig. 5.5). If the star were to turn out to be bound after later *Gaia* data releases, then the natural interpretation is that this star is a fast-moving denizen of the halo. An alternative possibility is that Li10 has a binary companion and thus that the radial velocity from LAMOST DR1 has a large contribution from the binary orbital motion. There is no source in *Gaia* DR2 within 45 arcsec of Li10 and thus any companion would need to be either a low-mass dwarf or a compact object (likely a white dwarf or neutron star).

To test the close binary hypothesis we obtained a spectrum of LAMOST J115209.12+120258.0 with the Goodman Spectrograph (Clemens, Crain, & Anderson, 2004) on the SOAR telescope on UT 2018 Apr 29. We used a 0.95 arcsec slit and a  $1200 \text{ l mm}^{-1}$  grating, giving a spectral resolution of about  $1.7 \text{ \AA}$ . A single 1800-sec exposure was obtained. The spectrum was reduced and optimally extracted in the usual manner. We determined the barycentric radial velocity of the star through cross-correlation with a template of similar spectral type taken with the same set-up, finding a value of  $v_r = 234 \pm 5 \text{ km s}^{-1}$  which we use throughout this work. The LAMOST DR1 velocity of this star is listed as  $206 \pm 15 \text{ km s}^{-1}$ , which is marginally consistent with the new measurement. To check this, we downloaded the LAMOST spectrum and re-derived the radial velocity through cross-correlation. In the region of the Mg b line we reproduce the published

velocity; if instead we use the Ca triplet region, the LAMOST velocity is  $223 \pm 5 \text{ km s}^{-1}$ , (random uncertainty only), which is closer to the SOAR/Goodman value. We conclude there is no significant evidence for a radial velocity shift between these two spectra and hence no evidence that this star is in a close binary. Thus, Li10 appears to be the only known late-type hypervelocity star.

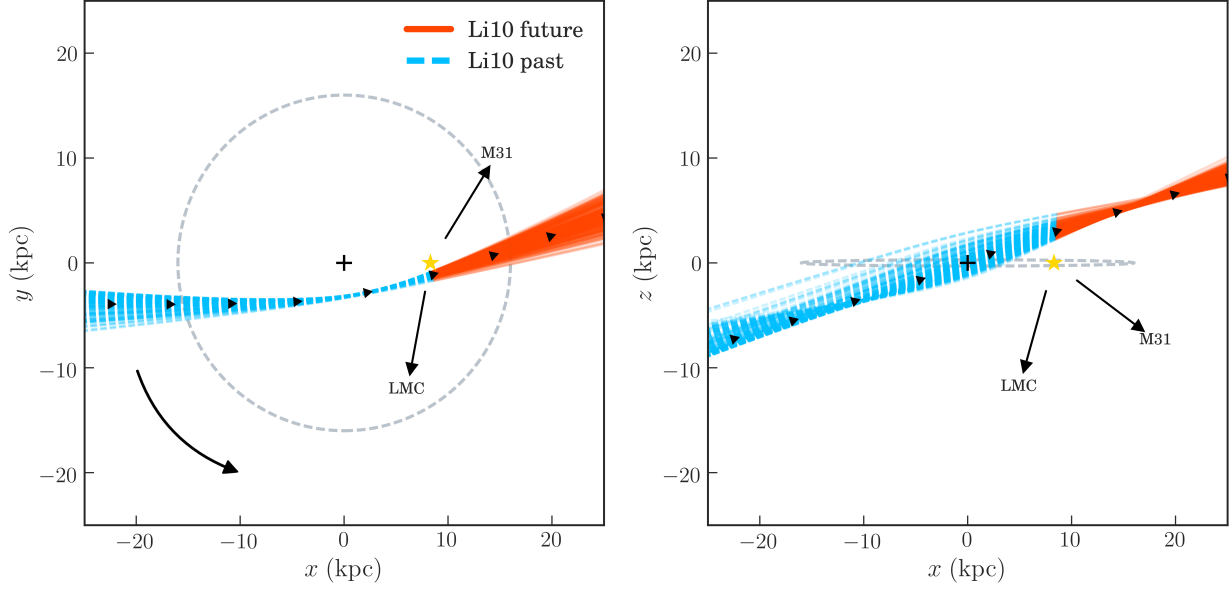


Figure 5.5: Past (dashed components of each curve) and future (solid components of each curve) realizations of the trajectory of the candidate high-velocity late-type star LAMOST J115209.12+120258.0. The size of the Milky Way’s thin disc, assumed to be 32 kpc in diameter and 0.6 kpc in height, is shown by the dashed grey contours. Arrows pointing in the directions of M31 and the LMC are labelled. Orbits were calculated in the MWPotential2014 potential using the PYTHON Galactic dynamics framework GALPY (Bovy, 2015). The rotation direction of the Milky Way disc is indicated by the long arrow and the short arrows indicate time steps of 10 Myr along the orbit.

### 5.1.3 Summary

In this Section, I have combined the historical data on high-velocity stars with data from *Gaia*’s second data release. There is a single candidate late-type high-velocity object (LAMOST J115209.12+120258.0) that has a reasonably high probability of being unbound from the Milky Way and thus hypervelocity. However, the overwhelming majority of the historical late-type high-velocity candidates are almost certainly bound to the Milky Way. This is a clear demonstration of the superiority of space-based astrometry from *Gaia* over the earlier ground-based proper motion catalogues. It is anticipated that further *Gaia* DR2 studies will reveal many late-type high-velocity candidates,

which will be added to the Open Fast Stars Catalog when they are announced.

## 5.2 A HYPERVELOCITY STAR FROM THE LMC

*Based on work originally published in Erkal et al. (2018).<sup>2</sup>*

The lack of proper motions for the late B-type hypervelocity stars in the halo had long been a barrier to deducing their origin. The only proper motions of these stars prior to *Gaia* came from Brown et al. (2015), who used multiple epochs of Hubble Space Telescope (HST) measurements to derive proper motions for 16 hypervelocity and hypervelocity candidate stars. Brown et al. (2015) then attempted to infer the origin of these stars by integrating their orbits back to the Galactic plane, however the HST proper motions were not sufficiently constraining; the proper motion of HVS1 was measured to be  $(\mu_{\alpha*}, \mu_{\delta}) = (+0.08 \pm 0.26, -0.12 \pm 0.22)$  and this resulted in the  $1\sigma$  contour of the Galactic plane intersection enclosing an area of  $2 \times 10^3 \text{ kpc}^2$ . *Gaia* should obtain proper motions for all extant hypervelocity stars that are more precise than those from HST by the end of the mission, however DR2 is already competitive. In Erkal et al. (2018) we took the proper motion from HST or *Gaia*, whichever had the smallest uncertainty on the total proper motion, and integrated their orbits in a potential containing both the Milky Way and the LMC. By Monte Carlo sampling in the uncertainties, we determined both the closest approach to the Milky Way  $\min(r_{\text{MW}})$  and LMC  $\min(r_{\text{LMC}})$  and the probability that that closest approach was less than 5 kpc (see Fig. 5.6). My primary contributions were the literature review of hypervelocity stars and assembling the catalogue of measurements which were used as the initial conditions of the integrations (see Tab. 5.2).

The two main results of the study were that the nearest hypervelocity stars to the Milky Way (LAMOST-HVS1-3, HD 271791 and HIP 60350, see Fig. 5.6) are highly likely to originate inside the Galaxy and that HVS3 must originate in the LMC. It is clear from Fig. 5.6 that the origin of the remaining hypervelocity stars is unconstrained at present. In Fig. 5.7, I show the distribution of the ejection time from the LMC and the relative velocity at ejection; HVS3 was ejected from the LMC  $21.1^{+6.1}_{-4.6}$  Myr ago at  $870^{+69}_{-66} \text{ km s}^{-1}$ . Gualandris, Portegies Zwart, and Sipior (2005) argued that, because HVS3 is an  $8 M_{\odot}$  star,

<sup>2</sup> Denis Erkal and I conceived this project in collaboration. My contribution was consulting as an expert on the hypervelocity star literature; I wrote the literature review and assembled the catalogue of late-B hypervelocity stars including the synthesis of HST and *Gaia* proper motions.



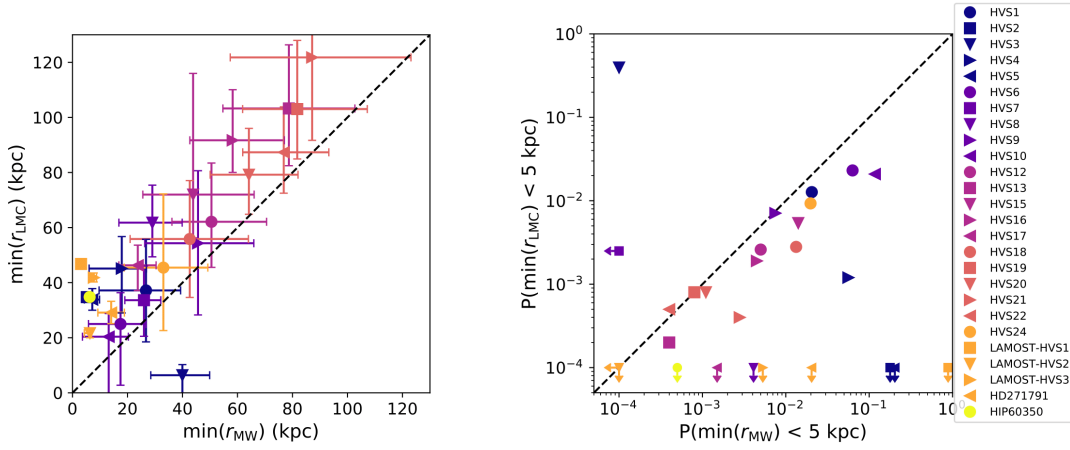


Figure 5.6: **Left:** Minimum approach distance to the Milky Way and the LMC for the 26 HVSs in our sample. HVS3 stands out as being far more likely to have originated near the LMC than near the Milky Way. **Right:** Probability of passing within 5 kpc of the Milky Way and the LMC over the past 500 Myr. Again, HVS3 clearly stands out as being significantly more likely to originate from near the centre of the LMC ( $p = 0.40$ ) than the MW ( $p = 10^{-4}$ ). Originally published in Erkal, Boubert, Gualandris, Evans, and Antonini (2018).

it's large velocity relative to the LMC requires it to have been ejected by the Hills mechanism and Gualandris and Portegies Zwart (2007) find that a black hole more massive than  $10^3 M_{\odot}$  is required. Based on the new *Gaia* DR2 proper motions we found that a mass of at least  $4 \times 10^3 - 10^4 M_{\odot}$  is required.

### 5.3 THREE NEW HYPERVELOCITY WHITE DWARFS

Based on work originally published in Shen et al. (2018).<sup>3</sup>

One of the proposed routes to a Type Ia supernova is the double-degenerate channel, where mass transfer in a double white dwarf binary causes the detonation of one of the components. For reasons beyond the scope of this thesis to explain, one particularly interesting variant of this channel has been named the *dynamically-driven double degenerate double detonation* or D<sup>6</sup> channel. In this channel the binary will be extremely short period and thus if the mass donor survives the supernova then it will be flung away at a couple thousand kilometres per second (Shen & Schwab, 2016). If one of these objects was

<sup>3</sup> I was involved at an early stage of this project. I pointed out that these objects, if they existed, would be some of the fastest stars known and would be unbound from the Galaxy. I collaborated with Ken Shen to predict the number we should expect to find, calculated a distance prior for converting the *Gaia* parallax to a distance, integrated the orbits of the candidates in a Milky Way potential to prove that they did not originate in the Galactic centre, and was responsible for identifying that one of the candidates tracked back to the centre of a supernova remnant. I invite the reader to read the acknowledgements of the 26 authors in Shen et al. (2018).



Table 5.2: The 26 hypervelocity stars considered in this work. Almost all of the proper motion measurements are from *Gaia* DR2 except for HVS1, HVS4, HVS13, and HIP60350. **References:** (1) Brown et al. (2015) (2) Gaia Collaboration et al. (2018), (3) Geier et al. (2018), (4) Brown, Geller, and Kenyon (2014), (5) Zheng et al. (2014), (6) Huang et al. (2017), (7) Heber, Edelmann, Napiwotzki, Altmann, and Scholz (2008), (8) Irgang, Przybilla, Heber, Nieva, and Schuh (2010).

ID	R.A.	Dec.	$\mu_{\alpha*}$ (mas yr <sup>-1</sup> )	$\mu_{\delta}$ (mas yr <sup>-1</sup> )	Corr( $\mu_{\alpha*}, \mu_{\delta}$ )	$v_{\text{hel}}$ (km s <sup>-1</sup> )	$D_{\text{hel}}$ (kpc)	Ref.
HVS1	09:07:44.99	+02:45:06.90	+0.1 ± 0.3	-0.1 ± 0.2	...	831.1 ± 5.7	107.0 ± 15.0	1
HVS2	09:33:20.86	+44:17:05.40	-5.363 ± 0.391	+1.285 ± 0.382	-0.2092	917.0 ± 7.0	8.5 ± 1.0	1,2,3
HVS3	04:38:12.80	-54:33:12.00	+0.851 ± 0.110	+1.936 ± 0.162	+0.1899	723.0 ± 3.0	61.0 ± 10.0	1,2
HVS4	09:13:01.01	+30:51:19.80	-0.2 ± 0.4	-0.4 ± 0.4	...	600.9 ± 6.2	64.0 ± 9.8	1
HVS5	09:17:59.48	+67:22:38.30	-0.023 ± 0.176	-1.179 ± 0.268	+0.2162	545.5 ± 4.3	45.0 ± 5.2	1,2
HVS6	11:05:57.45	+09:34:39.47	-0.378 ± 0.664	-0.503 ± 0.507	-0.0242	609.4 ± 6.8	55.0 ± 6.9	1,2
HVS7	11:33:12.12	+01:08:24.90	-0.677 ± 0.373	+0.457 ± 0.253	-0.2767	526.9 ± 3.0	52.0 ± 6.4	1,2
HVS8	09:42:14.04	+20:03:22.10	-0.972 ± 0.365	+0.117 ± 0.369	-0.3844	499.3 ± 2.9	53.0 ± 9.8	1,2
HVS9	10:21:37.08	-00:52:34.80	+0.412 ± 0.743	-0.213 ± 0.747	-0.2503	616.8 ± 5.1	74.0 ± 12.0	1,2
HVS10	12:03:37.85	+18:02:50.40	-2.597 ± 1.288	-0.788 ± 0.494	+0.0151	467.9 ± 5.6	52.0 ± 5.8	1,2
HVS12	10:50:09.59	+03:15:50.67	+0.420 ± 1.377	+0.285 ± 0.993	+0.2614	552.2 ± 6.6	66.0 ± 8.5	1,2
HVS13	10:52:48.30	-00:01:33.94	-0.9 ± 0.4	+0.5 ± 0.4	...	569.3 ± 6.1	105.0 ± 19.0	1
HVS15	11:33:41.09	-01:21:14.25	-0.498 ± 1.291	-0.487 ± 0.567	-0.0546	461.0 ± 6.3	67.0 ± 10.0	2,4
HVS16	12:25:23.40	+05:22:33.84	-1.895 ± 1.518	-1.145 ± 0.856	-0.4290	429.8 ± 7.0	71.0 ± 12.0	2,4
HVS17	16:41:56.39	+47:23:46.12	-1.034 ± 0.198	-1.065 ± 0.323	+0.0801	250.2 ± 2.9	49.0 ± 4.0	2,4
HVS18	23:29:04.94	+33:00:11.47	-0.123 ± 0.656	-0.119 ± 0.495	+0.2130	237.3 ± 6.4	80.0 ± 11.0	2,4
HVS19	11:35:17.75	+08:02:01.49	-0.295 ± 1.790	+0.413 ± 1.224	-0.3625	592.8 ± 11.8	98.0 ± 15.0	2,4
HVS20	11:36:37.13	+03:31:06.84	+0.453 ± 1.451	+0.569 ± 1.014	-0.2955	512.1 ± 8.5	76.0 ± 11.0	2,4
HVS21	10:34:18.25	+48:11:34.57	+0.099 ± 0.693	-0.263 ± 0.881	-0.3749	356.8 ± 7.5	113.0 ± 21.0	2,4
HVS22	11:41:46.44	+04:42:17.29	+0.184 ± 2.024	+1.987 ± 1.443	-0.2758	597.8 ± 13.4	85.0 ± 13.0	2,4
HVS24	11:11:36.44	+00:58:56.44	+0.301 ± 0.777	-0.408 ± 0.578	-0.1616	492.5 ± 5.3	56.0 ± 7.0	2,4
LAMOST-HVS1	09:12:06.52	+09:16:21.80	-3.537 ± 0.110	-0.62 ± 0.093	-0.2516	611.7 ± 4.6	13.9 ± 2.0	2,5
LAMOST-HVS2	16:20:20.77	+37:47:39.90	-2.563 ± 0.056	-0.924 ± 0.072	+0.2943	341.1 ± 7.8	22.2 ± 4.6	2,6
LAMOST-HVS3	03:21:17.08	+19:07:36.20	+1.509 ± 0.199	-0.281 ± 0.155	+0.0972	361.5 ± 12.5	22.3 ± 2.5	2,6
HD271791	06:02:27.88	-66:47:28.68	-0.619 ± 0.067	4.731 ± 0.071	+0.0996	441.0 ± 1.0	21.0 ± 4.0	2,7
HIP60350	12:24:30.23	+34:57:58.72	-13.51 ± 1.31	+16.34 ± 1.37	...	262.0 ± 5.0	3.1 ± 0.6	8

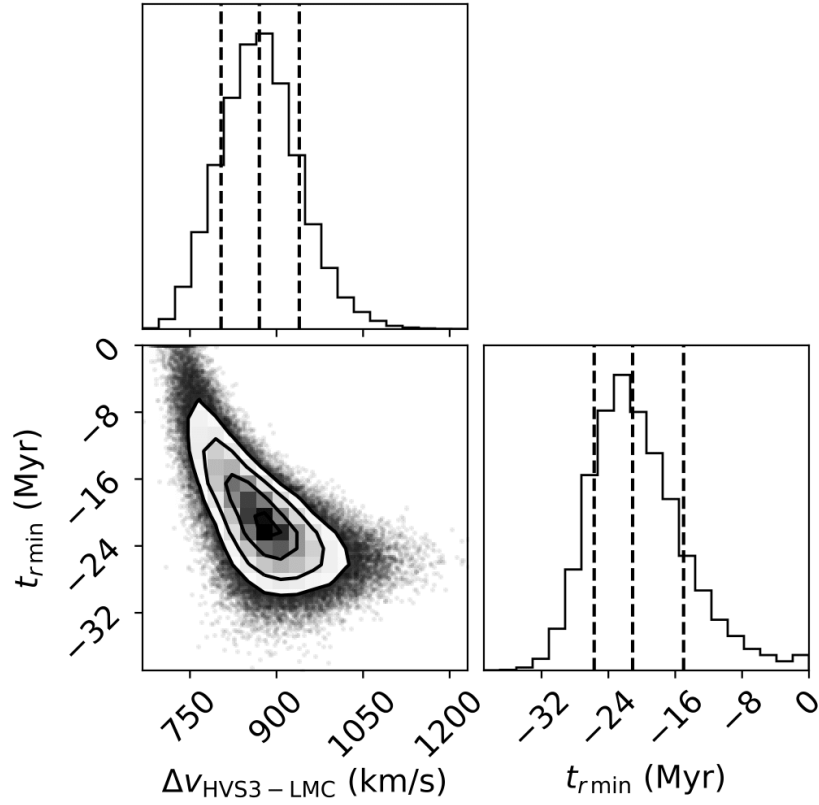


Figure 5.7: Distribution of relative velocities to the LMC and ejection times for HVS3. The dashed lines show the 15.9, 50, and 84.1 percentiles of each 1d distribution. The contours shown are 0.5, 1, 1.5, and  $2\sigma$ . Originally published in Erkal, Boubert, Gualandris, Evans, and Antonini (2018).

travelling parallel to the sky at a distance of 1 kpc, then these velocities translate to a  $0.5 \text{ mas yr}^{-1}$  proper motion which should be obvious with *Gaia* DR2. A search for these objects was lead by Ken Shen and described in Shen et al. (2018). The strategy of the search was to use *Gaia* astrometry and photometry to identify candidates and then obtain spectroscopic follow-up.

I was heavily involved in the project and was consequently second author. I worked with Ken Shen to estimate the number of these objects: we assumed that one such object is produced in each of the  $10^{-13} \text{ SNe yr}^{-1} \text{ M}_{\odot}^{-1}$  estimated for the Milky Way (Li, Chornock, et al., 2011) and that the progenitor binaries reside in the thin disc, with an exponential scale length of 2.6 kpc, an exponential scale height of 0.3 kpc, and a normalization that yields a total stellar mass of  $5 \times 10^{10} \text{ M}_{\odot}$  (Bland-Hawthorn & Gerhard, 2016). Objects moving at these velocities travel in essentially straight lines and thus we neglected the Milky Way potential. The number within 1 kpc of the Sun can then be obtained by an integral over the location of ejection

and the ejection direction, and if we assume that all such objects are objected at  $1800 \text{ km s}^{-1}$  we would expect between 17 and 39 of these objects. Note that this number is not a prediction for the number of objects we should find in DR2, because it assumes that we see objects if and only they are within 1 kpc and we will only be able to identify these objects if they have a sufficiently large proper motion and are still bright. Note that these objects are likely to rapidly cool.

I was also involved in determining an initial filter to apply to *Gaia* DR2. Ken Shen identified that a useful selection was to take only those stars with total proper motion  $\mu > \chi \text{ mas yr}^{-1}$ , and then to rank the remaining stars by  $v_{3\sigma} \equiv \mu/(\varpi + 3\sigma_\varpi)$  and take the top N stars as likely candidates for follow-up. Note that  $\mu/\varpi$  is proportional to the tangential velocity of the star, and thus by including the  $3\sigma_\varpi$  term we are calculating a lower bound on the tangential velocity. This selection has two parameters,  $\chi$  and N, and I explored these by constructing a synthetic population of contaminants and hypervelocity white dwarfs. I obtained the contaminants by querying the *Gaia* DR2 mock of Rybizki et al. (2018). The synthetic white dwarf population was obtained by Monte-Carlo sampling  $10^4$  realisations of the hypervelocity white dwarf model described in the previous paragraph (the white dwarfs were statistically down-weighted by  $10^4$  to account for this). I assumed an absolute magnitude of the white dwarfs and only included those with an apparent magnitude brighter than  $G = 20.7$ . The filter described above will only pull out the nearest white dwarfs and so it was found that the choice of absolute magnitude was not overly important. Using the apparent magnitude and a typical colour of  $V - I = -0.3$ , I estimated the *Gaia* DR2 parallax uncertainty using the fit provided on the ESA webpages<sup>4</sup> and convolved the parallax with this uncertainty. I applied the selection described above to the combined synthetic population, varying both  $\chi$  and N. It was found that a choice of  $\chi = 211 \text{ mas yr}^{-1}$  and  $N = 500$  resulted in a true positive to false positive ratio of 35 : 465 (although note this is a conservative choice, because changing N to 100 reduced this to 32 : 68).

After ranking, the next step of the search was to use a Bayesian method to estimate the distance to each star, using as a prior the exponentially-decreasing volume prior of Astraatmadja and Bailer-Jones (2016), and then to calculate  $P_{1000}$  (probability the tangential velocity is greater than  $1000 \text{ km s}^{-1}$ ) and  $P_{1000-3000}$  (probability the tangential velocity is between  $1000$  and  $3000 \text{ km s}^{-1}$ ). A distance prior should always be tuned to the specific subset of *Gaia* sources that are being considered and thus I tuned the scale-length of

<sup>4</sup> Accessed at <https://www.cosmos.esa.int/web/gaia/science-performance> on 06/07/2018.

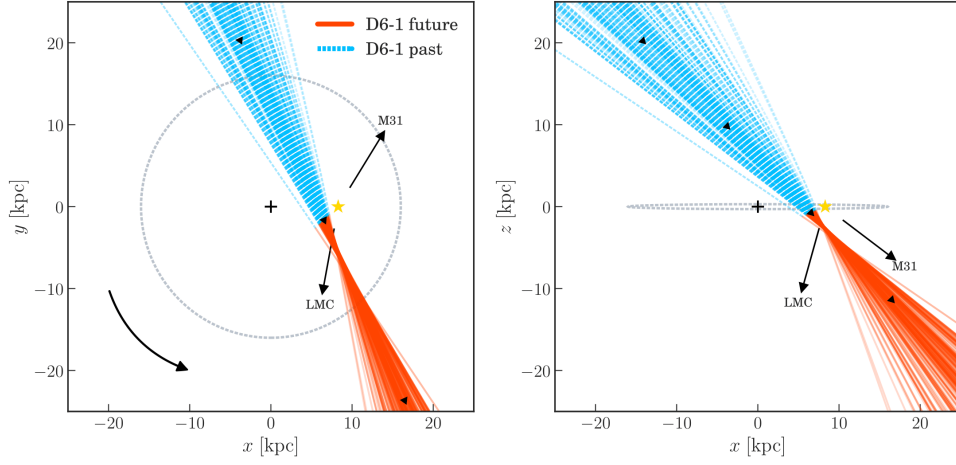
<i>Gaia</i> DR2 ID	Name	Parallax (mas)	$\mu$ (mas)	$v_{3\sigma}$ ( km s <sup>-1</sup> )	P <sub>1000</sub>	RV ( km s <sup>-1</sup> )	$v_{\text{Galacto}}$ ( km s <sup>-1</sup> )
5805243926609660032	D6-1	$0.47 \pm 0.10$	$211.7 \pm 0.2$	1293	1.00	$1200 \pm 40$	2300 [1600 – 6600]
1798008584396457088	D6-2	$1.05 \pm 0.11$	$259.8 \pm 0.2$	894	0.98	$20 \pm 60$	1300 [1000 – 1900]
2156908318076164224	D6-3	$0.43 \pm 0.13$	$211.7 \pm 0.3$	1247	1.00	$-20 \pm 80$	2400 [1400 – 9000]

Table 5.3: Properties of the three hypervelocity white dwarfs identified in Shen et al. (2018). This Table is an amalgamation of Table 1 and Table 3 of Shen et al. (2018).

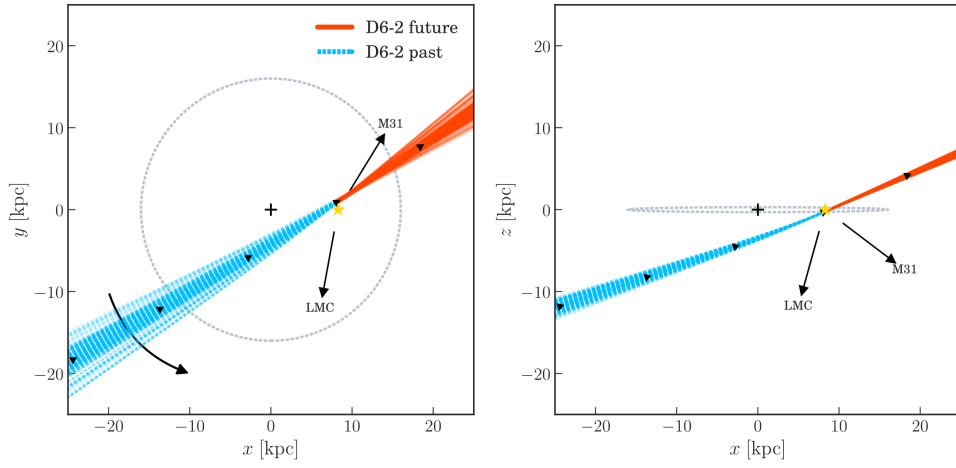
the prior using the true distances of the synthetic population above. We expected our selection to be highly efficient, because the high proper motion contaminants should be stars which are nearby (within 0.5 kpc) and so should have well-measured parallaxes and thus well-constrained tangential velocities.

I was not involved in carrying out the search on *Gaia* DR2 nor the spectroscopic follow-up to obtain radial velocities (RVs), however the search went well and three sources were confirmed to be high velocity objects (listed in Tab. 5.3). All three of these objects have truly fast Galactocentric velocities  $v_{\text{Galacto}}$  and are likely to be the three fastest known stars in the Milky Way, with the possible exception of pulsars kicked in core-collapse supernova or the S-stars in orbit around the massive black hole at the Galactic centre. Our interpretation is that D6-1, D6-2 and D6-3 are runaway companions of Type Ia supernova, however the tidal disruption of white dwarf binaries in the Hills mechanism could produce white dwarfs travelling at these speeds. I verified that this was not the case by integrating the orbits of the three objects (Fig. 5.8) using the MW POTENTIAL2014 in the Galactic dynamics PYTHON module GALPY (Bovy, 2015). It is clear that all three candidates are unbound from the Milky Way and that almost none of the orbital solutions passes near the Galactic centre. Taken as a group, it is highly unlikely that the hypervelocity nature of these stars is due to ejection from the Galactic centre by the Hills mechanism.

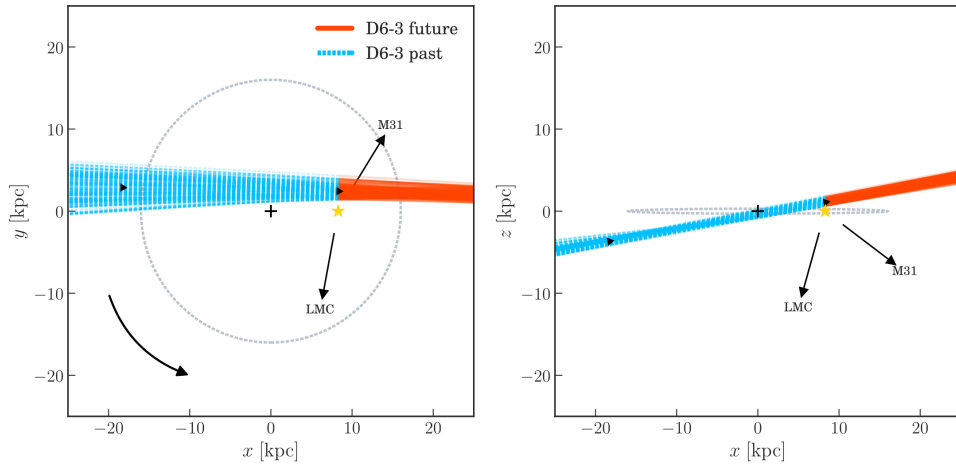
I obtained one of the crucial pieces of evidence that affirmed the connection with Type Ia supernovae by showing that D6-2 tracks back to the centre of the supernova remnant G70.0-21.5 roughly  $9 \times 10^4$  yr ago. G70.0-21.5 is the furthest known supernova remnant from the Galactic plane, making it unlikely that this is a chance alignment, and the age of this supernova remnant estimated by Fesen, Neustadt, Black, and Koepfel (2015) is consistent with the track-back time of D6-2. Taken together with the extreme radial velocity of D6-1 ( $1200 \pm 40$  km s<sup>-1</sup>) and that all three object lie together in the *Gaia* colour-magnitude diagram (see. Fig. 10 of Shen et al., 2018), these three fast stars are strong evidence for the D<sup>6</sup> model of Type Ia supernovae.



(a) Orbit solution of D6-1.



(b) Orbit solution of D6-2.



(c) Orbit solution of D6-3.

Figure 5.8: Sample realizations of the orbital solutions (past trajectories in blue; future trajectories in red). The Milky Way's thin disc is overlaid in gray contours. A face-on view is shown in the left panel; the right panel shows an edge-on perspective. The Sun's location is marked with a star, and the Galaxy's rotation and the directions to the LMC and M31 are denoted with arrows. Originally published in Shen et al. (2018).

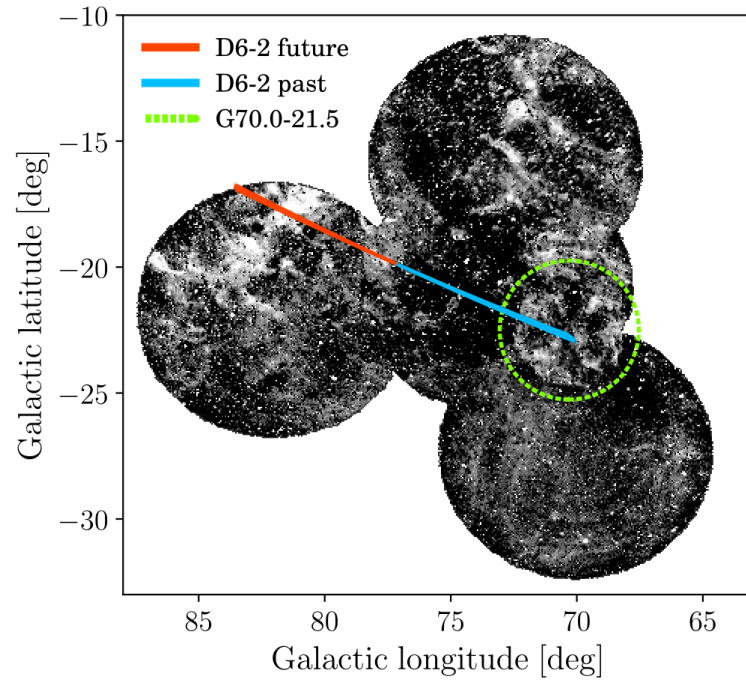


Figure 5.9: The orbital solution of D6-2 overlaid on  $H\alpha$  images from Virginia Tech Spectral Line Survey (VTSS; Dennison, Simonetti, and Topasna 1998). The blue and red trajectories extend  $9 \times 10^4$  yr into D6-2's past and future, respectively. The green circle encompasses the spherical shell of the remnant G70.0-21.5. Originally published in Shen et al. (2018).

## CONCLUSION

---

Fast stars trace back to the most energetic stellar events in the Universe: the tidal disruption of binaries by massive black holes and thermonuclear and core-collapse supernovae. If we can connect them to their place of birth they can be used to measure the shape and mass of the Galaxy or to infer the history of the progenitor supernova. Fast stars can, however, be secretive about where they come from. This thesis was dedicated to decoding the origins of fast stars: by tracking B stars and white dwarfs back to the centres of supernova remnants; by deducing why the Be stars are spinning from their speed; by showing that the hypervelocity stars might have travelled from another galaxy.

This thesis can be broadly split into two parts: in Chapters 2 and 3 I laid the groundwork for the proper Bayesian study of Galactic runaway stars with *Gaia*, while in Chapters 4 and 5 I rewrote the paradigm of the hypervelocity stars.

Companions left behind in supernovae are sought because they can tell us the evolutionary history of the system and thus be used to constrain theories of binary stellar physics. The history of searches for these companions contains a number of successes, the most convincing example being the association of HD 37424 with S147 by Dinçel et al. (2015), but these searches have been limited in scope; they were tailored to individual remnants and relied on qualitative judgements of candidates. I have moved the field onward by building a statistical framework to judge candidates in a quantitative way, incorporating data from *Gaia* DR1 and APASS with a 3D Galactic dust-map and binary stellar population synthesis. My approach is able to confidently recover HD 37424 and thus is at least as effective as tailored searches. My method will transform the search for supernova remnant companions from tailored hunts in the nearest and youngest supernova remnants to the wholesale analysis of tens or hundreds of supernova remnants using data from *Gaia* DR2.

It is widely-accepted that the emission lines of a Be star arise from a decretion disc launched from the equator of a critically-rotating B star; it is, however, not known how these stars came to be spinning so rapidly. If the Be stars were spun up by mass transfer from a companion (Pols et al., 1991) then many Be stars should be runaway stars. Berger and Gies (2001) tested this prediction by calculating the fraction of Be stars that had peculiar velocities greater than  $40 \text{ km s}^{-1}$ ,



however this ignores that many runaway Be stars will have been kicked with velocities less than  $20 \text{ km s}^{-1}$ . By properly applying a Bayesian methodology to this problem, I was able to show that the occurrence of Be star runaways was consistent with the mass transfer hypothesis. I made several novel advances in this work, particularly the use of spectral types and luminosity classes to account for the selection bias towards brighter Be stars. The work presented in Chapter 3 demonstrates that the kinematics of Be stars is vital to understanding the phenomenon; I plan to construct an Open Be Stars Catalog, in analogy with the Open Fast Stars Catalog, which will combine the extensive spectra from the Be Star Spectra database with kinematic information from *Gaia* DR2. I will then apply my Bayesian methodology to this new catalogue and determine conclusively whether Be stars have an exclusively binary origin.

Brown (2015) stated that ‘there is no good explanation for the anisotropic distribution of unbound late B-type stars in the halo’. I have answered this challenge by exposing a widely-held misconception about the hypervelocity stars: it is not a certainty that the two dozen B-type hypervelocity stars have escaped from the Galactic centre. On the contrary, I have shown through simulation that they are best explained as Hills or runaway stars from the Large Magellanic Cloud. Questions remain regarding my hypothesis: we have not yet found a massive black hole in the LMC and the runaway stars we would predict are too low mass, however, there is emerging evidence in support of my hypothesis including proof of an  $8 M_{\odot}$  hypervelocity stars ejected at  $870 \text{ km s}^{-1}$  from the LMC (Erkal et al., 2018) and a vindication of my prediction that some of the young stars on the outskirts of the LMC discussed by Moni Bidin et al. (2017) are runaway stars (Casetti-Dinescu et al., 2018). My hypothesis predicts the existence of hundreds more hypervelocity stars in the Southern hemisphere and work is on-going with *Gaia* DR2 to make this test. I have been awarded three nights of telescope time in late December to follow-up the candidates I identify.

In my opening sentence I facetiously described the literature as being littered with fast stars; in all seriousness, it was littered with hypervelocity star candidates. I performed a service for the community by cataloguing all of the candidates in the Open Fast Stars Catalog and then re-analysing every candidate with *Gaia* DR2 data. In the remainder of Chapter 5, I described by contributions to the proof that HVS3 was ejected from the LMC and to the discovery of three hypervelocity runaway white dwarfs from Type Ia supernovae.

While I have made substantial progress towards answering the open questions I posed in the Introduction, the work done prior to *Gaia* DR2 was truly only preparation for that dataset. In the coming



years I will be able to use tens of runaway supernova remnant companions and the kinematics of runaway Be stars to shine a light on the unconquered problems in binary stellar evolution and to use hypervelocity stars to map the dynamics of the Local Group. The era of fast stars is fast-approaching.



## APPENDIX

## A.1 THE LOCAL SUPERNOVA REMNANTS (SNRS)

*Based on work originally published in Boubert, Fraser, et al. (2017).*

My strategy to obtain distances is simple. I begin with the list of SNRs with known distances in the literature which Pavlovic, Dobardzic, Vukotic, and Urosevic, 2014 used to calibrate their  $\log D$  relation. I check the source cited by Pavlovic et al., 2014 for each measurement. I then conduct my own literature search to see if there are more recent distances available, starting with the SNR catalogues of Green (2014) and Ferrand and Safi-Harb (2012). Some distances for SNRs in the Green (2014) catalogue are given in the more detailed online version<sup>1</sup>. Below I discuss my arguments for the chosen distance and age used for each SNR. However, I emphasise that the distance is not a major factor in my method because I constrain the runaways to lie on the main sequence and so constrain the distance to a narrow range. For the SNRs where there is no error attached to the best distance estimate, I assume a nominal 50% error.

1. G065.3+5.7 : Boumis et al. (2004) combined an expansion velocity measurement of  $155 \text{ km s}^{-1}$  with a proper motion in the optical of  $2.1 \pm 0.4 \text{ arcsec}$  in 48 years to derive a distance  $0.77 \pm 0.2 \text{ kpc}$ .
2. G069.0+2.7 (CTB 80) : A commonly cited distance estimate for G069.0+02.7 is 2 kpc from Koo, Reach, Heiles, Fesen, and Shull (1990), however in the original paper the estimate is given in the form  $2d_2 \text{ kpc}$  where  $d_2$  is a scaling factor of order unity. Koo, Yun, Ho, and Lee (1993) constrained this parameter to  $1.0 \pm 0.3$ . Leahy and Ranasinghe (2012) bound the distance to the range 1.1–2.1 kpc and pick a nominal distance of 1.5 kpc. I assume a distance  $1.5 \pm 0.5 \text{ kpc}$ , where I have added a nominal 0.5 kpc error.

<sup>1</sup> Green D. A., 2014, ‘A Catalogue of Galactic Supernova Remnants (2014 May version)’, Cavendish Laboratory, Cambridge, United Kingdom (available at <http://www.mrao.cam.ac.uk/surveys/snrs/>).

3. G074.0–8.5 (Cygnus Loop) : Blair, Sankrit, and Raymond (2005) used a measured shock velocity of  $155 \text{ km s}^{-1}$  with HST proper motion of  $0.070 \pm 0.008 \text{ arcsec yr}^{-1}$  to derive a distance  $0.54^{+0.10}_{-0.08} \text{ kpc}$ .
4. G089.0+4.7 (HB 21) : There are two competing distance estimates in the literature. Tatematsu, Fukui, Landecker, and Roger (1990) arrived at a distance estimate by establishing an interaction with molecular clouds in the Cyg OB7 association and then taking the distance of that association  $0.80 \pm 0.07 \text{ kpc}$  (Humphreys, 1978) to be the distance of the SNR. Note, however, that a more recent distance estimate of Cyg OB7 using *Hipparcos* parallaxes (ESA, 1997) gives the distance  $0.6 \text{ kpc}$  (Mel’Nik & Dambis, 2009). Byun, Koo, Tatematsu, and Sunada (2006) discussed the link between HB 21 and molecular clouds in Cyg OB7 and argued that, while there were morphological similarities, there was no direct evidence for the association. Byun et al. (2006) discusses other distance estimates in the literature and arrives at a distance estimate of  $1.7 \pm 0.5 \text{ kpc}$ . One key argument used by Byun et al. (2006) is that the X-ray surface brightness of HB 21 is too faint for  $0.8 \text{ kpc}$  and that it must be beyond  $1.6 \text{ kpc}$  (Yoshita, 2001). Updating the distance of Cyg OB7 using the *Hipparcos* parallaxes increases this tension and favours the distance  $1.7 \pm 0.5 \text{ kpc}$ . I assume that HB 21 lies at  $1.7 \pm 0.5 \text{ kpc}$ .
5. G093.7–0.2 (CTB 104A, DA 551) : Uyaniker, Kothes, and Brunt (2002) calculated a distance of  $1.5 \pm 0.2 \text{ kpc}$  based on the kinematics of HI features associated with the remnant. I assume this distance estimate.
6. G114.3+0.3 : The most recent estimate of  $0.7 \text{ kpc}$  is based on association with HI emission features (Yar-Uyaniker, Uyaniker, & Kothes, 2004). I assume a distance estimate of  $0.70 \pm 0.35 \text{ kpc}$  with a nominal 50% error.
7. G119.5+10.2 (CTA 1) : Pineault, Landecker, Madore, and Gaumont-Guay (1993) calculated a distance of  $1.4 \pm 0.3 \text{ kpc}$  based on an association with an HI shell.
8. G160.9+2.6 (HB 9) : Leahy and Tian (2007) estimated the distance at  $0.8 \pm 0.4 \text{ kpc}$  using HI absorption.
9. G180.0–1.7 (S147) : G180.0–01.7 is notable for being a nearby SNR with a convincing runaway candidate (Dinçel et al., 2015). Sallmen and Welsh (2004) noted that HD 36665 at  $880 \text{ pc}$  (photometric distance from Phillips, Gondhalekar, & Blades, 1981)

and HD 37318 at 1380 pc had absorption lines at a similar velocity to the expansion of the SNR shell, while HD 37367 at  $361^{+150}_{-85}$  pc (parallax from ESA, 1997) did not have such lines. Sallmen and Welsh (2004) estimated a distance of 0.62 kpc based on the SNR lying in between HD 37367 and HD 36665. I was unable to locate the original source for the distance estimate of HD 37318. Dinçel et al. (2015) argued that the likely association of G180.0–01.7 with the pulsar PSR J0538+2817 makes the most accurate distance  $1.30^{+0.22}_{-0.16}$  kpc (parallax measurement by Chatterjee et al., 2009). The tension between the distance derived by looking for stars in front and behind the supernova shell and the distance obtained from the parallax of the associated pulsar may be relieved by more accurate distance measurements from the second *Gaia* data release. I assume the distance estimate  $1.30^{+0.22}_{-0.16}$  kpc.

10. G205.5+0.5 (Monoceros Loop) : There are two distances in the literature. A distance of 0.6 kpc based on the mean optical velocity and a distance of 1.6 kpc from Xiao and Zhu (2012). I assume a distance of  $1.2 \pm 0.6$  kpc, where I take a nominal 50% error.

## A.2 BINARY\_C

*Based on work originally published in Boubert, Erkal, et al. (2017), Boubert, Fraser, et al. (2017) and Boubert and Evans (2018).*

Throughout this thesis I model the evolution of binaries across a grid in parameter space using the BINARY\_C population-synthesis framework (Izzard et al., 2006; Izzard et al., 2009; Izzard et al., 2004). This code is based on the binary-star evolution (BSE) algorithm of Hurley et al. (2002) expanded to incorporate nucleosynthesis, wind-Roche-lobe-overflow (Abate, Pols, Izzard, Mohamed, & de Mink, 2013; Abate et al., 2015), stellar rotation (de Mink et al., 2013), accurate stellar lifetimes of massive stars (Schneider et al., 2014), dynamical effects from asymmetric supernovae (Tauris & Takens, 1998), an improved algorithm describing the rate of Roche-lobe overflow (Claeys, Pols, Izzard, Vink, & Verbunt, 2014), and core-collapse supernovae (Zapartas, de Mink, Van Dyk, et al., 2017). In particular, I take my black hole remnant masses from Spera, Mapelli, and Bressan (2015) and use a fit to the simulations of Liu et al. (2015) to determine the impulse imparted by the supernova ejecta on the companion.

Grids of stars are modelled using the BINARY\_GRID2 module to explore the single-star parameter space as a function of stellar mass  $M$ ,

and the binary-star parameter space in primary mass  $M_1$ , secondary mass  $M_2$  and orbital period  $P_{\text{orb}}$ .

### A.3 IMPLEMENTATION OF MULTINEST

*Based on work originally published in Boubert, Fraser, et al. (2017).*

MULTINEST explores the parameter space of a model by choosing new samples from within an ellipse containing the current samples. This sampling requires that the prior be expressible as a uniform distribution on the unit hypercube. To encode non-trivial distributions, these  $N$  random variables distributed as  $U(0, 1)$  must be transformed into the parameter space. Through this procedure, the prior is automatically normalised. For independent random variables, this is a simple application of inverse transform sampling. However, for dependent variables  $\mathbf{x}$ , the simplest course is usually to move the prior  $f(\mathbf{x})$  to the likelihood function and use a uniform prior over the entire permitted parameter space for each variable when doing the transform. A correction must then be applied to remove the normalisation that MULTINEST has applied in the prior. This becomes non-trivial if there is any area of the parameter space where the likelihood function returns a negligibly small number, since MULTINEST treats that area of the parameter space as invalid and so renormalises the parameter space to exclude it. This behaviour is problematic if the likelihood is zero over large parts of the parameter space because it means that the calculated evidence is wrong. The reason for this behaviour is that it allows the user to encode constraints between variables in the prior. One physical example is if the radii  $R_1$  and  $R_2$  of two stars in a binary system are not constrained, but the separation  $a$  is known. This can be encoded as  $R_1 + R_2 < a$  and implemented by returning zero in the likelihood if the constraint is broken. MULTINEST then renormalises the prior to exclude those regions that break the constraint. This behaviour is one way to have a uniform distribution over an arbitrarily complicated support. To sidestep this behaviour I instead return  $ue^{-10^{20}}$  where  $u \sim U(1, 1.0001)$ , since this is both a negligibly small number and above the default threshold for MULTINEST to ignore. The reason for including the random variation is that in Nested Sampling the likelihood of the points is sorted as part of the algorithm and the case where two points have the same likelihood is important. Skilling (2006) mentions that it is necessary to resolve ties between points of equal likelihood and that this can be achieved by adding a small random number of sufficient precision that repeats are unlikely.

## A.4 THE OPEN FAST STARS CATALOG

*Based on work originally published in Boubert et al. (2018).<sup>2</sup>*

The papers which originally proposed the late-type hypervelocity candidates discussed in the main text often give measurements of properties not generically included in *Gaia*, such as spectral types, radial velocities and other spectroscopic parameters. Combining these properties in a systematic, rigorous fashion with *Gaia* astrometry and photometry is crucial to determining the nature of these candidates. To that end, we have created the Open Fast Stars Catalog (OFSC)<sup>3</sup> utilizing the AstroCats framework (Guillochon et al., 2017). The objective of the catalogue is to contain a curated collection of every measurement of all high-velocity star candidates in the literature, with each measurement having a citable origin, and to utilize the available data to provide additional value to the community interested in these objects. At present, the OFSC has targeted the data available for stars that may potentially be hypervelocity stars, however we plan to expand it to include pulsars, runaway stars, and halo stars in the near future.

Like the other Open Astronomy Catalogs<sup>4</sup>, the OFSC adds value to the existent data by providing derived quantities to the community. The catalog automatically computes the amount of extinction to each object (see Section A.4.2), velocities in various frames (heliocentric, Galactocentric), observability at a user-specified time from various observatory locations, probability of boundedness to the Milky Way, and correlations between observed and derived quantities. The catalog also provides an interface for each object with a near-complete collection of its data. At the moment, the catalog only includes fast star spectroscopy from the SDSS survey (Abolfathi et al., 2018) and the LAMOST survey (Luo et al., 2016), as little is available from public repositories; we plan to collect this data from the community in the near future.

---

<sup>2</sup> The idea of a hypervelocity star catalogue was proposed indepenently by Keith Hawkins and Idan Ginsburg, but I took the initiative to create the Open Fast Stars Catalog using the ASTROCATS framework of James Guillochon. I implemented much of the functionality of the catalogue, including the querying of external catalogues and the determination of whether a star is bound. James Guillochon created the website, implemented the querying of LAMOST, and fixed many of the bugs that I introduced.

<sup>3</sup> See <https://faststars.space>.

<sup>4</sup> See <https://astrocats.space>.

## A.4.1 Determination of boundedness

The question of whether a star is hypervelocity can be more plainly phrased as “is the total velocity  $v_{\text{grf}}$  in the Galactic rest-frame greater than the escape speed  $v_{\text{esc}}$  at its current location?” Many of the papers which present hypervelocity star candidates give both the Galactic speed and the escape speed. However, the Galactic speed is sensitive to the assumed Solar position and peculiar motion and the escape speeds can vary by as much as  $100 \text{ km s}^{-1}$  depending on the potential used. We therefore re-calculate the Galactic rest-frame speed and the escape speed for each candidate. Assuming that we have the equatorial position  $(\alpha, \delta)$  and proper motions  $(\mu_{\alpha*}, \mu_{\delta})$  and the heliocentric distance  $d$  and radial velocity  $v_r$ , Johnson and Soderblom (1987) provide formulae for obtaining the cylindrical Galactocentric position  $(R, \theta, z)$  and velocity  $(v_R, v_{\theta}, v_z)$ . The total Galactic rest-frame speed is then the magnitude of this velocity. The escape velocity can be obtained from a fiducial escape velocity curve  $v_{\text{esc}}(r)$ , for instance Williams et al. (2017) parametrized this through

$$v_{\text{esc}}(r) = v_{\text{esc},\odot} \left( \frac{r}{R_{\odot}} \right)^{-\alpha/2}, \quad (\text{A.1})$$

where  $v_{\text{esc},\odot}$  is the escape velocity at the position of the Sun, and obtained posterior constraints of  $\alpha = 0.37^{+0.09}_{-0.09}$  and  $v_{\text{esc},\odot} = 521.26^{+45.79}_{-30.23} \text{ km s}^{-1}$  using main-sequence turn-off, blue horizontal branch and K giant stars. We assume that the Milky Way disc rotates with a flat circular velocity of  $V_c = 238 \pm 9 \text{ km s}^{-1}$  and that the Sun orbits at the Galactocentric radius  $R_{\odot} = 8.27 \pm 0.29 \text{ kpc}$  with a peculiar velocity  $(U_{\odot}, V_{\odot}, W_{\odot}) = (11.1 \pm 0.75 \pm 1, 12.24 \pm 0.47 \pm 2, 7.25 \pm 0.37 \pm 0.5) \text{ km s}^{-1}$  (Schönrich, 2012; Schönrich et al., 2010).

The method outlined in the previous paragraph would give a single  $v_{\text{grf}}$  and  $v_{\text{esc}}$  for each candidate and thus reduces the question of boundedness to simply which quantity is the greater. However, in practise, each of the heliocentric quantities will have attached uncertainties and it is vital to account for these. Care is required, because the uncertainty in the distance causes the uncertainties in the Galactic speed and escape speed to be correlated. The uncertainties in different measurements may themselves be correlated, with the notable example of *Gaia* providing the covariance matrix between the positions, parallax and proper motions. An additional complication is the need to use a sensible prior on the true distance of a star when converting parallax to distance (Bailer-Jones, 2015). We assume the exponentially-decreasing volume prior of Astraatmadja and Bailer-Jones (2016) which is a Gamma distribution with shape parameter



$k = 3$  and scale parameter  $L$ . When applying this methodology to *Gaia* DR1 astrometry we used  $L = 1.35$  kpc as recommended by Asstraatmadja and Bailer-Jones (2016). For *Gaia* DR2 astrometry we used the more complicated spatially-varying scale-length of Bailer-Jones, Rybizki, Fouesneau, Mantelet, and Andrae (2018) which was tuned to a mock of the contents of *Gaia* DR2 (Rybizki et al., 2018). We assume that the uncertainty on the positions and velocities are adequately described by a multivariate normal distribution centred on the measured values and with covariance matrix  $\mathbf{C}$ , where the off-diagonal terms are zero unless the star has *Gaia* astrometry. For each star, we use EMCEE (Foreman-Mackey et al., 2012) to draw  $10^4$  samples from the multivariate normal likelihood and distance prior. For any star with a photometric distance that has an uncertainty we replace the standard prior with a Gaussian distance prior centred on the photometric distance and a width equal to the uncertainty on that distance. We additionally sample in the Gaussian statistical and systematic uncertainty of the Solar position and motion. A further complication is that we do not yet have a firm knowledge of the escape velocity from the Milky Way, which we account for by sampling the parameters of the escape velocity curve from the posterior of Williams et al. (2017). The sampled values are then processed as described in the previous paragraph to give samples of  $v_{\text{grf}}$  and  $v_{\text{esc}}$ . We can thus quantify the probability of a star being unbound by the fraction of samples where  $v_{\text{grf}} > v_{\text{esc}}$ .

To make this quantification rigorous we apply the Brown, Cai, and DasGupta (2001) methodology. The posterior on the probability of a star being bound after  $N$  trials with the star being bound in  $N_b$  trials is a  $\text{Beta}(N_b + \frac{1}{2}, N - N_b + \frac{1}{2})$  distribution. The one-sigma confidence interval centered on the median is thus easily calculable numerically.

In the subset of cases where we do not have either the proper motions or radial velocity then we assume that the missing component(s) exactly cancels the sampled solar reflex, which is equivalent to calculating the minimum Galactocentric rest-frame velocity. In this case the bound probability can be interpreted as an upper limit on the true bound probability.

One small caveat of using *Gaia* DR2 parallaxes is that Luri et al. (2018) identified a global parallax offset of  $-0.029$  mas. We have accounted for this offset in our analysis. The inclusion of this offset causes stars with proper motions to become slightly more likely to be bound, however this effect is sub-dominant to the other uncertainties that we account for when calculating the bound probability.

#### A.4.2 Automatic querying of *Gaia* and other catalogues

To ensure the catalogue incorporates the latest measurements of each star, we automatically query against large astronomical catalogues such as *Gaia*, SDSS and PPMXL. The querying of astrometric and photometric catalogues uses the `ASTROQUERY` affiliated package of the `ASTROPY PYTHON` framework. The line-of-sight extinction to each star  $E(B-V)$  is obtained from the `DUSTMAPS` package which allows us to query the Green et al. (2018), Green et al. (2015) dust maps for stars with measured distances and lying in the Pan-STARRS footprint and the Schlegel et al. (1998) dust map for the other candidates. The querying of external catalogues is done assuming a cross-match radius of  $\text{Min}(2 \text{ arcsec}, 3 \times 10 \text{ yr} \times \mu_{\text{tot}})$ , where  $\mu_{\text{tot}}$  is the total proper motion of the candidate. Within this search radius we take the nearest neighbour. We also query the stars against SIMBAD (Wenger et al., 2000) to obtain other aliases that the stars may have, which will allow users to access the catalogue independent of their preferred naming convention.

#### A.4.3 The fast star graveyard

It is standard practise among the Open Astronomy Catalogs to split off objects which are no longer of interest, for instance transients falsely identified as supernovae are split off from the main Open Supernova Catalog. This practise is known as putting an object in the ‘graveyard’. In the OFSC, this can be interpreted as a statement that a fast star is highly unlikely to be unbound and thus should not be considered to be a hypervelocity candidate. The criteria for putting a star in the graveyard is that i) each of the six kinematic components have been measured, ii) the star has 5D astrometry from *Gaia* DR2, and iii) the star was bound in all of the  $10^4$  samples. Note that a star being in the graveyard does not mean that it has been deleted and it will be possible for a star to be resurrected as new data is obtained, for instance when *Gaia* DR3 is released. The only practical result of a star being in the graveyard is that it is not shown in the main section of the OFSC. 159 previously-claimed hypervelocity candidate stars were in the OFSC graveyard as of 01/06/2018.

## BIBLIOGRAPHY

---

- Abadi, M. G., Navarro, J. F., & Steinmetz, M. (2009). *ApJ*, 691, L63.
- Abate, C., Pols, O. R., Izzard, R. G., Mohamed, S. S., & de Mink, S. E. (2013). *A&A*, 552, A26.
- Abate, C., Pols, O. R., Stancliffe, R. J., Izzard, R. G., Karakas, A. I., Beers, T. C., & Lee, Y. S. (2015). *A&A*, 581, A62.
- Abolfathi, B., Aguado, D. S., Aguilar, G., Prieto, C. A., Almeida, A., Ananna, T. T., . . . Zou, H. (2018). *ApJS*, 235, 42.
- Althaus, L. G., & Benvenuto, O. G. (1997). *ApJ*, 477, 313.
- Altmann, M., Roeser, S., Demleitner, M., Bastian, U., & Schilbach, E. (2017). *A&A*, 600, L4.
- Antoniou, V., & Zezas, A. (2016). *MNRAS*, 459, 528.
- Arenou, F. (2010). *The simulated multiple stars*. Gaia DPAC.
- Argelander, F. W. A. (1842). *Astron. Nachrichten*, 19(26), 393.
- Arzoumanian, Z., Chernoff, D. F., & Cordes, J. M. (2002). *ApJ*, 568, 289.
- Astraatmadja, T. L., & Bailer-Jones, C. A. L. (2016). *ApJ*, 832, 137.
- Astropy Collaboration, Robitaille, T. P., Tollerud, E. J., Greenfield, P., Droettboom, M., Bray, E., . . . Streicher, O. (2013). *A&A*, 558, A33.
- Aumer, M., & Binney, J. J. (2009). *MNRAS*, 397, 1286.
- Backer, D. C. (1998). *ApJ*, 493, 873.
- Bailer-Jones, C. A. L., Rybizki, J., Fouesneau, M., Mantelet, G., & Andrae, R. (2018). *arXiv:1804.10121*.
- Bailer-Jones, C. A. L. (2015). *PASP*, 127, 994.
- Barnard, E. E. (1916). *AJ*, 29, 181.
- Battaglia, G., Helmi, A., Morrison, H., Harding, P., Olszewski, E. W., Mateo, M., . . . Shectman, S. A. (2005). *MNRAS*, 364, 433.
- Bedin, L. R., Ruiz-Lapuente, P., González Hernández, J. I., Canal, R., Filippenko, A. V., & Mendez, J. (2014). *MNRAS*, 439, 354.
- Belokurov, V. A., & Evans, N. W. (2002). *MNRAS*, 331, 649.
- Berger, D. H., & Gies, D. R. (2001). *ApJ*, 555, 364.
- Bersten, M. C., Benvenuto, O. G., Folatelli, G., Nomoto, K., Kuncarayakti, H., Srivastav, S., . . . Sahu, D. K. (2014). *AJ*, 148, 68.
- Bersten, M. C., Benvenuto, O. G., Nomoto, K., Ergon, M., Folatelli, G., Sollerman, J., . . . Tomasella, L. (2012). *ApJ*, 757, 31.
- Besla, G., Hernquist, L., & Loeb, A. (2013). *MNRAS*, 428, 2342.
- Besla, G., Kallivayalil, N., Hernquist, L., Robertson, B., Cox, T. J., van der Marel, R. P., & Alcock, C. (2007). *ApJ*, 668, 949.
- Blaauw, A. (1961). *Bull. Astron. Institutes Netherlands*, 15, 265.

- Blaauw, A. (1956). *PASP*, 68, 495.
- Blaauw, A., & Morgan, W. W. (1954). *ApJ*, 119, 625.
- Blair, W. P., Sankrit, R., & Raymond, J. C. (2005). *AJ*, 129, 2268.
- Bland-Hawthorn, J., & Gerhard, O. (2016). *ARA&A*, 54, 529.
- Boubert, D., & Evans, N. (2016). *ApJ*, 825, L6.
- Boubert, D., Fraser, M., Evans, N., Green, D., & Izzard, R. (2017). *A&A*, 606, A14.
- Boubert, D., Erkal, D., Evans, N. W., & Izzard, R. G. (2017). *MNRAS*, 469, 2151.
- Boubert, D., & Evans, N. W. (2018). *MNRAS*, 477, 5261.
- Boubert, D., Guillochon, J., Hawkins, K., Ginsburg, I., & Evans, N. W. (2018). *MNRAS*, 479, 2789.
- Boumis, P., Meaburn, J., López, J. A., Mavromataki, F., Redman, M. P., Harman, D. J., & Goudis, C. D. (2004). *A&A*, 424, 583.
- Bovy, J. (2015). *ApJS*, 216, 29.
- Bovy, J., & Rix, H.-W. (2013). *ApJ*, 779, 115.
- Bovy, J., Rix, H.-W., Liu, C., Hogg, D. W., Beers, T. C., & Lee, Y. S. (2012). *ApJ*, 753, 148.
- Branch, D., & Wheeler, J. C. (2017). *Supernova Explosions*. Astronomy and Astrophysics Library. Berlin: Springer-Verlag GmbH.
- Bromley, B. C., Kenyon, S. J., Brown, W. R., & Geller, M. J. (2009). *ApJ*, 706, 925.
- Bromley, B. C., Kenyon, S. J., Geller, M. J., Barcikowski, E., Brown, W. R., & Kurtz, M. J. (2006). *ApJ*, 653, 1194.
- Brown, L. D., Cai, T. T., & DasGupta, A. (2001). *Stat. Sci.* 16(2), 101.
- Brown, W. R. (2015). *ARA&A*, 53, 15.
- Brown, W. R., Anderson, J., Gnedin, O. Y., Bond, H. E., Geller, M. J., & Kenyon, S. J. (2015). *ApJ*, 804, 49.
- Brown, W. R., Anderson, J., Gnedin, O. Y., Bond, H. E., Geller, M. J., Kenyon, S. J., & Livio, M. (2010). *ApJ*, 719, L23.
- Brown, W. R., Geller, M. J., & Kenyon, S. J. (2009). *ApJ*, 690, 1639.
- Brown, W. R., Geller, M. J., & Kenyon, S. J. (2012). *ApJ*, 751, 55.
- Brown, W. R., Geller, M. J., & Kenyon, S. J. (2014). *ApJ*, 787, 89.
- Brown, W. R., Geller, M. J., Kenyon, S. J., & Bromley, B. C. (2009). *ApJ*, 690, L69.
- Brown, W. R., Geller, M. J., Kenyon, S. J., & Kurtz, M. J. (2005). *ApJ*, 622, L33.
- Brown, W. R., Geller, M. J., Kenyon, S. J., & Kurtz, M. J. (2006a). *ApJ*, 640, L35.
- Brown, W. R., Geller, M. J., Kenyon, S. J., & Kurtz, M. J. (2006b). *ApJ*, 647, 303.
- Brown, W. R., Geller, M. J., Kenyon, S. J., Kurtz, M. J., & Bromley, B. C. (2007a). *ApJ*, 660, 311.

- Brown, W. R., Geller, M. J., Kenyon, S. J., Kurtz, M. J., & Bromley, B. C. (2007b). *ApJ*, 671, 1708.
- Buchner, J., Georgakakis, A., Nandra, K., Hsu, L., Rangel, C., Brightman, M., . . . Kocevski, D. (2014). *A&A*, 564, A125.
- Busha, M. T., Wechsler, R. H., Behroozi, P. S., Gerke, B. F., Klypin, A. A., & Primack, J. R. (2011). *ApJ*, 743, 117.
- Byun, D.-Y., Koo, B.-C., Tatematsu, K., & Sunada, K. (2006). *ApJ*, 637, 283.
- Carpenter, B., Gelman, A., Hoffman, M. D., Lee, D., Goodrich, B., Betancourt, M., . . . Riddell, A. (2017). *J. Stat. Softw.* 76(1).
- Casetti-Dinescu, D. I., Girard, T. M., Bidin, C. M., Mendez, R. A., Vieira, K., Korchagin, V. I., & van Altena, W. F. (2018). *ApJ*.
- Casetti-Dinescu, D. I., Moni Bidin, C., Girard, T. M., Mendez, R. A., Vieira, K., Korchagin, V. I., & van Altena, W. F. (2014). *ApJ*, 784, L37.
- Casetti-Dinescu, D. I., Vieira, K., Girard, T. M., & van Altena, W. F. (2012). *ApJ*, 753, 123.
- Castelli, F., & Kurucz, R. L. (2004). *arXiv:astro-ph/0405087*.
- Chambers, K. C., Magnier, E. A., Metcalfe, N., Flewelling, H. A., Huber, M. E., Waters, C. Z., . . . Wyse, R. (2016). *arXiv:1612.05560*.
- Chatterjee, S., Briske, W. F., Vlemmings, W. H. T., Goss, W. M., Lazio, T. J. W., Cordes, J. M., . . . Kramer, M. (2009). *ApJ*, 698, 250.
- Chernyakova, M., Babyk, I., Malyshev, D., Vovk, I., Tsygankov, S., Takahashi, H., & Fukazawa, Y. (2017). *MNRAS*, 470, 1718.
- Chojnowski, S. D., Whelan, D. G., Wisniewski, J. P., Majewski, S. R., Hall, M., Shetrone, M., . . . Simmons, A. (2015). *AJ*, 149, 7.
- Cignoni, M., Sabbi, E., van der Marel, R. P., Tosi, M., Zaritsky, D., Anderson, J., . . . Zeidler, P. (2015). *ApJ*, 811, 76.
- Cioni, M.-R. L., van der Marel, R. P., Loup, C., & Habing, H. J. (2000). *A&A*, 359, 601.
- Claeys, J. S. W., Pols, O. R., Izzard, R. G., Vink, J., & Verbunt, F. W. M. (2014). *A&A*, 563, A83.
- Clemens, J. C., Crain, J. A., & Anderson, R. (2004). The Goodman spectrograph. In A. F. M. Moorwood & I. Masanori (Eds.), *Ground-based instrumentation for astronomy* (Vol. 5492, p. 331). Proceedings of the SPIE.
- Cordes, J. M., & Chernoff, D. F. (1998). *ApJ*, 505, 315.
- Cui, X.-Q., Zhao, Y.-H., Chu, Y.-Q., Li, G.-P., Li, Q., Zhang, L.-P., . . . Zou, S.-C. (2012). *Res. Astron. Astrophys.* 12, 1197.
- De Marchi, G., Paresce, F., Panagia, N., Beccari, G., Spezzi, L., Sirianni, M., . . . Young, E. T. (2011). *ApJ*, 739, 27.
- De Marco, O., & Izzard, R. G. (2017). *PASA*, 34, e001.

- de Mink, S. E., Brott, I., Cantiello, M., Izzard, R. G., Langer, N., & Sana, H. (2012). Challenges for Understanding the Evolution of Massive Stars: Rotation, Binarity, and Mergers. In *Proc. a sci. meet. honor anthony f. j. moffat* (Vol. 465, p. 65). San Francisco: Astronomical Society of the Pacific.
- de Mink, S. E., Langer, N., Izzard, R. G., Sana, H., & de Koter, A. (2013). *ApJ*, 764, 166.
- de Mink, S. E., Sana, H., Langer, N., Izzard, R. G., & Schneider, F. R. N. (2014). *ApJ*, 782, 7.
- Dennison, B., Simonetti, J. H., & Topasna, G. A. (1998). *PASA*, 15, 147.
- Dewi, J. D. M., & Tauris, T. M. (2000). *A&A*, 360, 1043.
- Diñel, B., Neuhäuser, R., Yerli, S. K., Ankay, A., Tetzlaff, N., Torres, G., & Mugrauer, M. (2015). *MNRAS*, 448, 3196.
- Doppler, C. (1842). *Über das farbige Licht der Doppelsterne und einiger anderer Gestirne des Himmels*. Calve.
- Dravins, D., Lindegren, L., & Madsen, S. (1999). *A&A*, 348, 1040.
- Duchêne, G., & Kraus, A. (2013). *ARA&A*, 51, 269.
- Dufton, P. L., Dunstall, P. R., Evans, C. J., Brott, I., Cantiello, M., de Koter, A., ... Taylor, W. D. (2011). *ApJ*, 743, L22.
- Duquennoy, A., & Mayor, M. (1991). *A&A*, 248, 485.
- Edelmann, H., Napiwotzki, R., Heber, U., Christlieb, N., & Reimers, D. (2005). *ApJ*, 634, L181.
- Eldridge, J. J., Langer, N., & Tout, C. A. (2011). *MNRAS*, 414, 3501.
- Erkal, D., Boubert, D., Gualandris, A., Evans, N. W., & Antonini, F. (2018). *arXiv:1804.10197*.
- ESA. (1997). *The Hipparcos and Tycho catalogues*. Noordwijk: ESA Publications Division.
- Evans, D. S. (1967). The Revision of the General Catalogue of Radial Velocities. In A. H. B. Heard & J. Frederick (Eds.), *Iau colloq. 30: Determination of radial velocities and their applications* (Vol. 30, p. 57). London: Academic Press.
- Evans, K. A., & Massey, P. (2015). *AJ*, 150, 149.
- Evans, N. W., & Kerins, E. (2000). *ApJ*, 529, 917.
- Fang, J., Yu, H., & Zhang, L. (2017). *MNRAS*, 464, 940.
- Faucher-Giguère, C.-A., & Kaspi, V. M. (2006). *ApJ*, 643, 332.
- Feroz, F., Hobson, M. P., & Bridges, M. (2009). *MNRAS*, 398, 1601.
- Feroz, F., Hobson, M. P., Cameron, E., & Pettitt, A. N. (2013). *arXiv:1306.2144*.
- Feroz, F., & Hobson, M. P. (2008). *MNRAS*, 384, 449.
- Ferrand, G., & Safi-Harb, S. (2012). *Adv. Sp. Res.* 49, 1313.
- Fesen, R., Neustadt, J., Black, C., & Koepfel, A. (2015). *ApJ*, 812, 37.
- Folatelli, G., Bersten, M. C., Benvenuto, O. G., Van Dyk, S. D., Kuncarayakti, H., Maeda, K., ... Quimby, R. M. (2014). *ApJ*, 793, L22.
- Foreman-Mackey, D. (2016). *J. Open Source Softw.* 1.

- Foreman-Mackey, D., Hogg, D. W., Lang, D., & Goodman, J. (2012). *PASP*, 125, 306.
- Fragione, G., & Giacomo. (2018). *MNRAS*, 479, 2615.
- Freedman, W. L., Madore, B. F., Gibson, B. K., Ferrarese, L., Kelson, D. D., Sakai, S., . . . Stetson, P. B. (2000). *ApJ*, 553, 47.
- Fryer, C. L., Belczynski, K., Wiktorowicz, G., Dominik, M., Kalogera, V., & Holz, D. E. (2012). *ApJ*, 749, 91.
- Fryer, C., Burrows, A., & Benz, W. (1998). *ApJ*, 496, 333.
- Gaia Collaboration, Brown, A. G. A., Vallenari, A., Prusti, T., de Bruijne, J. H. J., Babusiaux, C., & Bailer-Jones, C. A. L. (2018). *A&A*.
- Gaia Collaboration, Brown, A. G. A., Vallenari, A., Prusti, T., de Bruijne, J. H. J., Mignard, F., . . . Zschocke, S. (2016). *A&A*, 595, A2.
- Gebel, W. L., & Shore, S. N. (1972). *ApJ*, 172, L9.
- Geier, S., Fürst, F., Ziegerer, E., Kupfer, T., Heber, U., Irrgang, A., . . . Waters, C. (2015). *Science*, 347, 1126.
- Geier, S., Marsh, T. R., Wang, B., Dunlap, B., Barlow, B. N., Schaffentroth, V., . . . Napiwotzki, R. (2013). *A&A*, 554, A54.
- Gelman, A., & Rubin, D. B. (1992). *Stat. Sci.* 457.
- Gies, D. R., Bagnuolo Jr., W. G., Ferrara, E. C., Kaye, A. B., Thaller, M. L., Penny, L. R., & Peters, G. J. (1998). *ApJ*, 493, 440.
- Gillessen, S., Eisenhauer, F., Trippe, S., Alexander, T., Genzel, R., Martins, F., & Ott, T. (2009). *ApJ*, 692, 1075.
- Gnedin, O. Y., Gould, A., Miralda-Escudé, J., & Zentner, A. R. (2005). *ApJ*, 634, 344.
- Gontcharov, G. A. (2006). *Astron. Lett.* 32, 759.
- González Hernández, J. I., Ruiz-Lapuente, P., Filippenko, A. V., Foley, R. J., Gal-Yam, A., & Simon, J. D. (2009). *ApJ*, 691, 1.
- González Hernández, J. I., Ruiz-Lapuente, P., Tabernero, H. M., Montes, D., Canal, R., Méndez, J., & Bedin, L. R. (2012). *Nature*, 489, 533.
- González-Galán, A., Oskinova, L. M., Popov, S. B., Haberl, F., Kühnel, M., Gallagher, J., . . . Guerrero, M. A. (2018). *MNRAS*, 475, 2809.
- Gould, A. (1997). *arXiv:astro-ph/9709263*.
- Gould, A. (1999). *ApJ*, 525, 734.
- Green, D. A. (2011). *Bull. Astron. Soc. India*, 39, 289.
- Green, D. A. (2014). *Bull. Astron. Soc. India*, 42, 47.
- Green, D. A., & Stephenson, F. R. (2003). Historical Supernovae. In *Supernovae and gamma-ray bursters* (Vol. 598, p. 7). Lecture Notes in Physics. Springer.
- Green, G. M., Schlafly, E. F., Finkbeiner, D., Rix, H.-W., Martin, N., Burgett, W., . . . Waters, C. (2018). *MNRAS*, 478, 651.
- Green, G. M., Schlafly, E. F., Finkbeiner, D. P., Rix, H.-W., Martin, N., Burgett, W., . . . Wainscoat, R. (2015). *ApJ*, 810, 25.
- Greenstein, J. L. (1957). *AJ*, 62, 16.

- Gualandris, A., & Portegies Zwart, S. (2007). *MNRAS*, 376, L29.
- Gualandris, A., Portegies Zwart, S., & Sipior, M. S. (2005). *MNRAS*, 363, 223.
- Guillochon, J., Parrent, J., Kelley, L. Z., & Margutti, R. (2017). *ApJ*, 835, 64.
- Guo, Q., White, S., Li, C., & Boylan-Kolchin, M. (2009). *MNRAS*, 404, 1111.
- Guseinov, O. H., Ankay, A., & Tagieva, S. O. (2005). *Astrophysics*, 48, 330.
- Halley, E. (1717). *Philos. Trans.* 30, 736.
- Han, Z. (2008). *ApJ*, 677, L109.
- Hansen, B. M. S., & Phinney, E. S. (1997). *MNRAS*, 291, 569.
- Hansen, C. J., Kawaler, S. D., & Trimble, V. (2004). *Stellar Interiors: Physical Principles, Structure, and Evolution* (2nd ed.). New York: Springer-Verlag.
- Harmanec, P. (1987). Emission-line stars as interacting binaries. In *Iau colloq. 92 phys. be stars* (p. 339). Cambridge: CUP.
- Harmanec, P., Koubský, P., & Krpata, J. (1972). *Astrophys. Lett.* 11, 119.
- Harris, J., & Zaritsky, D. (2009). *AJ*, 138, 1243.
- Hartman, J. W. (1997). *A&A*, 322, 127.
- Hattori, K., Valluri, M., & Castro, N. (2018). *arXiv:1804.08590*.
- Heber, U., Edelmann, H., Napiwotzki, R., Altmann, M., & Scholz, R.-D. (2008). *A&A*, 483, L21.
- Heger, A., Fryer, C. L., Woosley, S. E., Langer, N., & Hartmann, D. H. (2003). *ApJ*, 591, 288.
- Helfand, D. J., Taylor, J. H., & Manchester, R. N. (1977). *ApJ*, 213, L1.
- Hernquist, L. (1990). *ApJ*, 356, 359.
- Hillebrandt, W., & Niemeyer, J. C. (2000). *ARA&A*, 38, 191.
- Hills, J. G. (1988). *Nature*, 331, 687.
- Hirsch, H. A., Heber, U., O'Toole, S. J., & Bresolin, F. (2005). *A&A*, 444, L61.
- Hobbs, G., Lorimer, D. R., Lyne, A. G., & Kramer, M. (2005). *MNRAS*, 360, 974.
- Hoffman, M. D., & Gelman, A. (2011). *arXiv:1111.4246*.
- Høg, E., Fabricius, C., Makarov, V. V., Urban, S., Corbin, T., Wycoff, G., ... Wicenec, A. (2000). *A&A*, 355, L27.
- Hoogerwerf, R., de Bruijne, J. H. J., & de Zeeuw, P. T. (2001). *A&A*, 365, 49.
- Hou, W., Luo, A.-L., Hu, J.-Y., Yang, H.-F., Du, C.-D., Liu, C., ... Hou, Y.-H. (2016). *Res. Astron. Astrophys.* 16, 138.
- Huang, Y., Liu, X.-W., Zhang, H.-W., Chen, B.-Q., Xiang, M.-S., Wang, C., ... Wang, B. (2017). *ApJ*, 847, L9.
- Humphreys, R. M. (1978). *ApJS*, 38, 309.



- Hunter, J. D. (2007). *Comput. Sci. Eng.* 9(3), 90.
- Hurley, J. R., Pols, O. R., & Tout, C. A. (2000). *MNRAS*, 315, 543.
- Hurley, J. R., Tout, C. A., & Pols, O. R. (2002). *MNRAS*, 329, 897.
- Irrgang, A., Przybilla, N., Heber, U., Nieva, M. F., & Schuh, S. (2010). *ApJ*, 711, 138.
- Israelian, G., Rebolo, R., Basri, G., Casares, J., & Martín, E. L. (1999). *Nature*, 401, 142.
- Ivanova, N., Justham, S., Chen, X., De Marco, O., Fryer, C. L., Gaburov, E., . . . Webbink, R. F. (2013). *A&ARv*, 21, 59.
- Izzard, R. G., Dray, L. M., Karakas, A. I., Lugaro, M., & Tout, C. A. (2006). *A&A*, 460, 565.
- Izzard, R. G., Glebbeek, E., Stancliffe, R. J., & Pols, O. R. (2009). *A&A*, 508, 1359.
- Izzard, R. G., Hall, P. D., Tauris, T. M., & Tout, C. A. (2012). Common envelope evolution. In *Planetary nebulae: An eye to the future* (Vol. 283, p. 95). Proceedings of the International Astronomical Union. CUP.
- Izzard, R. G., Preece, H., Jofre, P., Halabi, G. M., Masseron, T., & Tout, C. A. (2018). *MNRAS*, 473, 2984.
- Izzard, R. G., Tout, C. A., Karakas, A. I., & Pols, O. R. (2004). *MNRAS*, 350, 407.
- Jaschek, M., Slettebak, A., & Jaschek, C. (1981). *Be Star Newsl.* 4, 9.
- Jerkstrand, A., Smartt, S. J., Fraser, M., Fransson, C., Sollerman, J., Taddia, F., & Kotak, R. (2014). *MNRAS*, 439, 3694.
- Jethwa, P., Erkal, D., & Belokurov, V. (2016). *MNRAS*, 461, 2212.
- Jing, Y., Du, C., Gu, J., Jia, Y., Peng, X., Chen, Y., . . . Zhang, Y. (2016). *MNRAS*, 463, 3390.
- Johnson, D. R. H., & Soderblom, D. R. (1987). *AJ*, 93, 864.
- Jones, E., Oliphant, T., Peterson, P., et al. (2001). *SciPy: Open source scientific tools for Python*.
- Jordi, C., Gebran, M., Carrasco, J. M., de Bruijne, J., Voss, H., Fabricius, C., . . . Mora, A. (2010). *A&A*, 523, A48.
- Justham, S., Wolf, C., Podsiadlowski, P., & Han, Z. (2009). *A&A*, 493, 1081.
- Kallivayalil, N., van der Marel, R. P., Besla, G., Anderson, J., & Alcock, C. (2013). *ApJ*, 764, 161.
- Kapteyn, J. C. (1898). *Astron. Nachrichten*, 145(9), 159.
- Kass, R. E., & Raftery, A. E. (1995). *J. Am. Stat. Assoc.* 90(430), 773.
- Kenyon, S. J., Bromley, B. C., Brown, W. R., & Geller, M. J. (2014). *ApJ*, 793, 122.
- Kenyon, S. J., Bromley, B. C., Geller, M. J., & Brown, W. R. (2008). *ApJ*, 680, 312.
- Kepler, S. O., Koester, D., & Ourique, G. (2016). *Science*, (6281), 67.

- Kerzendorf, W. E., Childress, M., Scharwächter, J., Do, T., & Schmidt, B. P. (2014). *ApJ*, 782, 27.
- Kerzendorf, W. E., Schmidt, B. P., Asplund, M., Nomoto, K., Podsiadlowski, P., Frebel, A., . . . Yong, D. (2009). *ApJ*, 701, 1665.
- Kerzendorf, W. E., Yong, D., Schmidt, B. P., Simon, J. D., Jeffery, C. S., Anderson, J., . . . Foley, R. J. (2013). *ApJ*, 774, 99.
- Kharchenko, N. V., Scholz, R.-D., Piskunov, A. E., Röser, S., Schilbach, E., Kharchenko, N. V., . . . Schilbach, E. (2007). *Astron. Nachrichten*, 328, 889.
- Kobulnicky, H. A., & Fryer, C. L. (2007). *ApJ*, 670, 747.
- Kobulnicky, H. A., Kiminki, D. C., Lundquist, M. J., Burke, J., Chapman, J., Keller, E., . . . Brotherton, M. M. (2014). *ApJS*, 213, 34.
- Kochanek, C. S. (2017a). *MNRAS*, 471, 3283.
- Kochanek, C. S. (2017b). *MNRAS*, 473, 1633.
- Kogure, T., & Leung, K.-C. (2014). *The Astrophysics of Emission-Line Stars (Astrophysics and Space Science Library)*. Springer.
- Koo, B.-C., Reach, W. T., Heiles, C., Fesen, R. A., & Shull, J. M. (1990). *ApJ*, 364, 178.
- Koo, B.-C., Yun, M.-S., Ho, P. T. P., & Lee, Y. (1993). *ApJ*, 417, 196.
- Kouwenhoven, M. B. N., Brown, A. G. A., Zwart, S. F. P., & Kaper, L. (2007). *A&A*, 474, 77.
- Kroupa, P. (2001). *MNRAS*, 322, 231.
- Lada, C. J., & Lada, E. A. (2003). *ARA&A*, 41, 57.
- Leahy, D. A., & Ranasinghe, S. (2012). *MNRAS*, 423, 718.
- Leahy, D. A., & Tian, W. W. (2007). *A&A*, 461, 1013.
- Lennon, D. J., Evans, C. J., van der Marel, R. P., Anderson, J., Platais, I., Herrero, A., . . . Schneider, F. R. N. (2018). *arXiv:1805.08277*.
- Lennon, D. J., van der Marel, R. P., Lerate, M. R., O'Mullane, W., & Sahlmann, J. (2016). *A&A*, 603, A75.
- Li, W., Bloom, J. S., Podsiadlowski, P., Miller, A. A., Cenko, S. B., Jha, S. W., . . . Shen, K. J. (2011). *Nature*, 480, 348.
- Li, W., Chornock, R., Leaman, J., Filippenko, A. V., Poznanski, D., Wang, X., . . . Mannucci, F. (2011). *MNRAS*, 412, 1473.
- Li, Y.-B., Luo, A.-L., Zhao, G., Lu, Y.-J., Wei, P., Du, B., . . . Yang, M. (2015). *Res. Astron. Astrophys.* 15, 1364.
- Li, Y., Luo, A., Zhao, G., Lu, Y., Ren, J., & Zuo, F. (2012). *ApJ*, 744, L24.
- Lindgren, L., Hernandez, J., Bombrun, A., Klioner, S., Bastian, U., Ramos-Lerate, M., . . . Vecchiato, A. (2018). *A&A*.
- Liu, Z.-W., Tauris, T. M., Röpke, F. K., Moriya, T. J., Kruckow, M., Stancliffe, R. J., & Izzard, R. G. (2015). *A&A*, 584, A11.
- Lu, Y., Yu, Q., & Lin, D. N. C. (2007). *ApJ*, 666, L89.
- Lu, Y., Zhang, F., & Yu, Q. (2010). *ApJ*, 709, 1356.

- Luo, A.-L., Zhao, Y.-H., Zhao, G., Deng, L.-C., Liu, X.-W., Jing, Y.-P., ... Zuo, F. (2016). *VizieR On-line Data Cat. V/149*.
- Luri, X., A Brown, A. G., Sarro, L., Arenou, F., Bailer-Jones, C. A., Castro-Ginard, A., ... Delgado, H. E. (2018). *A&A*.
- Lyne, A. G., & Graham-Smith, F. (1998). *Pulsar astronomy* (2nd ed.). Cambridge Astrophysics Series: 31. Cambridge: CUP.
- Mackey, A. D., Koposov, S. E., Erkal, D., Belokurov, V., Da Costa, G. S., & Gómez, F. A. (2016). *MNRAS*, 459, 239.
- Maeda, K., Kutsuna, M., & Shigeyama, T. (2014). *ApJ*, 794, 37.
- Manchester, R. N., Hobbs, G. B., Teoh, A., & Hobbs, M. (2005). *AJ*, 129, 1993.
- Manchester, R. N., Taylor, J. H., & Van, Y. Y. (1974). *ApJ*, 189, L119.
- Mannucci, F., Della Valle, M., Panagia, N., Cappellaro, E., Cresci, G., Maiolino, R., ... Turatto, M. (2005). *A&A*, 433, 807.
- Marchetti, T., Contigiani, O., Rossi, E. M., Albert, J. G., Brown, A. G. A., & Sesana, A. (2018). *MNRAS*, 476, 4697.
- Marchetti, T., Rossi, E. M., Kordopatis, G., Brown, A. G. A., Rimoldi, A., Starkenburg, E., ... Ashley, R. (2017). *MNRAS*, 470, 1388.
- Martin, J. C. (2006). *AJ*, 131, 3047.
- Martin, P., Jeffery, C. S., N., N., & Woolf, V. M. (2017). *MNRAS*, 467, 68.
- Martins, F., Mahy, L., Hillier, D. J., & Rauw, G. (2012). *A&A*, 538, 39.
- Maund, J. R., & Smartt, S. J. (2009). *Science*, 324, 486.
- McCully, C., Jha, S. W., Foley, R. J., Bildsten, L., Fong, W.-F., Kirshner, R. P., ... Stritzinger, M. D. (2014). *Nature*, 512, 54.
- McKinney, W. (2010). Data Structures for Statistical Computing in Python. In S. van der Walt & J. Millman (Eds.), *Proceedings of the 9th python in science conference* (p. 51).
- Mel'Nik, A. M., & Dambis, A. K. (2009). *MNRAS*, 400, 518.
- Meyer, L., Ghez, A. M., Schoedel, R., Yelda, S., Boehle, A., Lu, J. R., ... Matthews, K. (2012). *Science*, 338, 84.
- Michalik, D., Lindegren, L., & Hobbs, D. (2015). *A&A*, 574, A115.
- Miyamoto, M., & Nagai, R. (1975). *PASJ*, 27, 533.
- Moni Bidin, C., Casetti-Dinescu, D. I., Girard, T. M., Zhang, L., Mendez, R. A., Vieira, K., ... van Altena, W. F. (2017). *MNRAS*, 466(3), 3077.
- Munn, J. A., Monet, D. G., Levine, S. E., Canzian, B., Pier, J. R., Harris, H. C., ... Brinkmann, J. (2008). *AJ*, 136, 895.
- Munn, J. A., Monet, D. G., Levine, S. E., Canzian, B., Pier, J. R., Harris, H. C., ... Brinkmann, J. (2004). *AJ*, 127, 3034.
- Navarro, J. F., Frenk, C. S., & White, S. D. M. (1997). *ApJ*, 490, 493.
- Nazé, Y., Rauw, G., & Cazorla, C. (2017). *A&A*, 602, L5.

- Neiner, C., de Batz, B., Cochard, F., Floquet, M., Mekkas, A., & Desnoux, V. (2011). *AJ*, 142, 149.
- Nelemans, G., Tauris, T. M., & van den Heuvel, E. P. J. (1999). *A&A*, 352, L87.
- Németh, P., Ziegerer, E., Irrgang, A., Geier, S., Fürst, F., Kupfer, T., & Heber, U. (2016). *ApJ*, 821, L13.
- Noda, K., Suda, T., & Shigeyama, T. (2016). *PASJ*, 68, 11.
- Odegard, N. (1986). *ApJ*, 301, 813.
- Öpik, E. (1924). *Publ. Tartu Astrofiz. Obs.* 25.
- Paczynski, B. (1986). *ApJ*, 304, 1.
- Palladino, L. E., Schlesinger, K. J., Holley-Bockelmann, K., Allende Prieto, C., Beers, T. C., Lee, Y. S., & Schneider, D. P. (2014). *ApJ*, 780, 7.
- Pan, K.-C., Ricker, P. M., & Taam, R. E. (2014). *ApJ*, 792, 71.
- Pavlovic, M. Z., Dobardzic, A., Vukotic, B., & Urosevic, D. (2014). *Serbian Astron. J.* 189, 25.
- Peñarrubia, J., Gómez, F. A., Besla, G., Erkal, D., & Ma, Y.-Z. (2015). *MNRAS*, 456, L54.
- Pereira, C. B., Jilinski, E., Drake, N. A., de Castro, D. B., Ortega, V. G., Chavero, C., & Roig, F. (2012). *A&A*, 543, A58.
- Perets, H. B. (2009). *ApJ*, 690, 795.
- Perets, H. B., & Šubr, L. (2012). *ApJ*, 751, 133.
- Perryman, M. (2012). *Astrometry for astrophysics : methods, models, and applications* (W. F. van Altena, Ed.). Cambridge: Cambridge University Press.
- Peters, G. J., Gies, D. R., Grundstrom, E. D., & McSwain, M. V. (2008). *ApJ*, 686, 1280.
- Peters, G. J., Pewett, T. D., Gies, D. R., Touhami, Y. N., & Grundstrom, E. D. (2013). *ApJ*, 765, 2.
- Peters, G. J., Wang, L., Gies, D. R., & Grundstrom, E. D. (2016). *ApJ*, 828, 47.
- Pfahl, E., Rappaport, S., Podsiadlowski, P., & Spruit, H. (2001). *ApJ*, 574, 364.
- Pflamm-Altenburg, J., & Kroupa, P. (2010). *MNRAS*, 404, 1564.
- Phillips, A. P., Gondhalekar, P. M., & Blades, J. C. (1981). *MNRAS*, 195, 485.
- Piatti, A. E., & Geisler, D. (2013). *AJ*, 145, 17.
- Piazzzi, G. (1803). *Palermo Tip. Reg.*, 1803; XL, 76 p. ; folio; DCCC. f. 3.
- Pietrzyński, G., Graczyk, D., Gieren, W., Thompson, I. B., Pilecki, B., Udalski, A., ... Karczmarek, P. (2013). *Nature*, 495, 76.
- Pineault, S., Landecker, T. L., Madore, B., & Gaumont-Guay, S. (1993). *AJ*, 105, 1060.

- Podsiadlowski, P., Pfahl, E., & Rappaport, S. (2005). Neutron-Star Birth Kicks. In *Binary radio pulsars* (Vol. 328, p. 327). Astronomical Society of the Pacific Conference Series.
- Pols, O. R., Cote, J., Waters, L. B. F. M., & Heise, J. (1991). *A&A*, 241, 419.
- Popper, D. M. (1988). *AJ*, 95, 1242.
- Portegies Zwart, S. F. (2000). *ApJ*, 544, 437.
- Poveda, A., Ruiz, J., & Allen, C. (1967). *Bol. los Obs. Tonantzintla y Tacubaya*, 4, 86.
- Przybilla, N., Nieva, M. F., Heber, U., Firnstein, M., Butler, K., Napiwotzki, R., & Edelmann, H. (2008). *A&A*, 480, L37.
- Raddi, R., Hollands, M. A., Gaensicke, B. T., Townsley, D. M., Hermes, J. J., Fusillo, N. P. G., & Koester, D. (2018). *MNRAS*.
- Raghavan, D., McAlister, H. A., Henry, T. J., Latham, D. W., Marcy, G. W., Mason, B. D., . . . ten Brummelaar, T. A. (2010). *ApJS*, 190, 1.
- Reed, B. C. (2003). *AJ*, 125, 2531.
- Reig, P. (2011). *Astrophys. Space Sci.* 332, 1.
- Reines, A. E., Greene, J. E., & Geha, M. (2013). *ApJ*, 775, 116.
- Reynolds, S. P. (2008). *ARA&A*, 46, 89.
- Ridley, J. P., & Lorimer, D. R. (2010). *MNRAS*, 406, L80.
- Rinehart, S. A. (2000). *MNRAS*, 312, 429.
- Rivinius, T., Štefl, S., & Baade, D. (2006). *A&A*, 459, 137.
- Rivinius, T., Carciofi, A. C., & Martayan, C. (2013). *A&ARv*, 21, 69.
- Robitaille, T. P., & Whitney, B. A. (2010). *ApJ*, 710, L11.
- Rossi, E. M., Marchetti, T., Cacciato, M., Kuiack, M., & Sari, R. (2017). *MNRAS*, 467, 1844.
- Ruiz-Lapuente, P., Comeron, F., Méndez, J., Canal, R., Smartt, S. J., Filippenko, A. V., . . . Ibata, R. (2004). *Nature*, 431, 1069.
- Rybizki, J., Demleitner, M., Fouesneau, M., Bailer-Jones, C., Rix, H.-W., & Andrae, R. (2018). *PASP*, 130, 074101.
- Sallmen, S., & Welsh, B. Y. (2004). *A&A*, 426, 555.
- Sana, H., de Mink, S. E., de Koter, A., Langer, N., Evans, C. J., Gieles, M., . . . Schneider, F. R. N. (2012). *Science*, 337, 444.
- Schaefer, B. E., & Pagnotta, A. (2012). *Nature*, 481, 164.
- Schlafly, E. F., & Finkbeiner, D. P. (2011). *ApJ*, 737, 103.
- Schlegel, D. J., Finkbeiner, D. P., & Davis, M. (1998). *ApJ*, 500, 525.
- Schneider, F. R. N., Izzard, R. G., de Mink, S. E., Langer, N., Stolte, A., de Koter, A., . . . Sana, H. (2014). *ApJ*, 780, 117.
- Schönrich, R. (2012). *MNRAS*, 427, 274.
- Schönrich, R., Binney, J., & Dehnen, W. (2010). *MNRAS*, 403, 1829.
- Schultz, G. V., & Wiemer, W. (1975). *A&A*, 43, 133.

- Scott, D. W. (2015). *Multivariate density estimation: theory, practice, and visualization* (2nd ed.). Hoboken: John Wiley & Sons.
- Shen, K. J., & Schwab, J. (2016). *ApJ*, 834, 180.
- Shen, K. J., Boubert, D., Gänsicke, B. T., Jha, S. W., Andrews, J. E., Chomiuk, L., . . . Townsley, D. M. (2018). *ApJ*.
- Sherwin, B. D., Loeb, A., & O'Leary, R. M. (2008). *MNRAS*, 386, 1179.
- Skilling, J. (2006). *Bayesian Anal.* 1(4), 833.
- Slettebak, A., Wagner, R. M., & Bertram, R. (1997). *PASP*, 109, 1.
- Smartt, S. J. (2009). *ARA&A*, 47, 63.
- Smith, N., & Tombleson, R. (2015). *MNRAS*, 447, 598.
- Smits, R., Kramer, M., Stappers, B., Lorimer, D. R., Cordes, J., & Faulkner, A. (2009). *A&A*, 493, 1161.
- Spera, M., Mapelli, M., & Bressan, A. (2015). *MNRAS*, 451, 4086.
- Springel, V. (2005). *MNRAS*, 364, 1105.
- Stephenson, F. R., & Green, D. A. (2002). *Historical supernovae and their remnants*. Oxford: Clarendon Press.
- Struve, O. (1931). *ApJ*, 73, 94.
- Tatematsu, K., Fukui, Y., Landecker, T. L., & Roger, R. S. (1990). *A&A*, 237, 189.
- Tauris, T. M., & Takens, R. J. (1998). *A&A*, 330, 1047.
- Tauris, T. M. (2015). *MNRAS*, 448, L6.
- Tauris, T. M., & Dewi, J. D. M. (2001). *A&A*, 369, 170.
- Tetzlaff, N., Dinçel, B., Neuhäuser, R., & Kovtyukh, V. V. (2014). *MNRAS*, 438, 3587.
- The SDSS-II SEGUE Collaboration, Yanny, B., Rockosi, C., Newberg, H. J., Knapp, G. R., Allam, S., . . . Zucker, D. (2009). *AJ*, 137, 4377.
- Tillich, A., Geier, S., Heber, U., Hirsch, H., Maxted, P., Gänsicke, B., . . . Copperwheat, C. (2009). *J. Phys. Conf. Ser.* 172, 12009.
- Tollerud, E. J., Boylan-Kolchin, M., Barton, E. J., Bullock, J. S., & Trinh, C. Q. (2011). *ApJ*, 738, 102.
- Townsend, R. H. D., Owocki, S. P., & Howarth, I. D. (2004). *MNRAS*, 350, 189.
- Uyaniker, B., Kothes, R., & Brunt, C. M. (2002). *ApJ*, 565, 1022.
- van den Heuvel, E. P. J., Portegies Zwart, S. F., Bhattacharya, D., & Kaper, L. (2000). *A&A*, 364, 563.
- van der Marel, R. P. (2015). Local Group Proper Motion Dynamics. In *Iau colloq. 311: Galaxy masses as constraints of formation models* (p. 1). Cambridge: CUP.
- van der Marel, R. P., & Kallivayalil, N. (2014). *ApJ*, 781, 121.
- van der Walt, S., Colbert, S. C., & Varoquaux, G. (2011). *Comput. Sci. Eng.* 13(2), 22.

- van Leeuwen, F. (2007). *Hipparcos, the New Reduction of the Raw Data* (F. van Leeuwen, Ed.). Astrophysics and Space Science Library. Dordrecht: Springer Netherlands.
- van Rensbergen, W., Vanbeveren, D., & De Loore, C. (1996). *A&A*, 305, 825.
- Vennes, S., Nemeth, P., Kawka, A., Thorstensen, J. R., Khalack, V., Ferrario, L., & Alper, E. H. (2017). *Science*, 357, 680.
- Vickers, J. J., Smith, M. C., & Grebel, E. K. (2015). *AJ*, 150, 77.
- Voroshilov, V. I., Guseva, N. G., Kalandadze, N. B., Kolesnik, L. N., Kuznetsov, V. I., Metreveli, M. D., & Shapovalov, A. N. (1985). *Catalog of BV magnitudes and spectral classes of 6000 stars*. Kiev: Izdatel'stvo Naukova Dumka.
- Wang, L., Gies, D. R., & Peters, G. J. (2017). *ApJ*, 843, 60.
- Wang, X., & Loeb, A. (2017). *New Astron.* 61, 95.
- Wenger, M., Ochsenbein, F., Egret, D., Dubois, P., Bonnarel, F., Borde, S., ... Monier, R. (2000). *Astron. Astrophys. Suppl. Ser.* 143, 9.
- Williams, A. A., Belokurov, V., Casey, A. R., & Evans, N. W. (2017). *MNRAS*, 468, 2359.
- Wilson, R. E. (1953). *General catalogue of stellar radial velocities*. Washington D.C.: Carnegie Institute.
- Xiao, L., & Zhu, M. (2012). *A&A*, 545, A86.
- Xue, X. X., Rix, H. W., Zhao, G., Re Fiorentin, P., Naab, T., Steinmetz, M., ... Schneider, D. P. (2008). *ApJ*, 684, 1143.
- Xue, Z., & Schaefer, B. E. (2015). *ApJ*, 809, 183.
- Yanoff, M., & Duker, J. S. (2009). *Ophthalmology* (J. J. Augsburger, Ed.). Elsevier Health Sciences.
- Yao, J. M., Manchester, R. N., & Wang, N. (2017). *ApJ*, 835, 29.
- Yar-Uyaniker, A., Uyaniker, B., & Kothes, R. (2004). *ApJ*, 616, 247.
- Yoshita, K. (2001). *Ph.D. thesis*. Osaka Univ.
- Yu, Q., & Tremaine, S. (2003). *ApJ*, 599, 1129.
- Zacharias, N., Monet, D. G., Levine, S. E., Urban, S. E., Gaume, R., & Wycoff, G. L. (2005). *VizieR On-line Data Cat.* 1297.
- Zapartas, E., de Mink, S. E., Van Dyk, S. D., Fox, O. D., Smith, N., Bostroem, K. A., ... Ryder, S. (2017). *ApJ*, 842, 125.
- Zapartas, E., de Mink, S. E., Izzard, R. G., Yoon, S.-C., Badenes, C., Götberg, Y., ... Shrotriya, T. S. (2017). *A&A*, 601, A29.
- Zhang, F., Lu, Y., & Yu, Q. (2010). *ApJ*, 722, 1744.
- Zhang, F., Lu, Y., & Yu, Q. (2013). *ApJ*, 768, 153.
- Zhang, L., Bidin, C. M., Casetti-Dinescu, D. I., Méndez, R. A., Girard, T. M., Korchagin, V. I., ... Zhao, G. (2017). *ApJ*, 835, 285.
- Zhao, H. (1998). *MNRAS*, 294, 139.
- Zheng, Z., Carlin, J. L., Beers, T. C., Deng, L., Grillmair, C. J., Guhathakurta, P., ... Zhang, Y. (2014). *ApJ*, 785, L23.

- Ziegerer, E., Volkert, M., Heber, U., Irrgang, A., Gänsicke, B. T., & Geier, S. (2015). *A&A*, 576, L14.
- Zorec, J., & Briot, D. (1997). *A&A*, 318, 443.



## COLOPHON

This document was typeset using the typographical look-and-feel `classicthesis` developed by André Miede and Ivo Pletikosić.

*Final Version* as of October 8, 2018 (`classicthesis` version 0.1).